LIÈGE université
Sciences Appliquées

Optimized carbon supports for durable and high performance PEMFC electrodes

A thesis submitted in partial fulfillment of the requirements
for the degree of Doctor of Philosophy (PhD) in Engineering Sciences

by

Bryan CARRE

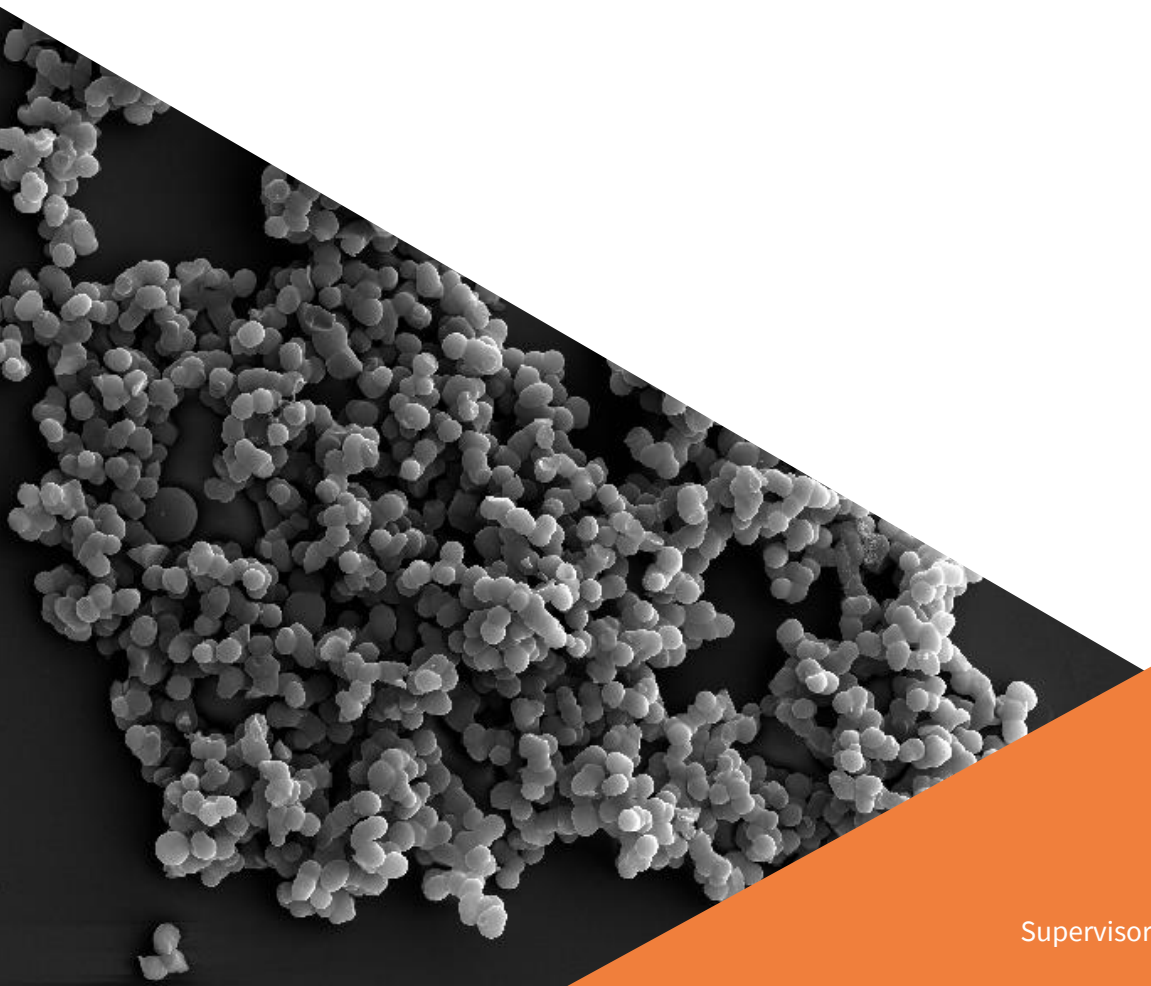

Supervisor: Nathalie JOB

DOCTORAL COLLEGE IN CHEMICAL ENGINEERING

APRIL 2026

Use of generative AI

Generative AI assistance tools were not used in this thesis, except for basic language assistance. The different figures presented in this thesis are my own, unless otherwise specified. Figures that are not my own were properly referenced and attributed to their rightful authors. Moreover, this thesis manuscript has been reviewed and edited by myself, and I take responsibility for the content presented in this thesis.

Acknowledgments

I would first like to thank my supervisor, Prof. Nathalie Job. Throughout the four years of my doctoral journey, Prof. Job has provided great guidance and was always available for support. I am truly grateful to have conducted a thesis under her supervision.

Then, I would like to thank Prof. Grégoire Léonard from Université de Liège and Prof. Philippe Vereecken from KU Leuven, who are members of my jury and were also part of my thesis committee. During my thesis, they have regularly provided constructive feedback that contributed to the development of my work. I would also like to thanks Prof. Motiar Rahaman from Université de Liège. Despite his relatively recent tenure, he has accepted to be part of my jury, and take time to review my work. I am thankful for that. Finally, I would also like to thank Prof. Jon Ustarroz Troyano from Université Libre de Bruxelles and Prof. Sara Cavalière, from Institut Charles Gerhardt Montpellier. They also accepted to be part of my jury and I appreciate the time they dedicated to evaluate my work.

I would like to also thank scientists who have helped me during my thesis. First, I am grateful to Dr. Alexandre F. Léonard, from the CARPOR platform in Université of Liège. Throughout my thesis, he provided valuable training and performed numerous measurements presented here. I also want to thank Dr. Cédric Vandenabeele and Driélle Müller da Silva, from Innovative Coating Solutions and Université de Namur, with whom I collaborated on the nitrogen-doping treatment described in this thesis. They have also been of immense help regarding the XPS analysis performed on my samples. I also want to thank Prof. Philippe Compère from Université of Liège, for his availability and assistance regarding the use of the Transmission Electron Microscope. Finally, I would also like to thank Dr. Jimena Castro-Guttiérez and Prof. Vanessa Fierro, from Institut Jean Lamour in Epinal, France. I am grateful for the collaboration we had.

I also want to thank the community of BE-HyFE project and all the PhD students involved with the project, as well as Marijke Mahieu. Over these four years, we have participated in numerous events, and had great discussions, on hydrogen-related topics, but not only.

Obviously, I would like to thank the Chemical Engineering department members from Université of Liège. This includes all the professors, post-doctoral researchers, and PhDs students I had the chance to meet throughout my thesis. I would like to thank particularly the

great people of the NCE group, in particular Dr. Berke Karaman, Tom Servais and Zoé Deckers with whom I shared so many memorable memories. I am glad to have met all of you.

Most importantly, I would like to thank my fiancée, Ezgi Uslu. I wouldn't have gotten this far without you. Thank you for sharing your life with me and for always being present for me. Last but not least, I would like to thank my family for the unconditional support they provided.

Abstract

This thesis aimed at developing an optimized carbon material to serve as a durable catalyst support in Proton Exchange Membrane Fuel Cell (PEMFC) electrodes. This optimization is crucial to mitigate the degradation phenomena encountered in these electrodes (such as migration, agglomeration or detachment of the active catalytic phase). To achieve this, a carbon xerogel (CX) was synthesized and subsequently modified through three post-treatments strategies. CXs were specifically selected as base materials in this thesis because their pore texture can be tailored to minimize mass transport limitations within the electrodes. The first post-treatment strategy consisted in the deposition of a secondary graphitizable carbon layer by Chemical Vapor Deposition (CVD). In a second step, CVD was followed by exposure at high temperature (1,500 ºC) under inert atmosphere to further graphitize the deposited carbon layer. A third post-treatment strategy consisted in the incorporation of nitrogen-containing groups at the surface of the CX with a N_2-based plasma treatment. This treatment was performed to increase the interaction between the carbon support and the Pt nanoparticles, so as to improve the durability of the catalytic layer.

Pt/CX catalysts (20 wt.% Pt) were obtained by depositing Pt nanoparticles onto the surface of the pristine and post-treated CXs *via* a formic acid reduction method. The complete electrochemical characterization of all Pt/CX catalysts was performed. To do so, the ElectroChemically Active Surface Area of Pt (*ECSA*, *i.e.* its exposed surface) and the catalytic activity towards oxygen reduction reaction were measured, both in Rotating Disk Electrode (RDE) and in Membrane-Electrodes Assembly (MEA) configurations. The electrochemical performances were benchmarked against those of a commercial carbon black-supported catalyst. Finally, the *ECSA* and catalytic activity towards ORR were evaluated upon accelerated aging. This evaluation was first conducted in RDE configuration in 0.5 M H_2SO_4 electrolyte, after 5,000 and 20,000 cycles of potential between 0.6 and 1.0 V *vs.* RHE at 80 ºC. The evaluation was then also carried out in MEA configuration, after 10,000 and 30,000 cycles of potentials holds at 0.6 and 1.0 V *vs.* RHE at 70 ºC.

It was observed that the secondary carbon layer deposited by CVD treatment covers the micropores but does not modify the meso/macroporosity of the CX, which is essential for ensuring proper gas transport and metal nanoparticle deposition. This secondary layer was

found to exhibit a graphitizable nature with an increase in crystallinity after the high temperature treatment. Regarding the catalytic performances of the different catalysts, the values of catalytic activities were found higher with post-treated CXs. Upon accelerated aging of the corresponding catalysts, the catalytic behavior observed for both the pristine and post-treated CXs was relatively similar, with an increase in specific activity (*i.e.* the current normalized by the accessible Pt surface area), while the mass activity (*i.e.* the current normalized by the total Pt mass) remained rather constant. Indeed, there is an optimal Pt nanoparticle diameter (~3 nm) at which the available *ECSA* is maximized and the surface atoms of Pt exhibit a balanced reactivity towards ORR. The approach or deviation from this optimal size was used to explain this electrocatalytic behavior. However, the presence of the CVD layer does not appear to significantly reduce nor aggravate Pt nanoparticles agglomeration upon aging. In MEA configuration, the catalyst based on the CX treated by CVD followed by graphitization at high-temperature exhibited the highest catalytic performances retention after aging. This approach thus appears promising to obtain more durable catalytic layers.

Regarding N-doping, nitrogen was introduced onto the carbon surface without altering the pore structure of the CX. However, in terms of catalytic performances observed upon aging, N-doped CXs behaved very similarly to their undoped counterpart, both in RDE and MEA configuration. These results are less optimistic than those generally reported in the literature. However, the interplay of modifications possibly induced by the nitrogen doping treatment, such as changes in Pt nanoparticles size in the fresh catalyst, can make it difficult to properly compare materials, and may lead to biased conclusions. Overall, these results highlight that, while tailoring the carbon support surface to improve the catalytic layer durability is achievable, improving significantly the catalyst durability remains challenging.

Résumé

L'objectif de cette thèse consiste à développer et optimiser un matériau carboné pour une utilisation en tant que support de catalyseur durable dans les couches catalytiques de piles à combustible à membranes échangeuses de protons (Proton Exchange Membrane Fuel Cell – PEMFC). L'optimisation de ce matériau est cruciale pour atténuer les phénomènes de dégradation rencontrés dans ces couches catalytiques, comme la migration, l'agglomération ou le détachement de la phase active catalytique (nanoparticules de Pt). Dans cette optique, un xérogel de carbone a été synthétisé, puis sa surface a été modifiée en utilisant trois post-traitements distincts. Les xérogels de carbone ont été utilisés comme matériau de base dans cette thèse en raison de leur texture poreuse qui peut être aisément optimisée afin de minimiser les limitations dues au transport de matière rencontré dans les électrodes de PEMFC. Le premier post-traitement correspond au dépôt d'une couche de carbone secondaire à la surface du xérogel *via* un dépôt chimique en phase vapeur (Chemical Vapor Deposition – CVD). Ce traitement a été suivi par l'exposition du matériau carboné à une haute température (1.500 ºC) sous atmosphère inerte. Ce second traitement a été réalisé pour graphitiser davantage la couche de carbone déposée. Enfin, le xérogel de carbone a été soumis à un troisième post-traitement, consistant en un traitement au plasma en utilisant N_2 en tant que précurseur azoté. Ce traitement vise à incorporer des groupements azotés à la surface du carbone, afin d'améliorer l'interaction entre le support carboné et le platine, en vue d'accroître la durabilité de la couche catalytique.

Des catalyseurs ont ensuite été élaborés par dépôt de nanoparticules de Pt (20% en masse) à la surface des xérogels de carbone traités et non traité ; les nanoparticules ont été obtenues *via* une réduction à l'acide formique de H_2PtCl_6. Une caractérisation électrochimique complète de tous ces catalyseurs a été réalisée. Pour ce faire, la surface de Pt électrochimiquement active (*ECSA*, correspondant à la surface de Pt exposée), ainsi que l'activité catalytique pour la réaction de réduction de l'oxygène ont été évaluées, à la fois sur Electrode à Disque Tournant (EDT) ainsi qu'en Assemblage Membrane-Electrodes (AME). Ces performances électrochimiques ont également été comparées à celles d'un catalyseur commercial supportés sur noir de carbone. L'*ECSA* ainsi que l'activité catalytique ont aussi été évaluées après dégradation accélérée. Cette évaluation a d'abord été réalisée en configuration EDT, en milieu électrolytique H_2SO_4 0,5 M, après 5.000 et 20.000 cycles de potentiel électrique variant entre 0,6 et 1,0 V *vs.* RHE à 80 ºC.

Cette évaluation des performances catalytiques a ensuite été réalisée en configuration AME, après 10.000 et 30.000 marches de potentiel électrique fixées à 0,6 et 1,0 V *vs.* RHE à 70 ºC.

Il est observé que la couche de carbone secondaire déposée par CVD couvre les micropores du xérogel de carbone mais n'impacte pas la méso/macroporosité du matériau. Cette dernière est essentielle pour assurer un transport de matière efficace et un dépôt optimal des particules de métal. Les résultats indiquent que la cristallinité de la couche augmente après exposition à haute température (1.500 ºC), indiquant que la couche peut être graphitisée. Au niveau des performances catalytiques des différents catalyseurs, l'activité catalytique est plus importante pour les xérogels de carbone ayant été exposés aux post-traitements. Cependant, après vieillissement des catalyseurs, le comportement des catalyseurs supportés sur xérogels, modifiés ou non, reste similaire. En effet, une augmentation de l'activité spécifique (*i.e.* courant rapporté à la surface de Pt accessible) est observée, tandis que l'activité massique (*i.e.* courant rapporté à la masse de Pt total) reste plutôt constante. Or, il existe un diamètre de nanoparticule de Pt idéal (~3 nm), pour lequel l'*ECSA* est maximisée et où les atomes de Pt en surface possèdent une réactivité appropriée pour la réduction de l'oxygène. L'écart par rapport à ce diamètre idéal a été utilisé pour interpréter le comportement catalytique observé. Néanmoins, la présence de la couche secondaire ne réduit ni n'aggrave l'agglomération des nanoparticules de Pt après vieillissement. En configuration AME, le catalyseur utilisant le xérogel de carbone traité à la fois par CVD puis à haute température présente la meilleure rétention des performances catalytiques après vieillissement. Cette approche semble donc prometteuse pour obtenir une couche catalytique plus durable.

Concernant le dopage à l'azote, il a été constaté que l'azote est bien incorporé à la surface du xérogel de carbone sans altérer la structure poreuse de ce dernier. Cependant, en termes de performances catalytiques au cours du vieillissement, l'utilisation de xérogels de carbone dopés conduit à des performances catalytiques très similaires à leurs équivalents non dopés, à la fois en configuration EDT et AME. Ces résultats sont moins optimistes que ceux généralement rapportés dans la littérature. Néanmoins, les modifications qui peuvent être induites par le dopage, notamment les modifications dans la nucléation et croissance des nanoparticules de Pt, peut rendre complexe les comparaisons entre matériaux dopés et non dopés, et conduire à des conclusions biaisées. De manière globale, les résultats obtenus dans cette thèse démontrent qu'une amélioration de la durabilité des couches catalytiques peut être obtenue après optimisation de la surface du support carboné. Néanmoins, obtenir une amélioration significative de cette durabilité demeure un défi majeur.

Table of contents

Introduction

Context

Electrification, consisting in replacing fossil-fuel based technologies by other technologies powered by electricity produced from renewable sources, is essential for decarbonizing sectors such as industry or transport. To date, around 80% of the global energy production still relies heavily on fossil fuels [1], which is associated with severe environmental impacts on climate but also with finite resources depletion. Indeed, GreenHouse Gases (GHG) emissions associated with fossil fuels use are a major issue as they are a substantial contributor to global warming. In this context, the transition towards more sustainable sources of energy with low-carbon emissions has accelerated over the past decades.

Renewable electricity sources are diverse, including solar, wind, hydropower or thermal sources [2]. They are also intermittent, meaning that their production depends on the time of year/month/day, which calls for possibilities to store and release it in a timely and efficient way. Among the various options being explored, electrochemical energy conversion systems, such as batteries or fuel cells, have attracted considerable attention due to their high efficiencies and clean operation. These systems are well suited to support electricity produced from localized or intermittent renewable energy sources, such as solar or wind power [3]. In this context, H_2 has emerged as a clean energy carrier that can be efficiently converted into electricity without direct GHG emission, provided the hydrogen itself is produced from renewable sources [4]. Nonetheless, the utilization of hydrogen as energy carrier requires technologies capable of efficiently converting back its chemical energy into electrical power. For instance, fuel cells enable direct electrochemical conversion of a fuel such as H_2 into electricity, without emission of harmful by-products. Fuel cells are devices that can achieve high energy density, although their power density remains relatively low [5]. Nonetheless, fuel cells can operate with relatively high electrical conversion efficiencies, commonly ranging from 50 to 70% [6]. However, the round-trip efficiency of H_2 (*i.e.* the production of renewable H_2 *via* water electrolysis inside an electrolyzer followed by its conversion into electricity inside a fuel cell) generally falls between 30 to 50%, depending of the electrolyzer and fuel cell technology employed and their efficiencies (typically 60 to 80% for alkaline or PEM electrolyzers [7]).

Therefore, among the various electrochemical conversion technologies available, fuel cells represent, alongside batteries, efficient power sources that can be implemented in portable devices, or be used for automotive or stationary applications. Nevertheless, their respective characteristics can make them more suitable for different uses. For instance, battery systems are usually preferred to fuel cell systems for lightweight vehicles and portable device applications, owing to their high electrical conversion efficiency and technological maturity. Meanwhile, fuel cell systems find their most significant development in stationary power generation applications [8] and in heavy-duty automotive applications [9]. Indeed, in this case, owing to the large gravimetric density of H_2 (*ca.* 33 $kWh.kg^{-1}$ [10]), the use of fuel cells for heavyweight vehicles can become advantageous compared to batteries.

Fuel cells overview

Fuel Cells. Fuel cells are electrochemical systems capable of converting the chemical energy of a fuel and an oxidant into electrical energy through a pair of redox reactions. All fuel cells consist of an anode and a cathode, where the redox reactions take place from the fuel and the oxidant which are continuously fed to the system. The electrons produced at the anode travel to the cathode *via* an external electrical circuit, thus producing an electric current. Moreover, to ensure electroneutrality, ions have to travel from one electrode to the other *via* a medium enabling ion transport, *i.e.* an electrolyte, which separates the electrodes from each other. To ensure proper operation, the anode and cathode must indeed remain electrically separated to prevent short-circuits but also to prevent fuel or oxidant cross-over, detrimental to the cell yield.

Several fuel cell technologies exist, operating with different fuels and ion-conducting media, and in various temperature ranges. These fuel cell technologies can be broadly classified into different categories, based on the nature of the charge carrier, anion or cation, for example [11]. In the first category of fuel cells, the charge carrier is a cation, typically H^+. Proton Exchange Membrane Fuel Cells (PEMFCs) and Phosphoric Acid Fuel Cells (PAFCs) belong to this category. In this type of fuel cell, the fuel (H_2) is oxidized at the anode to provide protons. These protons travel to the cathode through a proton-exchange electrolyte, where they react with the oxidant. These fuel cells typically operate between ambient temperature and 200 ºC, respectively.

In the second category of fuel cells, the charge carrier is an anion. Alkaline Fuel Cells (AFC), Solid Oxide Fuel Cells (SOFC) and Molten Carbonate Fuel Cell (MCFC) belong to this category. The oxidant, O_2, reacts at the cathode with an intermediate molecule (often H_2O or CO_2), to provide anions, which travel from the cathode to the anode through an anion-exchange electrolyte, where they react with the fuel. These fuel cells can operate over a wide temperature range, from ambient temperature (AFC) up to 1,000 ºC (SOFC). A list of different fuel cell technology is provided in **Table 1**.

Table 1. Characteristics of common fuel cell types.

Fuel cell type	Fuel	Charge carrier	Typical electrolyte	Usual operating temperature range (°C)
Proton Exchange Membrane	H_2	H^+	Perfluorosulfonic membrane	60 – 110
Phosphoric acid	H_2	H^+	Liquid H_3PO_4	150 – 200
Alkaline	H_2	OH^-	Aqueous KOH	25 – 90
Molten Carbonate	H_2/CO	CO_3^{2-}	Molten carbonate salt	600 – 700
Solid Oxide	H_2/CO/CH_4	O^{2-}	Ceramic (yttria-stabilized zirconium)	700 – 1000

Among the various fuel cell technologies presented, PEMFCs have achieved the highest level of commercial development to date [12]. The description of PEMFC components, operating principles and associated limitations are described in the following sections.

PEMFC. PEMFCs belong to the class of fuel cells based on cation transport. A schematic of PEMFC technology is provided in **Figure 1**. They operate through the coupled oxidation of hydrogen and reduction of oxygen. In a PEMFC, hydrogen is injected at the anode and is oxidized into protons H^+ *via* the Hydrogen Oxidation Reaction (HOR):

$$H_2 \rightarrow 2H^+ + 2e^- \quad (1)$$

The protons are then transported to the cathode through a Proton Exchange Membrane (PEM). In practice, such membrane conduct protons inside the cell under their hydrated form, *i.e.* H_3O^+ [13]. As a result, proton conduction is strongly related to the membrane hydration, requiring a well-controlled humidification of both the fuel and oxidant streams. At the cathode, O_2 is injected and reacts with the protons *via* the Oxygen Reduction Reaction (ORR):

$$\frac{1}{2}O_2 + 2H^+ + 2e^- \rightarrow H_2 \quad (2)$$

Thus, the overall reaction is:

$$H_2 + \frac{1}{2}O_2 \rightarrow H_2O \quad (3)$$

The only by-products of PEMFCs are water and heat. The production of heat arises from the exothermic nature of the overall reaction (**(3)** and from the various overpotentials associated with energy losses encountered during operation.

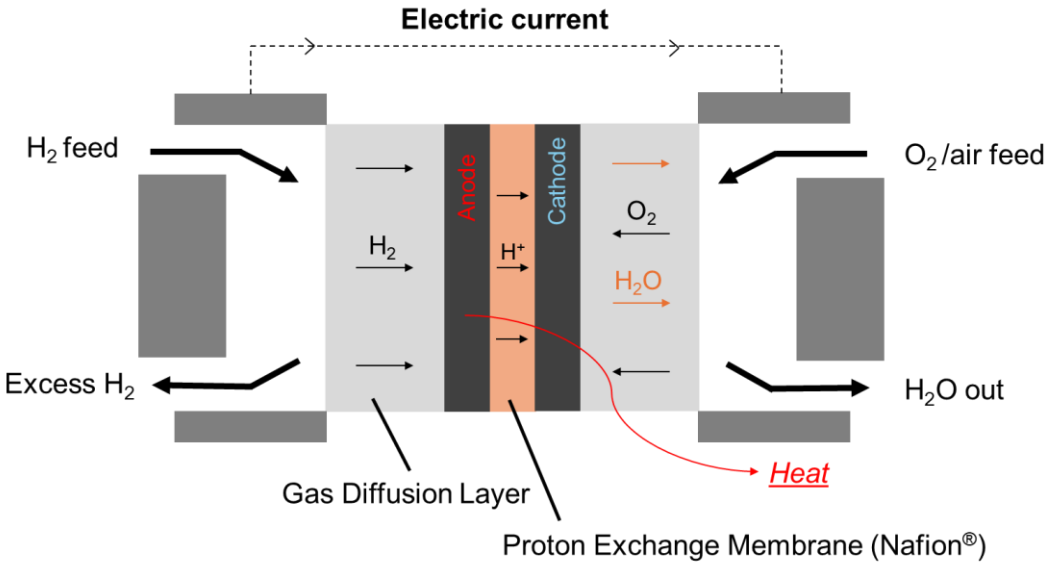

Figure 1. Schematic representation of a PEMFC.

Both HOR and ORR require a catalyst to proceed at practical kinetic rates. Platinum or Pt-based nanoparticles are the most commonly used catalysts for this purpose. On the one side, the HOR can be efficiently catalyzed using relatively small amounts of Pt catalyst. However, on the other side, the ORR is considerably more sluggish due to the strong resilience of the O=O bond (498

kJ.mol^{-1}) [14], resulting in a high activation energy for ORR [15]. As a result, a larger amount of Pt catalyst is required to ensure sufficient reaction rate, significantly increasing the overall cost of PEMFCs [16]. Commercial light-duty vehicles powered by PEMFC stacks (*e.g.* the Toyota Mirai) typically operate with a total Pt loading superior to 0.3 $mg_{Pt}.cm^{-2}_{electrode}$ in the catalytic layer. This loading is distributed between the anode side, with a loading around 0.05 $mg_{Pt}.cm^{-2}$, and the cathode side, with a loading superior to 0.25 $mg_{Pt}.cm^{-2}$ [17]. To reduce PEMFC systems costs, the U.S. Department of Energy (DoE) has set a target total Pt loading of 0.125 $mg_{Pt}.cm^{-2}_{electrode}$, for a produced power density of 8 $kW.g_{Pt}^{-1}$ [18]. This target corresponds approximately to a Pt loading distribution of 0.025 $mg_{Pt}.cm^{-2}$ for the anode side and 0.1 $mg_{Pt}.cm^{-2}$ for the cathode side.

PEMFC stacks typically exhibit an electrical efficiency in the order of 50–60% [19]. The remaining energy (40–50%) is dissipated as heat as a result of irreversible electrochemical losses observed upon operation (ohmic resistance, activation overpotential and diffusion overpotential) [20]. Because the quantity of heat generated is substantial, efficient heat recovery can enable better utilization of the PEMFC total delivered energy (*i.e.* both electrical and thermal energy). Such combined power and heat co-generation is well-documented [21,22]. A portion of the generated heat is also used for vaporizing the water produced within the CL. Nevertheless, the quantity of heat required for this process only requires about 5% of the total heat generated [23].

Among the various types of fuel cells developed, PEMFC technology is one of the most mature and has already reached commercial deployment, such as for automotive applications and stationary applications, particularly in China, Japan and South Korea [1]. PEMFCs operate at temperatures *ca.* 80 ºC and take advantage of the high gravimetric density of hydrogen (*ca.* 33 $kWh.kg^{-1}$ [10]). Nonetheless, on a volume basis the volumetric density of hydrogen is low under STP conditions, 3×10^{-3} $kWh.L^{-1}$, although it can be increased up 1.7 $kWh.L^{-1}$ when H_2 is compressed at 700 bar. Even under liquid form, H_2 possess a volumetric density (2.3 $kWh.L^{-1}$) lower than that of other fossil fuels such as diesel or gasoline (8-10 $kWh.L^{-1}$). Nevertheless, in the scope of GHG abatement, PEMFCs have potential in specific sectors requiring substantial payloads, where battery-powered systems may not suffice. For instance, PEMFC can be used in the heavy-duty transport sector [24] where power demand can typically exceed 200 kW [25]. PEMFCs can also be considered for stationary applications, either as the primary power source or as a supplemental power provider [26,27]. However, their large-scale deployment is more limited compared to battery systems due to hydrogen production costs, expenses related to

PEMFC assembly and materials (including precious metal catalysts and membrane) and to the general lack of infrastructure, such as refueling networks.

PEMFCs assembling

Each type of fuel cell relies on a specific set of fuel, catalysts, electrolyte and auxiliary components. In the context of this thesis, only the elements used in PEMFC are described. Comprehensive reviews on alternative fuel cell technologies are available in the literature [26,28]. A schematic illustration of the different component and assembling of a PEMFC stack can be found in **Figure 2**).

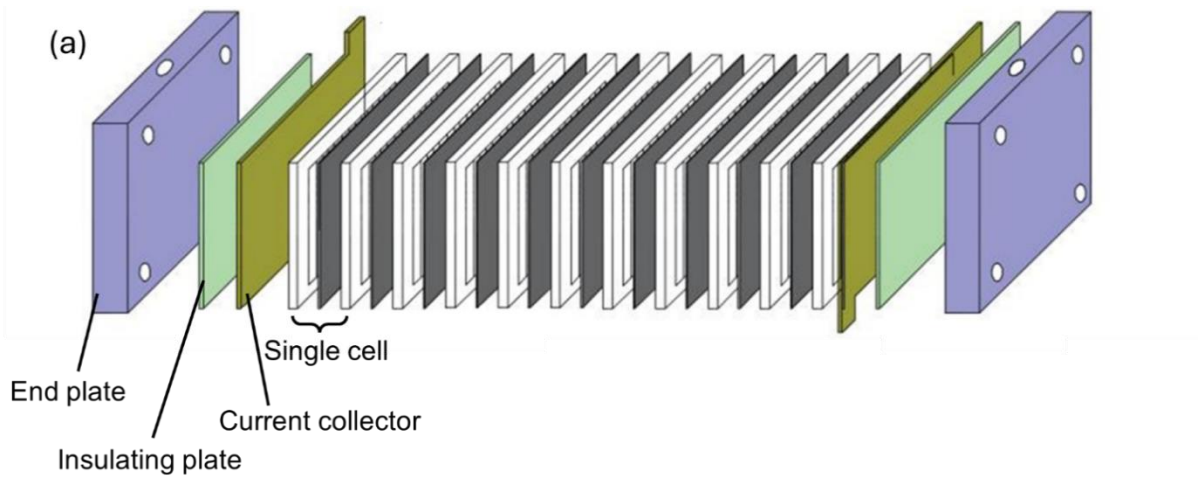

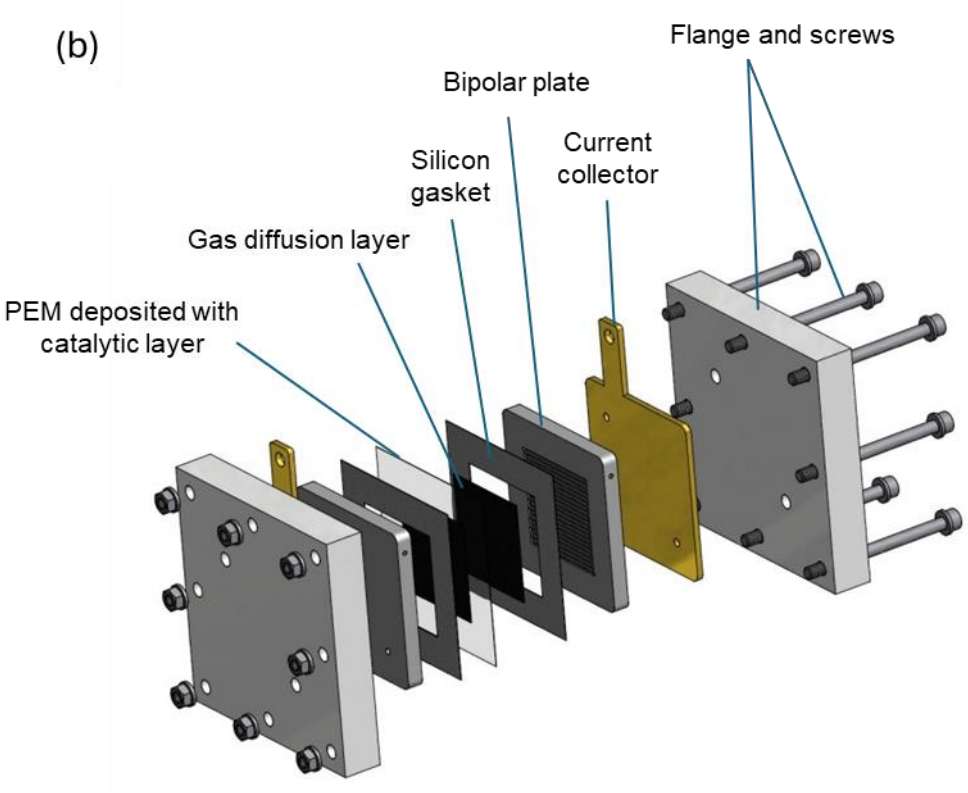

Figure 2. Schematic representation of (a) a PEMFC stack (adapted from [29]) and (b) the main components of a PEMFC single cell, as used on the laboratory test bench (adapted from [30]).

Proton Exchange Membrane (PEM). The primary function of the PEM is to transport the protons generated at the anode towards the cathode. The PEM also acts as an electrically insulating and impermeable barrier to prevent other species, *i.e.* electrons and gases, from travelling between the two electrodes. By far, the most common materials used are Nafion® membranes, combining low resistance to proton conduction, high electronic insulation and high chemical and mechanical stability. Nafion® is a co-polymer constituted of a hydrophobic polytetrafluoroethylene (PTFE) backbone providing both mechanical and chemical stability, and perfluorinated side chains terminated by hydrophilic sulfonate (SO_3^-) groups that enable the transport of protons in their hydrated form, H_3O^+ (**Figure 3**) [31].

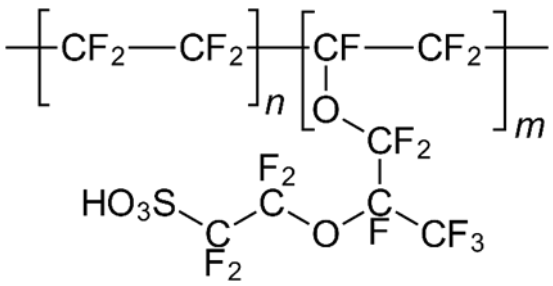

Figure 3. Chemical structure of Nafion®.

Electrodes/Catalytic layers. The anode and cathode constitute the core of a fuel cell. They are the locations where the redox reactions occur and where the electrons are exchanged. Because a catalyst is required for these redox reactions to proceed at practical rates, electrodes are referred to as catalytic layers (CL). As shown in **Figure 4a**, PEMFC CLs are composed of three elements:

(i) a catalyst, capable of promoting the targeted electrode reaction, *i.e.* either the HOR or the ORR, and be readily accessible to the gaseous reactants;

(ii) a proton-conducting medium, the ionomer, which enables the transport of protons inside the CL;

(iii) a solid substrate, *i.e.* a material capable of acting both as a physical support for the ionomer and the catalyst, but also capable of conducting electrons. The geometry of this material must allow for gas transport inside the CL but also for the removal of water produced at the cathode side, usually in vapor form although water condensation may also occur.

All these elements must be uniformly distributed within the CL to maximize the number of triple phase boundaries. Triple phase boundaries are the regions of contact between the support, the ionomer and the catalyst (**Figure 4b**). They constitute the actual electrochemically active sites within the CL, given that they are accessible to all reactants (gas, electrons and protons) on both sides of the fuel cell. The electrode must be sufficiently porous for the gaseous reactants to efficiently access these triple phase boundaries. Moreover, the CL structure must allow for the efficient evacuation of produced water at the cathode side, without blocking the arrival of oxygen. Each of the elements constituting the CL are described in details below.

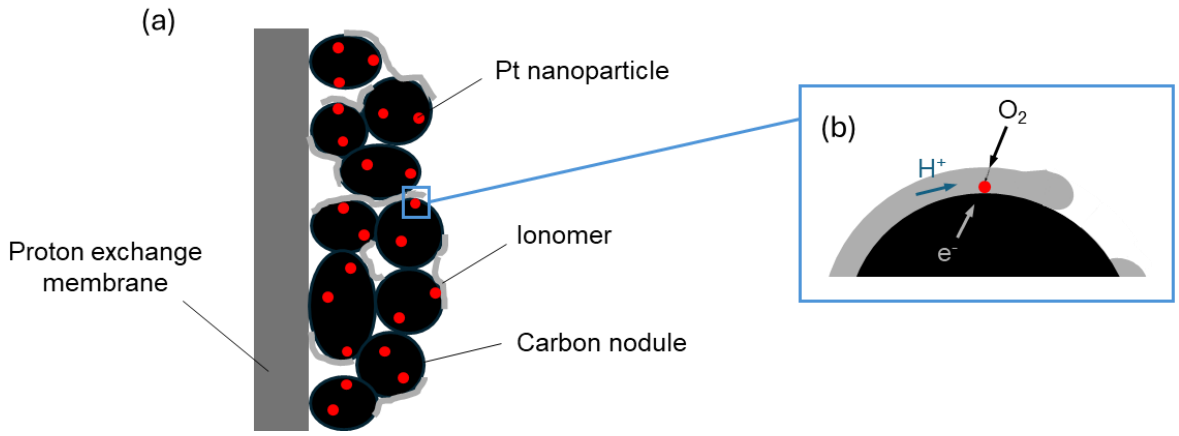

Figure 4. (a) Schematic representation of a CL and (b) enlargement on a triple phase boundary.

Gas diffusion layer (GDL). The GDL is placed on each side of the cell and serves three main functions: (1) ensuring a homogeneous distribution of the reactant gases (O_2 and H_2 at the cathode and anode, respectively) to the CL, (2) providing an electrically conductive pathway between the CL and the next component, the bipolar plates, and (3) managing water and facilitating its removal from the CL through capillary effects [32]. GDLs generally consist in a dual-layer carbon structure: a macroporous layer coated with a microporous layer. The macroporous layer faces the bipolar plates and acts as a porous current collector. It is usually made of carbon fibers or carbon felt [33]. The microporous layer faces the CL and plays a role in assisting water removal management. To this end, the microlayer is made of an electronically conductive carbon, such as carbon black or carbon nanotubes, mixed with a hydrophobic agent, typically PTFE [34]. The latter acts both as a binder and as a hydrophobic component that increases the contact angle with water, helping to remove evaporated water [35,36].

Bipolar plates. Bipolar plates, or flow-field plates, are responsible for transporting hydrogen and oxygen inside the cell. They incorporate flow channels, that allow for the gas transport to the GDL. The characteristics of these flow channels, such as their size, shape and pattern greatly influence both the gas distribution to the electrodes and other transport properties [37]. Poorly designed bipolar plates lead to large thermal gradients and zones of slow water evacuation. Thus, the optimization of the geometry of the flow channels is a very active and relevant area of research [38]. The choice of bipolar plate material is also crucial. Their thermal, mechanical, electrical properties and corrosion resistance greatly influence the overall operation of a PEMFC stack. For instance, flow-field plates must be highly electrically conductive and be impermeable to gases. As they are needed at both sides of the cell, bipolar plates must also be

resistant to both oxidant and reductant environments. Graphite can be used thanks to its favorable properties [39]. However, its brittleness and high machining costs, especially at large scale, are notable drawbacks. Plus, graphite bipolar plates are typically thick (and thus both bulky and heavy) because of the difficulty to machine thin graphite components. Metallic plates, typically made of thin stainless steel sheets (~0.1 mm), are more commonly used for commercial applications than graphite; those are manufactured by embossing of steel coils. This steel is generally stripped to remove its native oxide layer and is subsequently coated with an electrically conductive layer to prevent corrosion. Bipolar plates manufactured from composite materials, such as polymer-graphite composites, or from titanium are also actively investigated [40].

Assembling. Proper assembling of all these components is essential to ensure a maximal and durable power output from the fuel cell. In the assembling process, the membrane, CLs and GDLs are first assembled together into a Membrane Electrode Assembly (MEA). The catalyst, generally processed under the form of an ink containing also some ionomer, can be deposited on a substrate to finally form a CL. The CL can either be deposited on the PEM and then assembled with the GDL, or on the GDL and then assembled with the membrane. Many deposition methods exist for both approaches, including, but not limited to, spreading, spraying or impregnation methods [41]. After its deposition, the CL is assembled into an MEA by sandwiching it with the remaining components. Typically, silicon gaskets are also placed around the GDL to prevent gases from leaking out of the cell. The sandwiching of the above-mentioned components is commonly achieved *via* hot-pressing [42]. The resulting MEA is then positioned between the bipolar plates and current collectors on each side. All components are then secured together using flanges and screws (see **Figure 2b**).

Catalytic layer composition

As previously mentioned, the CL is the central component of the fuel cell. The selection of the materials constituting the CL, as well as the optimization of its design, are critical as they strongly govern the fuel cell performances and power output. Properly designed and optimized CLs maintain better performances upon prolonged fuel cell operation.

Catalysts for ORR and HOR. A major limitation of PEMFC technology lies in the sluggish kinetics of the redox reactions, particularly the ORR. Therefore, the use of a catalyst is required to accelerate the reactions rates. Experimentally, Pt nanoparticles have long been identified as

efficient catalysts towards both HOR and ORR [43]. From a theoretical perspective, density functional theory studies can also predict the catalytic activity of different transition metals towards ORR and HOR as a function of the binding energy of oxygen intermediates [44], or hydrogen intermediates [45]. The relationships between binding energies and catalyst activities (or current exchange densities), represented as Volcano plots, show that, for pure transition metals, the highest catalytic activity towards both HOR and ORR is indeed reached with Pt (**Figure 5**). As can be observed in this figure, Pd also demonstrates a catalytic activity that, although lower than that of Pt, remains of significant interest [46,47].

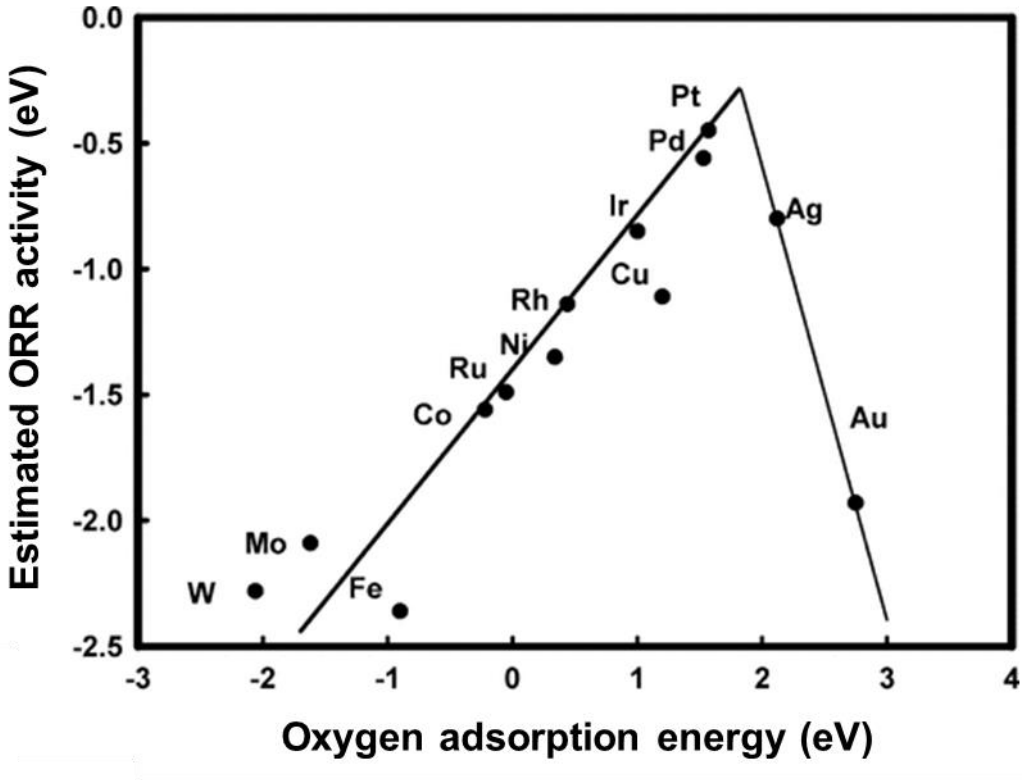

Figure 5. Representation of Sabatier's principle, showing the deviation from the theoretical maximum activity towards ORR of different metals, plotted as a function of oxygen adsorption energy (adapted from [44]). The ORR activity is defined here as $A = k_B T \min_i(\log(k_i/k_0))$, where k_i is the rate constant of each elementary step.

Nevertheless, the scarcity and cost of Pd is equivalent to that of Pt, limiting its potential as a substitute to Pt. It should also be noted that the alloying of Pt or Pd with transition metals can lead to enhanced catalytic activities towards ORR [48]. In particular, alloying Pt with transition

metals such as Co or Ni has also emerged as an effective strategy to increase the catalytic activity of Pt-based catalysts while simultaneously reducing the Pt loading [49]. Notably, Pt-alloy catalysts have already been successfully implemented into commercialized PEMFC systems [50].

Hydrogen Oxidation Reaction. The HOR occurs at the anode through a two-step mechanism [51,52]. In the first step, hydrogen adsorbs on the catalyst surface (Equation 4), following either a Tafel pathway (Equation 4) or a Heyrovsky pathway (Equation 5):

$$H_2 \rightleftharpoons 2H_{ads} \tag{4}$$

$$H_2 \rightleftharpoons H_{ads} + H^+ + e^- \tag{5}$$

In a second step, the adsorbed hydrogen species are transformed into protons:

$$H_{ads} \rightleftharpoons H^+ + e^- \tag{6}$$

The interaction between the electrocatalyst surface and the adsorbed species must be balanced: the interaction should be sufficiently strong to enable adsorption, yet no so strong as to hinder the reaction shown in Equation 6. As previously mentioned, Pt is by far the most commonly used catalyst for HOR. However, identifying the dominant reaction pathway and the rate-determining step is challenging, as both are structure-sensitive and thus strongly dependent on the configuration of the Pt atoms [53]. Each of these atom configurations (see **Figure 6**), and the different Pt crystallographic planes have a different reactivity. Nonetheless, overall, the kinetics of HOR in the presence of Pt is fast compared to the ORR [54]. Therefore, the Pt loading required for the CL at the anode side is low, in the range of 0.05 $mg_{Pt}.cm^{-2}_{electrode}$ [55], and the anode accounts for only a minor fraction, roughly 20%, of the total cost associated with the PEMFC electrodes [56].

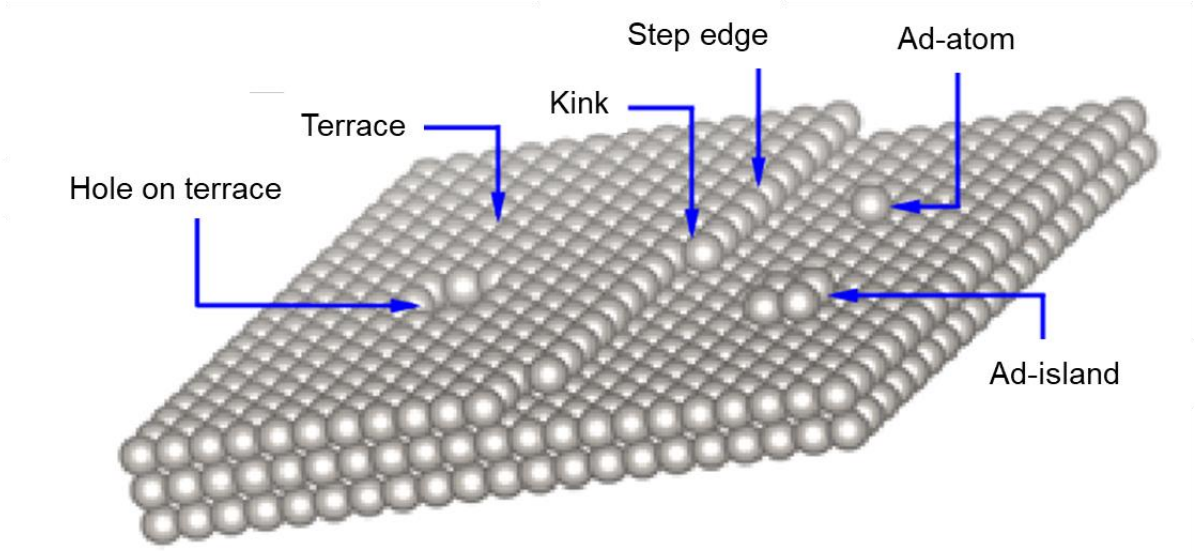

Figure 6. Model of a Pt(111) surface, with the representation of different atomic sites (adapted from [57]).

Oxygen Reduction Reaction. The ORR occurs at the cathode side and proceeds through a considerably more complex route than the HOR. The ORR is therefore much slower than the HOR by approximately six orders of magnitude [58], which can be attributed to the high bond dissociation energy of O_2 [59]. In addition, oxygen reduction into H_2O involves multiple adsorbed oxygen intermediates and determining the exact magnitude of each reaction mechanisms is often difficult, as they can occur simultaneously. Possible O_2 reduction mechanisms are shown in **Figure 7**. ORR is believed to proceed through three main routes: (1) a 4-electron dissociation pathway, considered as direct, (2) a 4-electron association pathway, and (3) a (2+2)-electron association pathway, both considered as indirect [60]. For PEMFC applications, the (2+2)-electron association pathway is the most undesirable as it can lead to the formation of hydrogen peroxide. H_2O_2 chemically attacks the PEM and the ionomer sulfonate groups [61]; its formation must therefore be avoided. Each catalyst has its own selectivity towards ORR but some trends can be observed in the literature. The use of noble metal electrocatalysts, such as Pt, is usually correlated to the 4-electron association pathway while Au is commonly reported to lead to a (2+2)-electron association pathway [62]. Single-atom transition metals catalysts (M-N-C, where M can be Fe, Co or Ni, for example [63]) usually lead to the 4-electron dissociation pathway [64]. Nevertheless, several parameters, such as the crystallographic orientation of the catalyst can drastically influence the relative contribution of each observed mechanism [65].

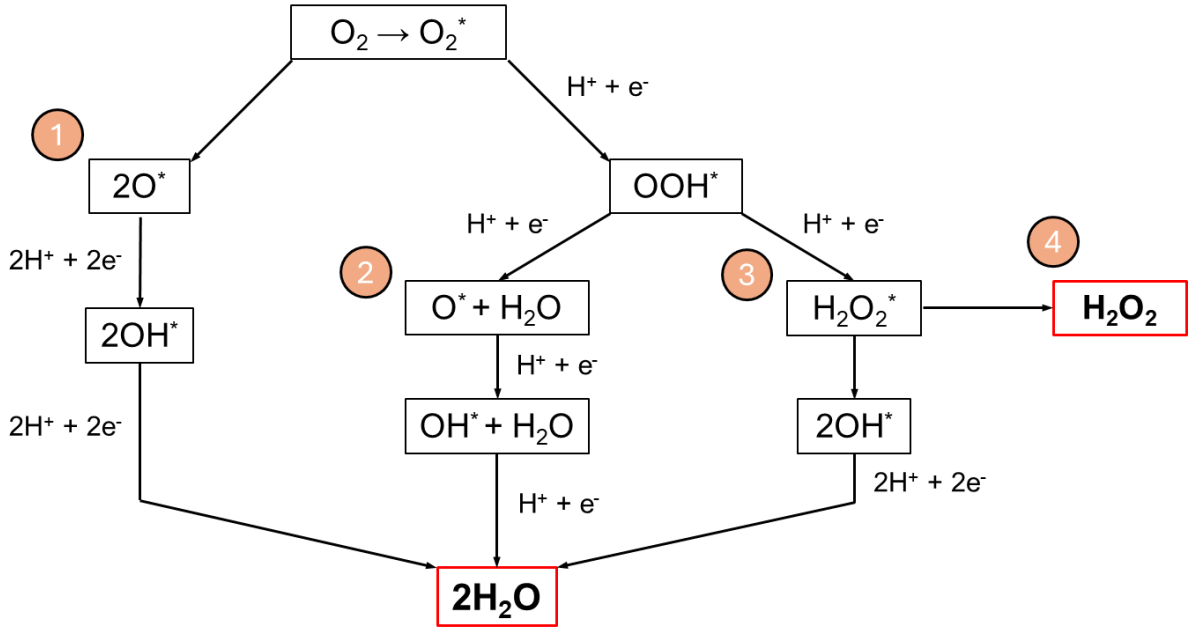

Figure 7. Proposed oxygen reduction reaction routes. (1) 4-e^- dissociation mechanism, (2) 4-e^- association mechanism, (3) (2+2)-e^- association mechanism and (4) 2-e^- reduction of O_2 to H_2O_2. *: adsorbed species.

Just as for HOR, the bonding between the catalyst and the oxygen-derived intermediates should be neither too strong nor too weak. If the interaction is too strong, the energy required for desorption becomes limiting. This causes the reaction intermediates to linger on the Pt catalytic sites, further preventing new O_2 molecules from reacting. Conversely, if the interaction is too weak, the O_2 molecule, or its intermediate species, such as H_2O_2 (see Route 4 in **Figure 7**), might desorb before the full reduction to H_2O is completed.

Ionomer. A proton-conducting medium, known as the ionomer, is also required in the CL. The ionomer shares many similarities and prerequisites with the PEM. For instance, the ionomer must also exhibit low resistance to proton conduction, as well as good thermal and chemical stability, and should not exhibit excessive swelling upon water intake. Thus, the same material, Nafion®, is used for both the ionomer and the PEM. Nevertheless, a key distinction should be noted. The PEM should have a low gas permeability, to avoid the crossover of H_2 into the cathode and the crossover of O_2 into the anode. The former, H_2 crossover, is commonly observed in PEMFC and can lead to fast and severe performance degradation due to the formation of radicals and to parasitic H_2 reaction at the cathode [66]. Meanwhile, the ionomer present in the CL, should have a higher gas permeability, to allow for the gas dissolution and

diffusion into the ionomer film so that it can reach the Pt nanoparticles (**Figure 4b**) [67]. Thus, research is also directed towards the synthesis of ionomers with high permeability towards O_2 [68]. Additionally, the fraction of ionomer in the CL must be carefully controlled as excessive amounts can clog the pore network, especially upon water uptake, and impair gas transport [69].

Carbon supports overview. In the CL, a support material is also required. This material plays different roles such as providing mechanical support for the catalyst and for the ionomer, but also acting as a medium for electron transport within the CL. Carbon materials are by far the most widely used type of catalyst supports thanks to their abundance, conductivity, relative inertness and versatility [70]. The selected carbon material must exhibit an accurate combination of many properties to be suitable for being used in a CL. First, it must provide sufficient accessible surface area to enable the deposition of metal nanoparticles a few nanometers in diameter. This is essential to ensure good dispersion and uniform distribution of the catalyst at the surface of the support [71,72]. Besides, the carbon material must have a large, open pore network. This is also of absolute necessity to facilitate transport of reactant gases, H_2 at the anode and O_2 at the cathode, and to efficiently remove the water produced at the cathode side. The carbon support must also exhibit good electrical conductivity to promote electron transfer between the carbon and the catalyst [73], and a suitable level of hydrophobicity is necessary to prevent flooding within the cathodic catalytic layer upon water production, especially at high current density [74]. Moreover, the material must be as stable as possible, with limited carbon oxidation rates (*i.e.* carbon corrosion) despite the oxidative environment present at the cathode side of PEMFCs [75], where the catalyst itself can accelerate carbon oxidation [76]. The carbon material must also be in powder form to process it into a active layer. To minimize mass transport limitations and prevent water flooding, this active layer should exhibit an appropriate thickness, between 10 – 30 µm [77]. Finally, cost considerations are important, particularly for large-scale production and commercialization.

Common carbon supports. Selecting a carbon material that meets all the above-mentioned requirements is more challenging than it seems. Among the different carbon materials available, carbon blacks have long been known to possess sufficient porosity to combine proper deposition of the catalytic phase and satisfactory mass transport of species within the electrodes [78]. Moreover, carbon blacks are relatively inexpensive and produced at large scale, primarily *via* incomplete combustion of hydrocarbons. Carbon blacks consist in covalently-bonded primary carbon particles fused together, forming aggregates. These aggregates are in turn linked in a random branching structure, forming agglomerates. Their high electrical conductivity and

porosity make them good candidates as electrocatalyst carbon supports in CL. Nevertheless, the use of carbon blacks also presents some drawbacks. For instance, their pore texture is not easily adjustable. Indeed, the spatial arrangement of agglomerates can be altered during the electrode processing, thereby modifying the final electrode porosity, which often leads to mass transport limitations at high current densities inside PEMFC stacks [79,80]. Moreover, impurities, such as sulfur, can be present in the carbon black due the precursors employed during production. Thus, a post-treatment or a careful selection of precursors [81] is needed to prevent these contaminants from poisoning Pt catalytic sites when the carbon black is assembled into an MEA.

Besides carbon blacks, other carbons can be used as catalyst support [70]. Carbon materials with a sp^2-bonded network, such as graphene, nanotubes or nanofibers have attracted considerable interest (see **Figure 8**). These materials show higher corrosion resistance because they contain fewer structural defects, which are the primary sites for electrochemical oxidation [82,83]. Nevertheless, due to the inherent stability of their sp^2 oriented structure, their surface is chemically inert, leading to weak interactions between the support and the catalyst [84]. Thus, depositing metal nanoparticles is challenging without prior surface functionalization treatment. These surface functionalities are required to increase the number of anchoring sites and the bonding energy between the nanoparticles and the support [85]. Surface functionalization of carbon nanomaterials can take various forms, including the insertion functional groups containing p-block elements, grafting of polymers, as well as the formation of surface defects [86,87]. Moreover, the final pore texture of these materials cannot be easily controlled during their processing and manufacturing into an MEA configuration.

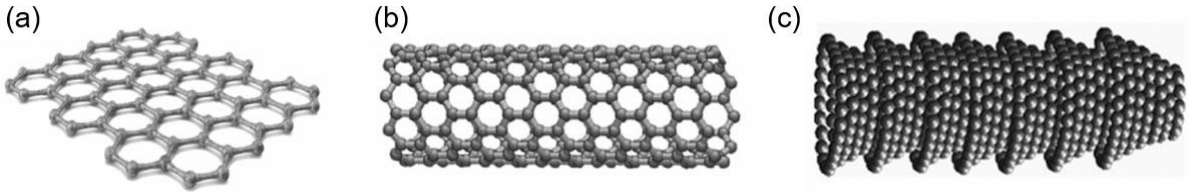

Figure 8. Schematic representation of some carbon nanomaterials. (a) Graphene, (b) carbon nanotube and (c) carbon nanofiber (fishbone-type illustrated here).

Carbon xerogels. Numerous novel carbon materials are also investigated in the literature, among which are carbon gels. Their synthesis was first described by Pekala *et al.* [88] in 1989,

and this class of materials has since been reported to be a fitting material for fuel cell applications [79,89]. Carbon gels are obtained by drying and pyrolysis of an organic gel, prepared *via* the sol-gel polycondensation of two organic monomers in aqueous medium. The first monomer is a hydroxylated benzene, typically resorcinol, but the use of various phenols and polyphenols compounds is common [90]. The second monomer is an aldehyde, usually formaldehyde, although the use of furfural was also reported [91]. Resorcinol–formaldehyde organic and carbon gels are the most widely studied type of carbon gels [92]. A base is often added to the mix to adjust the pH of the mixture. Indeed, the pH of the precursor solution is a key variable that strongly affects the final structure of the gel (**Figure 9**) [93]. The selected pH modifier must not react with either of the monomer. To this end, Na_2CO_3 or NaOH are commonly used.

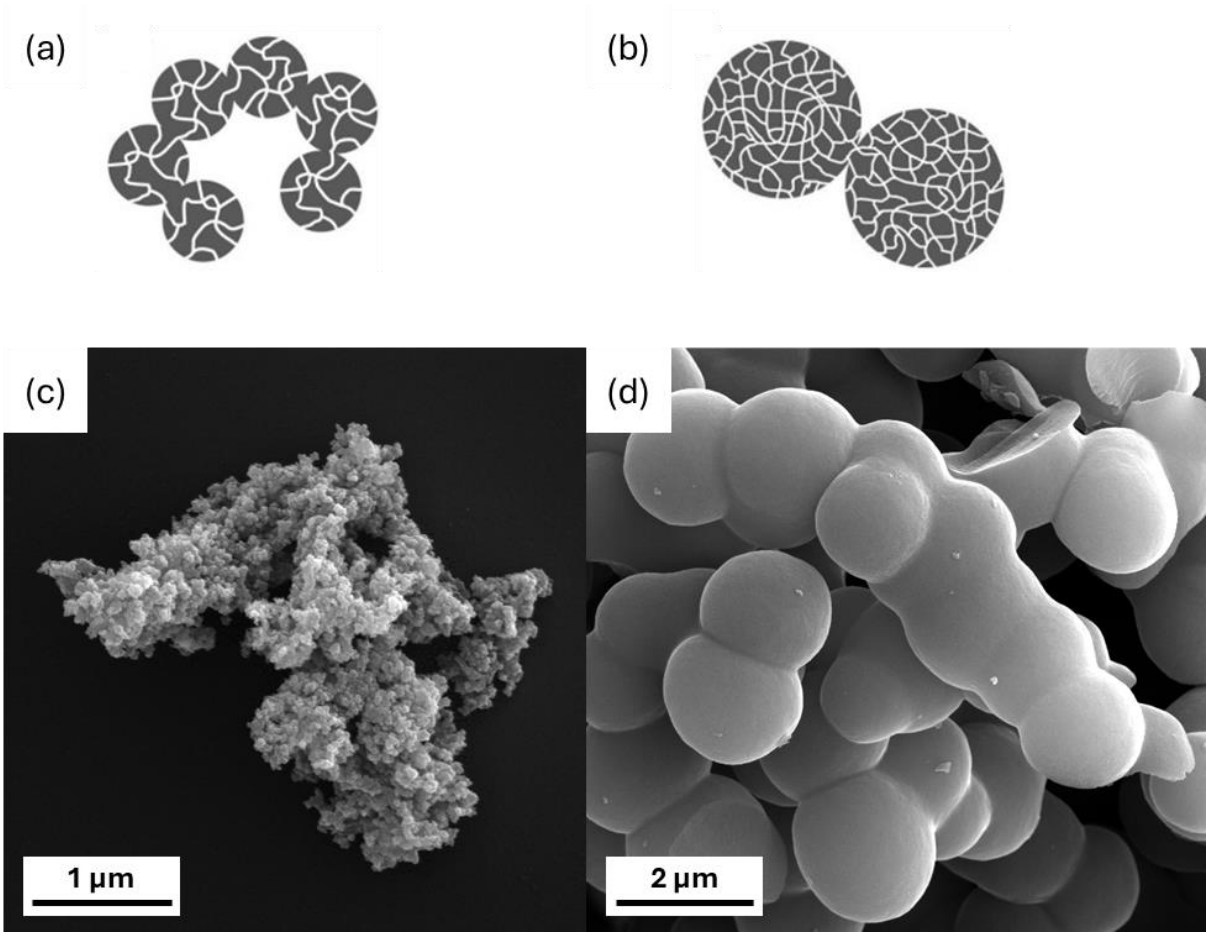

Figure 9. Schematic representation (adapted from [94]) of a carbon xerogel with (a) small nodule size prepared at pH ~ 5, (b) large nodule size prepared at pH ~2, and (c,d) SEM images of the corresponding carbon xerogels (also from reference [94]).

Carbon gels are made of primary carbon particles, that can be referred to as carbon nodules. These spherical nodules are microporous (*i.e.* comprising pores with a diameter < 2 nm according to IUPAC's classification) and are bonded covalently to one another. A key advantage of carbon gels is that the size of the nodules is controllable by selecting appropriate values of the reaction variables [93]. As previously mentioned, the pH is a key variable in determining the nodules size and thus the final pore texture. The nodules can range from nano- to microscale and the corresponding pore size of carbon gels typically ranges from ~5 nm to ~5 µm. Thus, a wide spectrum of mesoporous (*i.e.* with a mean pore size between 2 and 50 nm) or macroporous materials (*i.e.* with a mean pore size > 50 nm), usable for different applications, can be obtained [95]; applications of course include catalyst support materials for PEMFC electrodes [79]. Carbon gels can be classified on the basis on many different parameters, such as their preparation method, their appearance, their microstructure or their skeletal framework [96]. For instance, based on the drying method performed during synthesis, carbon gels can be classified in three categories: supercritically dried gels are usually referred to as "aerogels", gels dried *via* simple evaporation of the solvent are often called "xerogels" and, finally, freeze-dried gels are called "cryogels". Note however that no official labelling is defined: in some cases, the criterion used is the porosity, and materials with large void fraction are called "aerogel", whatever the drying method used.

PEMFC performances

Several sources of voltage loss are present in a PEMFC, thereby decreasing the cell electrical output, as evidenced by the voltage – current polarization curves (**Figure 10**). These losses, also referred to as overpotentials, actually reflect the chemical energy that is dissipated under the form of heat rather than converted into electrical work. These overpotentials arise from three main phenomena [6]:

(i) activation overpotential, where voltage losses occur due to the sluggish kinetics of the ORR, *i.e.* by the energy barrier to overcome for the ORR to occur. The activation overpotential associated with the HOR is typically low enough in presence of Pt-based catalysts to be considered negligible;

(ii) ohmic overpotential, where voltage losses occur due the ionic and electronic resistances generated by the different cell elements, which causes a part of the chemical energy to be converted to heat *via* the Joule effect;

(iii) mass-transport overpotential, where voltage losses occur caused by the limited diffusion of O_2 molecules inside the CL.

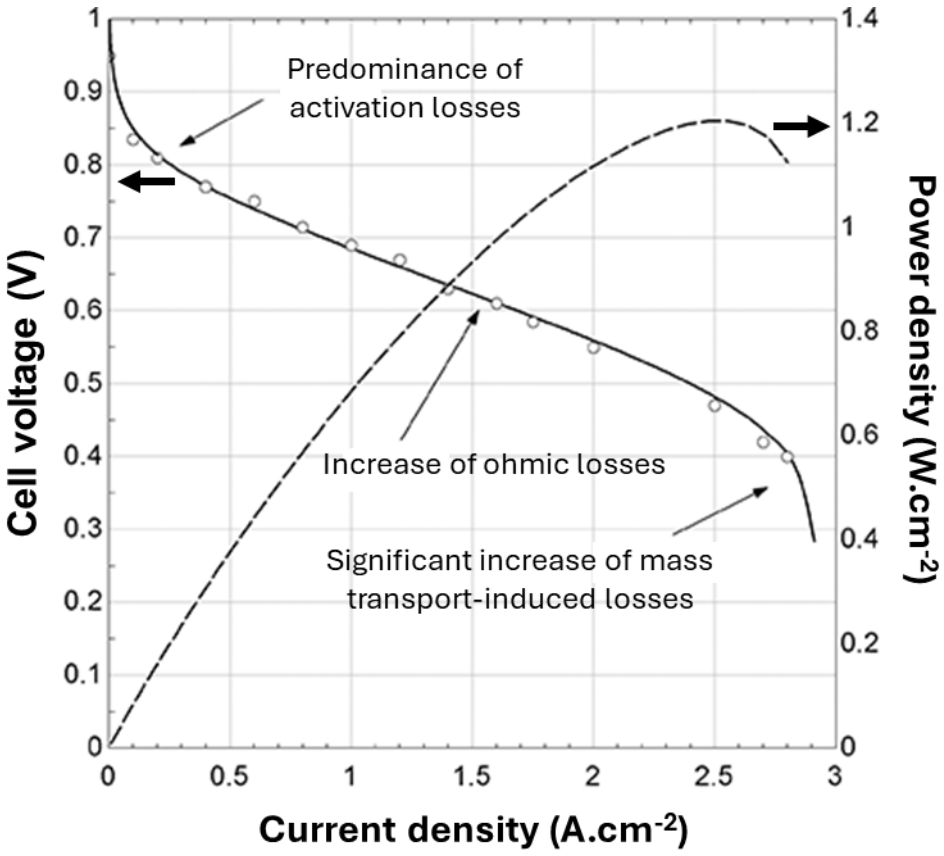

Figure 10. Polarization curve of a PEMFC (adapted from [97]).

At high voltages, activation overpotentials are dominant and cause a rapid initial voltage drop. At intermediates voltages, ohmic losses increase and start significantly contributing to the overall overpotential. Finally, at low voltages, mass-transport resistance further adds up to the activation overpotential and ohmic losses. Overall, the power output is constrained by these three types of overpotentials. In spite of these losses, the U.S. DoE has estimated that commercial PEMFC systems should achieve a current density of 0.3 $A.cm^{-2}_{electrode}$ while keeping a voltage as high as 0.8 V [12].

Catalytic layers degradation

Commercial fuel cells are expected to undergo roughly 30,000 start-up/shut-down cycles during their whole lives [98]. The unavoidable potential ramps and exposure to prolonged temperature and oxidant conditions encountered during operation inevitably damage the cell components. For instance, the main degradation modes concerning catalytic layers are related to the dissolution, migration and poisoning of the catalytic phase, and to the carbon support oxidation (**Figure 11**). All these phenomena contribute in decreasing the power output of the cell.

Dissolution. Platinum nanoparticles used as catalysts for the ORR and HOR are typically nanometer-sized, with an ideal size ranging from 3 to 4 nm [99]. Owing to their small dimensions, such nanoparticles exhibit significant specific surface energy. This makes them highly susceptible to dissolution into cationic species [100]:

$$Pt \rightarrow Pt^{2+} + 2e^{-} \quad (7)$$

Pt dissolution can occur either *via* this direct electrochemical oxidation, but also *via* the chemical dissolution of the oxide film that can form on the nanoparticle surface:

$$PtO + 2H^{+} \rightarrow Pt^{2+} + H_2O \quad (8)$$

The rate of dissolution depends on many variables, such as the temperature, the relative humidity inside the cell [101], as well as the cell potential [102]. The Pt dissolution rate increases with potential and become significant around 0.8 V *vs*. RHE upon reaching a maximum around 1.2 V *vs.* RHE [103]. Such potentials can be observed at the cathode side during the start-up/shut-down of the cell [104]. Moreover, smaller nanoparticles dissolve at a higher rate than larger ones due to their higher surface energy. The dissolved Pt cations coming from these smaller nanoparticles subsequently re-precipitate on bigger ones, thereby decreasing the nanoparticle dispersion, a phenomenon known as Ostwald ripening. Here, “dispersion” refers to the fraction of atoms (in %) located at the surface of nanoparticles and thus accessible to the gaseous reactants. In addition, cationic species can even diffuse through the ionomer or through the liquid water and redeposit within the PEM [105]. There, they may react with cross-over hydrogen according to:

$$Pt^{2+} + H_2 \rightarrow Pt + 2H^{+} \quad (9)$$

This process results in the formation of a Pt-band inside the PEM. The precise impact of the Pt-band on the PEM, whether beneficial or detrimental, is not fully understood [106].

Nevertheless, this Pt-band has been reported to contribute to PEM degradation by promoting the formation of radicals inside the PEM, around the Pt sites. Furthermore, the Pt located within the PEM becomes inactive and lost for catalyzing the redox reactions occurring at the anode or cathode.

Coalescence. Over time, metal nanoparticles migrate across the surface of the carbon supports [107]. The extent of their mobility is tied to the strength of the catalyst – support interactions. Poor interactions lead to nanoparticles that move easily on the surface of the carbon support, collide with each other and grow together, a phenomenon known as coalescence. The nanoparticle mobility is highly dependent on the type of carbon used and on the nanoparticle size [108], and is linked to the bonding energy between the Pt and the C atoms of the support [109].

Poisoning. The catalytic sites of Pt can be blocked by adsorbed contaminants, thereby decreasing the number of catalytic sites active towards ORR and HOR. Contaminants can also interact with the PEM and ionomer present in the CL and increase the resistance to proton conduction [110]. The source of contaminants in a PEMFC stack are multiple and they typically originate from the hydrogen and oxygen injected at the anode and cathode, respectively. Regarding hydrogen, around 60% of the H_2 produced worldwide comes from Steam Methane Reforming (SMR) from natural gas, while around 40% of the H_2 is coal-based or recovered from gaseous streams in refineries and petrochemical facilities [1]. To date, less than 1% of the H_2 produced comes from low-emission sources. Indeed, SMR and coal-based processes are among the most cost-effective methods for H_2 production. Nevertheless, they are associated with the production of H_2 of relatively low purity, for instance because of unreacted methane, sulfur and nitrogen compounds from the feedstock, or CO and CO_2 generation as by-products of the SMR [111], thus requiring an additional purification step to provide a suitable H_2 purity. Regarding oxygen, actual PEMFC stacks typically operate with air-fed cathodes, rather than using pure O_2. However, the presence of air-borne particles (dust, salts) or air pollutants (NO_x, SO_2, CO) necessitate the presence of a cathode air filter upstream of the PEMFC [112]. Nonetheless, even with preliminary purification, the presence of CO, CO_2, NO_x and SO_x contaminants in the H_2 and/or air PEMFC feed can still be observed [113]. CO is a common poison for Pt catalysts given that it adsorbs readily and quite strongly onto Pt catalytic sites [114]. Trace levels of CO can significantly decrease the cell performances [115], although mitigation strategies exist, such as pulsation techniques to periodically oxidize the CO adsorbed on Pt catalytic sites [116]. Finally, regarding contaminants, the release of cations as a

consequence of metallic bipolar plates corrosion can be observed [117]. These cations can migrate and diffuse throughout the cell, and compete with the protons for the $-SO_3^-$ sites in the ionomer and PEM.

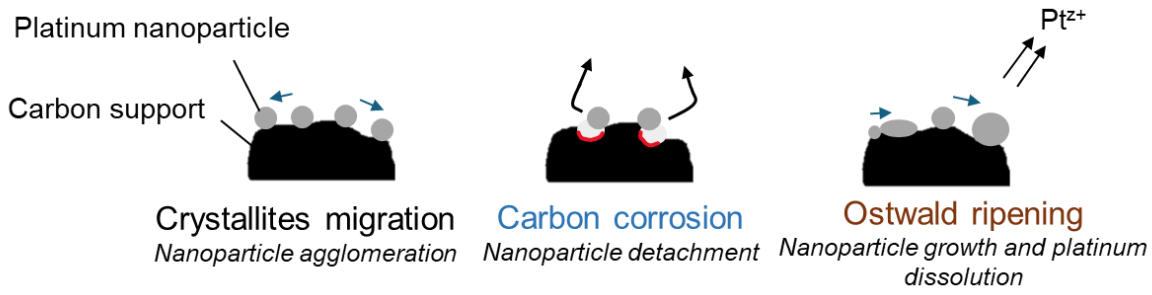

Figure 11. Schematic representation of different CL degradation mechanisms.

Carbon support oxidation and catalyst detachment. Carbon supports are not thermodynamically stable in oxidative environments, as the oxidation of carbon occurs above 0.207 V *vs.* RHE at 25 ºC [75]:

$$C + 2H_2O \rightarrow CO_2 + 4H^+ + 4e^- \quad (10)$$

In an operating PEMFC, the anode operates at potentials close to 0 V *vs.* RHE and the reference potential can be defined by the HOR at the anode. Indeed, the anode potential can reasonably be considered equal to 0 V *vs.* RHE as the overpotentials encountered for the HOR in presence of Pt catalyst are very low. The anode can thus constitute an internal hydrogen reference. Moreover, given this potential and absence of oxidant species, the carbon support in the anode is not exposed to an oxidant environment under normal operating conditions. Meanwhile, the cathode of PEMFCs typically operates at potentials around 0.6 to 0.8 V *vs.* RHE. While the carbon corrosion remains kinetically slow at potential around 0.207 V *vs.* RHE, these higher potentials encountered at the cathode, coupled with the presence of Pt, water, oxygen and relatively high temperature, accelerate the corrosion kinetics of carbon supports, and leads to efficiency decrease upon prolonged fuel cell operation [118–120]. Moreover, severe conditions such as start-stop cycles and fuel starvation can expose the cathode side to high potentials that can exceed 1.1 V *vs.* RHE, and reach values ~1.5 V *vs.* RHE [121]. Under these conditions, the corrosion rate drastically accelerates and the carbon support at the cathode side degrades faster than under usual operating conditions [122,123]. In the most severe cases, corrosion may even

lead to the collapse of carbon support if more than ~10% is turned into CO_2 [124,125]. Moreover, carbon oxidation is a complex process that also involves the formation of various oxygen functional groups at the carbon surface, such as quinones/hydroquinones, phenols or carbonyls [126]. Oxygen groups are known to increase the hydrophilicity of the carbon support, which in turn can impede water management [127]. Finally, carbon oxidation is also detrimental to the catalytic performances as the Pt nanoparticles can detach from their support upon carbon oxidation to CO_2 [128].

Mitigation strategies

Mitigating the degradation mechanisms outlined above is essential to improve the durability of PEMFCs and several strategies can be implemented [129]. For instance, catalyst and PEM poisoning can be limited by using high-purity reactant gases. H_2 generated from water electrolysis (green hydrogen) is known to be of higher purity than H_2 produced by SMR. Indeed, H_2 produced from hydrocarbons or coal-based processes usually exhibits a purity of 40 to 70%, requiring a purification step before use, adding to the overall cost. In contrast, electrolysis typically yields H_2 with a purity > 99%, although trace impurities of water vapor or oxygen may still be present [130]. Although the production of green hydrogen is, to date, very limited (<1%), this hydrogen could be used in priority for applications that requires high-purity H_2, such as PEMFCs [1]. The choice of catalyst is also of importance. For instance, alloyed Pt can exhibit better stability compared to pure Pt catalysts [131], although the alloying element may be prone to faster dissolution than Pt [132]. Regarding the carbon support, other approaches include strengthening the interaction between the support and the catalyst to reduce the rate of migration and coalescence of particles. Increasing the resistance of the carbon support to oxidation should also be a priority to avoid structural collapse and prevent nanoparticle detachment. Finally, optimizing the operational conditions inside the cell, such as the temperature, gas humidification or backpressure to ensure that no major deviation from the operating conditions (voltage, temperature, gas flow rates, *etc.*) occurs could help mitigating the different degradation phenomena as well [133]. Regarding the carbon support, two common strategies can be applied, as detailed below.

Surface graphitization. One direct strategy to limit the kinetics of carbon corrosion consists in using inherently graphitic carbons, such as graphene or carbon nanotubes [134]. These materials show better corrosion resistance because they contain fewer structural defects, which

are the primary sites for electrochemical oxidation [82,83]. While these materials are widely investigated, it is important to note that their final pore texture cannot be easily controlled during their processing and manufacturing into a Membrane-Electrodes Assembly configuration. Another approach consists in using a carbon material with a pore texture of interest, and to subsequently increase the degree of graphitization of its surface [135,136]. For instance, carbon gels derived from well-ordered carbon nanomaterials, typically graphene or carbon nanotubes, exhibit a high crystallinity. In contrast, carbon gels derived from phenolic resins, such as resorcinol-formaldehyde carbon gels, display a lower carbon surface ordering than graphene or carbon nanotubes-derived carbon gels [137].

Graphitization of carbon materials is typically achieved through high-temperature treatments [138]. Alternative methods such as microwave heating can also be performed [139]. Nevertheless, these methods are difficult to perform on carbon gels: these materials only possess short-ranged graphitic domains [140] and are classified as hard carbons, *i.e.* non-graphitizable carbons [141]. Their graphitization upon thermal treatment is thus very limited without the use of graphitization catalytic agents [142]. Another possible strategy consists in depositing a layer of graphitizable carbon onto the carbon xerogel surface [94]. Such a continuous coating should ideally conform to the surface while preserving the overall meso/macroporosity of the material and further controlled graphitization of the coated layer could be subsequently performed.

Heteroatom incorporation. The incorporation of earth-abundant p-block elements inside a carbon matrix has been widely reported to increase the interaction between the carbon support and the Pt nanoparticles [143], and numerous studies have highlighted the beneficial role of heteroatom doping on the durability of PEMFC catalytic layers [144]. The incorporation of heteroatoms can enhance the dispersion of Pt nanoparticles and increase their stabilization on the carbon support, and can also help mitigate issues related to carbon corrosion [145]. Among the various dopant elements, nitrogen stands out as one of the most extensively studied. Indeed, the incorporation of nitrogen atoms within a carbon surface can be conveniently performed since the atomic radius of N (65 pm) is close to that of C (70 pm) [146]. This enables to induce changes in the electronic environment of the carbon support while minimizing the carbon lattice mismatch [147]. Moreover, several nitrogen precursors can be safely used, even at large scale, facilitating the implementation of the nitrogen doping process. As a result, N-doping has been successfully applied to most carbon support materials: carbon black [148], graphene [149], carbon nanotubes [150], ordered mesoporous carbon [151], as well as carbon gels [152]. Other

dopants, such as B [153], S [154], and P [155], have been reported both theoretically and experimentally to have a positive effect towards the activity and stability of Pt catalysts [109]. Note that synergistic effects of dual-doping are also frequently reported [156], although at the cost of increased synthesis complexity.

Two main approaches can be considered to introduce dopants into a carbon structure [157]. The first approach can be seen as *in situ* doping, in which both the carbon material synthesis and the incorporation of the doping agent occur at once. In this approach, a precursor, rich in the doping element, is directly added to the synthesis mixture. The second approach usually consists in a post-treatment method (or *ex situ* doping), where an already-synthesized carbon material is treated with a source containing the doping element. In contrast to *in situ* approaches, post-treatments tend to modify only the surface chemistry of the carbon while the bulk remains untouched. For catalytic applications, where only surface-level dopant atoms are required, both approaches can be suitable. A wide variety of post-treatment methods exist, including thermal annealing, ion implantation or plasma treatment [158], each with advantages and drawbacks [159]. Similarly, a wide range of doping precursors can be used. For instance, in the case of carbon materials, many nitrogen-rich sources including gaseous precursors, such as NH_3 or N_2, or solid precursors, such as melamine or urea, are reported, although many other available precursors can be found [160].

Objectives of the thesis

PEMFCs are promising electrochemical systems for efficient energy conversion of hydrogen, particularly in some heavy-duty transport and stationary applications. However, their widespread deployment is limited by the cost of Pt-based CLs and deep performance degradation upon prolonged operation. Addressing these durability challenges, particularly concerning the catalyst and carbon support is critical to improve the activity, stability and cost-effectiveness of PEMFCs, but solving performance, durability, and cost issues simultaneously is challenging. Nonetheless, the objective of this thesis is to achieve a compromise by developing an optimized carbon material, so as to obtain a robust and durable catalyst support for PEMFC electrodes. This optimization is essential to obtain carbon supports more resilient towards the operating conditions encountered in PEMFCs. Carbon xerogels were selected as base material for this thesis; these specific carbons are promising model materials for PEMFC applications thanks to their tunable pore texture properties, which enable obtaining optimal

mass transport properties within the final electrode. Therefore, a carbon xerogel with an appropriate pore texture was synthesized, and the above-mentioned mitigation strategies towards carbon corrosion were applied to this material. Three different post-treatment approaches were explored in this thesis: (i) the deposition of a partially crystallized carbon coating onto the carbon xerogel surface *via* Chemical Vapor Deposition (CVD), (ii) a high-temperature thermal treatment of this secondary carbon layer and (iii) the incorporation of nitrogen heteroatoms on the carbon xerogel surface. Some of these approaches were also combined with each other. The aim of these treatments is to increase the resistance of the carbon support to oxidation and increase the interaction between the carbon support and the Pt nanoparticles used as catalyst without compromising the mass transport within the CL. The deposition of Pt nanoparticles was then performed on both pristine and post-treated carbon xerogels, under identical conditions, targeting 20 wt.% of Pt, to enable meaningful comparison. All the catalysts were subjected to accelerated aging tests in a three-electrode setup configuration in liquid electrolyte, and the corresponding catalytic activity were evaluated. The most promising catalysts were also aged, and their performance assessed in more realistic operating conditions, *i.e.* as MEA assembly in a PEMFC test bench.

This thesis was conducted as part of the BE-HyFE project, which aimed at fostering collaborations among Belgian institutions, in order to establish a hydrogen research network at the scale of Belgium. The project was supported by the federal Energy Transition Fund which provided funding for 16 early-stage researchers to carry out their doctoral research on a hydrogen-related topic, with the aim of addressing key challenges related to their respective fields. The present work is positioned within the scope of H_2 utilization and particularly on the use of H_2 as a fuel in PEMFCs to efficiently convert its chemical energy into electrical power. Further information can be found in the project's official website: www.behyfe.be.

Thesis Outline

This thesis is divided into four chapters. The first chapter examines the physico-chemical modifications of the carbon xerogel induced by different CVD treatment variables and by the high-temperature treatment performed after CVD coating. Then, both Chapters 2 and 3 focus on the electrochemical characterization of the catalysts supported on the carbon xerogel that was submitted to different post-treatments. In the last chapter, the most promising materials were selected and both their initial performance and their resistance to aging were characterized

in MEA configuration, on a PEMFC test bench representing the most realistic operating conditions.

Chapter 1. The first chapter describes the synthesis of a carbon xerogel with a tailored and appropriate pore texture for PEMFC catalytic layers. This material was then subjected to Chemical Vapor Deposition (CVD) of a secondary carbon layer, by ethylene cracking. The treatment duration was varied to obtain materials with deposited layers of increasing thickness, meant to cover the whole surface of the pristine carbon xerogel. One selected CVD-treated carbon xerogel was also subsequently subjected to a thermal treatment at 1,500 °C under inert atmosphere to graphitize the secondary carbon layer. Physico-chemical properties of the resulting materials were determined to identify the most suitable materials for subsequent deposition of the active catalytic phase (Pt nanoparticles).

Chapter 2. This chapter focuses on the electrochemical assessment of the catalysts using the most suitable the carbon xerogels, identified in Chapter 1, as supports for Pt nanoparticles. Pt was deposited on the support using a direct reduction method in liquid phase previously developed at the laboratory. After thorough physico-chemical characterization, the electrochemical properties of the catalysts were assessed before and after aging, in a three-electrode configuration (rotating disk electrode), in an acidic liquid electrolyte mimicking the PEM fuel cell conditions. The electrochemical properties of the synthesized carbon xerogel-supported catalysts were also compared to those of a commercial catalyst (Pt/carbon black) with the same Pt loading.

Chapter 3. This chapter examines the incorporation of nitrogen atoms into the carbon matrix of both the pristine and one of the CVD-treated carbon xerogel obtained in Chapter 1. The presence of nitrogen was investigated, as well as the effect of the N-doping treatment on the physico-chemical properties. Additionally, following the deposition of Pt nanoparticles on these N-doped carbon xerogels under the same conditions as in Chapter 2, the electrochemical properties of catalysts were again evaluated in a three-electrode setup configuration, before and after aging, in an acidic liquid electrolyte.

Chapter 4. In the final chapter, the most promising carbon xerogel-supported catalysts for ORR, identified in Chapters 2 and 3, were incorporated into Membrane-Electrodes Assemblies at the cathode side of a PEM fuel cell. The electrochemical properties of the catalysts were then assessed *in situ* in a PEMFC characterization test bench. Electrochemical properties were also

evaluated upon accelerated aging, and again compared to that of the same commercial catalyst, characterized in Chapter 2.

Publications

All the results coming from the physico-chemical and electrochemical evaluation of the catalysts tested in Chapter 2, as well as the corresponding results in MEA from Chapter 4 were compiled for publication:

> Bryan Carré, Berke Karaman, Zoé Deckers, Tom Servais, Alexandre F. Léonard, Nathalie Job, "Carbon-coated carbon xerogels as catalyst supports for Proton Exchange Membrane Fuel Cell electrodes" to be submitted in ACS Applied Energy Materials.

The physico-chemical and electrochemical characterization of catalysts supported on N-doped carbon xerogels presented in Chapter 3, and corresponding results from Chapter 4, will be compiled into a second publication:

> Bryan Carré, Berke Karaman, Zoé Deckers, Tom Servais, Driélle Müller, Cédric Vandenabeele, Jimena Castro-Gutiérrez, Vanessa Fierro, Alexandre F. Léonard, Nathalie Job, "Does N-doping improve the stability of PEM fuel cell Pt catalysts supported on carbon xerogels?", in preparation.

References

[1] International Energy Agency, Global Hydrogen Review 2025, (2025).

[2] T.-Z. Ang, M. Salem, M. Kamarol, H.S. Das, M.A. Nazari, N. Prabaharan, A Comprehensive Study of Renewable Energy Sources: Classifications, Challenges and Suggestions, *Energy Strategy Reviews*, 43 (2022) 100939.

[3] T. Fang, A. von Jouanne, A. Yokochi, Review of Electrochemical Systems for Grid Scale Power Generation and Conversion: Low- and High-Temperature Fuel Cells and Electrolysis Processes, *Energies*, 18 (2025) 2493.

[4] M.M. Hossain Bhuiyan, Z. Siddique, Hydrogen as an Alternative Fuel: A Comprehensive Review of Challenges and Opportunities in Production, Storage, and Transportation, *International Journal of Hydrogen Energy*, 102 (2025) 1026–1044.

[5] V. Aravindan, J. Gnanaraj, Y.-S. Lee, S. Madhavi, Insertion-Type Electrodes for Nonaqueous Li-Ion Capacitors, *Chemical Reviews*, 114 (2014) 11619–11635.

[6] P. Sharma, O.P. Pandey, Proton Exchange Membrane Fuel Fells: Fundamentals, Advanced Technologies, and Practical Applications, in: PEM Fuel Cells, Elsevier, 2022: pp. 1–24.

[7] M.E. Şahin, An Overview of Different Water Electrolyzer Types for Hydrogen Production, *Energies*, 17 (2024) 4944.

[8] V. Cigolotti, M. Genovese, P. Fragiacomo, Comprehensive Review on Fuel Cell Technology for Stationary Applications as Sustainable and Efficient Poly-Generation Energy Systems, *Energies*, 14 (2021) 4963.

[9] P. Talebi, H. Singh, M.F. Shehzad, D. Layzell, M.A. Khan, Strategic Deployment of Hydrogen Fuel Cell Buses and Fueling Stations: Insights from Fleet Transition Models, *International Journal of Hydrogen Energy*, 138 (2025) 1201–1212.

[10] Wolf. Vielstich, Arnold. Lamm, H.A.. Gasteiger, Harumi. Yokokawa, Handbook of Fuel Cells : Fundamentals, Technology, and Applications, Wiley, 2003.

[11] G.R. Molaeimanesh, F. Torabi, Fuel cell fundamentals, in: Fuel Cell Modeling and Simulation, Elsevier, 2023: pp. 1–56.

[12] C. Vallejo-Cervantes, M. Espinoza-Andaluz, A. Iranzo, Technical Review of Commercial LT-PEMFC Technologies: Performance, Applications and Challenges, *International Journal of Hydrogen Energy*, 176 (2025) 151480.

[13] S.P. Jiang, Q. Li, Introduction to Fuel Cells, Springer Singapore, Singapore, 2022.

[14] Y. Li, H. Dai, Recent Advances in Zinc–Air Batteries, *Chem. Soc. Rev.*, 43 (2014) 5257–5275.

[15] A.J. Appleby, Electrocatalysis of Aqueous Dioxygen Reduction, *Journal of Electroanalytical Chemistry*, 357 (1993) 117–179.

[16] Y. Wang, Y. Pang, H. Xu, A. Martinez, K.S. Chen, PEM Fuel Cell and Electrolysis Cell Technologies and Hydrogen Infrastructure Development – A Review, *Energy & Environmental Science*, 15 (2022) 2288–2328.

[17] Y. Wang, H. Yuan, A. Martinez, P. Hong, H. Xu, F.R. Bockmiller, Polymer Electrolyte Membrane Fuel Cell and Hydrogen Station Networks for Automobiles: Status, Technology, and Perspectives, *Advances in Applied Energy*, 2 (2021) 100011.

[18] U.S. Department of Energy, Technical Targets for Polymer Electrolyte Membrane Fuel Cell Components, (2015).

[19] H. Lohse-Busch, K. Stutenberg, M. Duoba, X. Liu, A. Elgowainy, M. Wang, T. Wallner, B. Richard, M. Christenson, Automotive Fuel Cell Stack and System Efficiency and Fuel Consumption Based on Vehicle Testing on a Chassis Dynamometer at minus 18 °C to Positive 35 °C Temperatures, *International Journal of Hydrogen Energy*, 45 (2020) 861–872.

[20] K. Scott, A.K. Shukla, Polymer Electrolyte Membrane Fuel Cells: Principles and Advances, *Reviews in Environmental Science and Bio/Technology*, 3 (2004) 273–280.

[21] W.-Y. Lee, M. Kim, Y.-J. Sohn, S.-G. Kim, Power Optimization of a Combined Power System Consisting of a High-Temperature Polymer Electrolyte Fuel Cell and an Organic Rankine Cycle System, *Energy*, 113 (2016) 1062–1070.

[22] M. Hasani, N. Rahbar, Application of Thermoelectric Cooler as a Power Generator in Waste Heat Recovery from a PEM Fuel Cell – An Experimental Study, *International Journal of Hydrogen Energy*, 40 (2015) 15040–15051.

[23] H.Q. Nguyen, B. Shabani, Proton Exchange Membrane Fuel Cells Heat Recovery Opportunities for Combined Heating/Cooling and Power Applications, *Energy Conversion and Management*, 204 (2020) 112328.

[24] T. Abedin, J. Pasupuleti, J.K.S. Paw, Y.C. Tak, M. Mahmud, M.P. Abdullah, M. Nur-E-Alam, Proton Exchange Membrane Fuel Cells in Electric Vehicles: Innovations, Challenges, and Pathways to Sustainability, *Journal of Power Sources*, 640 (2025) 236769.

[25] T. Al Rafei, N.Y. Steiner, E. Pahon, D. Hissel, Polymer Electrolyte Membrane Fuel Cell for Medium- and Heavy-Duty Vehicles: An Opportunity for Commercialization, *Energy Conversion and Management: X*, 27 (2025) 101070.

[26] N.A.A. Qasem, G.A.Q. Abdulrahman, A Recent Comprehensive Review of Fuel Cells: History, Types, and Applications, *International Journal of Energy Research*, 2024 (2024).

[27] T. Wilberforce, A. Alaswad, A. Palumbo, M. Dassisti, A.G. Olabi, Advances in Stationary and Portable Fuel Cell Applications, *International Journal of Hydrogen Energy*, 41 (2016) 16509–16522.

[28] K.-Dieter. Kreuer, Fuel Cells : Selected Entries from the Encyclopedia of Sustainability Science and Technology, Springer, 2013.

[29] L. Fan, Z. Tu, S.H. Chan, Recent Development of Hydrogen and Fuel Cell Technologies: A Review, *Energy Reports*, 7 (2021) 8421–8446.

[30] A. Zubiaur, Development of New Catalysts for Proton Exchange Membrane Fuel Cells (PEMFCs), PhD thesis, Université de Liège, 2017.

[31] C. Heitner-Wirguin, Recent Advances in Perfluorinated Ionomer Membranes: Structure, Properties and Applications, *Journal of Membrane Science*, 120 (1996) 1–33.

[32] V. Gurau, M.J. Bluemle, E.S. De Castro, Y.-M. Tsou, J.A. Mann, T.A. Zawodzinski, Characterization of Transport Properties in Gas Diffusion Layers for Proton Exchange Membrane Fuel Cells, *Journal of Power Sources*, 160 (2006) 1156–1162.

[33] F. Lapicque, M. Belhadj, C. Bonnet, J. Pauchet, Y. Thomas, A Critical Review on Gas Diffusion Micro and Macroporous Layers Degradations for Improved Membrane Fuel Cell Durability, *Journal of Power Sources*, 336 (2016) 40–53.

[34] S. Park, J.-W. Lee, B.N. Popov, Effect of Carbon Loading in Microporous Layer on PEM Fuel Cell Performance, *Journal of Power Sources*, 163 (2006) 357–363.

[35] S. Zhang, X. Yuan, H. Wang, W. Merida, H. Zhu, J. Shen, S. Wu, J. Zhang, A Review of Accelerated Stress Tests of MEA Durability in PEM Fuel Cells, *International Journal of Hydrogen Energy*, 34 (2009) 388–404.

[36] T. Kim, S. Lee, H. Park, A Study of Water Transport as a Function of the Micro-porous Layer Arrangement in PEMFCs, *International Journal of Hydrogen Energy*, 35 (2010) 8631–8643.

[37] X. Li, I. Sabir, Review of Bipolar Plates in PEM Fuel Cells: Flow-field Designs, *International Journal of Hydrogen Energy*, 30 (2005) 359–371.

[38] M. Marappan, K. Palaniswamy, T. Velumani, K.B. Chul, R. Velayutham, P. Shivakumar, S. Sundaram, Performance Studies of Proton Exchange Membrane Fuel Cells with Different Flow Field Designs – Review, *The Chemical Record*, 21 (2021) 663–714.

[39] Y. Song, C. Zhang, C.-Y. Ling, M. Han, R.-Y. Yong, D. Sun, J. Chen, Review on Current Research of Materials, Fabrication and Application for Bipolar Plate in Proton Exchange Membrane Fuel Cell, *International Journal of Hydrogen Energy*, 45 (2020) 29832–29847.

[40] Y. Wang, Z. Wang, J. Qiao, H. Li, X. Wang, B. Cao, T. Zhu, B. Zhang, M. Wang, Materials and Flow Fields of Bipolar Plates in Polymer Electrolyte Membrane Water Electrolysis: A Review, *Energy Reviews*, 4 (2025) 100132.

[41] V. Mehta, J.S. Cooper, Review and Analysis of PEM Fuel Cell Design and Manufacturing, *Journal of Power Sources*, 114 (2003) 32–53.

[42] A. Therdthianwong, P. Manomayidthikarn, S. Therdthianwong, Investigation of Membrane Electrode Assembly (MEA) Hot-Pressing Parameters for Proton Exchange Membrane Fuel Cell, *Energy*, 32 (2007) 2401–2411.

[43] K.F. Blurton, P. Greenberg, H.G. Oswin, D.R. Rutt, The Electrochemical Activity of Dispersed Platinum, *Journal of The Electrochemical Society*, 119 (1972) 559.

[44] J.K. Nørskov, J. Rossmeisl, A. Logadottir, L. Lindqvist, J.R. Kitchin, T. Bligaard, H. Jónsson, Origin of the Overpotential for Oxygen Reduction at a Fuel-Cell Cathode, *The Journal of Physical Chemistry B*, 108 (2004) 17886–17892.

[45] J.K. Nørskov, T. Bligaard, A. Logadottir, J.R. Kitchin, J.G. Chen, S. Pandelov, U. Stimming, Trends in the Exchange Current for Hydrogen Evolution, *Journal of The Electrochemical Society*, 152 (2005) J23.

[46] V. Di Noto, E. Negro, S. Polizzi, P. Riello, P. Atanassov, Preparation, Characterization and Single-Cell Performance of a New Class of Pd-carbon Nitride Electrocatalysts for Oxygen Reduction Reaction in PEMFCs, *Applied Catalysis B: Environmental*, 111–112 (2012) 185–199.

[47] Z.A. Che Ramli, J. Pasupuleti, N.F.H. Nik Zaiman, T.S. Tengku Saharuddin, S. Samidin, W.N.R. Wan Isahak, A.G.N. Sofiah, S.K. Kamarudin, S.K. Tiong, Evaluating Electrocatalytic Activities of Pt, Pd, Au and Ag-based Catalyst on PEMFC Performance: A Review, *International Journal of Hydrogen Energy*, 104 (2025) 463–486.

[48] J. Greeley, I.E.L. Stephens, A.S. Bondarenko, T.P. Johansson, H.A. Hansen, T.F. Jaramillo, J. Rossmeisl, I. Chorkendorff, J.K. Nørskov, Alloys of Platinum and Early Transition Metals as Oxygen Reduction Electrocatalysts, *Nature Chemistry*, 1 (2009) 552–556.

[49] C. Lim, A.R. Fairhurst, B.J. Ransom, D. Haering, V.R. Stamenkovic, Role of Transition Metals in Pt Alloy Catalysts for the Oxygen Reduction Reaction, *ACS Catalysis*, 13 (2023) 14874–14893.

[50] C. Wang, J.S. Spendelow, Recent Developments in Pt–Co Catalysts for Proton-Exchange Membrane Fuel Cells, *Current Opinion in Electrochemistry*, 28 (2021) 100715.

[51] P.J. Rheinländer, J. Herranz, J. Durst, H.A. Gasteiger, Kinetics of the Hydrogen Oxidation/Evolution Reaction on Polycrystalline Platinum in Alkaline Electrolyte Reaction Order with Respect to Hydrogen Pressure, *Journal of The Electrochemical Society*, 161 (2014) F1448–F1457.

[52] N. Markovic, Surface Science Studies of Model Fuel Cell Electrocatalysts, *Surface Science Reports*, 45 (2002) 117–229.

[53] N.M. Marković, B.N. Grgur, P.N. Ross, Temperature-Dependent Hydrogen Electrochemistry on Platinum Low-Index Single-Crystal Surfaces in Acid Solutions, *The Journal of Physical Chemistry B*, 101 (1997) 5405–5413.

[54] H.A. Gasteiger, J.E. Panels, S.G. Yan, Dependence of PEM Fuel Cell Performance on Catalyst Loading, *Journal of Power Sources*, 127 (2004) 162–171.

[55] T. Takahashi, T. Ikeda, K. Murata, O. Hotaka, Shigeki Hasegawa, Y. Tachikawa, M. Nishihara, J. Matsuda, T. Kitahara, S.M. Lyth, A. Hayashi, K. Sasaki, Accelerated Durability Testing of Fuel Cell Stacks for Commercial Automotive Applications: A Case Study, *Journal of The Electrochemical Society*, 169 (2022) 044523.

[56] A. Pedersen, J. Pandya, G. Leonzio, A. Serov, A. Bernardi, I.E.L. Stephens, M.-M. Titirici, C. Petit, B. Chachuat, Comparative Techno-Economic and Life-Cycle Analysis of Precious *versus* Non-Precious Metal Electrocatalysts: the Case of PEM Fuel Cell Cathodes, *Green Chemistry*, 25 (2023) 10458–10471.

[57] M.J.S. Farias, J.M. Feliu, Determination of Specific Electrocatalytic Sites in the Oxidation of Small Molecules on Crystalline Metal Surfaces, *Topics in Current Chemistry*, 377 (2019) 5.

[58] H.A. Gasteiger, W. Gu, R. Makharia, M.F. Mathias, B. Sompalli, Handbook of Fuel Cells, Wiley, 2010.

[59] A.A. Gewirth, M.S. Thorum, Electroreduction of Dioxygen for Fuel-Cell Applications: Materials and Challenges, *Inorganic Chemistry*, 49 (2010) 3557–3566.

[60] J. Gan, W. Luo, W. Chen, J. Guo, Z. Xiang, B. Chen, F. Yang, Y. Cao, F. Song, X. Duan, X. Zhou, Mechanistic Understanding of Size-Dependent Oxygen Reduction Activity and Selectivity over Pt/CNT Nanocatalysts, *European Journal of Inorganic Chemistry*, 2019 (2019) 3210–3217.

[61] E. Wallnöfer-Ogris, F. Poimer, R. Köll, M.-G. Macherhammer, A. Trattner, Main Degradation Mechanisms of Polymer Electrolyte Membrane Fuel Cell Stacks – Mechanisms, Influencing Factors, Consequences, and Mitigation Strategies, *International Journal of Hydrogen Energy*, 50 (2024) 1159–1182.

[62] A. Tricase, M. Muhyuddin, B. Erable, P. Atanassov, D. Pant, C. Santoro, P. Bollella, Bio- and Electrocatalysts for Oxygen Reduction Reaction in Neutral Media: From Mechanisms to Practical Applications, *Journal of Power Sources*, 646 (2025) 237267.

[63] J. Guo, H. Liu, D. Li, J. Wang, X. Djitcheu, D. He, Q. Zhang, A Minireview on the Synthesis of Single Atom Catalysts, *RSC Advances*, 12 (2022) 9373–9394.

[64] X. Li, D. Wang, S. Zha, Y. Chu, L. Pan, M. Wu, C. Liu, W. Wang, N. Mitsuzaki, Z. Chen, Active Sites Identification and Engineering of M-N-C Electrocatalysts toward Oxygen Reduction Reaction, *International Journal of Hydrogen Energy*, 51 (2024) 1110–1127.

[65] S. Štrbac, R.R. Adžić, The Influence of pH on Reaction Pathways for O2 Reduction on the Au(100) Face, *Electrochimica Acta*, 41 (1996) 2903–2908.

[66] Q. Tang, B. Li, D. Yang, P. Ming, C. Zhang, Y. Wang, Review of Hydrogen Crossover through the Polymer Electrolyte Membrane, *International Journal of Hydrogen Energy*, 46 (2021) 22040–22061.

[67] A. Kongkanand, M.F. Mathias, The Priority and Challenge of High-Power Performance of Low-Platinum Proton-Exchange Membrane Fuel Cells, *The Journal of Physical Chemistry Letters*, 7 (2016) 1127–1137.

[68] R. Jinnouchi, K. Kudo, K. Kodama, N. Kitano, T. Suzuki, S. Minami, K. Shinozaki, N. Hasegawa, A. Shinohara, The Role of Oxygen-Permeable Ionomer for Polymer Electrolyte Fuel Cells, *Nature Communications*, 12 (2021) 4956.

[69] J. Huang, Z. Li, J. Zhang, Review of Characterization and Modeling of Polymer Electrolyte Fuel Cell Catalyst Layer: The Blessing and Curse of Ionomer, *Frontiers in Energy*, 11 (2017) 334–364.

[70] S. Sharma, B.G. Pollet, Support Materials for PEMFC and DMFC Electrocatalysts—A Review, *Journal of Power Sources*, 208 (2012) 96–119.

[71] E. Antolini, Carbon Supports for Low-Temperature Fuel Cell Catalysts, *Applied Catalysis B: Environmental*, 88 (2009) 1–24.

[72] A. Bharti, G. Cheruvally, Influence of Various Carbon Nano-forms as Supports for Pt Catalyst on Proton Exchange Membrane Fuel Cell Performance, *Journal of Power Sources*, 360 (2017) 196–205.

[73] A.S. Aricò, P. Bruce, B. Scrosati, J.M. Tarascon, W. Van Schalkwijk, Nanostructured Materials for Advanced Energy Conversion and Storage Devices, *Nature Materials*, 4 (2005) 366–377.

[74] L. Yang, W. Li, X. Du, Y. Yang, Effect of Hydrophobicity in Cathode Porous Media on PEM Fuel Cell Performance, *Journal of Fuel Cell Science and Technology*, 7 (2010).

[75] S. Maass, F. Finsterwalder, G. Frank, R. Hartmann, C. Merten, Carbon Support Oxidation in PEM Fuel Cell Cathodes, *Journal of Power Sources*, 176 (2008) 444–451.

[76] F. Maillard, A. Bonnefont, F. Micoud, An EC-FTIR Study on the Catalytic Role of Pt in Carbon Corrosion, *Electrochemistry Communications*, 13 (2011) 1109–1111.

[77] L. Xia, M. Ni, Q. Xu, H. Xu, K. Zheng, Optimization of Catalyst Layer Thickness for Achieving High Performance and Low Cost of High Temperature Proton Exchange Membrane Fuel Cell, *Applied Energy*, 294 (2021) 117012.

[78] E. Auer, A. Freund, J. Pietsch, T. Tacke, Carbons as Supports for Industrial Precious Metal Catalysts, *Applied Catalysis A: General*, 173 (1998) 259–271.

[79] N. Job, J. Marie, S. Lambert, S. Berthon-Fabry, P. Achard, Carbon Xerogels as Catalyst Supports for PEM Fuel Cell Cathode, *Energy Conversion and Management*, 49 (2008) 2461–2470.

[80] Y.C. Park, H. Tokiwa, K. Kakinuma, M. Watanabe, M. Uchida, Effects of Carbon Supports on Pt Distribution, Ionomer Coverage and Cathode Performance for Polymer Electrolyte Fuel Cells, *Journal of Power Sources*, 315 (2016) 179–191.

[81] T. Laithong, T. Nampitch, P. Ourapeepon, N. Phetyim, Quality Improvement of Recycled Carbon Black from Waste Tire Pyrolysis for Replacing Carbon Black N330, *Scientific Reports*, 15 (2025) 23726.

[82] Y. Shao, G. Yin, Y. Gao, Understanding and Approaches for the Durability Issues of Pt-based Catalysts for PEM Fuel Cell, *Journal of Power Sources*, 171 (2007) 558–566.

[83] D. Bom, R. Andrews, D. Jacques, J. Anthony, B. Chen, M.S. Meier, J.P. Selegue, Thermogravimetric Analysis of the Oxidation of Multiwalled Carbon Nanotubes: Evidence for the Role of Defect Sites in Carbon Nanotube Chemistry, *Nano Letters*, 2 (2002) 615–619.

[84] L. Yan, Y.B. Zheng, F. Zhao, S. Li, X. Gao, B. Xu, P.S. Weiss, Y. Zhao, Chemistry and Physics of a Single Atomic Layer: Strategies and Challenges for Functionalization of Graphene and Graphene-based Materials, *Chemical Society Reviews*, 41 (2012) 97–114.

[85] J.C. Ortiz-Herrera, H. Cruz-Martínez, O. Solorza-Feria, D.I. Medina, Recent Progress in Carbon Nanotubes Support Materials for Pt-based Cathode Catalysts in PEM Fuel Cells, *International Journal of Hydrogen Energy*, 47 (2022) 30213–30224.

[86] V.D. Punetha, S. Rana, H.J. Yoo, A. Chaurasia, J.T. McLeskey, M.S. Ramasamy, N.G. Sahoo, J.W. Cho, Functionalization of Carbon Nanomaterials for Advanced Polymer Nanocomposites: A Comparison Study between CNT and Graphene, *Progress in Polymer Science*, 67 (2017) 1–47.

[87] X. Shi, K. Pérez-Salcedo, S. Hanif, R. Anwar, L. Cindrella, N. Iqbal, S. Jose, A.M. Kannan, Progress on the Functionalization of Carbon Nanostructures for Fuel Cell Electrocatalysts, in: Advanced Electrocatalysts for Low-Temperature Fuel Cells, Springer International Publishing, Cham, 2018: pp. 215–234.

[88] R.W. Pekala, Organic Aerogels from the Polycondensation of Resorcinol with Formaldehyde, *Journal of Materials Science*, 24 (1989) 3221–3227.

[89] C. Moreno-Castilla, F.J. Maldonado-Hódar, Carbon Aerogels for Catalysis Applications: An Overview, *Carbon*, 43 (2005) 455–465.

[90] J.-H. Lee, S.-J. Park, Recent Advances in Preparations and Applications of Carbon Aerogels: A Review, *Carbon*, 163 (2020) 1–18.

[91] R.W. Pekala, C.T. Alviso, X. Lu, J. Gross, J. Fricke, New Organic Aerogels Based upon a Phenolic-Furfural Reaction, *Journal of Non-Crystalline Solids*, 188 (1995) 34–40.

[92] S.A. Al-Muhtaseb, J.A. Ritter, Preparation and Properties of Resorcinol–Formaldehyde Organic and Carbon Gels, *Advanced Materials*, 15 (2003) 101–114.

[93] N. Job, R. Pirard, J. Marien, J.P. Pirard, Porous Carbon Xerogels with Texture Tailored by pH Control During Sol-Gel Process, *Carbon*, 42 (2004).

[94] B. Karaman, H. Tonnoir, D. Huo, B. Carré, A.F. Léonard, J.C. Gutiérrez, M.L. Piedboeuf, A. Celzard, V. Fierro, C. Davoisne, R. Janot, N. Job, CVD-Coated Carbon Xerogels for Negative Electrodes of Na-Ion Batteries, *Carbon*, 225 (2024) 119077.

[95] A. Arenillas, J.A. Menéndez, G. Reichenauer, A. Celzard, V. Fierro, F.J. Maldonado Hodar, E. Bailón-Garcia, N. Job, Carbon Gels for Electrochemical Applications, in: Organic and Carbon Gels, 2019: pp. 149–189.

[96] E.B. Chemere, T.L. Mhlabeni, W. Mhike, M.L. Mavhungu, M.B. Shongwe, A Comprehensive Review of Types, Synthesis Strategies, Advanced Designing and Applications of Aerogels, *Royal Society Open Science*, 12 (2025).

[97] T. Fuller, Fuel Cells and Hydrogen Production, in: Renewable Fuels, Cambridge University Press, 2022: pp. 161–192.

[98] R. Makharia, S. Kocha, P. Yu, M.A. Sweikart, W. Gu, F. Wagner, H.A. Gasteiger, Durable PEM Fuel Cell Electrode Materials: Requirements and Benchmarking Methodologies, *ECS Transactions*, 1 (2006) 3–18.

[99] M. Peuckert, T. Yoneda, R.A.D. Betta, M. Boudart, Oxygen Reduction on Small Supported Platinum Particles, *Journal of The Electrochemical Society*, 133 (1986) 944–947.

[100] G. Lin, Q. Ju, Y. Jin, X. Qi, W. Liu, F. Huang, J. Wang, Suppressing Dissolution of Pt-Based Electrocatalysts through the Electronic Metal–Support Interaction, *Advanced Energy Materials*, 11 (2021).

[101] R.L. Borup, J.R. Davey, F.H. Garzon, D.L. Wood, M.A. Inbody, PEM Fuel Cell Electrocatalyst Durability Measurements, *Journal of Power Sources*, 163 (2006) 76–81.

[102] X. Wang, R. Kumar, D.J. Myers, Effect of Voltage on Platinum Dissolution, *Electrochemical and Solid-State Letters*, 9 (2006) A225.

[103] R.M. Darling, J.P. Meyers, Kinetic Model of Platinum Dissolution in PEMFCs, *Journal of The Electrochemical Society*, 150 (2003) A1523.

[104] A.P. Soleymani, L. Bonville, C. Wang, S. Schaefer, J. Waldecker, J. Jankovic, Quantifying Key Parameters to Provide Better Understating of Microstructural Changes in Polymer Electrolyte Membrane Fuel Cells during Degradation: A Startup/Shutdown Case Study, *Journal of Power Sources*, 563 (2023) 232807.

[105] E. Guilminot, A. Corcella, F. Charlot, F. Maillard, M. Chatenet, Detection of Pt[sup z+] Ions and Pt Nanoparticles Inside the Membrane of a Used PEMFC, *Journal of The Electrochemical Society*, 154 (2006) B96.

[106] E.F. Johnson, R. Mukundan, A.Z. Weber, Membrane Degradation in PEM Fuel Cells: Part I Modeling Gas Crossover and the Pt Band, *Journal of The Electrochemical Society*, 173 (2026) 024504.

[107] J. Chen, K.-Y. Chan, Size-Dependent Mobility of Platinum Cluster on a Graphite Surface, *Molecular Simulation*, 31 (2005) 527–533.

[108] B.H. Morrow, A. Striolo, Morphology and Diffusion Mechanism of Platinum Nanoparticles on Carbon Nanotube Bundles, *The Journal of Physical Chemistry C*, 111 (2007) 17905–17913.

[109] C.K. Acharya, D.I. Sullivan, C.H. Turner, Characterizing the Interaction of Pt and PtRu Clusters with Boron-Doped, Nitrogen-Doped, and Activated Carbon: Density Functional Theory Calculations and Parameterization, *The Journal of Physical Chemistry C*, 112 (2008) 13607–13622.

[110] X. Cheng, Z. Shi, N. Glass, L. Zhang, J. Zhang, D. Song, Z.-S. Liu, H. Wang, J. Shen, A review of PEM hydrogen fuel cell contamination: Impacts, mechanisms, and mitigation, *Journal of Power Sources*, 165 (2007) 739–756.

[111] T. Bacquart, A. Murugan, M. Carré, B. Gozlan, F. Auprêtre, F. Haloua, T.A. Aarhaug, Probability of Occurrence of ISO 14687-2 Contaminants in Hydrogen: Principles and Examples from Steam Methane Reforming and Electrolysis (Water and Chlor-Alkali) Production Processes Model, *International Journal of Hydrogen Energy*, 43 (2018) 11872–11883.

[112] C. Özyalcin, P. Mauermann, S. Dirkes, P. Thiele, S. Sterlepper, S. Pischinger, Investigation of Filtration Phenomena of Air Pollutants on Cathode Air Filters for PEM Fuel Cells, *Catalysts*, 11 (2021) 1339.

[113] J. Mitzel, Q. Zhang, P. Gazdzicki, K.A. Friedrich, Review on Mechanisms and Recovery Procedures for Reversible Performance Losses in Polymer Electrolyte Membrane Fuel Cells, *Journal of Power Sources*, 488 (2021) 229375.

[114] J.J. Baschuk, X. Li, Carbon Monoxide Poisoning of Proton Exchange Membrane Fuel Cells, *International Journal of Energy Research*, 25 (2001) 695–713.

[115] S. Gottesfeld, J. Pafford, A New Approach to the Problem of Carbon Monoxide Poisoning in Fuel Cells Operating at Low Temperatures, *Journal of The Electrochemical Society*, 135 (1988) 2651–2652.

[116] V.F. Valdés-López, T. Mason, P.R. Shearing, D.J.L. Brett, Carbon Monoxide Poisoning and Mitigation Strategies for Polymer Electrolyte Membrane Fuel Cells – A Review, *Progress in Energy and Combustion Science*, 79 (2020) 100842.

[117] S. Komini Babu, T. O'Brien, M.J. Workman, M. Wilson, R. Mukundan, R. Borup, Editors' Choice—Diffusion Media for Cation Contaminant Transport Suppression into Fuel Cell Electrodes, *Journal of The Electrochemical Society*, 168 (2021) 024501.

[118] K.H. Kangasniemi, D.A. Condit, T.D. Jarvi, Characterization of Vulcan Electrochemically Oxidized under Simulated PEM Fuel Cell Conditions, *Journal of The Electrochemical Society*, 151 (2004) E125.

[119] N. Macauley, D.D. Papadias, J. Fairweather, D. Spernjak, D. Langlois, R. Ahluwalia, K.L. More, R. Mukundan, R.L. Borup, Carbon Corrosion in PEM Fuel Cells and the Development of Accelerated Stress Tests, *Journal of The Electrochemical Society*, 165 (2018) F3148–F3160.

[120] L.M. Roen, C.H. Paik, T.D. Jarvi, Electrocatalytic Corrosion of Carbon Support in PEMFC Cathodes, *Electrochemical and Solid-State Letters*, 7 (2004) A19.

[121] C.A. Reiser, L. Bregoli, T.W. Patterson, J.S. Yi, J.D. Yang, M.L. Perry, T.D. Jarvi, A Reverse-Current Decay Mechanism for Fuel Cells, *Electrochemical and Solid-State Letters*, 8 (2005) A273.

[122] M.L. Perry, T. Patterson, C. Reiser, Systems Strategies to Mitigate Carbon Corrosion in Fuel Cells, *ECS Transactions*, 3 (2006).

[123] F. Zhou, S.J. Andreasen, S.K. Kær, D. Yu, Analysis of Accelerated Degradation of a HT-PEM Fuel Cell Caused by Cell Reversal in Fuel Starvation Condition, *International Journal of Hydrogen Energy*, 40 (2015) 2833–2839.

[124] L. Strandberg, V. Shokhen, M. Skoglundh, B. Wickman, Carbon Support Corrosion in PEMFCs Followed by Identical Location Electron Microscopy, *ACS Catalysis*, 14 (2024) 8494–8504.

[125] E. Guilminot, A. Corcella, M. Chatenet, F. Maillard, F. Charlot, G. Berthomé, C. Iojoiu, J.-Y. Sanchez, E. Rossinot, E. Claude, Membrane and Active Layer Degradation upon PEMFC Steady-State Operation, *Journal of The Electrochemical Society*, 154 (2007) B1106.

[126] Z.R. Yue, W. Jiang, L. Wang, S.D. Gardner, C.U. Pittman, Surface characterization of electrochemically oxidized carbon fibers, *Carbon*, 37 (1999) 1785–1796.

[127] K. Kinoshita, Carbon : Electrochemical and Physicochemical Properties, Wiley, 1988.

[128] L. Dubau, L. Castanheira, G. Berthomé, F. Maillard, An Identical-Location Transmission Electron Microscopy Study on the Degradation of Pt/C Nanoparticles under Oxidizing, Reducing and Neutral Atmosphere, *Electrochimica Acta*, 110 (2013) 273–281.

[129] J. Wu, X.Z. Yuan, J.J. Martin, H. Wang, J. Zhang, J. Shen, S. Wu, W. Merida, A Review of PEM Fuel Cell Durability: Degradation Mechanisms and Mitigation Strategies, *Journal of Power Sources*, 184 (2008) 104–119.

[130] Y. Kim, H. Yang, Hydrogen Purity: Influence of Production Methods, Purification Techniques, and Analytical Approaches, *Energies*, 18 (2025) 741.

[131] L. Macheli, G.M. Leteba, S.L. George, C.I. Lang, L.L. Jewell, Pt-Based Electrocatalysts for Oxygen Reduction Reaction: Core–Shell Architectures and High-Entropy Alloy Nanoparticles, *Advanced Energy and Sustainability Research*, 6 (2025).

[132] H.R. Colón-Mercado, B.N. Popov, Stability of Platinum Based Alloy Cathode Catalysts in PEM Fuel Cells, *Journal of Power Sources*, 155 (2006) 253–263.

[133] D.P. Wilkinson, J. St-Pierre, In-Plane Gradients in Fuel Cell Structure and Conditions for Higher Performance, *Journal of Power Sources*, 113 (2003) 101–108.

[134] C. Alegre, D. Sebastián, M.J. Lázaro, Carbon Xerogels Electrochemical Oxidation and Correlation with their Physico-Chemical Properties, *Carbon*, 144 (2019) 382–394.

[135] P.T. Yu, W. Gu, J. Zhang, R. Makharia, F.T. Wagner, H.A. Gasteiger, Carbon-Support Requirements for Highly Durable Fuel Cell Operation, in: Polymer Electrolyte Fuel Cell Durability, 2009: pp. 29–53.

[136] F. Coloma, A. Sepulveda-Escribano, J.L.G. Fierro, F. Rodriguez-Reinoso, Preparation of Platinum Supported on Pregraphitized Carbon Blacks, *Langmuir*, 10 (1994) 750–755.

[137] R. Reyhani, A. Zadhoush, N.S. Tabrizi, H. Nazockdast, M. Naeimirad, Synthesis and Characterization of Powdered CNT-doped Carbon Aerogels, *Journal of Non-Crystalline Solids*, 571 (2021) 121058.

[138] Z. Wang, Y. Wang, Q. Luo, S. Wang, Y. Yi, Synthesis of Novel Porous Graphitic Carbon Xerogel-Supported Uniform Platinum Nanoparticle for Oxygen Reduction Reaction, *ChemistrySelect*, 10 (2025).

[139] M. Canal-Rodríguez, A. Arenillas, J.A. Menéndez, D. Beneroso, N. Rey-Raap, Carbon Xerogels Graphitized by Microwave Heating as Anode Materials in Lithium-Ion Batteries, *Carbon*, 137 (2018) 384–394.

[140] C. Lin, J.A. Ritter, Effect of Synthesis pH on the Structure of Carbon Xerogels, *Carbon*, 35 (1997) 1271–1278.

[141] M. Kakunuri, C.S. Sharma, Resorcinol-Formaldehyde Derived Carbon Xerogels: A Promising Anode Material for Lithium-Ion Battery, *Journal of Materials Research*, 33 (2018) 1074–1087.

[142] M.M. Gaikwad, M. Kakunuri, C.S. Sharma, Enhanced Catalytic Graphitization of Resorcinol Formaldehyde derived Carbon Xerogel to Improve its Anodic Performance for Lithium Ion Battery, *Materials Today Communications*, 20 (2019) 100569.

[143] R. Jasinski, A New Fuel Cell Cathode Catalyst, *Nature*, 201 (1964) 1212–1213.

[144] Y. Shao, J. Sui, G. Yin, Y. Gao, Nitrogen-Doped Carbon Nanostructures and their Composites as Catalytic Materials for Proton Exchange Membrane Fuel Cell, *Applied Catalysis B: Environmental*, 79 (2008) 89–99.

[145] A. Kozhushner, Q. Li, L. Elbaz, Heteroatom-Doped Carbon Supports with Enhanced Corrosion Resistance in Polymer Electrolyte Membrane Fuel Cells, *Energies*, 16 (2023) 3659.

[146] J.C. Slater, Atomic Radii in Crystals, *The Journal of Chemical Physics*, 41 (1964) 3199–3204.

[147] L. Dai, Y. Xue, L. Qu, H.-J. Choi, J.-B. Baek, Metal-Free Catalysts for Oxygen Reduction Reaction, *Chemical Reviews*, 115 (2015) 4823–4892.

[148] V.A. Golovin, N.V. Maltseva, E.N. Gribov, A.G. Okunev, New Nitrogen-containing Carbon Supports with Improved Corrosion Resistance for Proton Exchange Membrane Fuel Cells, *International Journal of Hydrogen Energy*, 42 (2017) 11159–11165.

[149] H. Wang, T. Maiyalagan, X. Wang, Review on Recent Progress in Nitrogen-Doped Graphene: Synthesis, Characterization, and Its Potential Applications, *ACS Catalysis*, 2 (2012) 781–794.

[150] K. Chizari, I. Janowska, M. Houllé, I. Florea, O. Ersen, T. Romero, P. Bernhardt, M.J. Ledoux, C. Pham-Huu, Tuning of Nitrogen-doped Carbon Nanotubes as Catalyst Support for Liquid-Phase Reaction, *Applied Catalysis A: General*, 380 (2010) 72–80.

[151] J.A. Prithi, N. Rajalakshmi, G. Ranga Rao, Nitrogen Doped Mesoporous Carbon Supported Pt Electrocatalyst for Oxygen Reduction Reaction in Proton Exchange Membrane Fuel Cells, *International Journal of Hydrogen Energy*, 43 (2018) 4716–4725.

[152] C. Alegre, D. Sebastián, M. Gálvez, E. Baquedano, R. Moliner, A. Aricò, V. Baglio, M. Lázaro, N-Doped Carbon Xerogels as Pt Support for the Electro-Reduction of Oxygen, *Materials*, 10 (2017) 1092.

[153] X. Jing, H. Lan, C. Liu, R. Ding, X. Yin, Performance Evaluation of Boron-Doped Carbon-Supported Platinum Catalysts for Oxygen Reduction Reaction in Proton Exchange Membrane Fuel Cells, *Journal of Power Sources*, 658 (2025) 238227.

[154] W.S. Baker, J.W. Long, R.M. Stroud, D.R. Rolison, Sulfur-functionalized Carbon Aerogels: A New Approach for Loading High-Surface-Area Electrode Nanoarchitectures with Precious Metal Catalysts, *Journal of Non-Crystalline Solids*, 350 (2004) 80–87.

[155] B.-A. Lu, N. Tian, Z.-Y. Zhou, S.-G. Sun, Phosphorus-Enhanced Oxygen Reduction Activity and Stability of Commercial Pt/C, *ECS Meeting Abstracts*, MA2017-02 (2017) 1534–1534.

[156] S. Wang, E. Iyyamperumal, A. Roy, Y. Xue, D. Yu, L. Dai, Vertically Aligned BCN Nanotubes as Efficient Metal-Free Electrocatalysts for the Oxygen Reduction Reaction: A Synergetic Effect by Co-Doping with Boron and Nitrogen, *Angewandte Chemie International Edition*, 50 (2011) 11756–11760.

[157] X. Feng, Y. Bai, M. Liu, Y. Li, H. Yang, X. Wang, C. Wu, Untangling the Respective Effects of Heteroatom-Doped Carbon Materials in Batteries, Supercapacitors and the ORR to Design High Performance Materials, *Energy & Environmental Science*, 14 (2021) 2036–2089.

[158] W. Al-Hajri, Y. De Luna, N. Bensalah, Review on Recent Applications of Nitrogen-Doped Carbon Materials in CO_2 Capture and Energy Conversion and Storage, *Energy Technology*, 10 (2022).

[159] C. Bie, H. Yu, B. Cheng, W. Ho, J. Fan, J. Yu, Design, Fabrication, and Mechanism of Nitrogen-Doped Graphene-Based Photocatalyst, *Advanced Materials*, 33 (2021).

[160] S. Ott, F. Du, M.L. Luna, T.A. Dao, S. Selve, B.R. Cuenya, A. Orfanidi, P. Strasser, Property-Reactivity Relations of N-Doped PEM Fuel Cell Cathode Catalyst Supports, *Applied Catalysis B: Environmental*, 306 (2022) 121118.

- Chapter 1 -

SYNTHESIS AND PHYSICO-CHEMICAL CHARACTERIZATION OF CARBON-COATED CARBON XEROGELS

Abstract

This first chapter describes the synthesis of a carbon xerogel with controlled porosity, followed by surface modifications through Chemical Vapor Deposition (CVD) of a secondary carbon layer and high-temperature treatment. A selected carbon xerogel was subjected to CVD of various durations, using ethylene as precursor, which led to the deposition of a carbon layer of increasing thickness on the surface of the carbon xerogel nodules. One of the CVD-treated sample was submitted to a high-temperature post-treatment at 1,500 ºC in order to graphitize the secondary layer. All samples were fully characterized in terms of surface composition, crystallinity, and pore texture. The results showed that, while microporosity was progressively reduced, the overall meso/macropore texture was maintained. The degree of surface graphitization tends to slightly increase with the duration of the CVD processing and increases markedly after high-temperature treatment. Based on the properties obtained, four of these samples were selected for further evaluation as catalyst supports in proton exchange membrane fuel cell catalytic layers.

Contributions

The carbon xerogel synthesis and the CVD treatment of varying durations were carried out by the PhD candidate. The SEM photographs, N_2 adsorption-desorption measurements, He pycnometry and XRD diffractograms were also performed by the PhD candidate. The high-temperature post-treatment and the elemental analysis were performed by Dr. Jimena Castro-Guttiérez from the team Matériaux Bio-Sourcés in Institut Jean Lamour, located in Epinal, France. The HR-TEM photographs were collected by Dr. Carine Davoisne from Laboratoire de Réactivité et de Chimie des Solides (LRCS) located in Amiens, France. The XPS analysis and data treatment were performed in Université de Namur, by Driélle Müller da Silva. Finally, the mercury porosimetry measurements were performed by Dr. Alexandre F. Léonard from the CARPOR platform in Université de Liège.

1.1. Introduction

The performances of Proton Exchange Membrane Fuel Cells (PEMFCs) are limited by the inherently slow kinetics of the oxygen reduction reaction (ORR) at the cathode, and hydrogen oxidation reaction (HOR) at the anode, thereby requiring Pt-based catalysts supported on conductive, porous and corrosion-resistant carbon materials [1]. For commercial applications, carbon blacks are widely used as carbon support for electrocatalysts, due to their large-scale production and established properties. However, as detailed in the general introduction, the carbon blacks used as supports for Pt/C catalysts of PEMFCs are not optimal because their pore texture is not easily adjustable, which often leads to mass transport limitations at high current densities [2,3], and because they are subjected to oxidation due to the high potentials encountered during PEMFC operation and start-stop events [4]. The oxidation of the carbon support remains kinetically slow at low potential values, such as those encountered at the anode. Nevertheless, the higher potentials encountered at the cathode side of operating PEMFCs (>0.6 V *vs.* RHE), coupled with the presence of Pt, water, oxygen and relatively high temperature, accelerate the corrosion kinetics [5,6]. This carbon oxidation leads to structural degradation and Pt nanoparticle detachment, particularly inside the cathode catalytic layer [7], thereby limiting the long-term fuel cell performances.

One direct strategy to limit the carbon corrosion kinetics consists in using inherently graphitic carbons, such as graphene or carbon nanotubes [8]. These materials show higher corrosion resistance because they contain fewer structural defects, which are the primary sites for electrochemical oxidation [9,10]. However, their final pore structure cannot be easily controlled during their processing and manufacturing into a Membrane Electrode Assembly configuration. Another approach consists in using a carbon material with an adequate porosity, and then to increase the degree of graphitization of the surface to enhance the support resistance towards degradation and corrosion [11]. This transformation is typically achieved through high-temperature treatments, either in the presence [12] or absence [13] of catalytic agents. Alternative methods such as microwave heating can also be performed [14].

In this context, carbon xerogels (CXs) are materials of interest. Their structure consists of interconnected carbon nodules, the size of which can be tuned by adjusting the synthesis variables, enabling control of the final pore texture. Their pore texture can therefore be tailored to minimize gas diffusion limitations, facilitate water management, while also providing enough surface for homogeneous deposition of an active catalytic phase. Nevertheless, the

above-mentioned graphitization treatments are difficult to perform on carbon xerogels: indeed, those only possess short-ranged graphitic domains [15] and are classified as hard carbons [16], meaning that they cannot be graphitized upon thermal treatment. Therefore, increasing the surface crystallinity is inherently difficult. Consequently, another possible strategy would be to deposit a layer of graphitizable carbon onto the xerogel surface. Such a continuous coating should ideally conform to the surface of the xerogel nodules while preserving the overall meso/macroporosity of the material.

In this chapter, a CX with a chosen meso/macropore texture, appropriate for fuel cell applications, was first synthesized. Then, a secondary carbon layer was deposited onto the carbon xerogel surface, *via* CVD using ethylene as carbon precursor. Different CVD treatment durations were chosen to investigate the deposition process and its impact on the carbon xerogel textural properties. From previous measurements, it was observed that the deposited layer exhibits a more ordered structure than the pristine support [17]. Based on this observation, a graphitization treatment at high temperature (1,500 ºC) was then applied, with the aim of increasing the structural order of the surface. The physico-chemical properties of this carbon xerogel were determined before and after these post-treatments, to identify which modified materials are the most suitable for use as a catalyst supports in the subsequent chapters of this thesis.

1.2. Experimental

1.2.1. Carbon xerogel synthesis

The pristine carbon xerogel was obtained *via* polycondensation of resorcinol with formaldehyde in water, followed by drying under vacuum and subsequent pyrolysis under inert atmosphere. In the present study, the pore size was targeted between 50 and 100 nm. Empirically, small macropores have shown to be a good balance to minimize mass transport limitations within fuel cell catalytic layers while simultaneously promoting efficient catalyst utilization and deposition of nanoparticles of adequate size [2,18]. The carbon xerogel was synthesized following a previously established protocol [19]. Briefly, resorcinol ($C_6H_6O_2$ – Merck, for synthesis) was dissolved in ultrapure Milli-Q® water (18.2 MΩ.cm) with sodium carbonate (Na_2CO_3, Merck, for analysis EMSURE® ISO) acting as a pH regulator. After full dissolution of resorcinol in

water, formaldehyde (Sigma-Aldrich, 37 wt.% in water, stabilized with 10-15 wt.% of methanol) was added to the mixture.

The pore size of CXs can be adjusted by varying the amounts of reactants introduced in the precursors solution [15]. For this reason, the molar resorcinol/formaldehyde ratio, *R/F*, and the molar dilution ratio, *D* (water/(resorcinol + formaldehyde)) were respectively set at 0.5 and 5.7. Note that the numerator of *D* accounts for the amount of water contained in the formaldehyde solution. Meanwhile, the resorcinol/Na_2CO_3 molar ratio, *R/C*, was fixed at 450. A pH of 5.0 was obtained for this solution. Following previous results, such a pH value should yield a pore size close in the desired range (50-100 nm) [19]. Note that, given the instability of the formaldehyde in water, which impacts the pH of the pristine solution [20], the measurement of the pH is a much better variable to control the final carbon properties than *R/C*. Indeed, upon similar *R/C* values, very different pore textures are obtained with distinct formaldehyde aqueous solutions. It is thus recommended to adjust the pH, and not *R/C*. The mixture was transferred to a sealed flask and then placed in an oven at 85 ºC for 72 h to ensure gelling and aging of the xerogel [21]. The drying of the material was performed under vacuum: the flask was opened and the pressure was decreased to 920 mPa at 60 ºC for 32 h. The pressure was then gradually decreased by 100 mPa every 2 h, until a pressure of 20 mPa was reached. The sample was then left at 20 mPa for 46 h at 60 ºC. Note that the drying step can be significantly shortened below 24 h [22].

After drying, the organic xerogel obtained was crushed in a Fritsch planetary mill (Mono Mill P6) with 20 agate balls of 1 cm in diameter, in order to obtain a fine powder. The milling was performed for 30 min at 400 rpm. The powder obtained was then sieved on a 710 µm mesh to remove the largest lumps. Grinding of carbon xerogels does not affect their meso/macropore texture. Nevertheless, crushing the material prior to pyrolysis also is essential to obtain a narrow grain size distribution. The grinding of carbon xerogels in these conditions yields carbon grains typically 5 to 20 µm in size [23]. The organic xerogel powder was subsequently pyrolyzed *via* a thermal treatment at 800 ºC under continuous N_2 flow (Air Liquide ALPHAGAZ™ 1, ≥ 99.999 %) following ramps of temperature as follows: (i) heating at 1.7 ºC.min^{-1} up to 150 ºC and hold for 15 min, (ii) heating at 5 ºC.min^{-1} up to 400 ºC and hold for 60 min, (iii) heating at 5 ºC.min^{-1} up to 800 ºC and hold for 60 min. The carbon xerogel retrieved from this pyrolysis step is denoted as CX0.

Chemical Vapor Deposition (CVD) of carbon using ethylene as precursor was performed at 670 ºC in a stainless-steel tubular oven (Thermolyne 79400 Tube furnace). After increasing the oven temperature to 670 ºC, 0.5 g of CX0 were introduced in the oven using a reverse flow, which allowed for the inert atmosphere of N_2 to be retained inside the oven. A gaseous mix of 80 vol.% ethylene (AirLiquide, ≥ 99.5 %, 1.32 NL.min^{-1}) and 20 vol.% nitrogen (Air Liquide ALPHAGAZ™ 1, ≥ 99.999 %, 0.35 NL.min^{-1}) was introduced inside the oven. As previously mentioned, the CVD treatment is expected to cover the carbon xerogel surface with a more crystalline layer [17]. The contact time between CX0 and the gaseous ethylene/nitrogen mixture was varied to investigate the evolution of the carbon xerogel surface. Five CVD treatment durations were selected: 5, 10, 20, 30, and 60 min. After purging ethylene from the oven by flushing with N_2, the temperature was subsequently increased at 900 ºC and held for 120 min, still under N_2 flow. The sample was then removed from the oven while maintaining the reverse flow and was left to cool to room temperature. The carbon xerogels obtained from these treatments are denoted as CX0-C5, CX0-C10, CX0-C20, CX0-C30, and CX0-C60, corresponding to CVD treatment durations of 5, 10, 20, 30, and 60 min, respectively.

In addition to CVD carbon deposition, a high-temperature post-treatment at 1,500 °C was applied to CX0-C20. Since the deposited layer is expected to be partially organized already [24], a high temperature treatment could further increase its degree of graphitization. The treatment was performed in a Carbolite 18/300 tube furnace, as follows: (i) the sample was introduced in the oven, and an Ar flow of 0.15 mL.min^{-1} was applied, then (ii) the sample was heated at 900 ºC at 3 ºC.min^{-1}, (iii) and finally heated at 1,500 ºC at 1 ºC.min^{-1}. This temperature was held for 1 h. The oven was left to cool down to room temperature, still under N_2 flow. This sample is referred to as CX0-C20-HT1500.

1.2.2. Physicochemical characterization

The textural properties of the carbon xerogels were obtained using a combination of nitrogen adsorption–desorption and mercury intrusion porosimetry, enabling analysis across the full pore size range. Nitrogen adsorption-desorption measurements provide insights into both micropore and mesopore volume. The isotherms were obtained at 77 K with a Micromeritics ASAP 2420 multi-sampler volumetric device. Prior to measurements, the samples underwent degassing under vacuum conditions (1.33×10^{-2} Pa) at room temperature for 5 h, followed by a heating phase to 270 °C for 2 h, while the pressure was kept at 13.33 Pa. The specific surface area,

A_{BET}, was evaluated using the Brunauer, Emmett and Teller (BET) equation. The micropore volume, V_{DUB}, was calculated using Dubinin-Radushkevich equation. The external surface area of the carbon xerogels was also calculated. This area corresponds to the outer surface of the carbon xerogel nodules. It was determined using two approaches: (i) with the t-plot method, using the Harkins–Jura equation (S_{ext}) and (ii) using geometric calculations considering the carbon xerogel structure ($S_{n,ext}$). Indeed, $S_{n,ext}$ is equal to the area per mass of a nodule ($m^2.g^{-1}$),

$$S_{\mathrm{n,ext}} = \frac{S_{\mathrm{nodule}}}{m_{\mathrm{nodule}}} \tag{1.1}$$

where S_{nodule} is the outer surface of the nodule (m^2) and m_{nodule}, the mass of the nodule (kg).

Considering:

$$m_{\mathrm{nodule}} = V_{\mathrm{nodule}}\rho_{\mathrm{nodule}} \tag{1.2}$$

where V_{nodule} is the volume of the nodule (m^3) and ρ_{nodule} the density of the nodule ($kg.m^{-3}$), and provided nodules are spherical and monodisperse in size, one obtains:

$$S_{\mathrm{n,ext}} = \frac{\pi d_{\mathrm{nodule}}^2}{\frac{\pi}{6} d_{\mathrm{nodule}}^3 \rho_{\mathrm{nodule}}} = \frac{6}{d_{\mathrm{nodule}}\rho_{\mathrm{nodule}}} \tag{1.3}$$

where d_{nodule} is the mean nodule diameter (m). This parameter can be deduced from microscopy images, as detailed below. The nodule density needs to be accounted for the nodule microporosity. The total volume of a carbon nodule corresponds to the sum of the solid volume, V_{sol}, and the micropores volume, V_{micro}, within the nodule:

$$V_{\mathrm{tot}} = V_{\mathrm{sol}} + V_{\mathrm{micro}} \tag{1.4}$$

Thus, provided volumes are taken per g of carbon,

$$V_{\mathrm{tot}} = \frac{m_{\mathrm{sol}}}{\rho_{\mathrm{sol}}} + V_{\mathrm{micro}} = \frac{1}{\rho_{\mathrm{s}}} + V_{\mathrm{micro}} \tag{1.5}$$

where m_{sol} is the mass of solid (equal to 1 g, as volumes are considered per g of carbon), ρ_{sol} is the density of the carbon, *i.e.* the skeletal density of the material, ρ_s ($g.cm^{-3}$), and V_{micro} is the micropore volume per gram of carbon ($cm^3.g^{-1}$).

Consequently, for 1 g of material,

$$\rho_{\text{nodule}} = \frac{m_{\text{tot}}}{V_{\text{tot}}} = \frac{1}{\frac{1}{\rho_{\text{s}}} + V_{\text{DUB}}} \tag{1.6}$$

ρ_s corresponds to the skeletal density of the material obtained with He pycnometry measurements, described below. V_{micro} corresponds to V_{DUB}, obtained *via* N_2 adsorption-desorption measurements.

The thickness of the carbon layer can also be estimated geometrically, considering the layer is deposited on the surface of the nodules without filling the micropores:

$$t = \frac{V_{\text{CVD}}}{S_{\text{n,ext}}} \tag{1.7}$$

where V_{CVD} (cm^3) corresponds to the volume occupied by the carbon layer deposited by CVD and $S_{n,ext}$ (cm^2), determined from **Equation (1.3)**, is the external surface area of the carbon nodules estimated geometrically.

Meanwhile,

$$V_{\text{CVD}} = \frac{m_{\text{CVD}}}{\rho_{\text{CVD}}} \tag{1.8}$$

where m_{CVD} denotes the mass of carbon deposited on the carbon xerogel after CVD treatment, and ρ_{CVD} is the density of the deposited carbon layer, taken equal to 2.2 $g.cm^{-3}$, as the carbon layer deposited is assumed to be graphitic carbon [24].

Helium pycnometry was performed using a Quantachrome Ultrapycnometer 1000e, set at a temperature of 20 °C. The skeletal density, ρ_s, *i.e.* the density of the material composing the carbon xerogel nodules (open pores excluded), was obtained with these measurements. Mercury intrusion porosimetry allows to measure the size and volume of pores larger than approximately 3.25 or 7.5 nm, depending on the maximal pressure attainable by the device, and up to 500 nm [25]. Mercury intrusion porosimetry measurements were performed on carbon xerogel powders between 0.01 and 400 MPa by using a Quantachrome Poremaster 60 device, allowing to retrieve the pore size distribution of pores with a width *d* greater than 3.7 nm. The specific pore volume, V_{Hg}, and the pore size distribution were also obtained with this technique by using the Washburn equation on the Hg intrusion jump [26,27]:

$$d = \frac{-4\sigma\cos(\theta)}{P} \tag{1.9}$$

The equation parameters were selected as (i) 140° for the liquid/solid average angle, θ, and (ii) 0.485 $N.m^{-1}$ for the surface tension of mercury, σ.

X-ray diffractograms were obtained on a Bruker D8 Advance powder diffractometer with a copper X-ray source. To minimize background noise and to ensure that no diffraction signal comes from the sample holder itself, a zero-background sample holder (KS Analytic Systems – 32 mm PMMA) was used. The results were obtained with diffraction angles 2θ between 10º and 80º in a Bragg-Bentano configuration. From the obtained diffractograms, crystalline parameters can be retrieved. The lateral size (L_a, a-axis) and stacking height (L_c, c-axis) of crystallites were calculated from the carbon 10 and (002) reflection peaks respectively, using Scherrer's equation [28]:

$$L_a = \frac{k\lambda}{\beta\cos(\theta)} \tag{1.10}$$

where k is a shape factor without dimension, equal to 1.84 for L_a and 0.89 for L_c [29], λ is the X-ray wavelength ($\lambda_{K\alpha}$ = 0.15418 nm), β is the Full Width at Half Maximum (FWHM) and θ is the Bragg angle (º). The interlayer spacing $d_{(002)}$, corresponding to the distance between two layers of graphene, was calculated from Bragg's law [30],

$$n\lambda = 2d\sin(\theta) \tag{1.11}$$

For a first-order reflection, n = 1. Therefore:

$$d_{(002)} = \frac{\lambda}{2\sin(\theta)} \tag{1.12}$$

where λ is the X-ray wavelength and θ is the Bragg angle (º) of the graphene 002 peak.

A Tescan CLARA FEG-SEM at 15 kV under high-vacuum conditions was used to observe carbon xerogels morphology as well as the size of the carbon nodules. Before observation, the samples were sputter-coated with gold (Balzers, SCD004 Sputter-coater, Vaduz, Liechtenstein) and mounted on the sample holder using conductive carbon adhesive. CX0, CX0-C20, CX0-C60 and CX0-C20-HT1500 were also observed with a High-Resolution Transmission Electron Microscope (HR-TEM) using a FEI Tecnai F20–S-TWIN microscope and a JEOL JEM-ARM 200F Cold FEG equipped with a spherical aberration probe corrector; both operations were run using an acceleration voltage of 200 kV. HR-TEM was used to observe the structural difference of the carbon xerogel surface before and after CVD treatment, but also after the high-temperature treatment at 1,500 ºC.

X-ray photoelectron spectrometry (XPS) analysis was used to probe the atomic percentages of carbon and oxygen present at the surface (<10 nm in depth). Analysis was performed using a ThermoFisher K-Alpha photoelectron spectrometer. The sample powders were deposited onto double-sided copper tape. A monochromatized Al Kα line (1486.6 eV) served as the photon source. Survey spectra and high-resolution spectra were recorded at pass energies of 150 eV and 20 eV, respectively, with 3 scans for survey spectra and 20 scans for high-resolution spectra, using a 250 μm diameter X-ray spot. An electron flood gun was activated during analysis to prevent charging. Data were analyzed with Thermo Avantage software (Version 6.6.0). XPS was performed on CX0, CX0-C20, CX0-C60 and CX0-C20-HT1500.

Elemental analysis was performed on CX0 and CX0-C20 as a complementary validation step to investigate bulk composition. Experiments were done in a Vario EL Cube analyzer (Elementar) to measure the bulk C, H, N and O contents. Prior to measurements, the samples were dried overnight at 105 °C to remove moisture. Then, a small amount of material (~2 mg) was placed in the equipment to be burned in a furnace from which the gas was separated using trapping and chromatographic columns. A thermal conductivity detector quantified the gases, from which carbon, hydrogen and nitrogen contents can be calculated. The oxygen content was measured separately in another column using a similar procedure. It must be noted that only the bulk carbon and oxygen content were reported in the results section. The nitrogen content was not reported as its presence was not observed above the detection limit. Moreover, the hydrogen content was also not reported to allow for a fair comparison of the atomic surface compositions determined by XPS. Indeed, the hydrogen content cannot be observed using regular laboratory-based X-ray sources [31], such as the one used here.

1.3. Results and discussion

CX0 was subjected to CVD treatments of varying durations (5–60 min), and the corresponding mass increases were recorded. Several trials were done for each deposition time. Based on the average of at least two samples, the mass increased by approximately 1%, 8%, 16%, 22%, and 25% for CVD durations of 5, 10, 20, 30, and 60 min, respectively. The CX0, CX0-C20 and CX0-60 powders were observed with a Scanning Electron Microscope (SEM) to determine their general morphology and to identify any morphological change upon intermediate (20 min) and long (60 min) CVD treatment. SEM micrographs indicate that CXs are materials composed of interconnected nodules of approximately 50 nm (**Figure 1.1a-b**), as expected [24]. Moreover,

large grains of size >5 µm can be observed. This is in accordance with Piedboeuf *et al*. [23] who found that organic xerogels with a pore size between 50 and 100 nm ground in dry conditions for 30 min often show a grain size distribution centered around 10 µm. Prolonging the ball-milling duration beyond 30 min does not significantly reduce the average grain size. No significant changes are observed upon CVD treatment (**Figure 1.1c-f**). Large carbon agglomerates are not observed, even after a CVD treatment duration of 60 min, indicating that heterogeneous carbon deposition in localized regions does not occur. The nodule size (D_n ~ 50 nm) does not seem affected by the coating process and the deposited carbon layer cannot be seen by this technique. Nevertheless, the thickness of this layer can be estimated considering the nodules external surface area (see **Equation (1.3)**) and the mass of carbon deposited upon CVD treatment. As a reminder, the calculation of the carbon layer thickness was performed assuming that micropores are covered by the secondary CVD layer, but not filled by it. Using **Equation (1.7)**, the thickness t of the carbon layer was estimated to be 0.78 nm for CX0-C20 and 1.22 nm for CX0-C60. Given the nanometric scale of the thickness, this layer cannot be visually observed from SEM micrographs.

The evolution of the pore texture upon CVD treatment was determined using both N_2 adsorption and mercury intrusion porosimetry. Carbon xerogels exhibit a dual pore texture, consisting of micropores, located within the nodules, and interconnected mesopores and macropores, corresponding to the internodular voids [19]. Both techniques are therefore required to obtain a comprehensive assessment of the pore texture of the material. Textural properties are gathered in **Table 1.1**.

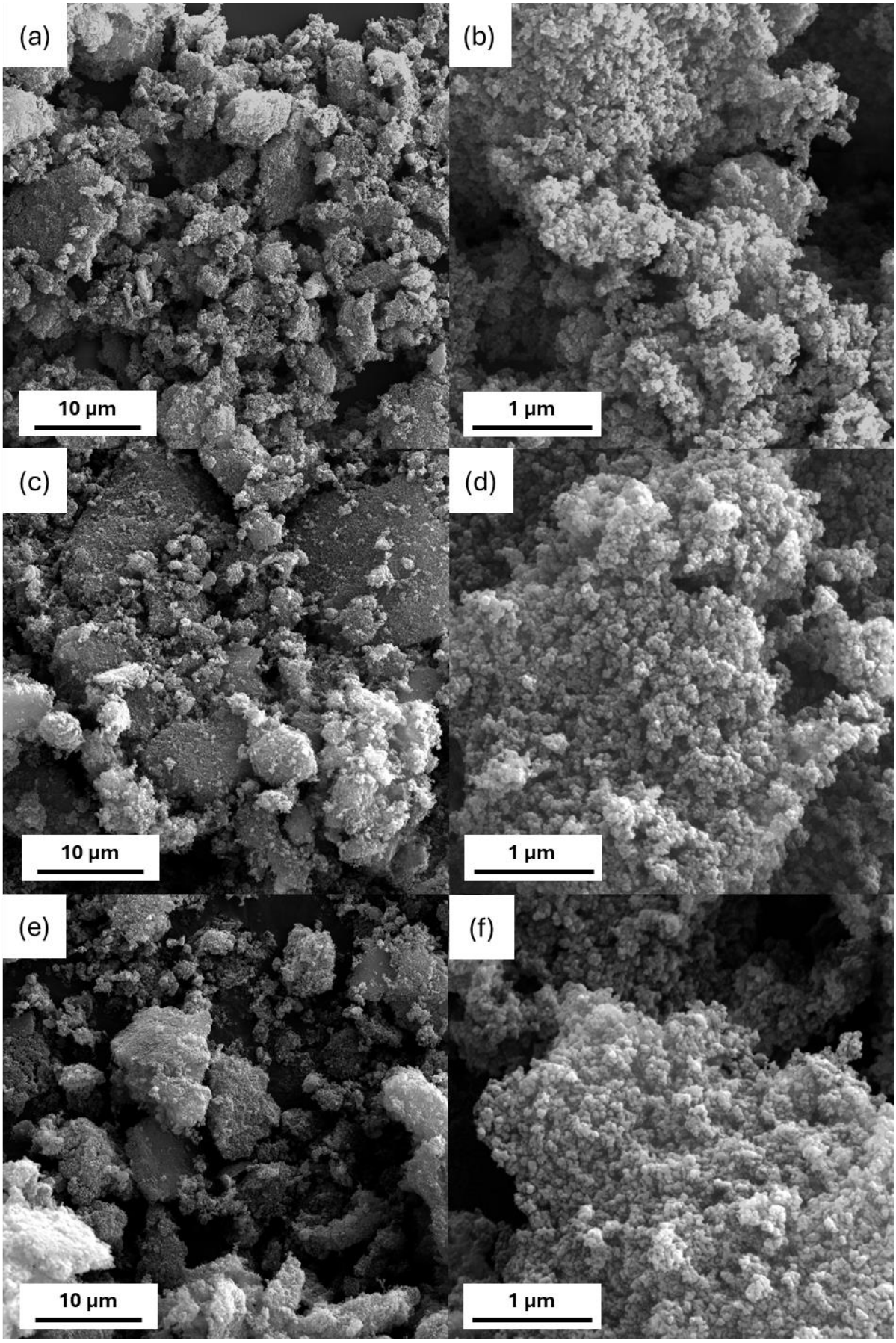

Figure 1.1. SEM images of (a,b) CX0, (c,d) CX0-C20 and (e,f) CX0-C60.

Table 1.1. Textural properties and morphological parameters.

Sample	N_2 adsorption			He pycnometry
	A_{BET}[a] ($m^2.g^{-1}$) ± 5%	S_{ext}[b] ($m^2.g^{-1}$) ± 5%	V_{DUB}[c] ($cm^3.g^{-1}$) ± 0.01	ρ_s[d] ($g.cm^{-3}$) ± 0.02
CX0	674	201	0.26	1.93
CX0-C5	361	166	0.14	1.91
CX0-C10	210	143	0.08	1.93
CX0-C20	174	128	0.07	1.71
CX0-C30	139	126	0.05	1.63
CX0-C60	100	103	0.04	n.d.[e]
CX0-C20-HT1500	187	141	0.08	n.d.[e]

[a] A_{BET}: BET surface area, calculated from nitrogen adsorption-desorption isotherms at 77 K.

[b] S_{ext}: external surface area, calculated from nitrogen adsorption-desorption isotherms at 77 K, from t-plot.

[c] V_{DUB}: micropore volume, calculated from calculated from nitrogen adsorption-desorption isotherms at 77 K using Dubinin-Radushkevich equation.

[d] ρ_s: skeletal density measured by He pycnometry.

[e] Not determined due to measurement reproducibility issues.

Mercury porosimetry was used to characterize pores larger than 3.7 nm and was performed on CX0, CX0-C20, and CX0-C60, under powder form. The intrusion curves (**Figure 1.2a**) show two main parts: (i) a progressive compaction of the powder at low pressures, up to approximately 10^7 Pa, and (ii) a distinct intrusion step at pressures higher than 10^7 Pa. The latter region of the curve was used to determine the mean pore size of the materials (**Figure 1.2b**). For CX0, the average pore size, d_p, was found equal to 70 nm. Upon CVD treatment, only minor variations are observed as d_p slightly increases to 75 nm and to 78 nm for CX0-C20 and CX0-C60, respectively. This slight change indicates that exposure to extended CVD durations does not significantly affect the meso-macropore texture of the carbon xerogels.

N_2 adsorption-desorption isotherms were measured to gain more information about the micropore and mesopore texture, *i.e.* up to 50 nm [32]. The isotherms are presented in **Figure 1.3a-b**. All samples present a type I + II isotherm, according to the IUPAC classification. The adsorbed quantity rises quickly at low relative pressure, indicating the presence of micropores. Moreover, this type of isotherm confirms the dual pore texture of carbon xerogels, which are both microporous and meso/macroporous materials. The shape of the isotherms after CVD treatment and after high-temperature treatment remains similar at large relative pressure (P/P_0

> 0.9). This suggests that these processes affect neither the size of the nodules, D_n, nor the space between the nodules. This in accordance with observations from SEM and Hg porosimetry. At low relative pressures (P/P_0 < 0.1), the N_2 uptake gradually decreases with increasing CVD duration (**Figure 1.3a**), indicating the progressive disappearance of the micropores.

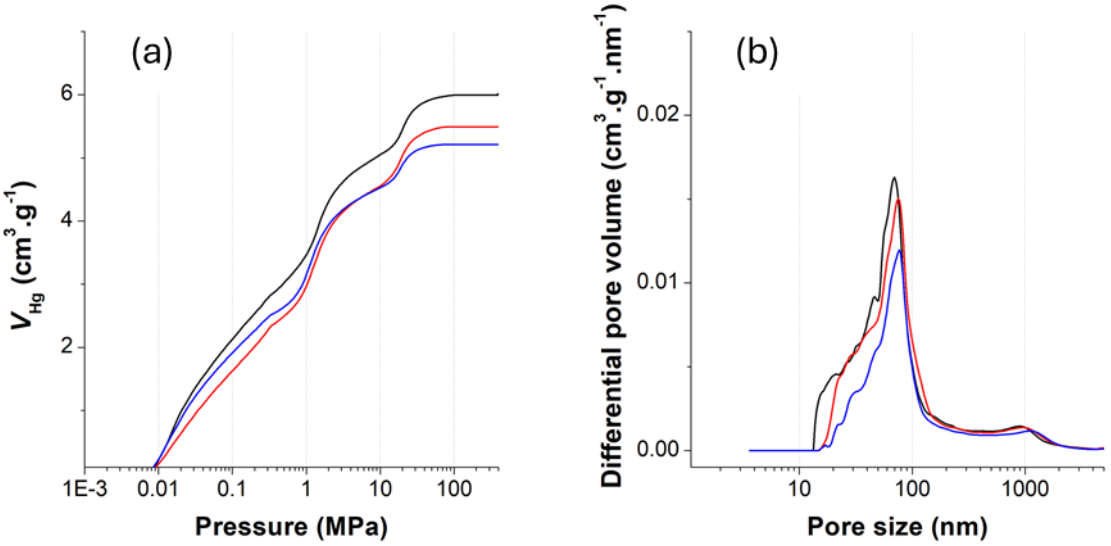

Figure 1.2. (a) Cumulative pore volume and (b) differential pore volume distribution, from Hg intrusion porosimetry of CX0 (—) and CX0-C20 (—), CX0-C60 (—).

The textural properties are compiled in **Table 1.1**. CX0 displays a high A_{BET} of 674 m².g^{-1}, corresponding to V_{DUB} of 0.26 cm³.g^{-1}, which are usual values observed with carbon xerogels prepared under similar conditions. A_{BET} and V_{DUB} decrease to 174 m².g^{-1} and 0.07 cm³.g^{-1} after 20 min of CVD processing, and decrease further with the duration of the CVD treatment, until it reaches a plateau around 100 m².g^{-1} and 0.04 cm³.g^{-1} (after 60 min, **Figure 1.3c**). This corresponds to a surface loss of 74.2 and 85.1%, respectively. The A_{BET} and V_{DUB} of CX0-C20-HT1500 are measured equal to 187 m².g^{-1} and 0.08 cm³.g^{-1}, similar to that of CX0-C20. Thus, no significant changes in pore texture are observed after exposure to high temperature.

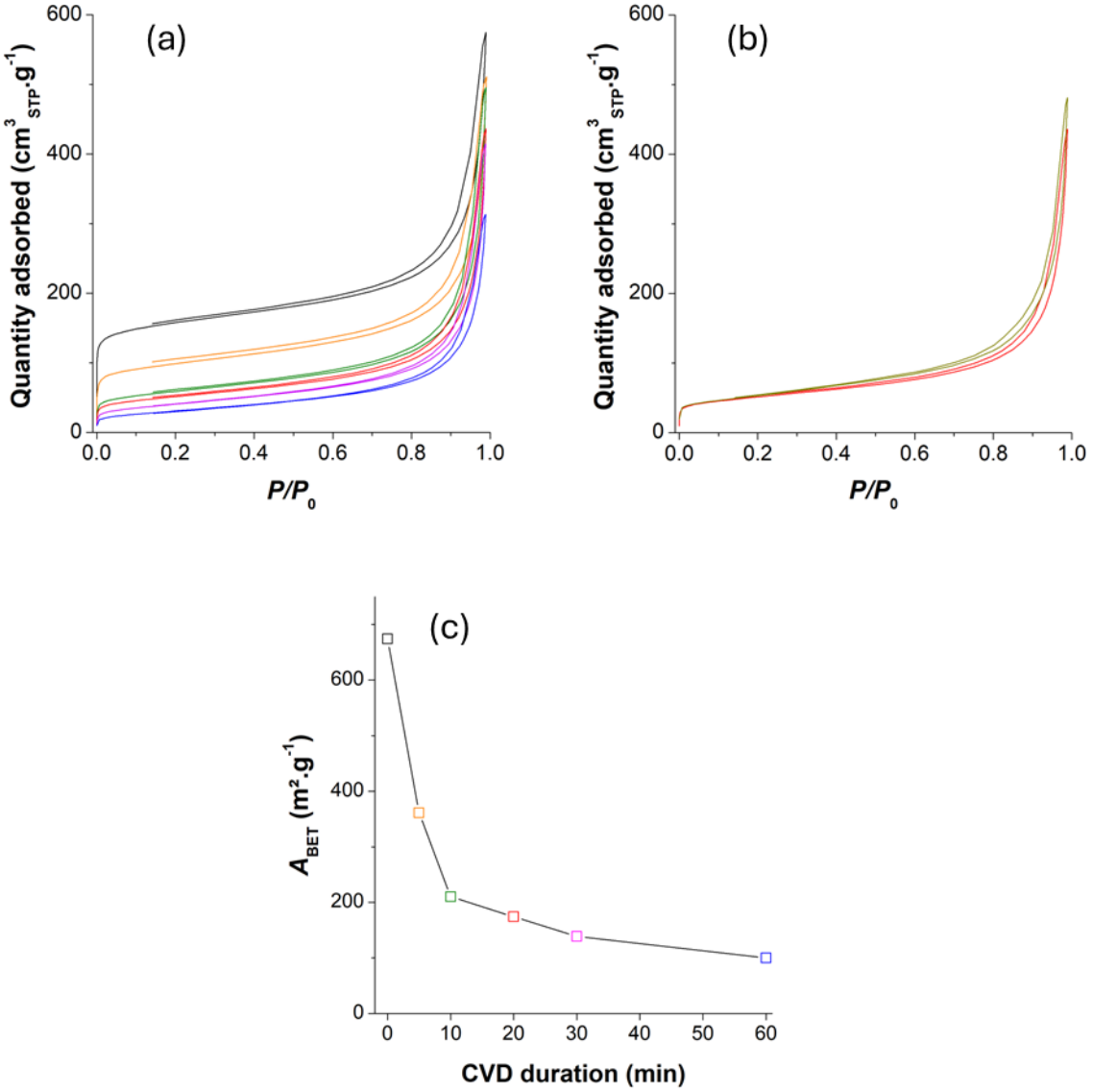

Figure 1.3. Nitrogen adsorption-desorption isotherms of (a) Pristine and CVD-treated xerogels: CX0 (—), CX0-C5 (—), CX0-C10 (—), CX0-C20 (—), CX0-C30 (—) and CX0-C60 (—) and (b) CX0-C20 (—) and CX0-C20-HT1500 (—) (c) Evolution of A_{BET} as a function of the duration of the CVD treatment. The color code remains the same as for figures (a) and (b).

This decrease in the low-pressure region of nitrogen adsorption-desorption isotherms and the subsequent decrease in A_{BET} and V_{DUB} is attributed to the covering and obstruction of the micropores by the CVD carbon layer. However, fully characterizing the extent of micropore coverage remains challenging, as it is unclear whether the layer deposited by CVD completely fills the micropores or only blocks their entrance. Considering the fact that the nodules are of

relatively small size (D_n = 50 nm), micropores are not expected to be deep [24]. Consequently, their filling upon CVD treatment could be significant. Plus, this developed meso/macroporous network observed here offers a large substrate area available for carbon layer deposition, and could explain why the mass increases recorded after CVD treatment were relatively high.

Then, the external surface area of the nodules (*i.e.* excluding the internal micropores) was estimated first using the t-plot method. For CX0, S_{ext} was measured equal to 201 $m^2.g^{-1}$, notably lower than A_{BET} (674 $m^2.g^{-1}$), which reflects the substantial contribution of microporosity to the total surface area measured. For CX0-C20, A_{BET} and S_{ext} are measured at 174 and 128 $m^2.g^{-1}$, respectively. For CX0-C60, A_{BET} and S_{ext} become almost identical, *i.e.* 100 and 103 $m^2.g^{-1}$ respectively. As the CVD duration increases, the proportion of blocked micropores progressively increases. After 60 min of CVD, it is expected that most of the micropores are covered (V_{DUB} = 0.04 $cm^3.g^{-1}$), so $A_{BET} \approx S_{ext}$.

The external surface area of CX0 was also calculated from geometric considerations. Firstly, the nodules density, ρ_{nodule}, was calculated from **Equation (1.6)**. The skeletal density ρ_s of CX0 was measured by He pycnometry, and was found equal to 1.93 $g.cm^{-3}$. The micropore volume obtained from the N_2 adsorption-desorption isotherms was 0.26 $cm^3.g^{-1}$. Thus, ρ_{nodule} was calculated as 1.28 $g.cm^{-3}$. Secondly, using **Equation (1.3)**, $S_{n,ext}$ was found equal to 93 $m^2.g^{-1}$. This value is in good agreement with that of S_{ext} measured after 60 min of CVD (S_{ext} = 100 $m^2.g^{-1}$). Therefore, extending the CVD duration beyond 60 min is not expected to further reduce the surface area to values below $S_{n,ext}$.

The skeletal density was also measured for each CVD duration. As previously stated, the original ρ_s of CX0 was found equal to 1.93 $g.cm^{-3}$. Initially, for short CVD durations (CX0-C5 and CX0-C10), ρ_s remains constant. However, it tends to decrease as the CVD duration increases, to 1.71 $g.cm^{-3}$ for CX0-C20 and 1.63 $g.cm^{-3}$ for CX0-C30. For longer CVD durations, it was observed that the micropores become extensively covered by the secondary layer of carbon. As a result, a large portion of the micropores could become inaccessible to helium, causing the skeletal density to decrease and get close to the nodules density (calculated as 1.28 $g.cm^{-3}$ from **Equation (1.6)**). In contrast, the negligible density change observed for CX0-C5 and CX0-C10 could be attributed to the lower quantity of carbon layer deposited, resulting in a more limited micropores coverage. Note that values for CX0-C60 and CX0-C20-HT1500 were very challenging to obtain, due to difficult pressure equilibration, leading to very long acquisition times and results variability: in those cases, no reliable skeletal density value could

be obtained. Generally speaking, skeletal density values should be considered with some caution, as variations in the density measured can be observed with the amount of material analyzed or with the instrument used to perform the measurement.

In summary, the pore size distribution of the carbon xerogel was found centered around 70 nm and A_{BET} ranges from ~100 to 650 $m^2.g^{-1}$, depending on the CVD duration. Empirically, the pore texture of both pristine and CVD-covered carbon xerogel is suitable for those materials to be used as Pt support for PEMFC catalytic layer [33]. Indeed, the ability of reactant gases to travel within the catalytic layer and reach catalytic sites is highly dependent on the meso/macropores network of the carbon xerogel. Materials containing essentially small mesopores suffer from more significant mass transport limitations due to the narrowness of the pore network. Moreover, catalyst formation and distribution are strongly influenced by the nature and pore texture of the carbon support [18]. It is essential to have sufficient accessible surface area for the deposition of the catalytic phase. Nevertheless, excessively large pores also reduce the available surface area for the deposition of Pt nanoparticles, and can result in poor Pt dispersion. In that case, large Pt particles are formed, which decreases the ElectroChemically active Surface Area (*ECSA*), ultimately affecting the overall fuel cell performances. For these reasons, carbon xerogels with small macropores (approximately 50–100 nm) are often reported as a good compromise: in that case, sufficient gas diffusion can be achieved while ensuring uniform deposition and high utilization of the catalyst [34,35].

The crystallinity of the carbon xerogel upon CVD treatment and high-temperature treatment was then assessed. To that aim, X-ray diffraction (XRD) patterns were collected (**Figure 1.4a-b**). Two main peaks are observed on all diffractograms. A broad and intense peak is observed around 23° and corresponds to the (002) reflection. The Bragg angle and broadness of this peak is typical of materials with a large degree of amorphousness, containing only short-range graphitic domains. A second peak of lower intensity around 44° corresponds to the carbon 10 reflection [36].

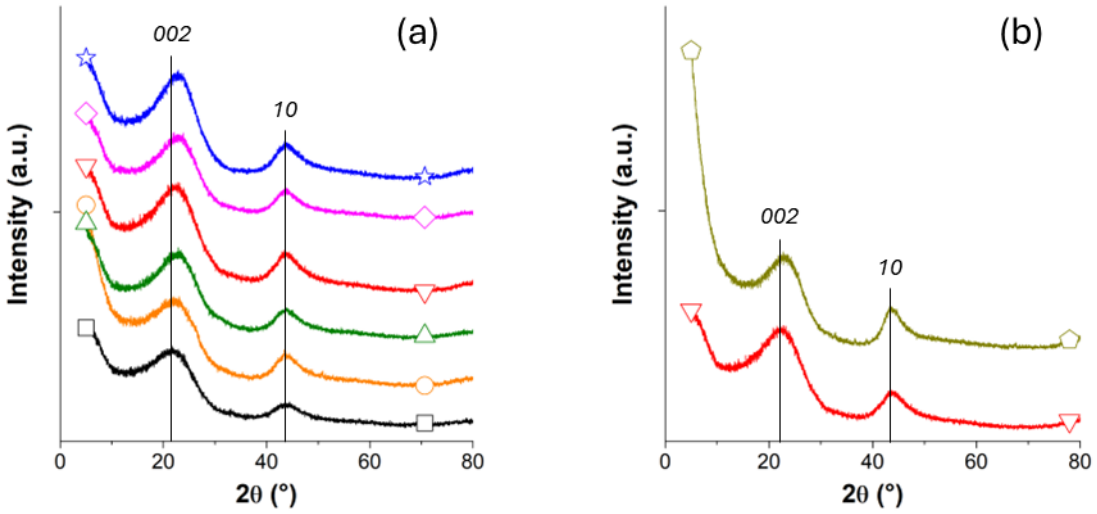

Figure 1.4. X-ray diffractograms of (a) Pristine and CVD-treated CX: CX0 (—□—), CX0-C5 (—○—), CX0-C10 (—△—), CX0-C20 (—▽—), CX0-C30 (—◇—) and CX0-C60 (—☆—); (b) CX0-C20 and CX0-C20-HT1500 (—⬠—). The diffractograms are shifted vertically for legibility.

As observed on the diffractograms, when the CVD duration increases, the carbon 002 diffraction peak becomes narrower and shifts towards higher angles. Consequently, a progressive decrease in d_{002} is observed (**Table 1.2**). d_{002} is equal to 0.405 nm for CX0, which is typical of highly disordered carbons [24]. d_{002} then decreases down to 0.384 nm after 60 min of CVD. The post-treatment at 1,500 ºC also has an effect as d_{002} is equal to 0.393 nm for CX0-20 and decreases to 0.378 nm for CX0-C20-HT1500. The peak behavior upon both CVD treatment and high-temperature treatment is consistent with an increase in structural ordering as the material gets closer to the diffraction characteristics of graphite (d_{002} = 0.335 nm) [36].

An increase in L_a and L_c is also observed, upon both CVD and high-temperature treatments. L_a and L_c are equal to 3.45 and 0.99 nm for CX0, and increase to 3.88 and 1.06 nm for CX0-C60. For CX0-C20, L_a and L_c were measured at 3.61 and 1.03 nm respectively, and increased to 4.67 and 1.28 nm for CX0-C20-HT1500. An increase in L_c, along with a decrease of d_{002}, is a clear indicator that the carbon layer deposited by CVD is more ordered than the initial carbon xerogel surface. Moreover, the secondary layer undergoes further graphitization when processed at high temperature. The values of crystalline parameters remain significantly lower than those of highly crystalline carbons such as graphite [37], but indicate that a higher degree of

graphitization can be achieved. Further investigation with treatments at temperatures above 1,500 °C would be of interest for fundamental studies, but would require both specific equipment and high energy consumption. It should be noted that the high-temperature treatment was not applied to the pristine carbon xerogel. Carbon xerogels are classified as hard carbons (*i.e.* non-graphitizable carbons) [16]. Therefore, their surface is not expected to undergo significant crystalline changes under a catalyst-free high-temperature treatment.

Table 1.2. Crystalline parameters determined by X-ray diffraction.

Sample	L_a[a] (nm) ± 0.03	L_c[b] (nm) ± 0.03	d_{002}[c] (nm) ± 0.004
CX0	3.45	0.99	0.405
CX0-C5	3.74	0.99	0.398
CX0-C10	3.79	1.03	0.394
CX0-C20	3.81	1.03	0.393
CX0-C30	3.94	1.04	0.386
CX0-C60	3.88	1.06	0.384
CX0-C20-HT1500	4.61	1.20	0.378

[a] L_a: Lateral crystallite size, calculated from Scherrer's equation, from the carbon 10 reflection peak.

[b] L_c: Crystallite stacking length, calculated from Scherrer's equation, from the carbon 002 reflection peak.

[c] d_{002}: Graphene interlayer distance, calculated from Bragg's law.

High-resolution transmission electron microscopy (HR-TEM) was used to examine the samples at higher magnification. CX0 exhibits a predominantly amorphous structure, with only short-range graphitic domains (**Figure 1.5a**). The micrographs of CX0-C20 and CX0-C60 remain fairly similar to CX0 (**Figure 1.5b-c**). Previous works were performed with CVD-treated carbon xerogels in our laboratory, in the context of Li-ion batteries. In these studies, it was observed that, upon cyclic voltammetry in half-cell configuration, CVD-coated carbon xerogels display a small peak typical of Li^+ insertion into graphite [22,24]. This peak was totally absent in the case of pristine carbon xerogels. It was thus concluded that the carbon layer deposited by CVD is at least partially graphitized. Even though it is difficult to observe graphitic domains from the HR-TEM micrographs only, the presence of graphene-like sheets in localized regions of CX0-C20 and CX0-C60 is expected. It is thus suggested that the secondary carbon layer deposited by CVD is more ordered than the initial carbon xerogel surface. HR-TEM micrographs of CX0-C20-HT1500 were also acquired (**Figure 1.5d**). Compared to CX0-C20, CX0-C20-HT1500 seems to exhibit increased structural ordering at the edges, and graphene-like sheets in localized regions, suggesting that the high-temperature treatment, despite its

relatively moderate temperature and absence of graphitization catalyst, also has an impact on the carbon surface ordering.

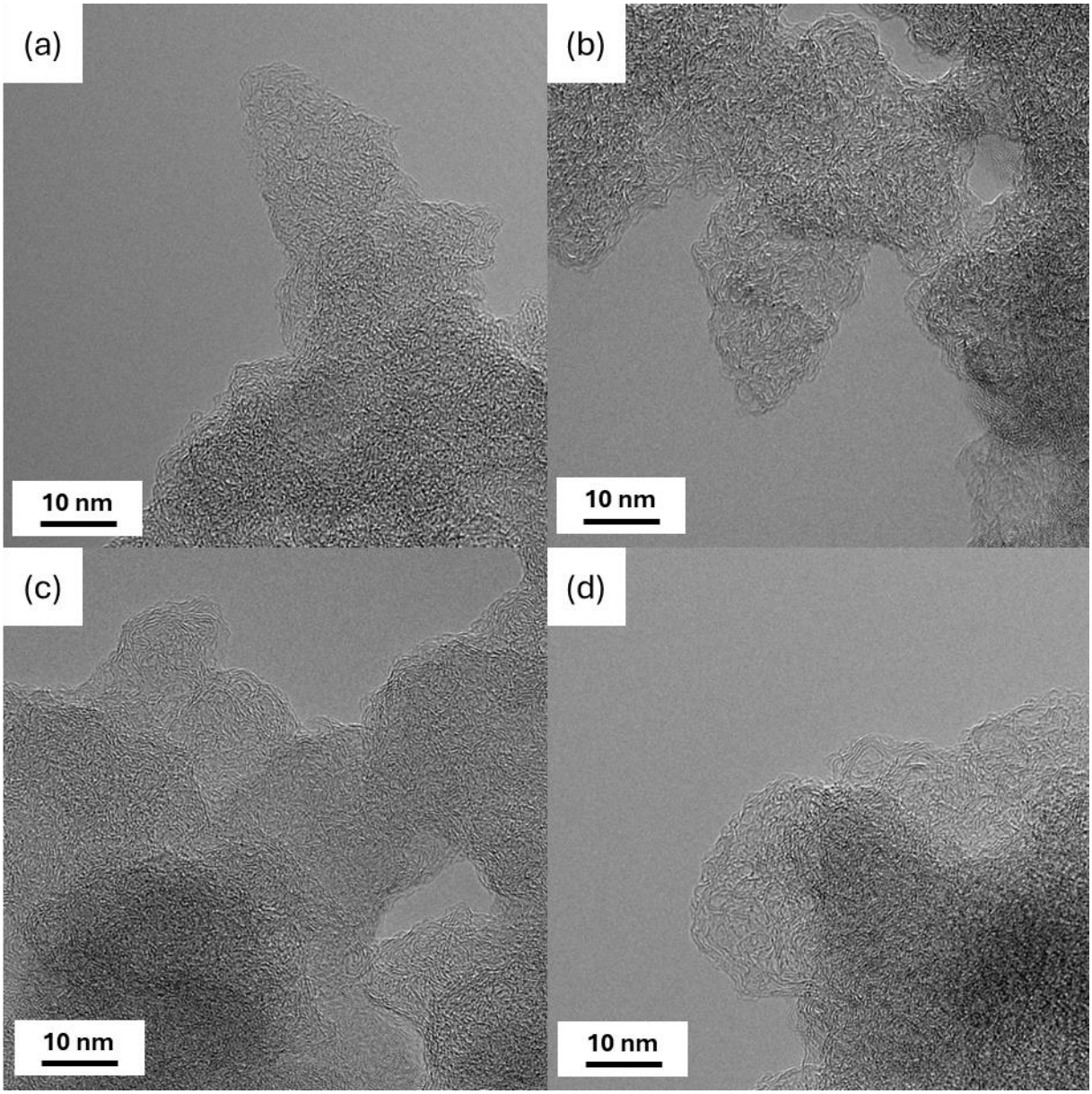

Figure 1.5. HR-TEM micrographs of (a) CX0, (b) CX0-C20, (c) CX0-C60 and (c) CX0-C20-HT1500.

Finally, XPS analysis was conducted on CX0, CX0-C20, CX0-C60 and CX0-C20-HT1500 to investigate the evolution of surface functional groups upon CVD and high-temperature treatments. It should be noted that XPS can detect atomic species with a limit as low as 0.1 at. %. Nevertheless, the error on the atomic percentage can be in the range of 1 at.%, due to

background and quality of peak fitting. Elemental analysis was also performed to get information about the global composition of the samples. The atomic composition of samples observed with both XPS and elemental analysis is compiled in **Table 1.3**. Using XPS, the surface of CX0 was found to contain 96.7 at.% of C, and 3.3 at.% of O. Elementary analysis confirms a bulk composition of 97.5 at.% C and 2.5 at.% O for CX0. After CVD treatment, CX0-C20 and CX0-C60 exhibit surface compositions of 98.4 and 98.0 at.% of C, and 1.6 and 2.0 at.% of O, respectively. For CX0-C20-HT1500, the surface composition remain similar with 98.0 at.% of C and 2.0 at.% of O. Elemental analysis was also performed on CX0-C20: its bulk composition is comprised of 98.8 at.% C and 1.2 at.% O, in agreement with the XPS analysis. An increase in carbon content and small drop in oxygen content is observed upon CVD treatment, both from XPS and elemental analysis. This behavior is likely associated to the carbon coating. Finally, no presence of nitrogen was found, either from XPS or Elemental Analysis.

Table 1.3. Atomic surface composition determined by XPS and elemental analysis.

Sample	XPS (at.%) ± 0.5		Elemental analysis[a] (at.%) ± 0.5	
	C	O	C	O
CX0	96.7	3.3	97.5	2.5
CX0-C20	98.4	1.6	98.8	1.2
CX0-C60	98.0	2.0	n.d.[b]	n.d.[b]
CX0-C20-HT1500	98.4	1.6	n.d.[b]	n.d.[b]

[a] Hydrogen content not considered here for fairer comparison with XPS.

[b] : Not determined due to time constraints.

The XPS spectra of C1s were then deconvoluted (**Figure 1.6**). The predominant surface species are sp_3 C–C / C–H, characteristic of amorphous carbons. They represent 40–60% of the total carbon-carbon bonding. The presence of sp_2 C=C bonds could be associated with small-range graphitic order observed on carbon xerogels. These bonds represent 10–20% of the total carbon-carbon bonds. The presence of oxygen surface groups is also detected. When the organic xerogel is transformed into a carbon xerogel during the thermal treatment at 800 ºC, dangling

bonds are generated at the carbon surface [38]. While these bonds remain inactive under the inert atmosphere of the pyrolysis, they can directly react with O_2 upon exposure to air when the sample is removed from the oven. Simple bond oxygen groups (C-O), double bond (C=O) and carboxyl groups (O-C=O) are present with 14–18%, 3–8% and 5–7% respectively. Aromatic π–π* bonds are also present, with 5–7%. The relative proportions of carbon–oxygen and carbon–carbon bonds remain largely unchanged after both CVD and high-temperature treatments.

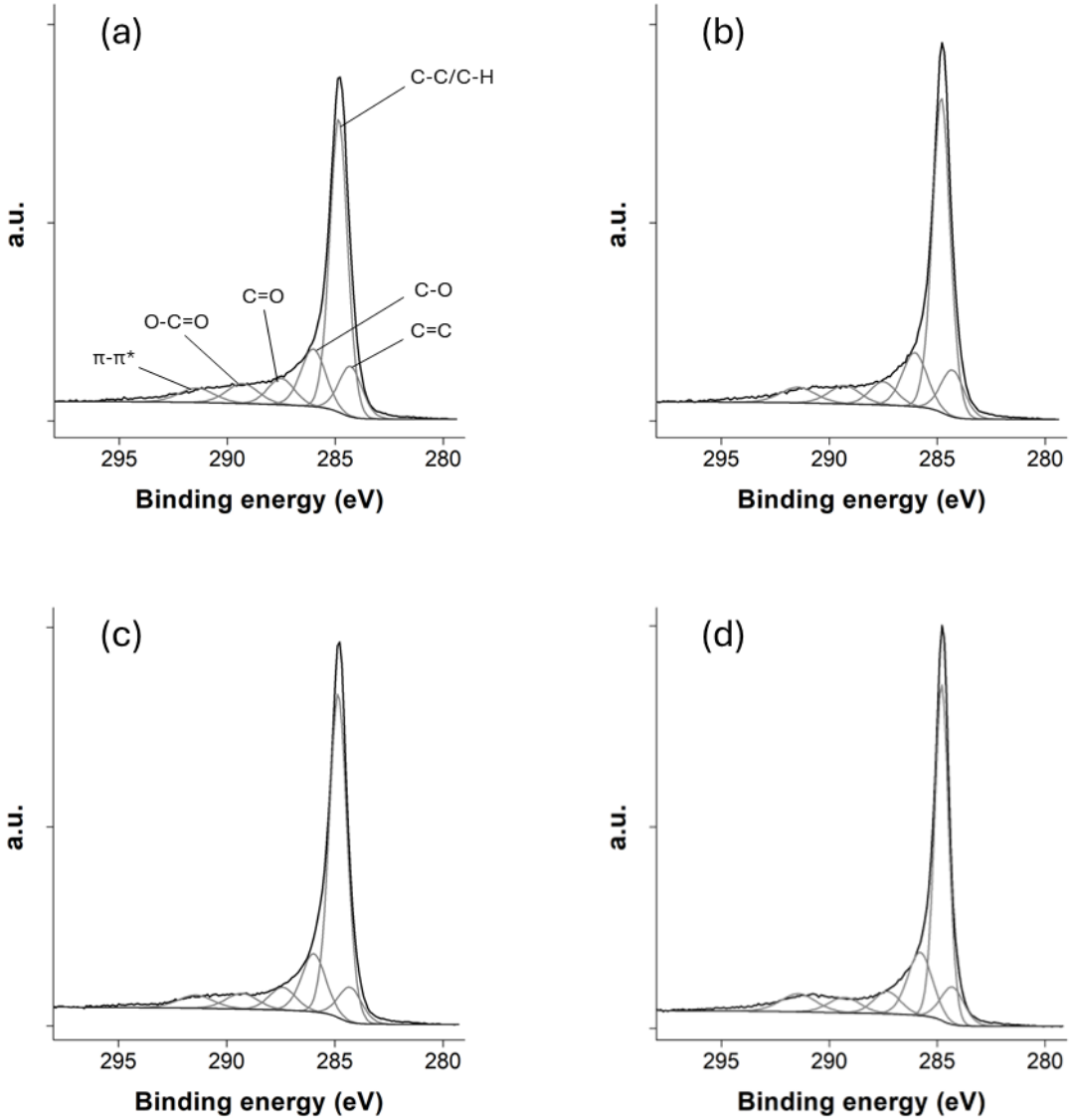

Figure 1.6. Deconvolution of C1s XPS spectra of (a) CX0, (b) CX0-C20, (c) CX0-C60 and (d) CX0-C20-HT1500.

The aim of the CVD treatment was to deposit a carbon coating more ordered than the native CX0 surface, while also preserving favorable mass transport properties associated with the meso/macropores structure. Those two specific features were targeted to design carbon materials with improved properties compared to both carbon black and carbon xerogels in view of their use as catalyst supports in PEMFCs. Based on the observations made on the morphology of the corresponding samples and the evolution of the pore texture and carbon crystallinity, both intermediate (CX0-C20) and long (CX0-C60) CVD treatments seem to produce samples of interest. Indeed, both maintain a meso-macroporosity of interest (with an average pore size around 70-75 nm), that is not affected by the secondary layer. Plus, a large number of micropores are covered by this new carbon layer. Nevertheless, these micropores are not expected to impact the catalyst performances in PEMFC catalytic layers, as they cannot accommodate catalyst nanoparticles whose diameter is usually superior to 2 nm. Additionally, the secondary carbon layer deposited on the xerogel surface is more graphitized than the original xerogel surface. This feature is interesting to enhance resistance to carbon corrosion in PEMFC catalytic layers. Finally, CX0-C20 was also post-treated in an oven at 1,500 ºC. This treatment affects neither the meso/macropore texture of the carbon nor its surface composition, but it allowed to obtain carbon materials with increased surface crystallinity. For this reason, the pristine xerogel (CX0), two CVD-coated carbon xerogels (CX0-C20 and CX0-C60) and the post-treated material (CX0-C20-HT1500) were selected for their evaluation as carbon supports in PEMFC catalytic layers. They will be used in the next chapter to deposit Pt nanoparticles and study the impact of the support surface on the catalyst ageing.

1.4. Conclusion

In this chapter, a carbon xerogel of appropriate meso/macropore size (d_p = 70 nm) for an application in PEMFC was synthesized. This carbon xerogel was subsequently coated with a secondary carbon layer *via* a Chemical Vapor Deposition (CVD) treatment, using ethylene as precursor. The CVD treatment duration was increased from 5 to 60 min in order to obtain samples with various coverage. One of these carbon-coated carbon xerogel was also subjected to a high-temperature treatment at 1,500 ºC. These treatments were designed to modify the surface of the carbon xerogel, by depositing a secondary carbon layer with a higher degree of graphitization and by further increasing the crystallinity level of this layer upon exposure to high temperature; indeed, it was assumed that, given its more ordered structure, the secondary

carbon layer could be graphitizable. Such modifications are expected to yield a carbon material with better resilience and durability properties towards carbon oxidation, when employed as a carbon support for PEMFC catalytic layer, without impacting the meso/macropore texture that will ultimately govern mass transport within the layer.

The evolution of pore texture, degree of graphitization and atomic composition of the carbon xerogel was examined upon exposure to CVD processing and/or high-temperature heat treatment. SEM micrographs and Hg porosimetry confirmed that neither the overall morphology nor the meso/macropore network are modified by the secondary layer deposition. This is essential to ensure efficient mass transport of reactants and products in the PEMFC catalytic layer. In addition, sufficient external surface area, measured between 100 to 140 $m^2.g^{-1}$, remains available on the carbon nodules to homogeneously disperse the metal catalyst nanoparticles in the subsequent parts of this thesis.

The crystallinity of the carbon xerogels was also evaluated with XRD and HR-TEM analysis. The pristine carbon xerogel displays features typical of amorphous carbons with only short-range graphitic domains. Meanwhile, the secondary carbon layer deposited on the carbon xerogel by CVD displays a higher degree of ordering than the original carbon xerogel surface. Moreover, the crystalline parameters of the secondary layer treated at 1,500 ºC show a decrease in the graphene interlayer distance and an increase in carbon crystallite size, indicating that the high-temperature treatment leads to partial crystallization of the CVD-deposited carbon layer.

The change in carbon surface crystallinity is particularly relevant for PEMFC applications. Indeed, more ordered carbon structures are expected to be more resistant towards carbon corrosion. Based on these observations, four materials (CX0, CX0-C20, CX0-C60, and CX0-C20-HT1500) were selected for further evaluation as catalyst supports for synthesizing Pt/carbon electrocatalysts and evaluate their resistance to ageing. This will be the subject of Chapter 2.

1.5. References

[1] S. Maass, F. Finsterwalder, G. Frank, R. Hartmann, C. Merten, Carbon Support Oxidation in PEM Fuel Cell Cathodes, *Journal of Power Sources*, 176 (2008) 444–451.

[2] N. Job, J. Marie, S. Lambert, S. Berthon-Fabry, P. Achard, Carbon Xerogels as Catalyst Supports for PEM Fuel Cell Cathode, *Energy Conversion and Management*, 49 (2008) 2461–2470.

[3] Y.C. Park, H. Tokiwa, K. Kakinuma, M. Watanabe, M. Uchida, Effects of Carbon Supports on Pt Distribution, Ionomer Coverage and Cathode Performance for Polymer Electrolyte Fuel Cells, *Journal of Power Sources*, 315 (2016) 179–191.

[4] C.A. Reiser, L. Bregoli, T.W. Patterson, J.S. Yi, J.D. Yang, M.L. Perry, T.D. Jarvi, A Reverse-Current Decay Mechanism for Fuel Cells, *Electrochemical and Solid-State Letters*, 8 (2005) A273.

[5] K.H. Kangasniemi, D.A. Condit, T.D. Jarvi, Characterization of Vulcan Electrochemically Oxidized under Simulated PEM Fuel Cell Conditions, *Journal of The Electrochemical Society*, 151 (2004) E125.

[6] N. Macauley, D.D. Papadias, J. Fairweather, D. Spernjak, D. Langlois, R. Ahluwalia, K.L. More, R. Mukundan, R.L. Borup, Carbon Corrosion in PEM Fuel Cells and the Development of Accelerated Stress Tests, *Journal of The Electrochemical Society*, 165 (2018) F3148–F3160.

[7] L. Strandberg, V. Shokhen, M. Skoglundh, B. Wickman, Carbon Support Corrosion in PEMFCs Followed by Identical Location Electron Microscopy, *ACS Catalysis*, 14 (2024) 8494–8504.

[8] C. Alegre, D. Sebastián, M.J. Lázaro, Carbon Xerogels Electrochemical Oxidation and Correlation with their Physico-Chemical Properties, *Carbon*, 144 (2019) 382–394.

[9] Y. Shao, G. Yin, Y. Gao, Understanding and Approaches for the Durability Issues of Pt-based Catalysts for PEM Fuel Cell, *Journal of Power Sources*, 171 (2007) 558–566.

[10] D. Bom, R. Andrews, D. Jacques, J. Anthony, B. Chen, M.S. Meier, J.P. Selegue, Thermogravimetric Analysis of the Oxidation of Multiwalled Carbon Nanotubes: Evidence for the Role of Defect Sites in Carbon Nanotube Chemistry, *Nano Letters*, 2 (2002) 615–619.

[11] P.T. Yu, W. Gu, J. Zhang, R. Makharia, F.T. Wagner, H.A. Gasteiger, Carbon-Support Requirements for Highly Durable Fuel Cell Operation, in: Polymer Electrolyte Fuel Cell Durability, 2009: pp. 29–53.

[12] M.M. Gaikwad, M. Kakunuri, C.S. Sharma, Enhanced Catalytic Graphitization of Resorcinol Formaldehyde derived Carbon Xerogel to Improve its Anodic Performance for Lithium Ion Battery, *Materials Today Communications*, 20 (2019) 100569.

[13] Z. Wang, Y. Wang, Q. Luo, S. Wang, Y. Yi, Synthesis of Novel Porous Graphitic Carbon Xerogel-Supported Uniform Platinum Nanoparticle for Oxygen Reduction Reaction, *ChemistrySelect*, 10 (2025).

[14] M. Canal-Rodríguez, A. Arenillas, J.A. Menéndez, D. Beneroso, N. Rey-Raap, Carbon Xerogels Graphitized by Microwave Heating as Anode Materials in Lithium-Ion Batteries, *Carbon*, 137 (2018) 384–394.

[15] C. Lin, J.A. Ritter, Effect of Synthesis pH on the Structure of Carbon Xerogels, *Carbon*, 35 (1997) 1271–1278.

[16] M. Kakunuri, C.S. Sharma, Resorcinol-Formaldehyde Derived Carbon Xerogels: A Promising Anode Material for Lithium-Ion Battery, *Journal of Materials Research*, 33 (2018) 1074–1087.

[17] M.L.C. Piedboeuf, A.F. Léonard, G. Reichenauer, C. Balzer, N. Job, How Do the Micropores of Carbon Xerogels Influence their Electrochemical Behavior as Anodes for Lithium-Ion Batteries?, *Microporous and Mesoporous Materials*, 275 (2019) 278–287.

[18] N. Job, F. Maillard, J. Marie, S. Berthon-Fabry, J.-P. Pirard, M. Chatenet, Electrochemical Characterization of Pt/Carbon Xerogel and Pt/Carbon Aerogel Catalysts: First Insights into the Influence of the Carbon Texture on the Pt Nanoparticle Morphology and Catalytic Activity, *Journal of Materials Science*, 44 (2009) 6591–6600.

[19] N. Job, R. Pirard, J. Marien, J.P. Pirard, Porous Carbon Xerogels with Texture Tailored by pH Control during Sol–Gel Process, *Carbon*, 42 (2004) 619–628.

[20] I.D. Alonso-Buenaposada, N. Rey-Raap, E.G. Calvo, J. Angel Menéndez, A. Arenillas, Effect of Methanol Content in Commercial Formaldehyde Solutions on the Porosity of RF Carbon Xerogels, *Journal of Non-Crystalline Solids*, 426 (2015) 13–18.

[21] N. Job, F. Panariello, J. Marien, M. Crine, J.P. Pirard, A. Léonard, Synthesis Optimization of Organic Xerogels Produced from Convective Air-Drying of Resorcinol–Formaldehyde Gels, *Journal of Non-Crystalline Solids*, 352 (2006) 24–34.

[22] B. Karaman, H. Tonnoir, D. Huo, J. Castro Gutiérrez, B. Carré, A.F. Léonard, M. Bermont, Z. Deckers, A. Celzard, V. Fierro, C. Davoisne, R. Janot, N. Job, Post-Treatments on Carbon Xerogels to Improve their Performance as Negative Electrodes of Na-Ion Batteries, *Carbon*, 246 (2026) 120841.

[23] M.L.C. Piedboeuf, A.F. Léonard, K. Traina, N. Job, Influence of the Textural Parameters of Resorcinol-Formaldehyde Dry Polymers and Carbon Xerogels on Particle Sizes upon Mechanical Milling, *Colloids and Surfaces A: Physicochemical and Engineering Aspects*, 471 (2015) 124–132.

[24] B. Karaman, H. Tonnoir, D. Huo, B. Carré, A.F. Léonard, J.C. Gutiérrez, M.L. Piedboeuf, A. Celzard, V. Fierro, C. Davoisne, R. Janot, N. Job, CVD-Coated Carbon Xerogels for Negative Electrodes of Na-Ion Batteries, *Carbon*, 225 (2024) 119077.

[25] H. Giesche, Mercury Porosimetry: A General (Practical) Overview, *Particle & Particle Systems Characterization*, 23 (2006) 9–19.

[26] E.W. Washburn, Note on a Method of Determining the Distribution of Pore Sizes in a Porous Material, *Proceedings of the National Academy of Sciences*, 7 (1921) 115–116.

[27] R. Pirard, B. Heinrichs, O. Van Cantfort, J.P. Pirard, Mercury Porosimetry Applied to Low Density Xerogels; Relation between Structure and Mechanical Properties, *Journal of Sol-Gel Science and Technology*, 13 (1998) 335–339.

[28] G. Bergeret, P. Gallezot, Particle Size and Dispersion Measurements, in: Handbook of Heterogeneous Catalysis, Wiley, 2008: pp. 738–765.

[29] B.E. Warren, X-Ray Diffraction in Random Layer Lattices, *Physical Review*, 59 (1941) 693–698.

[30] M.A. Short, P.L. Walker, Measurement of Interlayer Spacings and Crystal Sizes in Turbostratic Carbons, *Carbon*, 1 (1963) 3–9.

[31] N. Stojilovic, Why Can't We See Hydrogen in X-ray Photoelectron Spectroscopy?, *Journal of Chemical Education*, 89 (2012) 1331–1332.

[32] P.S. Liu, G.F. Chen, Characterization Methods, in: Porous Materials, Elsevier, 2014: pp. 411–492.

[33] P. Kumar Mohanta, M.S. Ripa, F. Regnet, L. Jörissen, Effects of Supports BET Surface Areas on Membrane Electrode Assembly Performance at High Current Loads, *Catalysts*, 11 (2021) 195.

[34] N. Job, B. Heinrichs, S. Lambert, J.P. Pirard, J.F. Colomer, B. Vertruyen, J. Marien, Carbon Xerogels as Catalyst Supports: Study of Mass Transfer, *AIChE Journal*, 52 (2006) 2663–2676.

[35] N. Job, S. Berthon-Fabry, S. Lambert, M. Chatenet, F. Maillard, M. Brigaudet, J.-P. Pirard, Carbon Xerogels as Supports for Catalysts and Electrocatalysts, in: Proceedings of the International Carbon Conference, 2009.

[36] F.J. Maldonado-Hódar, C. Moreno-Castilla, J. Rivera-Utrilla, Y. Hanzawa, Y. Yamada, Catalytic Graphitization of Carbon Aerogels by Transition Metals, *Langmuir*, 16 (2000) 4367–4373.

[37] Y. Nakayasu, Y. Goto, Y. Katsuyama, T. Itoh, M. Watanabe, Highly Crystalline Graphite-Like Carbon from Wood via Low-Temperature Catalytic Graphitization, *Carbon Trends*, 8 (2022) 100190.

[38] A. Manivannan, M. Chirila, N.C. Giles, M.S. Seehra, Microstructure, Dangling Bonds and Impurities in Activated Carbons, *Carbon*, 37 (1999) 1741–1747.

- Chapter 2 -

CARBON-COATED CARBON XEROGELS AS CATALYST SUPPORT FOR PROTON EXCHANGE MEMBRANE FUEL CELL ELECTRODES

Abstract

A carbon xerogel (CX) with a pore size of ~70 nm, synthesized in Chapter 1, was selected as support for fuel cell electrocatalyst. While CXs offer excellent mass transport properties, their amorphous nature reduces their resistance towards carbon corrosion under the oxidizing conditions of PEMFC operation. To address this, a more organized carbon layer was deposited on the xerogel surface using Chemical Vapor Deposition (CVD), with two treatment durations: 20 and 60 min. The one treated 20 min was also further post-treated at 1,500 ºC under inert atmosphere for crystallization. This layer covers a large part of the micropores but keeps intact the interconnected meso/macropore network of the CX, essential to mass transport in the final electrode. Pt nanoparticles (20 wt.%) were then deposited on both the pristine and the CVD-treated CXs by reduction of hexachloroplatinic acid in liquid phase. The electrochemical properties of the resulting catalysts toward the Oxygen Reduction Reaction were evaluated and compared to those of a commercial carbon black-supported catalyst. The catalysts based on post-treated CX supports display initial catalytic activities comparable to those obtained on the pristine CX and on the commercial catalyst. After accelerated aging in RDE configuration, despite a decrease in the catalytic surface of Pt, carbon-xerogel supported catalysts exhibited an increase in specific activities while mass activities remained stable. This behavior was attributed to the evolution of nanoparticle size upon aging and their approach or deviation from their optimal size.

Contributions

The catalysts synthesis, N_2 adsorption-desorption measurements, XRD analyses, profilometry measurements and the complete electrochemical characterization of the catalysts were carried out by the PhD candidate. TEM micrographs were obtained by the PhD candidate, with the help of Dr. Philippe Compère, from Département de Biologie, Ecologie et Evolution in Université de Liège. The TGA curves were obtained by Dr. Alexandre F. Léonard from the CARPOR platform in Université de Liège.

2.1. Introduction

As developed in the General Introduction, Proton Exchange Membrane Fuel Cells (PEMFCs) are electrochemical systems capable of extracting electrical energy from hydrogen and oxygen through the Hydrogen Oxidation Reaction (HOR) and Oxygen Reduction Reaction (ORR). However, the biggest drawback of PEMFCs is found in the slow kinetics of the HOR and particularly of the ORR that leads to the necessary use of a catalytic layer at both electrodes. Catalytic layers of PEMFCs are usually made of Pt-based nanoparticles supported on a carbon structure and mixed with a proton-conducting ionomer [1,2]. In this assembly, carbon gels are a promising class of materials that can be effectively used as supports for the catalyst [3]. Indeed, the highly tunable porosity of carbon gels makes them good model materials for studying catalyst–support interactions [4,5]. Nevertheless, due to their highly amorphous nature, carbon gels are materials prone to corrosion and degradation compared to more graphitic materials, such as carbon nanotubes [6]. Indeed, high potentials encountered at the cathode of operating PEMFCs (>0.6 V *vs.* RHE), coupled with the presence of Pt, water and oxygen under relatively high temperature, accelerates the corrosion kinetics of carbon materials, and leads to performance losses upon prolonged fuel cell operation [7,8]. Therefore, increasing the resistance of the carbon support to oxidation is needed to yield highly durable catalytic layers, addressing a critical bottleneck in PEMFCs.

For this reason, a strategy explored in the previous chapter was the deposition of a graphitizable carbon layer onto a carbon xerogel (CX) surface. This strategy was applied to a CX with a mean pore of size of 70 nm (denoted as CX0), a material suitable for deposition of an electrocatalytic phase and compatible with PEMFC electrode manufacturing [3]. In Chapter 1, the carbon layer was deposited *via* Chemical Vapor Deposition (CVD) [9] using ethylene as a precursor. The CVD treatment duration was varied between 5 and 60 min to obtain samples with different degrees of coverage. Two main findings were obtained from this chapter. First, neither the overall morphology nor the meso/macropore network were modified by the secondary layer deposition, which is essential for allowing sufficient mass transport in the final catalytic layer, and enables homogeneous Pt deposition. Second, the secondary carbon layer exhibited a higher degree of ordering than the original carbon surface. Finally, CX0 treated 20 min by CVD was subjected to a subsequent post-treatment at 1,500 ºC under inert atmosphere, which led to further crystallization of the CVD-deposited carbon layer, hinting at the graphitizable nature of the deposited carbon layer [10].

In this chapter, the pristine CX0, along with the same CX0 subjected to three different post-treatments were selected to assess their quality as electrocatalyst supports: the CX subjected to 20 and 60 min of CVD, as well as the CX treated 20 min by CVD followed by a thermal treatment under inert atmosphere at 1,500 ºC. Afterwards, Pt nanoparticles (20 wt.%) were deposited on the surface of these samples *via* liquid-phase reduction of a Pt precursor, hexacholoroplatinic acid, using formic acid [11]. The obtained catalysts were then processed into inks, which were coated onto a Rotating Disk Electrode (RDE) for electrochemical characterization in liquid electrolyte. A commercially available carbon black–supported Pt catalyst was also included for comparison. The samples were analyzed on a 3-electrodes setup in acidic environment, namely in 0.5 M H_2SO_4, to simulate the acidic conditions of catalytic layers under use in PEMFCs. Active layers deposited on RDE were also submitted to Accelerated Stress Tests (AST) and the evolution of the catalytic activities and electroactive surface areas of Pt were analyzed through aging. The study enabled determining the impact of the secondary CVD-deposited carbon layer on the durability of Pt/CX catalysts.

2.2. Experimental

2.2.1. Synthesis of the carbon xerogel-supported Pt catalysts

The synthesis of the pristine carbon xerogel with adequate pore size was previously described in details in Chapter 1. Briefly, a polycondensation reaction between resorcinol and formaldehyde in an aqueous medium was performed, in presence of sodium carbonate acting as a pH regulator [5]. The pH of the mixture synthesis was measured equal to 5.0. A monolithic block of organic xerogel was obtained after polymerization and ageing at 80°C. After appropriate grinding, the powder was pyrolyzed in inert atmosphere at 800 ºC. This material was characterized by N_2 adsorption-desorption measurement and Hg porosimetry in the previous chapter. In short, the BET surface area and average pore size were found equal to 674 $m^2.g^{-1}$ and 70 nm respectively, *i.e.* a pore texture suitable for PEMFC applications [3]. The carbon xerogel powder retrieved from this pyrolysis step is denoted as CX0 hereafter, as in Chapter 1.

Moreover, in Chapter 1, the pristine CX0 was subjected to a Chemical Vapor Deposition (CVD) treatment, *via* ethylene cracking at 670 ºC, and two treatment durations (20 min and 60 min) were selected. Those samples are denoted as CX0-C20 and CX0-C60 hereafter. CX0-C20 was

identified as optimal, as it enabled efficient deposition of a secondary carbon layer with increased surface ordering without extensive treatment duration. This material was also subjected to a second post-treatment at 1,500 °C under inert atmosphere. It is referred to as CX0-C20-HT1500. All these materials were selected because they exhibited an increase in their surface ordering compared to the original CX0 surface, while still maintaining sufficient accessible surface area for Pt nanoparticle deposition, even after the post-treatments.

The synthesis of Pt/CX catalysts was then performed by reduction of Pt^{4+}, from $H_2PtCl_6.6H_2O$ platinum precursor, using formic acid as a reductant. Formic acid reduction is a simple one-step method suitable to homogeneously deposit small Pt nanoparticles on CXs without producing Pt aggregates [11,12]. The procedure was performed as follows, with a Pt loading target of 20 wt.%:

(i) 0.2 g of carbon xerogel powder were dispersed in 200 mL of a 2 $mol.L^{-1}$ formic acid solution (Sigma-Aldrich, reagent grade ≥ 95%);
(ii) The suspension was then heated to 80 ºC using an oil bath and mixed under magnetic stirring;
(iii) 50 mL of a 38 $mmol.L^{-1}$ solution of $H_2PtCl_6.6H_2O$ salt (Alfa-Aesar, 99.95% on metals basis, Pt 37.5% min) was added dropwise to the suspension at a rate of 2.5 $mL.min^{-1}$;
(iv) The mixture was stirred for 1 h at 80 ºC;
(v) The mixture was then filtered and washed with 600 mL of ultrapure Milli-Q® water;
(vi) The obtained Pt/CX was finally dried at 50 ºC under air in an oven, overnight.

The carbon xerogel-supported catalysts retrieved from the Pt deposition step are referred to as CX0-Pt, CX0-C20-Pt, CX0-C60-Pt and CX0-C20-HT1500-Pt. A commercial Pt/carbon black catalyst (De Nora, Vulcan XC-72, 20 wt. % Pt), denoted as Vulcan XC-72-Pt, was also chosen as benchmark.

2.2.2. Physicochemical characterization

The textural properties of the catalysts were determined with a combination of nitrogen adsorption-desorption, and compared to those of the supports, as described in Chapter 1. As a reminder, the specific surface area (A_{BET}) was evaluated using the Brunauer, Emmett and Teller (BET) equation selecting in each case the relative pressure range according to Rouquerol's criterion [13]. The micropore volume, V_{DUB}, was calculated using the Dubinin-Radushkevich equation and the external surface area of the carbon nodules, S_{ext}, was obtained through the t-

plot method. Note that the BET specific surface area, A_{BET}, corresponds to the sum of the micropore surface, located within the carbon nodules, and the external surface of the nodules. For catalysts however, the contribution of Pt to the mass measured was accounted for, and the different parameters are reported per mass unit of carbon for adequate comparison with the corresponding supports.

ThermoGravimetric Analysis (TGA) was employed to obtain the actual amount of Pt deposited on the carbon supports, as a comparison to the target Pt loading (20 wt.%), by burning the carbon and measuring the remaining mass. The measurements were performed on catalysts with a Setaram Sensys Evo microbalance, under air, with a constant heat of 5 ºC.min^{-1}.

X-ray diffractograms of the catalysts were obtained on a Bruker D8 Advance powder diffractometer with a copper X-ray source. To minimize background noise, and to ensure that no diffraction signal comes from the sample holder itself, a zero-background sample holder (KS Analytic Systems – 32 mm PMMA Zero-Background Sample Holder) was used. The results were obtained with diffraction angles 2θ between 10º and 80º in a Bragg-Bentano configuration. The crystal size of Pt nanoparticles (d_{XRD}) was determined from the XRD spectra of catalysts using the Pt(111) diffraction peak and Scherrer's equation:

$$d_{XRD} = \frac{k\lambda}{\beta\cos(\theta)} \tag{2.1}$$

where k is a shape factor without dimension, equal to 0.89 [14], λ is the X-ray wavelength ($\lambda_{K\alpha}$ = 0.15418 nm), β is the Full Width at Half Maximum (FWHM) of the considered peak and θ is the Bragg angle (º).

To determine the Pt nanoparticle size distribution, the catalysts were observed with a JEOL JEM-ARM 200F Cold FEG equipped with a spherical aberration probe corrector and operated with an acceleration voltage of 200 kV. Prior to observations, a few milligrams of the powder samples were dispersed into ethanol and mixed homogeneously with help of an ultrasonic bath. A drop of the suspension was then spread onto a copper grid (PELCO® TEM grid, 200 mesh Cu), and was left to dry under ambient air. From TEM micrographs, the arithmetic average diameter, d_{TEM}, of the Pt nanoparticles was calculated on a significantly large number of Pt nanoparticles (≥ 50). Note that only clearly isolated nanoparticles were taken into account for this analysis. Besides, both the surface-weighed (d_S) and volume-weighed (d_V) diameters of the nanoparticles were calculated as:

$$d_s = \sum \frac{n_i d_i^3}{n_i d_i^2} \quad (2.2)$$

$$d_V = \sum \frac{n_i d_i^4}{n_i d_i^3} \quad (2.3)$$

where n_i is the number of particles of diameter d_i. The volume-weighed diameter can be compared to the crystallite diameter obtained with XRD, as XRD is a volume-sensitive technique [15]. The surface-weighed diameter can be compared to that calculated from the CO stripping data (see **Section 2.2.3**), as CO stripping is a surface-sensitive technique [16].

2.2.3. Electrochemical characterization on Rotating Disk Electrode

Materials

The electrochemical characterization was performed in a four-neck glass cell designed to accommodate all the setup elements (see **Figure 2.1**). The glassware was cleaned overnight by immersion in a H_2SO_4:H_2O_2 solution, followed by thorough rinsing with ultrapure Milli-Q® water (18.2 MΩ.cm). The electrolyte solution was prepared using also ultrapure water and H_2SO_4 (Merck, 95-97% for analysis EMSURE® ISO). Catalysts underwent characterization using a Rotating Disk Electrode (RDE). A three-electrode setup was used with a Metrohm Autolab PGSTAT204 potentiostat. The electrodes were composed of (i) a 5-mm diameter glassy carbon EDT type (Origalys - A35T095) as working electrode; (ii) a platinum grid as counter-electrode; (iii) a saturated calomel electrode (SCE) as a reference (Origalys - OGR-Hg-Ø8-Rod-L120-S7). Note that all voltages are reported *versus* the reversible hydrogen electrode (RHE) hereafter, with values corrected to account for the change of reference. A gas inlet allowing O_2, Ar or CO to bubble in the solution, as well as a gas outlet were present in the glass cell. A Luggin capillary was used to physically separate the reference electrode from the working electrode while maintaining the ionic connection and keeping the working electrode close to the reference [17].

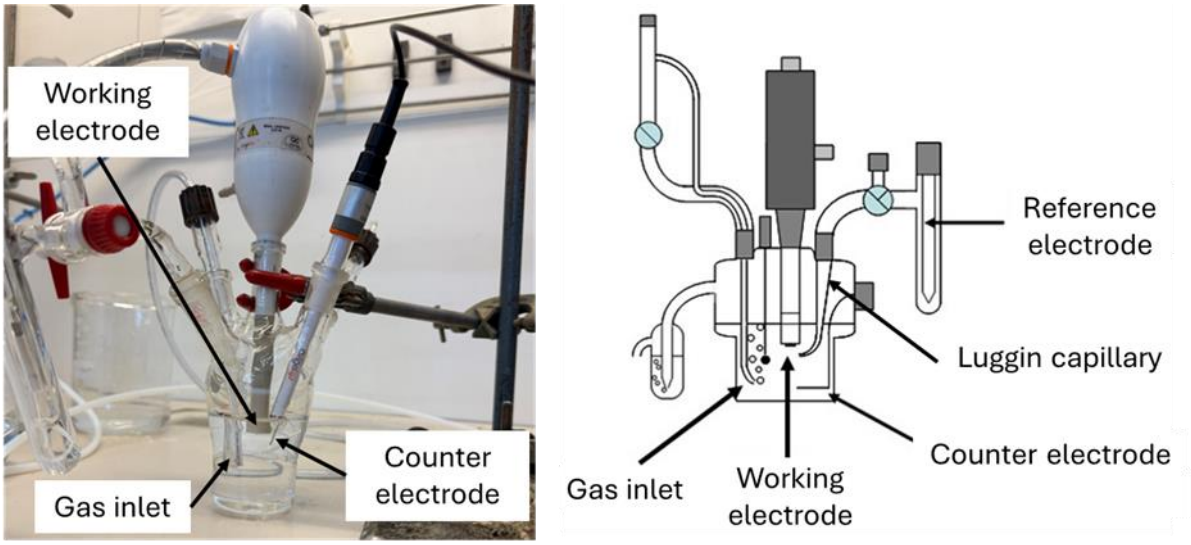

Figure 2.1. Picture and schematic (adapted from [18]) of a three-electrode setup.

Catalytic layer preparation

Measurements performed on RDE usually require homogenous and thin films; in particular, the thickness should be below 1 µm to avoid significant concentration gradients due to mass-transport limitations across the active layer [19]. However, CXs are challenging to grind below *ca.* ~5 µm [20]. As a result of this coarse grain size, active layers supported on CXs are thicker than those prepared with common carbon black supports [3]. Because of oxygen transport resistance within the layer and individual grains, concentration gradients of O_2 throughout the catalytic layer may occur. These gradients, which are worsened as the Pt loading increases, reduce the effectiveness factor of the catalyst, ultimately lowering the apparent catalytic activity [21]. Therefore, the catalyst ink was adjusted to achieve a working electrode Pt loading of 33 $\mu g_{Pt}.cm^{-2}_{geo}$ for all samples. This Pt loading on the electrode, selected on the basis of the work of Deschamps *et al.* [22], ensures sufficient Pt content to provide a reliable electrochemical signal while minimizing as much as possible the final catalytic layer thickness.

All inks were prepared by mixing 9.9 mg of catalyst with 1.8 mL of ultrapure Milli-Q® water, 0.7 mL of isopropanol, and 0.25 mL of Nafion® suspension in water and 1-propanol (Ion Power, 5 wt.%, 1100 EW). The mixture was then processed in an ultrasonic bath (VWR, Ultrasonic Cleaning Bath, Maximum Output Power 120 W) for 30 min so as to obtain a homogenous ink. 10 µL of the ink were then deposited on the glassy carbon tip. To evaporate the solvents and stick the sample onto the glassy carbon, the liquid was evaporated and Nafion® was sintered by processing the electrode in an oven at 100 ºC for 5 min. Profilometry measurements of the

catalytic layer were performed on a Bruker Dektak XT® stylus profilometer after sample deposition to check for the thickness and homogeneity of the layer. Prior to electrochemical characterization, a few drops of the electrolyte (H_2SO_4, 0.5 M) were deposited onto the active layer and put under vacuum to remove the air trapped in the active layer. Once no air bubbles were visible, the electrode and the electrolyte drop were returned to atmospheric pressure. This procedure allows the liquid to infiltrate the whole pore texture of the layer, which is necessary to ensure full use of the Pt nanoparticles.

A comprehensive assessment of the catalyst performances and durability before and after surface modification of the support was subsequently performed on RDE, using 0.5 M H_2SO_4 as electrolyte. To this end, cyclic voltammetry under argon, CO stripping and Oxygen Reduction Reaction (ORR) measurements were performed. To ensure reproducibility of the measurements, the initial electrocatalytic performances of at least three freshly prepared active layers were assessed. Provided no deviations exceeding ~20% were observed across measurements, the average of values was calculated and presented.

Cyclic voltammetry

Argon bubbling was performed to de-aerate the electrolyte for 20 min before conducting any measurement. Voltammetry cycles were then measured between 0.05 V and 1.23 V *vs.* RHE at a scanning rate of 100 $mV.s^{-1}$, and cycling was continued until stable voltammograms were obtained. Prior to measurements, three voltammetry cycles at a lower scan rate (20 $mV.s^{-1}$) were also recorded to check that the layer of sample was properly deposited and led to an appropriate signal. The double layer capacity per mass of carbon C_{dl} (in $F.g^{-1}_C$) was calculated from cyclic voltammetry at 20 $mV.s^{-1}$:

$$C_{\mathrm{dl}} = \frac{i_{\mathrm{capa}}}{m_{\mathrm{C}} v} \tag{2.4}$$

where i_{capa} is the capacitive current (A), taken in the area 0.4-0.5 V *vs.* RHE, v is the scan rate ($V.s^{-1}$), and m_C is the mass of carbon present in the active layer (g).

CO stripping

CO stripping measurements were used to determine the ElectroChemically active Surface Area (*ECSA*) of platinum [23]. To do so, gaseous CO (AirLiquide, N47, ≥ 99.997%) was bubbled in the electrolyte for 6 min while applying a steady potential of 0.1 V *vs.* RHE. This step is performed to saturate the available Pt catalytic sites with CO. The remaining CO present in the

electrolyte was subsequently purged from the cell by bubbling argon gas (AirLiquide, ALPHAGAZ™ 1, ≥ 99.999%) for 39 min. Three voltammetry cycles were then recorded from 0.05 to 1.23 V *vs.* RHE at 20 $mV.s^{-1}$. The first cycle represents the complete electro-oxidation of CO molecules adsorbed on Pt catalytic sites. The third cycle represents a regular cyclic voltammogram and was used as background curve. The *ECSA* was determined using the Faraday charge of the CO electro-oxidation peak between 0.65 and 1.23 V *vs.* RHE, assuming that a complete monolayer of CO adsorbed on Pt requires 4.2 $C.m^{-2}_{Pt}$ for being oxidized [24]. The *ECSA* and the CO equivalent nanoparticle diameter, d_{CO}, were determined as:

$$ECSA = \frac{Q_H}{4.2\ L\ A} \tag{2.5}$$

$$d_{CO} = \frac{6}{\rho_{Pt}\ ECSA} \tag{2.6}$$

where Q_H is the integral of the charge of the CO electro-oxidation peak (C), 4.2 ($C.m^{-2}_{Pt}$) is the theoretical adsorption charge density required to oxidize one complete monolayer of CO adsorbed onto Pt, L is the loading of Pt of the working electrode ($g_{Pt}.m^{-2}_{geo}$), A is the surface area of the electrode (m^2_{geo}), and ρ_{Pt} is the density of platinum (21.45×10^6 $g.m^{-3}$).

Oxygen Reduction Reaction measurement

The catalytic activity for the ORR was measured in O_2-saturated electrolyte. The electrocatalytic performances are reported as specific activity (*SA*) and mass activity (*MA*). *SA* corresponds to the activity expressed per Pt surface area exposed to the electrolyte. This activity is dependent of the spatial positions of Pt atoms in the nanoparticle structure as the catalytic activity of the surface atoms of Pt depend on their local atomic environment [25]. Meanwhile, *MA* corresponds to the activity expressed for the total mass of Pt present in the catalytic layer. It is more commonly used as a practical performance metric. Gaseous O_2 (AirLiquide, ALPHAGAZ™ 1, ≥ 99.995%) was bubbled in the electrolyte for 15 min, while the working electrode was kept at 0.05 V *vs.* RHE. ORR measurements were then carried out in an O_2-saturated electrolyte, kept under constant O_2 bubbling: the potential was increased to 1.05 V *vs.* RHE and decreased back to 0.3 V *vs.* RHE at a scan rate of 1 $mV.s^{-1}$, while the current was measured. To get rid of the capacitive current originating from the large specific surface area of the carbon supports, the background curves performed under the same conditions (Ar-saturated electrolyte, from 0.30 to 1.05 V *vs.* RHE at 1 $mV.s^{-1}$) were systematically subtracted from the ORR curves [22]. ORR measurements were recorded at different rotation speeds: 400,

900, 1600 and 2500 rpm. *SA* ($A.m_{Pt}^{-2}$) and *MA* ($A.g_{Pt}^{-1}$) were obtained from ORR curves plotted at 1600 rpm, using the following equations:

$$SA = \frac{i}{ECSA\ L} \tag{2.7}$$

$$MA = \frac{i}{L} \tag{2.8}$$

To ensure that the values of current measured are free of any mass transport limitations, it is essential to compare currents at potentials where mass transport limitations are negligible. However, both external and internal mass transport limitations must be considered. External mass transport contribution corresponds to the diffusion of O_2 from the bulk electrolyte to the external surface of the carbon grain, and is dictated by the rotation speed of the RDE. Meanwhile, internal mass transport contribution refers to the diffusion of O_2 from the external surface of the catalytic layer to the glassy carbon, to reach catalytic sites located close to it. ORR curves can be plotted at different RDE rotation speeds and the current values at which these curves are superimposing can be used to calculate the corresponding catalytic activities. However, this approach only allows to remove the contribution of external diffusion limitations. As previously mentioned, the use of CXs results in relatively thick active layers, and internal oxygen concentration gradients may develop across the porosity of the layer. Therefore, another approach must be followed.

The current at which internal mass transport limitations can be completely neglected is mostly dependent on the layer thickness and on the void fraction of the catalytic layer. If the gradient of O_2 concentration is small, with a difference lower than 10% between the O_2 concentration at both ends of the catalytic layer (*i.e.* between the catalytic layer surface exposed to the electrolyte and the glassy carbon surface), then internal diffusion limitations can be neglected. Using Fick's Law, Deschamps *et al*. [22] rationalized this statement by proposing a simple equation describing the maximum current density below which mass transport limitations can be neglected:

$$j = \left(\frac{C\varepsilon^2 D_{O_2} Fe}{h}\right) 10^{-1} \tag{2.9}$$

where *C* is the oxygen concentration at saturation in water, at 25 ºC and 10^5 Pa (1.2 $mol.m^{-3}$), D_{O2} is the diffusion coefficient of oxygen in water, at 25 ºC and 10^5 Pa (1.7×10^{-9} $m^2.s^{-1}$), *F* is

the Faraday constant (C.mol^{-1}), e is the number of exchanged electrons per reacted molecule of O_2 (dimensionless), h is the thickness of the active layer on the glassy carbon (m), and ε is the void fraction of the catalytic layer (dimensionless). Note that current densities obtained are expressed in absolute value, as reduction currents are reported as negative following the European convention. ORR can proceed through a (2+2)- or 4-electron pathway. As Pt catalyst is used, it is presumed that the number of electrons exchanged is close to 4 [26]. ε is defined as:

$$\varepsilon = \frac{V_{\text{layer}} - V_{\text{solid}}}{V_{\text{layer}}} \tag{2.10}$$

with:

$$V_{\text{solid}} = \frac{m_{\text{carbon}}}{\rho_{\text{carbon}}} + \frac{m_{\text{Pt}}}{\rho_{\text{Pt}}} + \frac{m_{\text{Nafion}}}{\rho_{\text{Nafion}}} \tag{2.11}$$

V_{solid} is the volume of solid material that constitutes the layer (cm^3), V_{layer} is the total volume of the layer (cm^3). m_{carbon}, m_{Pt} and m_{Nafion} are the mass of carbon, Pt and Nafion® deposited on the RDE, respectively (g). ρ_{carbon}, ρ_{Pt} and ρ_{Nafion} are the skeletal density of carbon (measured equal to 1.93 g.cm^{-3} by He pycnometry in Chapter 1), the density of Pt (21.45 g.cm^{-3}) and the density of Nafion® (1.97 g.cm^{-3}), respectively.
Meanwhile,

$$V_{\text{layer}} = \pi r_{\text{WE}}^2 h \tag{2.12}$$

V_{layer} is the total volume of the layer (cm^3), considering the active layer as a cylinder of material deposited on the working electrode. r_{WE} is the radius of the working electrode (2.5 cm).

Using **Equation (2.9)** is a simple yet efficient way to determine the current density range for which no internal mass transport limitations occur during ORR measurements. This consideration is particularly important for CX-based active layers. Due to their large thicknesses and developed porosity, currents must be compared at higher potentials (typically 0.95-0.98 V *vs.* RHE) than those commonly reported in the literature (0.9 V *vs.* RHE) for carbon-black supported catalysts [22].

Accelerated Stress Tests

Accelerated Stress Tests (AST) were performed both on the carbon xerogel-supported catalysts and on the commercial catalyst. After assessing the *Beginning of Life* (*BoL*) performances, the catalytic layer was subjected to 5,000 voltammetry cycles. Cycles were performed between 0.6

V and 1.0 V *vs.* RHE at 100 $mV.s^{-1}$, while the cell was kept at 80 ºC under constant Ar bubbling. This voltage range was selected as it is similar to the operating voltage of a typical PEMFC stack. It is also a voltage range that maximizes Pt degradation, while limiting severe carbon corrosion that would be drastically accelerated at potentials higher than 1.0 V *vs.* RHE [27]. After the 5,000 cycles, the temperature was decreased and the solution of 0.5 M H_2SO_4 was renewed, to prevent any catalytic activity underestimation associated with the use of aged electrolytes [28]. The catalytic layer was then characterized again using the same procedure, corresponding to the *Middle of Life* (*MoL*) status. Afterwards, the catalytic layer underwent 15,000 more voltammetry cycles between 0.6 and 1.0 V *vs.* RHE at 100 $mV.s^{-1}$. Once again, these cycles were performed under Ar bubbling and 80°C. Finally, the 0.5 M H_2SO_4 solution was replaced again and the cell was cooled down to ambient temperature. The catalytic layer was electrochemically characterized a third time at ambient temperature, corresponding to the *End of Life* (*EoL*) of the material. To ensure reproducibility of the measurements, aging and corresponding characterization was completed on a minimum of two active layers provided they presented no significant difference in *BoL* activity.

2.3. Results and discussion

2.3.1.Physico-chemical properties

Nitrogen adsorption-desorption measurements were obtained for the carbon black-supported catalyst, XC-72-Pt. These measurements were also obtained for CX0-Pt and CX0-C20-Pt and compared with those of the corresponding bare supports, CX0 and CX0-C20, to assess the impact of the deposition of Pt nanoparticles on the textural properties (**Figure 2.2**). Since N_2 does not adsorb on platinum, and in order to compare the supports only, the adsorbed quantity is reported per mass unit of carbon present in the catalyst samples. The commercial carbon black-supported catalyst XC-72-Pt presents a type I + II isotherm, according to the IUPAC classification. It displays a A_{BET} of 197 $m^2.g^{-1}_C$ and S_{ext} of 140 $m^2.g^{-1}_C$, which is typical of Vulcan carbon black materials [29]. Meanwhile, for CX0-Pt and CX0-C20-Pt, the type I + II isotherm shape already observed in Chapter 1 for the corresponding CX samples remains unchanged after Pt deposition. The A_{BET} of the pristine CX0, initially equal to 674 $m^2.g_C^{-1}$, slightly decreases to 603 $m^2.g_C^{-1}$ upon Pt deposition (CX0-Pt, **Table 2.1**). This decrease could be attributed to a partial blocking of micropores by Pt nanoparticles [30]. No change in S_{ext} is reported as it remains equal to 201 $m^2.g_C^{-1}$ before and after Pt deposition. Regarding CX0-C20,

A_{BET} and S_{ext} remain very similar upon Pt deposition, as they go from 174 to 173 $m^2.g_C^{-1}$ for A_{BET} and 128 to 131 $m^2.g_C^{-1}$ for S_{ext}. This result was expected as most micropores are already covered by the carbon layer formed during the CVD treatment, and therefore cannot be substantially blocked by the subsequent Pt nanoparticle deposition. Moreover, the dual porosity (micropore + meso/macropore texture) of CXs is also preserved after Pt deposition.

The N_2 adsorption-desorption were not collected for CX0-C20-HT1500-Pt and CX0-C60-Pt. For CX0-C20-HT1500-Pt, the high-temperature treatment does not influence the pore texture (see Chapter 1) and very similar results with CX0-C20-Pt would be expected. For CX0-C60-Pt, no differences in A_{BET} and S_{ext} are expected upon Pt deposition given the micropores are even more covered than for CX0-C20-Pt. Nevertheless, some pore properties of CX0-C60 and CX0-C20-HT1500, obtained in the previous chapter, are also given in **Table 2.1**.

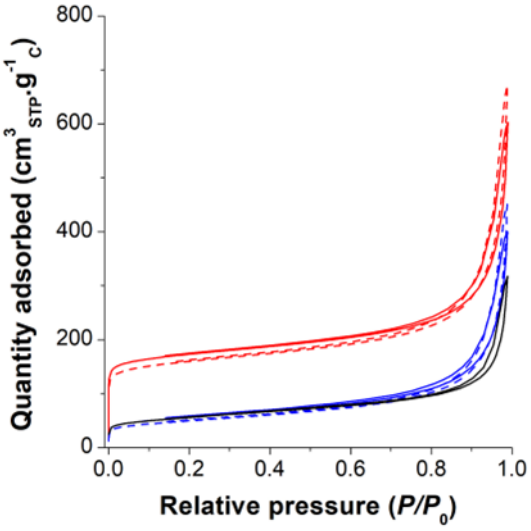

Figure 2.2. Comparison of N_2 adsorption-desorption isotherms before and after Pt deposition. The commercial catalyst is added as reference. XC-72-Pt (—), CX0 (—), CX0-Pt (----), CX0-C20 (—), and CX0-C20-Pt (----).

Table 2.1. Textural properties and morphological parameters of carbon materials and carbon-supported catalysts.

Sample	d_p[a] (nm) ± 5%	A_{BET}[b] ($m^2.g_C^{-1}$) ± 5%	S_{ext}[c] ($m^2.g_C^{-1}$) ± 5%	V_{DUB}[d] ($cm^3.g_C^{-1}$) ± 0.01
XC-72-Pt	[e]	197	140	0.08
CX0	70	674	201	0.26
CX0-Pt	[e]	603	201	0.24
CX0-C20	75	174	128	0.07
CX0-C20-Pt	[e]	173	131	0.07
CX0-C60	78	100	103	0.04
CX0-C20-HT1500	[e]	187	141	0.08

[a] d_p: average pore size measured by Hg porosimetry.

[b] A_{BET}: BET surface area, calculated from nitrogen adsorption-desorption isotherms at 77 K.

[c] S_{ext}: external surface area, calculated from nitrogen adsorption-desorption isotherms at 77 K using the t-plot method.

[d] V_{DUB}: micropore volume, calculated from calculated from nitrogen adsorption-desorption isotherms at 77 K using Dubinin-Radushkevich equation.

[e] Measurements not performed as the impact on the meso/macroporosity of the sample is expected to be very limited.

Thermogravimetric analysis under air was performed on the different catalysts to evaluate their actual Pt content (**Figure 2.3**). A first mass loss is observed at low temperatures, between 80 to 100 ºC. This behavior is usually associated with the removal of moisture from carbon powders [31]. Interestingly for CX samples, the mass loss observed becomes lower as the CVD treatment duration increases. For CX0-C60-Pt, this mass loss is practically not observed. This logically suggests that residual moisture inside the xerogel pore network decreases as the micropore coverage increases. At higher temperatures, between 300 and 600 ºC, the combustion of the carbon support is observed.

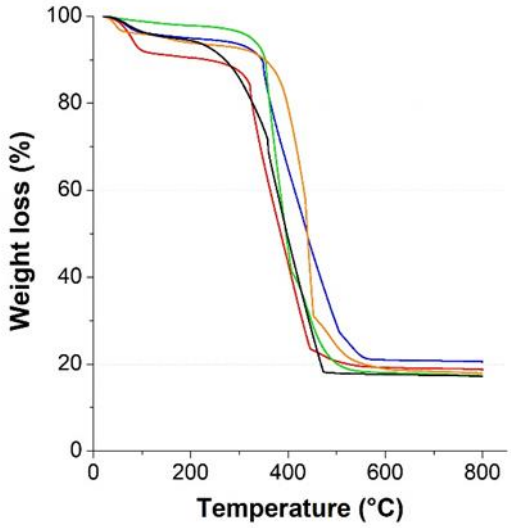

Figure 2.3. TGA curves under air of XC-72-Pt (—), CX0-Pt (—), CX0-C20-Pt (—), CX0-C60-Pt (—) and CX0-C20-HT1500-Pt (—).

One can however note that the burning of catalysts supported on post-treated CXs starts at slightly higher temperatures than in the case of CX0-Pt. This suggests that the CVD and high-temperature treatments provide a slightly higher thermal stability to the material, in agreement with a more crystalline structure of the CVD layer. The remaining mass observed above 600 ºC accounts for the quantity of Pt. The measured Pt content could be overestimated due to the potential formation of Pt oxides, as their growth and stability is observed in air between ambient temperature and 200 ºC [32]. Although, their decomposition is generally observed above 300 ºC [33], assuming that all Pt is converted into PtO_2 at 600 °C would result in an overestimation of Pt content that would not exceed 14% of the measured mass. The Pt content is thus relatively well estimated by TGA. Without correction, this Pt content is determined to be 17.3 wt.% for XC-72-Pt and, for carbon xerogel-supported catalysts, a Pt content of 18.7, 20.4, 17.5 and 18.0 wt.% was determined for CX0-Pt, CX0-C20-Pt, CX0-C60-Pt and CX0-C20-HT1500-Pt, respectively.

As shown on TEM micrographs in **Figure 2.4a-e**, the Pt nanoparticles are well distributed onto the carbon supports. On XC-72-Pt, Pt nanoparticles with an arithmetic average size of 3.4 ± 0.4 nm are observed. On the pristine CX, Pt nanoparticles also display an average diameter of 3.4 ± 0.4 nm. The large network of meso and macropores of this CX allows for uniform deposition

of Pt nanoparticles. On CX0-C20-Pt, CX0-C60-Pt and CX0-C20-HT1500-Pt, Pt nanoparticles display a very similar average diameter (d_{TEM} = 3.6 ± 0.6 nm for CX0-C20-Pt, d_{TEM} = 3.7 ± 0.6 nm for CX0-C60-Pt and CX0-C20-HT1500-Pt), but also a tendency for more agglomerated nanoparticles since bigger structures are also detected. The size distribution of Pt nanoparticles is shown on **Figure 2.4f**, and is based on the observation of more than 50 individual nanoparticles for each sample. As a reminder, only clearly isolated Pt nanoparticles were considered in this size distribution while agglomerates were excluded. The change of surface properties upon CVD and high-temperature treatment may affect the nanoparticle size and distribution. However, particle sizes remain in the requested range for PEMFC applications, whatever the catalyst considered. The surface-weighed and volume-weighed diameters, d_S and d_V, were calculated from the particle size distributions for all the catalysts. d_S and d_V were calculated from the particle size distribution to be later compared to d_{CO} and d_{XRD}, respectively. These values are gathered in **Table 2.2**.

Table 2.2. Catalysts properties determined by different analyses.

Catalyst	Pt_{TGA}[a] (wt.%)	d_{TEM}[b] (nm)	σ[c] (nm)	d_S[d] (nm)	d_V[d] (nm)	d_{XRD}[e] (nm) ± 0.3	d_{CO}[f] (nm) ± 10 %
XC-72-Pt	16.1 ± 1.2	3.4	0.4	3.5	3.5	2.9	3.8
CX0-Pt	17.4 ± 1.3	3.4	0.4	3.5	3.5	2.6	2.4
CX0-C20-Pt	19.0 ± 1.4	3.6	0.6	3.7	3.9	3.0	2.8
CX0-C60-Pt	16.3 ± 1.2	3.7	0.5	3.8	3.9	3.1	4.8
CX0-C20-HT1500-Pt	16.7 ± 1.3	3.7	0.6	3.8	3.9	3.2	2.9

[a] Pt_{TGA}: mass fraction remaining at the end of TGA experiment, and attributed to the Pt contained in the catalyst.
[b] d_{TEM}: average arithmetic diameter of nanoparticles estimated from TEM micrographs.
[c] σ: standard deviation associated with d_{TEM}.
[d] d_S and d_V: surface- and volume-weighted average diameter of nanoparticles calculated from **Equations (2.2)** and **(2.3)**, obtained from TEM micrographs.
[e] d_{XRD}: average size of crystallites calculated from X-ray diffraction peak of Pt(111) from **Equation (2.1)**.
[f] d_{CO}: CO equivalent particle diameter of the Pt particles determined from **Equation (2.6)**, obtained from CO stripping.

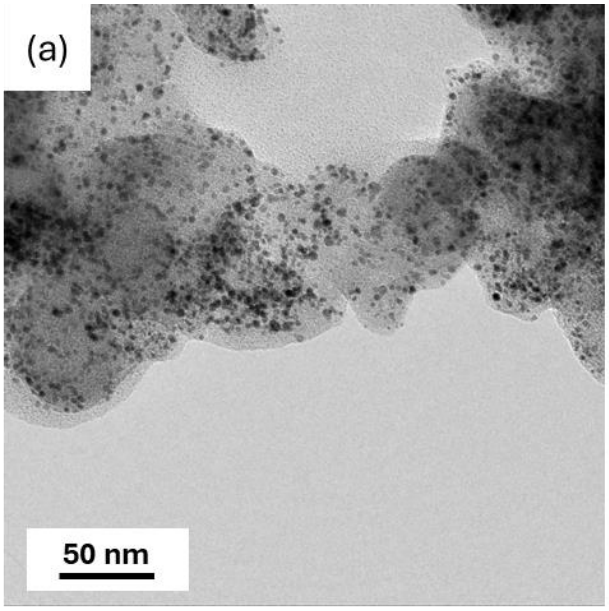
(a)
50 nm

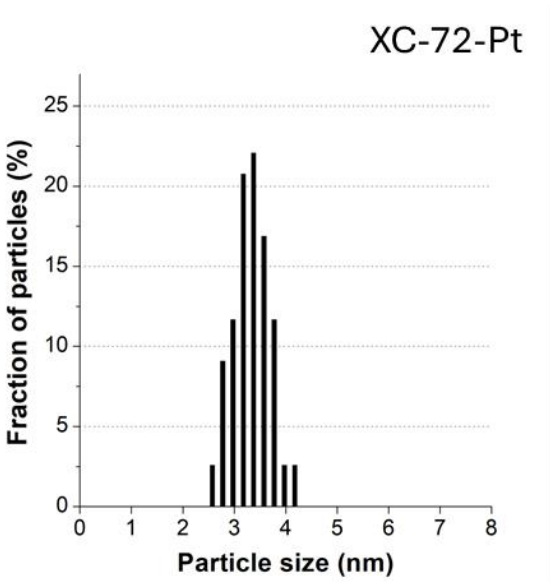
XC-72-Pt
Fraction of particles (%)
Particle size (nm)

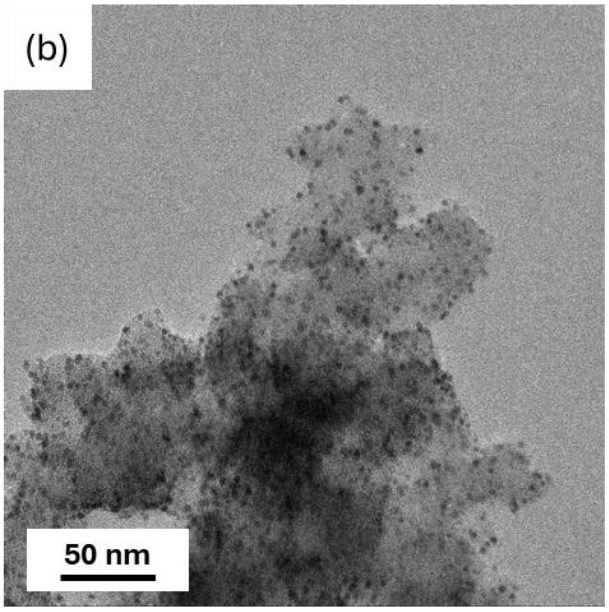
(b)
50 nm

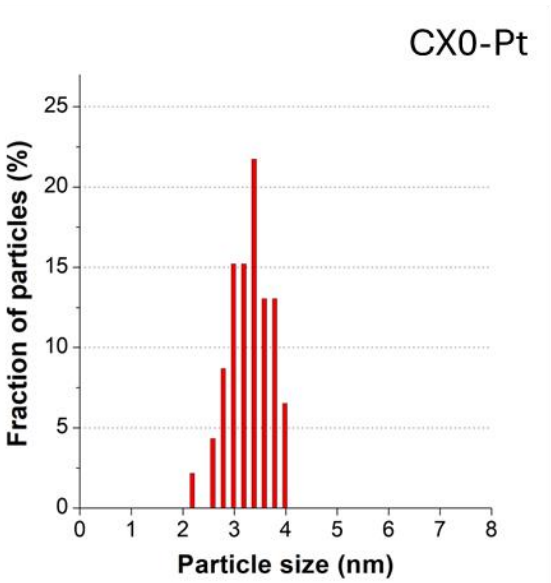
CX0-Pt
Fraction of particles (%)
Particle size (nm)

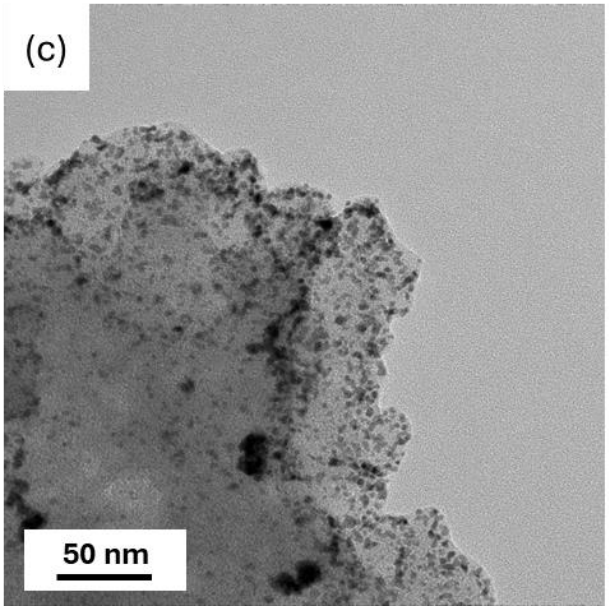
(c)
50 nm

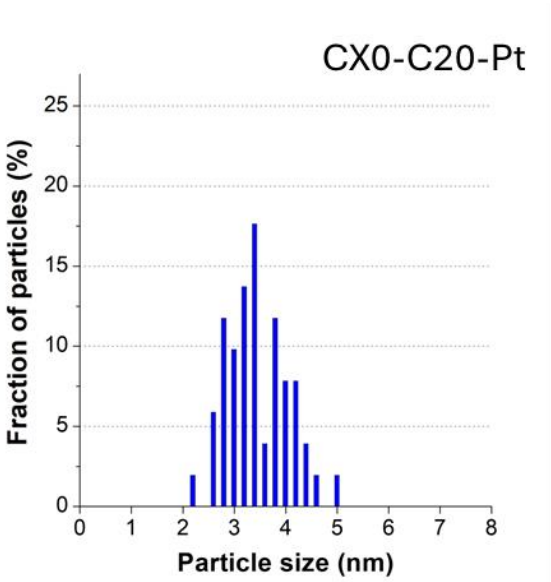
CX0-C20-Pt
Fraction of particles (%)
Particle size (nm)

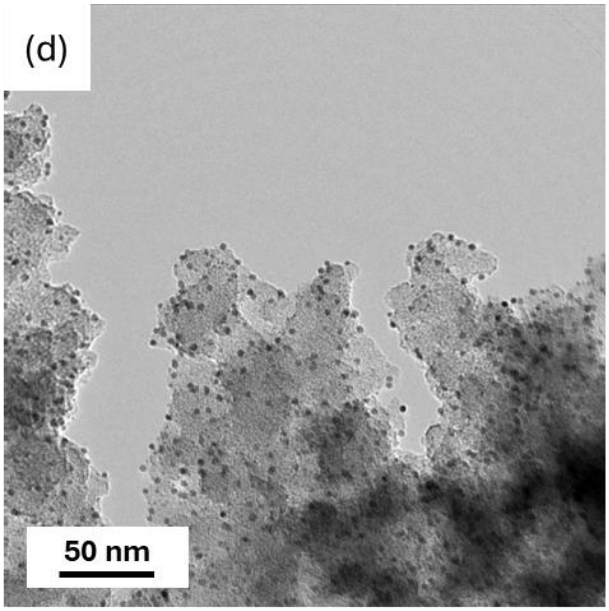
(d)
50 nm

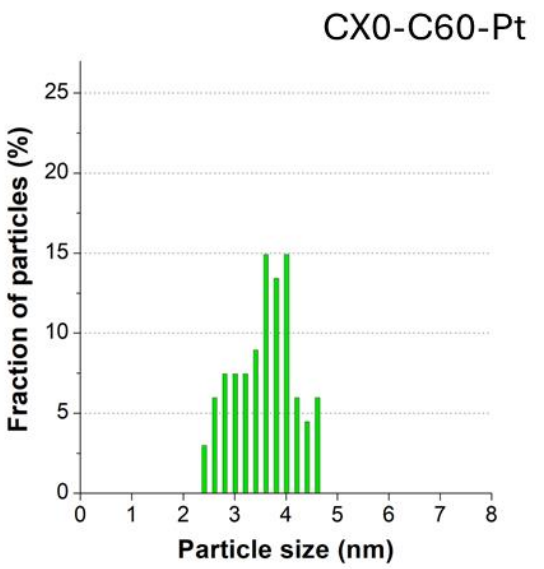
CX0-C60-Pt
Fraction of particles (%)
Particle size (nm)

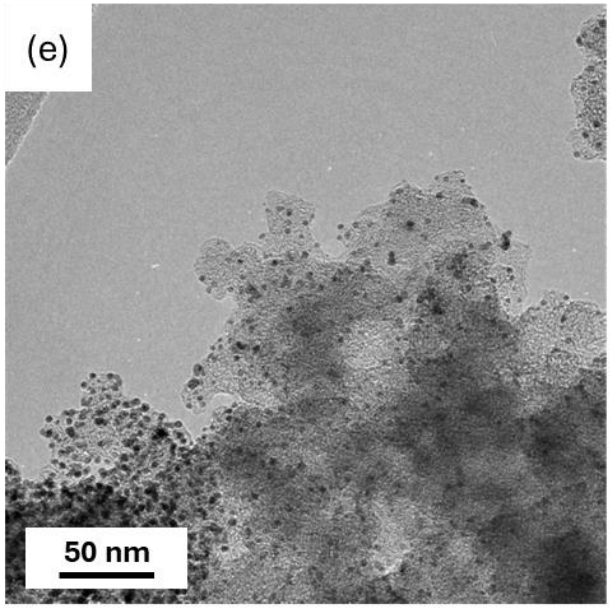
(e)
50 nm

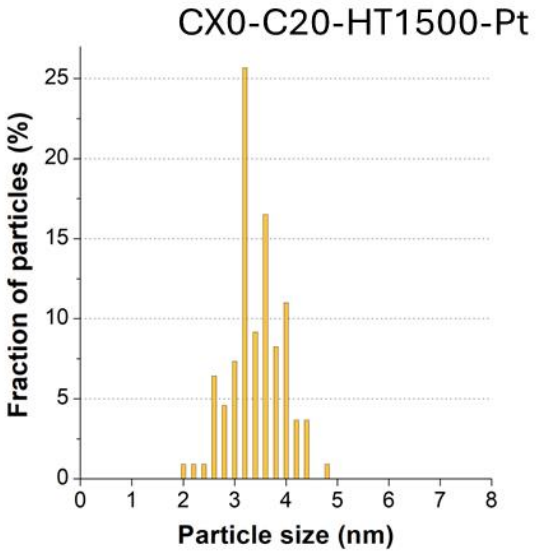
CX0-C20-HT1500-Pt
Fraction of particles (%)
Particle size (nm)

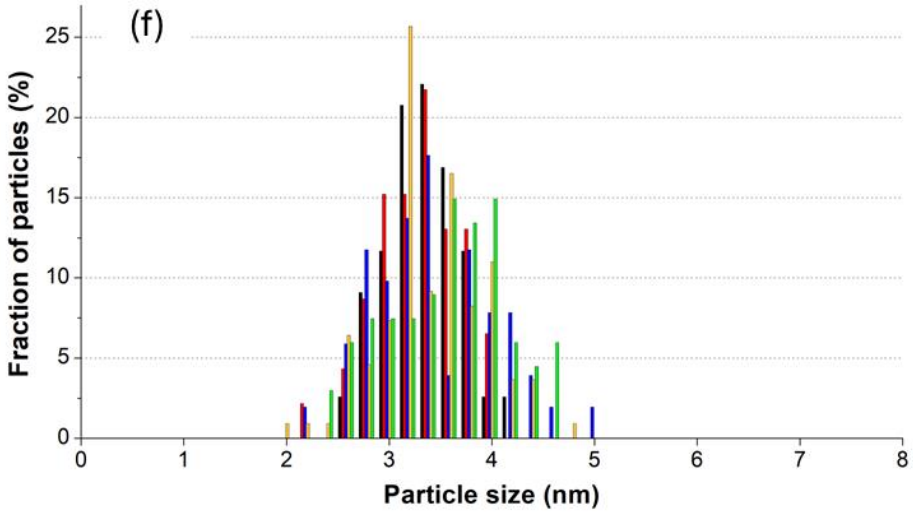
(f)
Fraction of particles (%)
Particle size (nm)

Figure 2.4. TEM micrographs and corresponding particle size distribution of (a) XC-72-Pt, (b) CX0-Pt, (c) CX0-C20-Pt, (d) CX0-C60-Pt (e) CX0-C20-HT1500-Pt and (f) total initial Pt nanoparticle size distribution of XC-72-Pt (■). CX0-Pt (■), CX0-C20-Pt (■), CX0-C60-Pt (■) and CX0-C20-HT1500-Pt (■).

To evaluate the crystalline structure of the materials, diffractograms of the catalysts are shown in **Figure 2.5.** A wide peak can be seen around 2θ = 22-25º for all samples. It corresponds to the small-range graphitic ordering in the primary particles of carbon xerogels and carbon black [12]. The peak appears narrower and at a larger angle for XC-72-Pt, compared to carbon xerogel-supported catalysts. This suggests that this carbon black support is more ordered than the pristine and post-treated CXs. Moreover, diffractograms display the characteristic face-centered cubic arrangement peaks found in platinum, namely 39.9º Pt(111), 46.6º Pt(200) and 67.1º Pt(220). Using Scherrer's equation (**Equation (2.1)**), crystallite sizes d_{XRD} were calculated equal to 2.9, 2.6, 3.0, 3.1 and 3.2 nm for XC-72-Pt, CX0-Pt, CX0-C20-Pt, CX0-C60-Pt and CX0-C20-HT1500-Pt respectively.

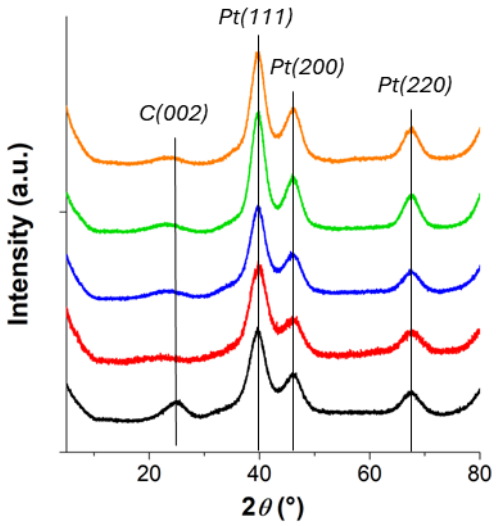

Figure 2.5. X-ray diffractograms of catalysts: XC-72-Pt (—), CX0-Pt (—), CX0-C20-Pt (—), CX0-C60-Pt (—) and CX0-C20-HT1500-Pt (—). The diffractograms are shifted vertically for legibility.

Based on TEM micrographs and XRD measurements, the smallest nanoparticles are observed on the pristine CX0 surface. d_{XRD} was also compared with d_V. In principle, d_v can be compared to d_{XRD} as X-ray diffraction is a volume-sensitive technique [15]. Small discrepancies were observed, as d_V is systematically higher (**Table 2.2**). Nevertheless, an overestimation of d_V is possible, and can ultimately be bound to TEM observation. Indeed, small nanoparticles (< 2 nm) are difficult to distinguish under TEM due to the operating limits of the device. Therefore, Pt nanoparticles seem relatively monocrystalline as both d_{XRD} and d_V remain close, even with the possible overestimation of d_V from TEM micrographs.

2.3.2. Electrochemical characterization of the fresh catalysts

Profilometry measurements were performed to determine the average thickness of active layers deposited on the 5-mm glassy carbon electrode with a loading of 33 $\mu g_{Pt}.cm^{-2}_{geo}$ (**Figure 2.6a**). In the case of the benchmark catalyst, XC-72-Pt, a thickness of 5 µm is observed, which is compatible with usual analysis of the catalyst activity. However, CXs are known to produce active layers with considerably higher thickness due to their internal porosity. As expected, profilometry measurements performed on CX0-Pt, deposited in the same conditions as XC-72-Pt, show that the thickness is in the range of 10-15 µm (**Figure 2.6b**).

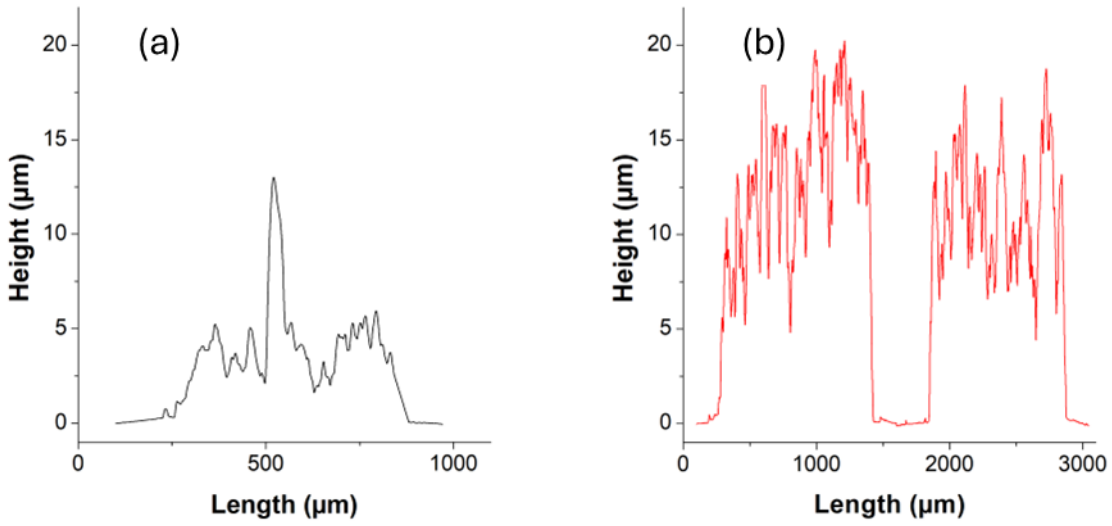

Figure 2.6. Thickness profiles of the active layer of (a) XC-72-Pt (—) and (b) CX0-Pt (—) deposited on the glassy carbon of the RDE.

Thus, to properly evaluate the catalytic activity of this type of thick active layers, it is essential to lower the scan rate to reach steady-state conditions and to ensure that the current measured is free of any mass transport contribution (*i.e.* only governed by the kinetics of the ORR). Indeed, the ORR curves plotted at different electrode rotations superimpose above 0.9 V *vs.* RHE (**Figure 2.7**), which indicates that no external mass transfer occurs in that region. Nevertheless, internal mass transfer limitations may still be present due to the thickness of the catalytic layer and the rotating speed has no impact on it.

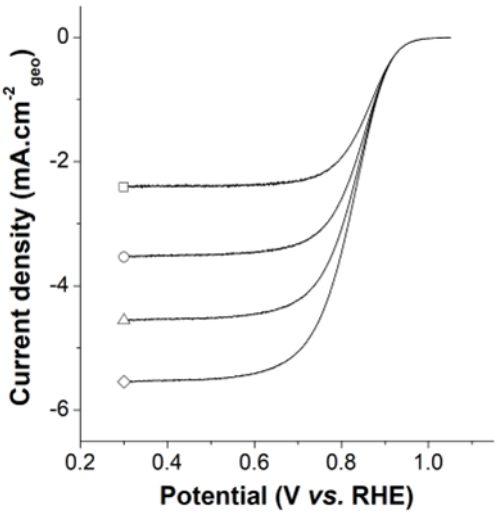

Figure 2.7. Cyclic voltammetry at *BoL* under O_2 and 25 ºC of CX0-Pt, performed with a scan rate of 1 $mV.s^{-1}$ and an electrode rotation of 400 (—□—), 900 (—○—), 1600 (—△—) and 2500 (—◇—) rpm.

To estimate the extent of internal mass transport limitations, **Equation (2.9)** was used in the case of the CX-supported samples, considering a maximum thickness observed of 15 µm. The different values used to calculate the void fraction of the active layer, ε, are provided in **Table 2.3**. ε was calculated equal to 0.87. Therefore, the current density at which internal mass transport can be neglected was found to be 0.35 $mA.cm^{-2}_{geo}$, assuming a 4-e^- mechanism. Such current densities are typically observed at potentials around 0.91-0.92 V *vs.* RHE for the materials tested. Catalytic activities should be measured and compared above this potential range. Therefore, ORR curves were recorded at a scan rate of 1 $mV.s^{-1}$ and corrected with the background to remove capacitive effects. In addition, all currents were retrieved at 0.95 V *vs.* RHE to ensure that catalytic activities are free of all mass transport limitations.

Table 2.3. Different values related to the active layer deposited on the working electrode.

V_{solid}						V_{layer}	
m_{carbon}[a] (g)	m_{Pt}[a] (g)	m_{Nafion}[a] (g)	ρ_{carbon}[b] (g.cm^{-3})	ρ_{Pt}[b] (g.cm^{-3})	ρ_{Nafion}[b] (g.cm^{-3})	h[c] (cm)	r_{WE}[d] (cm)
2.95×10^{-5}	6.48×10^{-6}	4.18×10^{-5}	1.93	21.45	1.97	1.5×10^{-3}	0.25

[a] m_{carbon}, m_{Pt} and m_{Nafion}: Mass of carbon, Pt, and dry Nafion® in the active layer.

[b] ρ_{carbon}, ρ_{Pt} and ρ_{Nafion}: Density of carbon, Pt and dry Nafion®.

[c] h: Thickness of the active layer, obtained *via* the thickness profile.

[d] r_{WE}: Radius of the working electrode.

From the CO stripping curves (**Figure 2.8a**), the electrooxidation peak of CO to CO_2, located between 0.65 and 1.23 V *vs.* RHE, is used to determine the ElectroCatalytically active Surface Area (*ECSA*), directly related to the available amount of platinum catalytic sites. The commercial catalyst displays an *ECSA* of 74 m².g$^{-1}_{Pt}$, which is consistent with values usually reported for carbon black-supported nanoparticles of 3–4 nm in size [34,35]. Note that the theoretical surface of nanoparticles of 3 to 4 nm in diameter, assuming purely spherical and monodisperse nanoparticles, would be comprised between 70 and 93 m².g$^{-1}_{Pt}$ (see **Equation (2.6)**). For catalyst supported on CX0, the *ECSA* is 117 m².g$^{-1}_{Pt}$ for CX0-Pt, 101 m².g$^{-1}_{Pt}$ for CX0-C20-Pt, 63 m².g$^{-1}_{Pt}$ for CX0-C60-Pt and 99 m².g$^{-1}_{Pt}$ for CX0-C20-HT1500-Pt. The CO equivalent particle diameter was determined from these *ECSA* values, also from **Equation (2.6)**, and compared with d_S obtained from TEM micrographs. In principle, d_S can be compared to d_{CO}, since CO stripping is a technique sensitive to surface [16]. As shown in **Table 2.2**, a significant gap between d_S and d_{CO} may suggest again that the smallest nanoparticles (<2 nm) are not visible enough on the micrographs of the carbon xerogel-supported catalysts. This proportion of small nanoparticles would nevertheless decrease as the carbon surface evolves upon CVD and high-temperature treatments, as d_{CO} is larger in the case of CX0-C20-Pt and CX0-C20-HT1500 (d_{CO} = 2.8 nm for both samples) than in the case of CX0-Pt (d_{CO} = 2.4 nm). CX0-C60-Pt exhibits a significantly larger d_{CO} of 4.4 nm. This result is somewhat unexpected given the similarity of d_{XRD} and d_{TEM} between CX0-C20-Pt and CX0-C60-Pt, and the absence of large Pt agglomerates in the TEM micrographs. Nevertheless, this behavior could originate from the hydrophobicity of the carbon material. As CX0-C60-Pt has the thickest carbon layer deposited, it could also present the most hydrophobic character. This could decrease the

electrolyte accessibility to some catalytic sites, thereby lowering the measured *ECSA* value, and thus lead to an overestimation of the d_{CO}.

Finally, the CO oxidation peak of XC-72-Pt is observed at 0.77 V *vs.* RHE. In contrast, the CO peak maximum occurs at 0.82 V *vs.* RHE for CX0-Pt, 0.80 V *vs.* RHE for CX0-C20-Pt, and 0.78 V *vs.* RHE for CX0-C60-Pt and CX0-C20-HT1500-Pt. As commonly observed, an increase in mean particle size under 3 nm causes the CO oxidation peak to shift to lower potentials [35]. This likely reflects the presence of larger Pt nanoparticles on XC-72-Pt. A shouldering peak can also be observed for CX0-C20-HT1500-Pt before the main CO electrooxidation peak. This peak is commonly associated with the presence of Pt agglomerates [35]. This suggests that CX0-C20-HT1500-Pt contains a larger proportion of agglomerates compared with the other catalysts. Therefore, despite using the same formic acid reduction for synthesizing Pt nanoparticles, the change of carbon surface after CVD and post-treatment at 1,500 ºC influences the Pt nanoparticles formation mechanism. This could possibly stem from the tendency of $PtCl_6^{2-}$ ions to adsorb inside the microporosity, ultimately affecting the final nanoparticle size [36,37]. Moreover, surface defects and functional groups become scarcer with the deposition of the carbon layer. This scarcity results in a lower quantity of anchoring sites for nanoparticles nucleation and ultimately lead to the growth of larger nanoparticles [38]. The tendency of nanoparticles to agglomerate more on CVD-treated CXs than on pristine CX0 can partly explain the drop of *ECSA* observed.

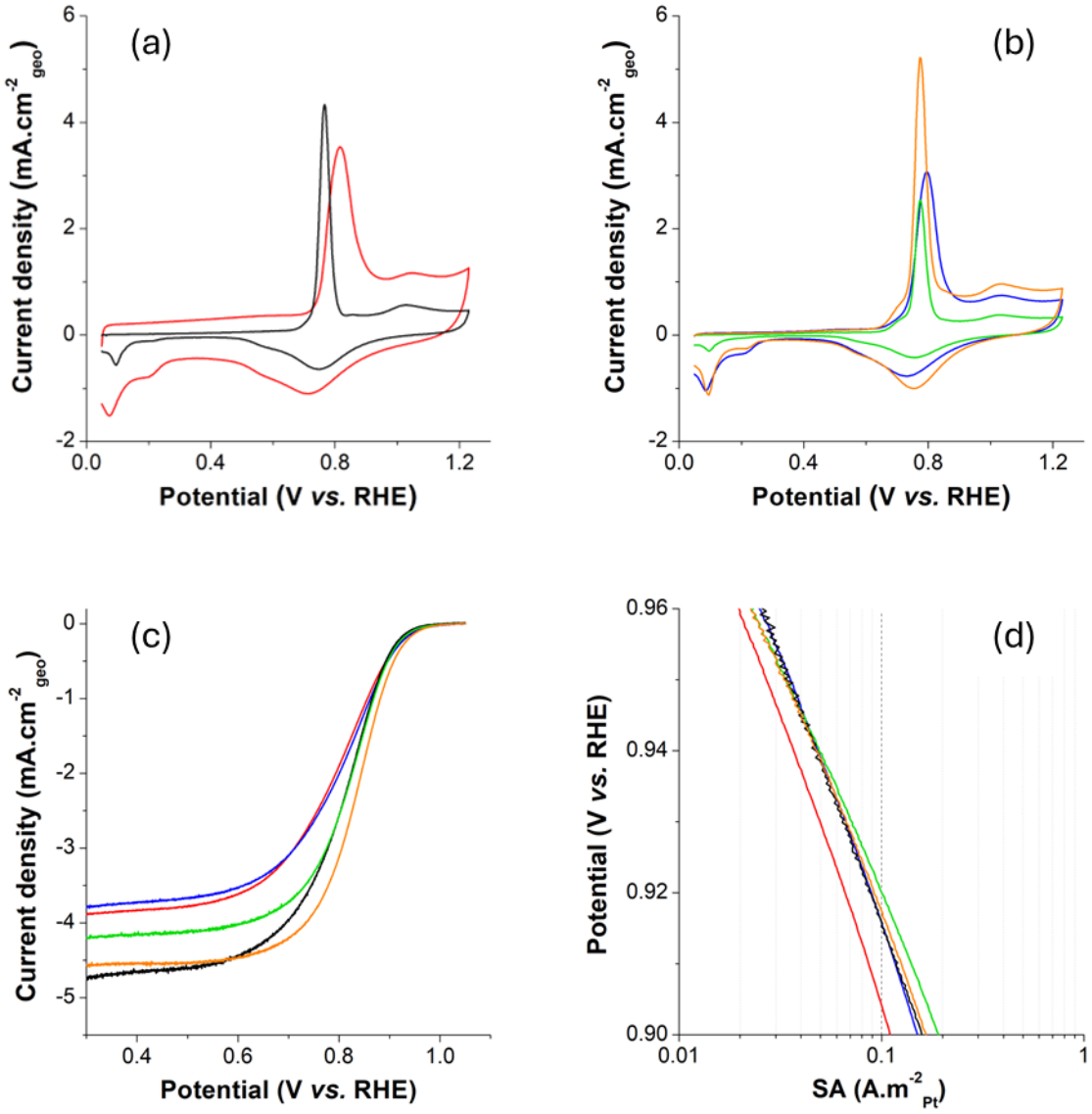

Figure 2.8. Electrochemical measurements of fresh catalysts performed in RDE configuration in 0.5 M H_2SO_4 at 25ºC. (a,b) CO electro-oxidation curves at a rate of 20 $mV.s^{-1}$, (c) Cyclic voltammetry under O_2 at a scan rate of 1 $mV.s^{-1}$ and an electrode rotation of 1600 rpm and (d) corresponding Tafel plots, of XC-72-Pt (—), CX0-Pt (—), CX0-C20-Pt (—), CX0-C60-Pt (—) and CX0-C20-HT1500-Pt (—). CO electro-oxidation curves were divided into two parts for better legibility.

Another notable difference in the CO stripping curves presented in **Figure 2.8a** is the evolution of the double layer capacitance of the carbon support, C_{dl}. XC-72-Pt displays a relatively low C_{dl}, calculated equal to 24 $F.g^{-1}$, while it significantly increases for CX0-Pt (128 $F.g^{-1}$). This

large value observed for CX0-Pt can be attributed to the extensive micropore network accessible to the electrolyte. This well-developed microporosity is consistent with the high A_{BET} measured for this material. A decrease in capacitive current is observed when comparing CX0-C20-Pt and CX0-C60-Pt to CX0-Pt, as their double layer capacitances drop to 33 $F.g^{-1}$ and 10 $F.g^{-1}$. It is worth noting that the decrease in C_{dl} mirrors the reduction in A_{BET} observed after CVD treatment. Indeed, the C_{dl} decreases by 74% from CX0-Pt to CX0-C20-Pt while A_{BET} decreases by 71%. For CX0-C60-Pt, C_{dl} decreases by 92%, while the A_{BET} decreases by 84%. Since the CVD treatment blocks most of the CX micropores, the surface onto which ions can accumulate is proportionally reduced [39]. Meanwhile, C_{dl} is slightly lower for CX0-C20-HT1500-Pt (22 $F.g^{-1}$) than its counterpart before high temperature treatment. This difference could be attributed to changes in surface rugosity induced by the surface crystallization, clearly evidenced from HR-TEM micrographs presented in Chapter 1. The capacitive contribution is relatively large in the case of CX0-Pt, and can ultimately affect the ORR curve. Therefore, all ORR measurements described hereafter have been corrected with the background performed under Ar.

Measurements under oxygen (**Figure 2.8b**, **Table 2.4**) allow to retrieve the catalytic activities of Pt nanoparticles towards ORR. The specific and mass activities at 0.95 V *vs.* RHE of XC-72-Pt, *SA* and *MA*, are measured equal to 0.029 $A.m^{-2}_{Pt}$ and 2.12 $A.g^{-1}_{Pt}$, respectively. In the case of carbon xerogel-supported catalysts, *SA* is equal to 0.022, 0.034, 0.029 and 0.033 $A.m^{-2}_{Pt}$ while *MA* is equal to 2.69, 3.29, 1.82 and 3.25 $A.g^{-1}_{Pt}$ for CX0-Pt, CX0-C20-Pt, CX0-C60-Pt and CX0-C20-HT1500-Pt, respectively. Values of specific activities remain in the expected range for Pt nanoparticles supported on a CX [11] and compare well with XC-72-Pt. Moreover, the specific activities of catalysts based on post-treated CXs are higher than that of the catalyst based on the pristine CX0. The same comment can be made for the mass activity, except for that of CX0-C60-Pt, which is drastically lower than other samples. Again, the behavior observed for CX0-C60-Pt could result from the hydrophobicity of the material, for which the *ECSA* was already measured smaller than other CX-supported catalysts, likely because the electrolyte has limited access to some catalytic sites. The effect of the nanoparticle size on catalytic activity will also be discussed in **Section 2.3.3**, when analyzing the AST results. Note that the half-wave potential, frequently used as a comparison parameter, was not considered here. Indeed, internal and external diffusion impacts the measured current in the region of the curve where it is observed.

Finally, the Tafel slope was used to determine through which mechanism the ORR occurs (**Figure 2.8c**). When the Tafel slope is in the range 60 – 70 mV.dec^{-1}, a 4-e$^-$ mechanism is expected. Meanwhile, when it is close to 120 mV.dec^{-1}, a (2+2)-e$^-$ mechanism occurs [40]. The latter mechanism is detrimental for catalytic layers and undesirable in PEMFCs as it yields hydrogen peroxide, which damages Nafion®. All samples display similar Tafel slopes: 66 mV.dec^{-1} for the commercial catalyst; 67, 71, 62 and 61 mV.dec^{-1} for CX0-Pt, CX0-C20-Pt, CX0-C60-Pt and CX0-C20-HT1500-Pt, respectively. A predominance of the 4-e$^-$ reduction route, desirable for PEMFC application, is thus confirmed. Therefore, selecting e = 4 in **Equation (2.9)** to determine the maximum current density below which mass transport limitations can be neglected, is accurate.

Table 2.4. Catalyst properties of fresh catalysts determined by electrochemical analyses.

	***ECSA*[a]** ($m^2.g^{-1}_{Pt}$)	***SA*[b]** ($A.m^{-2}_{Pt}$)	***MA*[b]** ($A.g^{-1}_{Pt}$)	***b*[c]** ($mV.dec^{-1}$)
XC-72-Pt	74 ± 4	0.029 ± 0.001	2.12 ± 0.05	66 ± 3
CX0-Pt	117 ± 7	0.022 ± 0.002	2.69 ± 0.42	67 ± 7
CX0-C20-Pt	101 ± 4	0.034 ± 0.001	3.29 ± 0.01	71 ± 1
CX0-C60-Pt	63 ± 6	0.029 ± 0.003	1.82 ± 0.43	62 ± 1
CX0-C20-HT1500-Pt	99 ± 23	0.033 ± 0.001	3.25 ± 0.39	61 ± 1

[a] *ECSA*: Electrochemically activity surface area of Pt normalized to the mass of Pt on the electrode, calculated from CO stripping measurement (**Equation (2.5)**).

[b] *SA* and *MA*: Specific Activity and Mass Activity measured at 0.95 V *vs.* RHE (**Equations (2.7)** and **(2.8)**).

[c] *b*: Tafel slope obtained calculated at 0.95 V *vs.* RHE from ORR measurement.

Carbon xerogel-supported catalysts show catalytic activities towards ORR on par with the commercial carbon black-supported catalyst. After 20 min of CVD, the partial covering of the micropores by the deposited carbon layer did not impact significantly the initial electrochemical properties of carbon xerogel-supported electrocatalyst. Since micropores can generate undesirable ohmic resistance in a catalytic layer [41], CVD treatment could form a continuous carbon layer and decrease the volume of micropores, which could in turn facilitate the transport of electrons. In this sense, it is expected that the blocking of the micropores, even partial, would lead to an increase of the electrical conductivity of the carbon material. This hypothesis was however not verified in this work.

2.3.3. Electrochemical characterization after AST

ASTs were performed at 80 ºC, a temperature representative of typical PEMFC operating conditions. Catalytic properties are found in **Table 2.5**. **Figure 2.9a-j** shows the evolution of the ORR curves and Tafel plots before (*BoL*), during (*MoL*) and after (*EoL*) the ASTs of all the catalysts. The bar graphs in **Figure 2.10a** show the *ECSA* of Pt normalized to its initial value for each catalyst. All samples exhibit a significant decrease of the *ECSA* during the first 5,000 cycles. XC-72-Pt exhibits a 39% decrease after 5,000 cycles and 46% after 20,000 cycles. Meanwhile, the lowest *ECSA* decrease is observed on the CX0-Pt: 33% and 41% after 5,000 and 20,000 cycles, respectively. CX0-C20-Pt, CX0-C60-Pt and CX0-C20-HT1500-Pt suffer on average a loss of 47%, 57% and 46% after 20,000 cycles, respectively.

TEM micrographs show that the nanoparticles increase in size as the catalyst undergoes aging (**Figure 2.11a-f**). This nanoparticle growth was anticipated and is due to well-known phenomena such as Ostwald ripening mechanism, migration and coalescence of Pt crystallites, as all of these phenomena are observable in the potential range of the AST (0.6 - 1.0 V *vs.* RHE) [42,43]. The evolution of the catalysts during the AST was also monitored using cyclic voltammetry (**Figure 2.12**). A decrease of the area under the different Pt peaks (H^+ adsorption/desorption on Pt in the range of 0.05 to 0.3 V *vs.* RHE, and Pt oxides formation and subsequent reduction in the range of 0.5 to 1.1 V *vs.* RHE) can be observed for all catalysts. The agglomeration and detachment of nanoparticles, already visible on the TEM micrographs of aged catalysts leads to this decrease in the intensity of the different Pt signals. However, quantifying the individual impact of these phenomena from the cyclic voltammetry curves remains challenging [78].

Table 2.5. Catalyst properties during accelerated stress tests, determined by RDE electrochemical analyses.

Catalyst		CO stripping		ORR			CV
		ECSA[a]	d_{CO}[b]	*SA*[c]	*MA*[c]	*b*[d]	C_{dl}[e]
		($m^2.g^{-1}_{Pt}$)	(nm)	($A.m^{-2}_{Pt}$)	($A.g^{-1}_{Pt}$)	($mV.dec^{-1}$)	($F.g^{-1}_{C}$)
XC-72-Pt	BoL	74 ± 4	3.8 ± 0.1	0.029 ± 0.001	2.12 ± 0.05	66 ± 13	24 ± 4
	MoL	45 ± 2	6.2 ± 0.1	0.037 ± 0.002	1.65 ± 0.11	71 ± 1	19 ± 2
	EoL	40 ± 7	7.1 ± 0.7	0.031 ± 0.001	1.24 ± 0.15	73 ± 3	19 ± 1
CX0-Pt	BoL	117 ± 7	2.4 ± 0.1	0.022 ± 0.002	2.69 ± 0.42	67 ± 7	128 ± 2
	MoL	78 ± 2	3.6 ± 0.1	0.043 ± 0.003	2.99 ± 0.36	64 ± 4	140 ± 13
	EoL	70 ± 3	4.0 ± 0.2	0.060 ± 0.009[f]	3.79 ± 0.95[f]	62 ± 3	142 ± 18
CX0-C20-Pt	BoL	101 ± 4	2.8 ± 0.1	0.034 ± 0.001	3.29 ± 0.01	71 ± 2	33 ± 2
	MoL	65 ± 1	4.3 ± 0.1	0.047 ± 0.001	3.06 ± 0.07	62 ± 1	26 ± 1
	EoL	53 ± 1	5.2 ± 0.1	0.059 ± 0.004	3.15 ± 0.19	61 ± 1	25 ± 1
CX0-C60-Pt	BoL	63 ± 6	4.4 ± 0.6	0.029 ± 0.003	1.82 ± 0.43	68 ± 11	10 ± 3
	MoL	35 ± 1	8.0 ± 0.1	0.046 ± 0.007	1.61 ± 0.26	62 ± 3	9 ± 3
	EoL	27 ± 1	10.2 ± 0.2	0.050 ± 0.003	1.37 ± 0.12	86 ± 13	9 ± 4
CX0-C20-HT1500-Pt	BoL	99 ± 23	2.9 ± 0.3	0.033 ± 0.001	3.25 ± 0.39	61 ± 1	22 ± 5
	MoL	50 ± 3	5.7 ± 0.4	0.052 ± 0.001	2.57 ± 0.14	63 ± 1	13 ± 2
	EoL	54 ± 6	5.2 ± 0.3	0.06 ± 0.002	3.25 ± 0.27	61 ± 1	11 ± 2

[a] *ECSA*: Electrochemically activity surface area of Pt normalized by the mass of Pt on the electrode, determined from CO stripping measurement (**Equation (2.5)**).

[b] d_{CO}: CO equivalent particle diameter of the Pt particles calculated from **Equation (2.6)**.

[c] *SA* and *MA*: Specific Activity and Mass Activity measured at 0.95 V *vs.* RHE (**Equations (2.7)** and **(2.8)**).

[d] *b*: Tafel slope calculated at 0.95 V *vs.* RHE from ORR measurement.

[e] C_{dl}: Double layer capacity measured from cyclic voltammetry plotted at 20 $mV.s^{-1}$, calculated from **Equation (2.4)**.

[f] At *EoL* of CX0-Pt, an error > 20% is observed between the three measurements.

Note: The values presented in this table correspond to the average of at least two measurements.

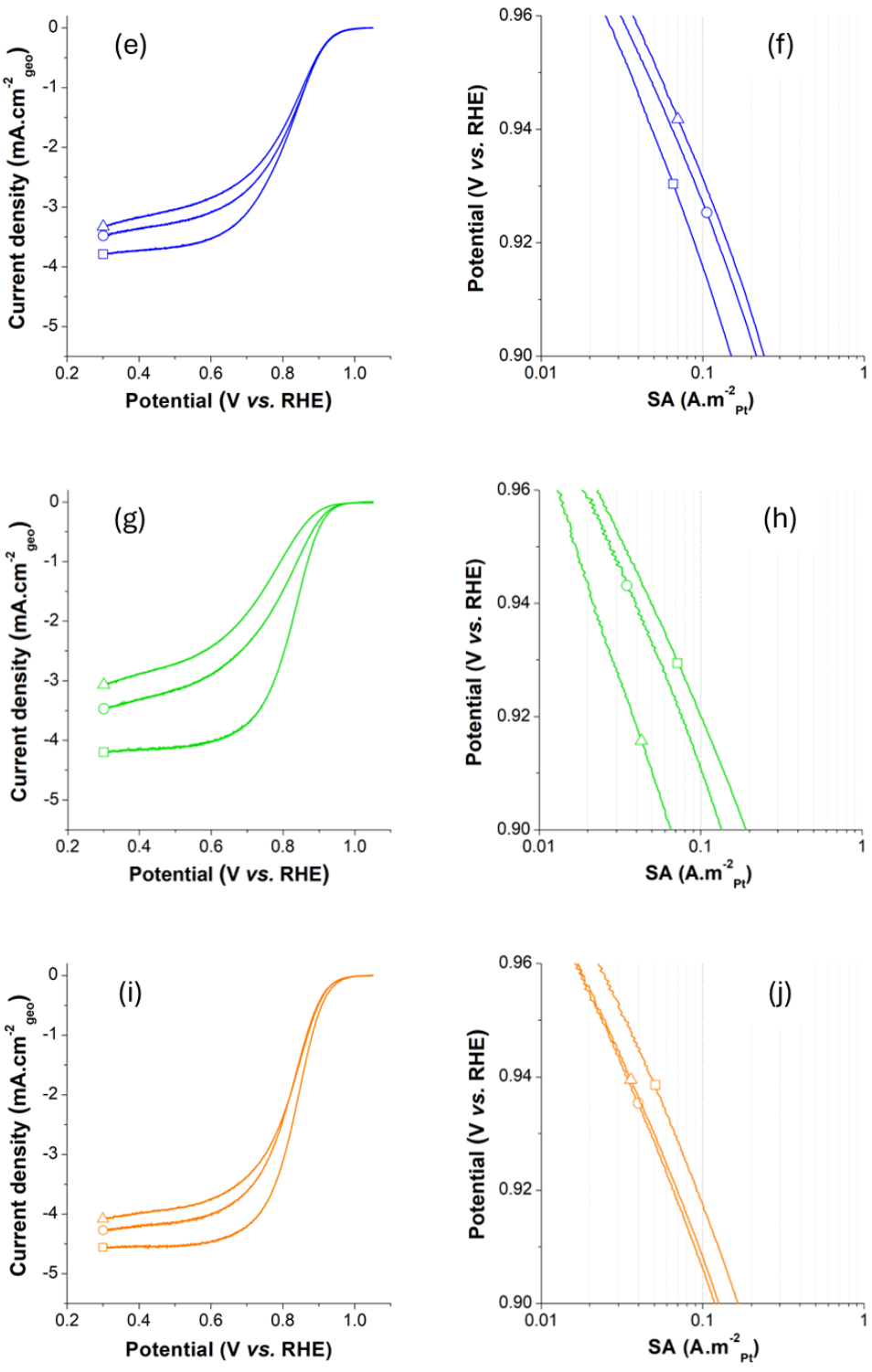

Figure 2.9. Electrochemical measurements performed in RDE configuration in 0.5 M H_2SO_4 and 25 ºC, at *BoL* (—□—), *MoL* (—○—) and *EoL* (—△—). Cyclic voltammetry under O_2 at a scan rate of 1 $mV.s^{-1}$ and an electrode rotation of 1600 rpm of (a) XC-72-Pt, (c) CX0-Pt, (e) CX0-C20-Pt (g) CX0-C60-Pt and (i) CX0-C20-HT1500-Pt, and Tafel plots of (b) XC-72-Pt, (d) CX0-Pt, (f) CX0-C20-Pt, (h) CX0-C60-Pt and (j) CX0-C20-HT1500-Pt.

Regarding catalytic activities, the *SA* of XC-72-Pt remains stable upon aging (7% increase after 20,000 cycles). In contrast, the carbon xerogel-supported catalysts exhibit a pronounced increase in *SA* upon aging (173% for CX0-Pt, 75% for CX0-C20-Pt, 73% for CX0-C60-Pt and 82% for CX0-C20-HT1500-Pt), demonstrating a different behavior compared to carbon black-supported catalysts (**Figure 2.10b**). The most significant change is observed for CX0-Pt, where the *SA* increases from 0.022 to 0.060 $A.m^{-2}_{Pt}$. The observed increase in specific activity could be explained as follows. First, aging induces a slight growth of Pt nanoparticles, as confirmed by TEM micrographs and the increase in d_{CO}. Second, the ratio between facet sites and edge or corner sites changes with the particle size. As the nanoparticles grow, fewer Pt atoms occupy low-coordination edge or corner sites. Due to this low coordination, such sites are highly binding to the reaction intermediates. Nevertheless, excessive adsorption binding energy between the oxygen intermediates and Pt ultimately hinders the ORR [44,45]. With accelerated aging of the catalytic layer and the consequent growth of nanoparticles, a larger proportion of facet sites can be present relative to the number of edge or corner sites. This may lead to a more optimal binding energy for ORR intermediates, ultimately increasing the specific activity.

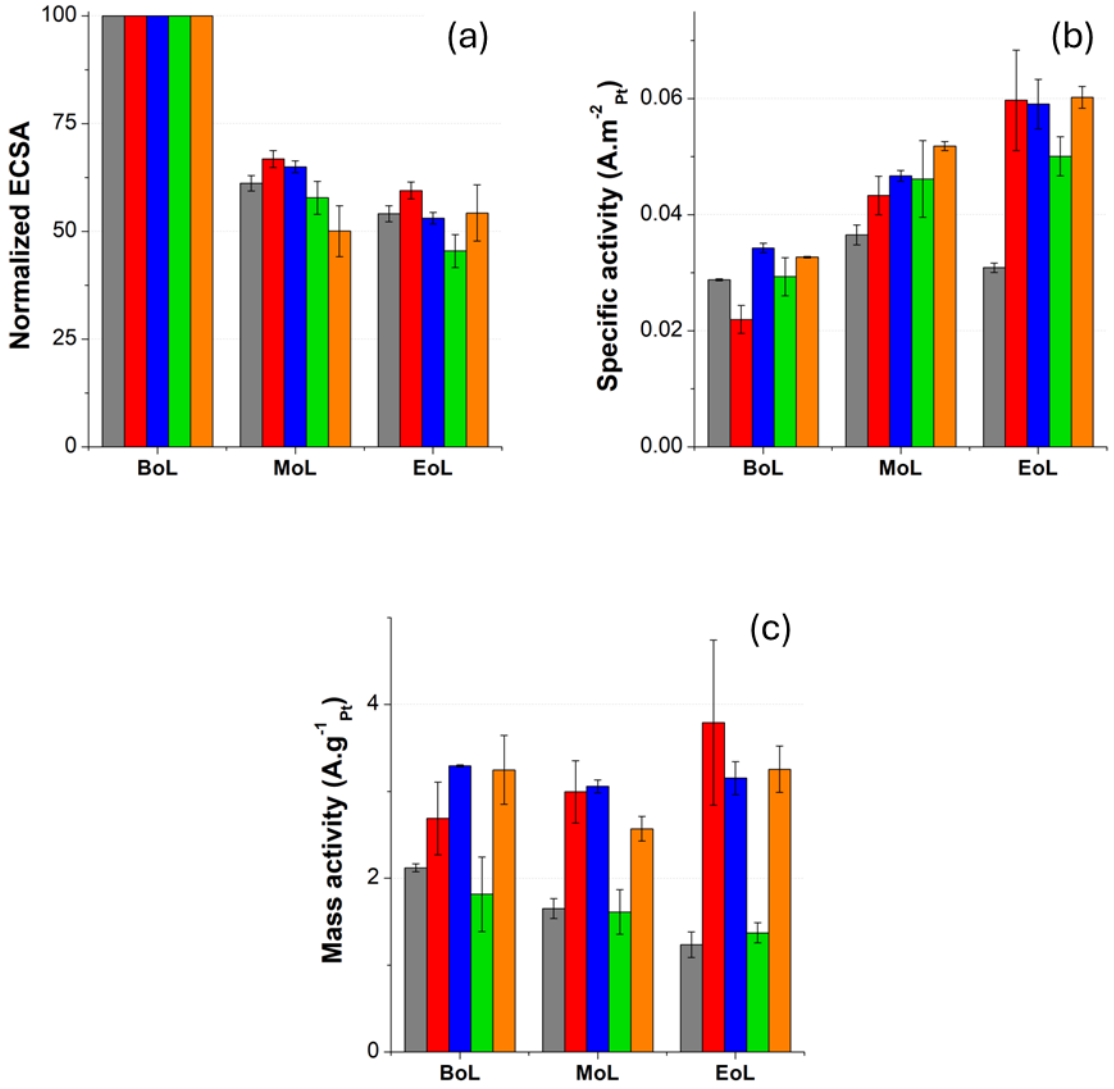

Figure 2.10. Evolution during AST in RDE configuration of (a) the normalized ElectroChemically active Surface Area of Pt, (b) the specific activity (*SA*) at 0.95 V *vs.* RHE, and (c) the mass activity (MA) at 0.95 V *vs.* RHE, of XC-72-Pt (■), CX0-Pt (■), CX0-C20-Pt (■), CX0-C60-Pt (■) and CX0-C20-HT1500-Pt (■).

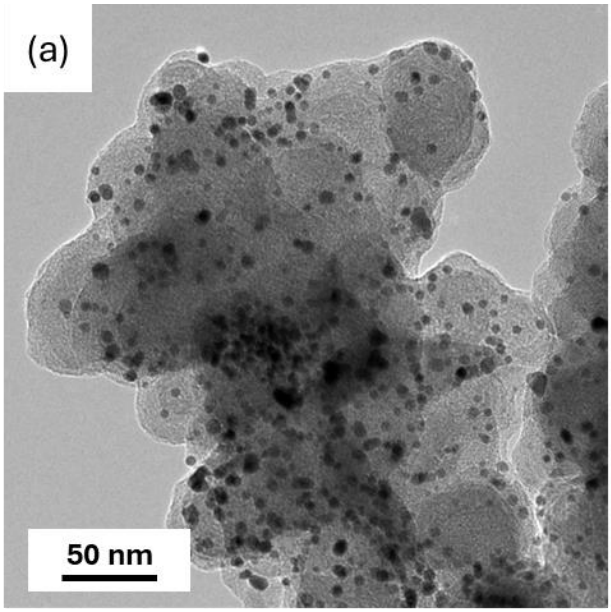
(a)
50 nm

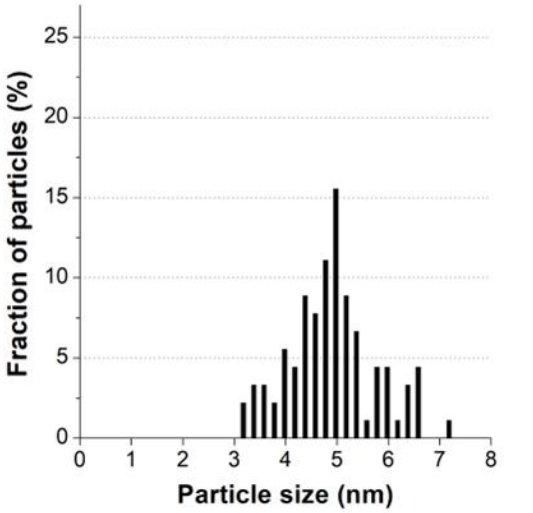
XC-72-Pt
Fraction of particles (%)
Particle size (nm)

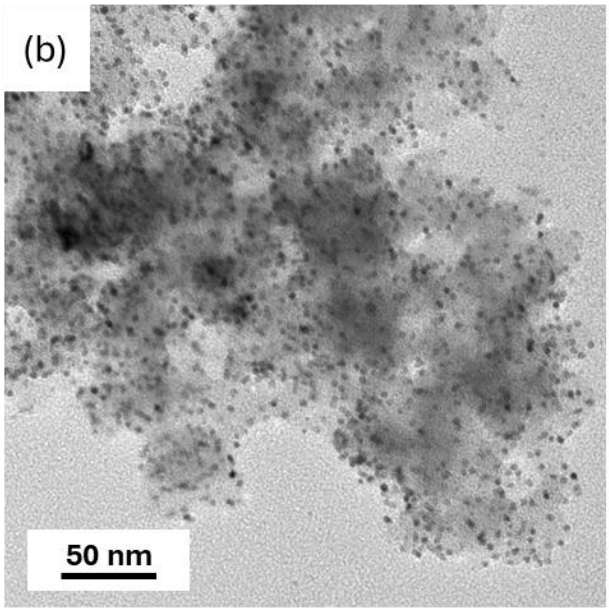
(b)
50 nm

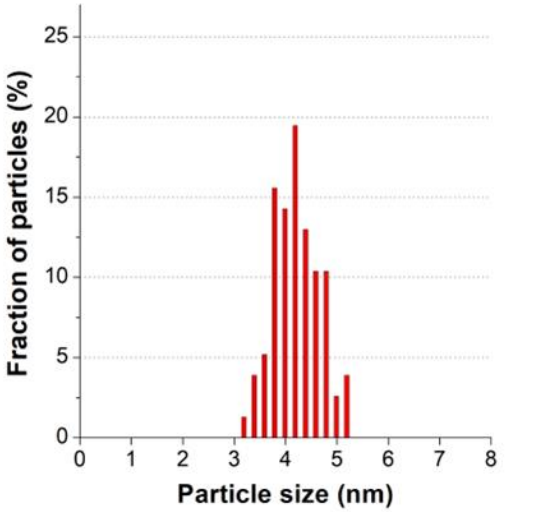
CX0-Pt
Fraction of particles (%)
Particle size (nm)

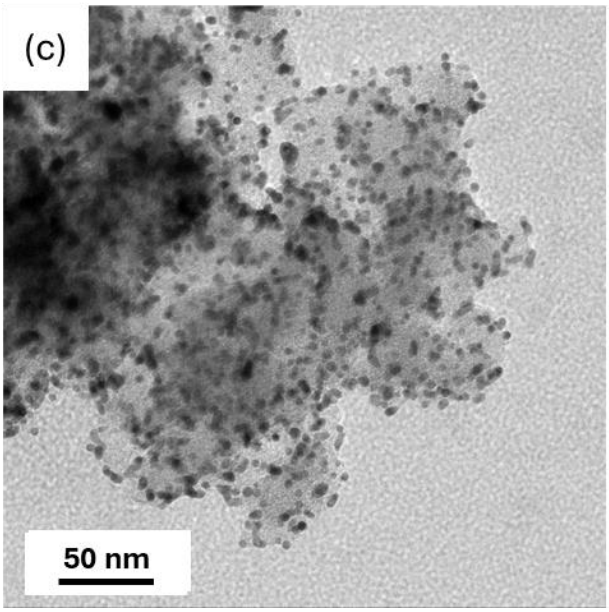
(c)
50 nm

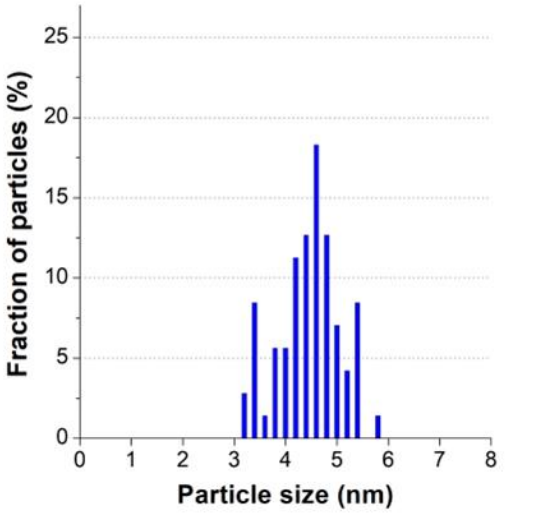
CX0-C20-Pt
Fraction of particles (%)
Particle size (nm)

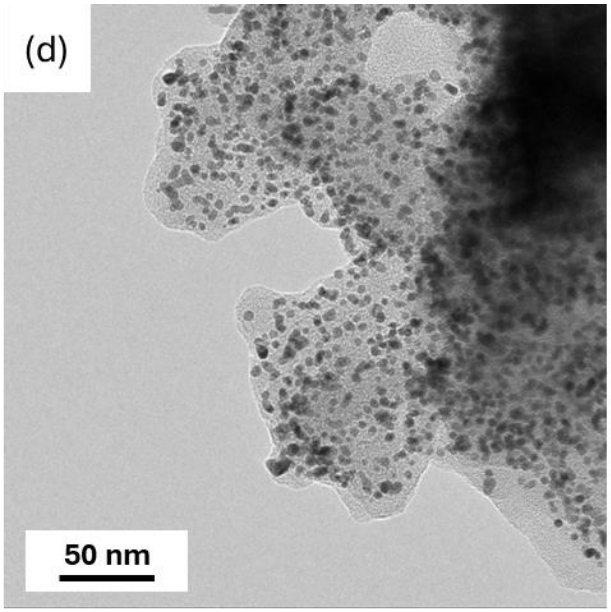
(d)
50 nm

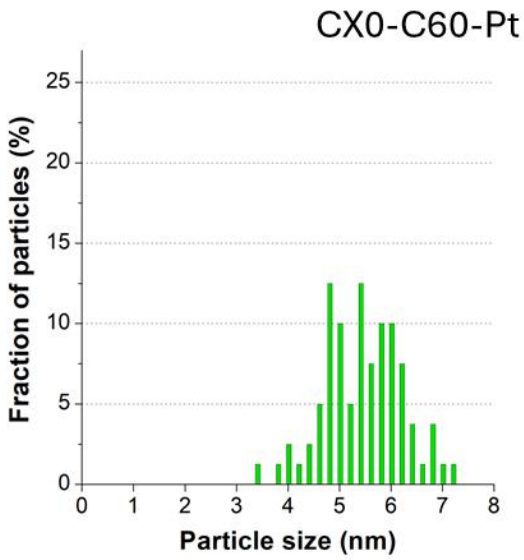
CX0-C60-Pt
Fraction of particles (%)
Particle size (nm)

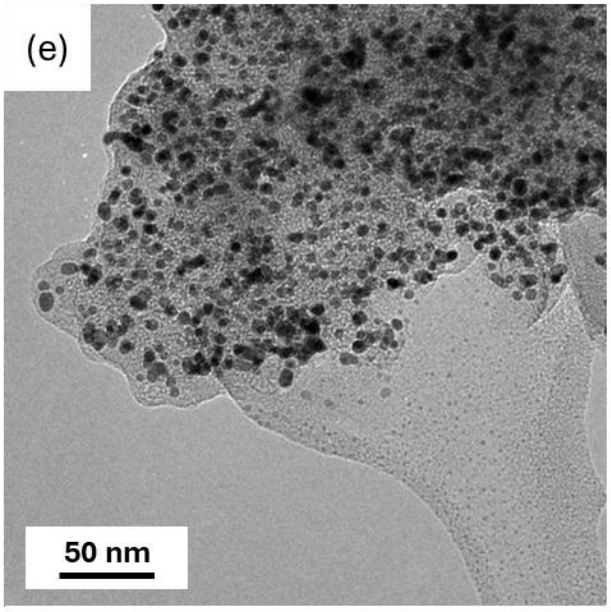
(e)
50 nm

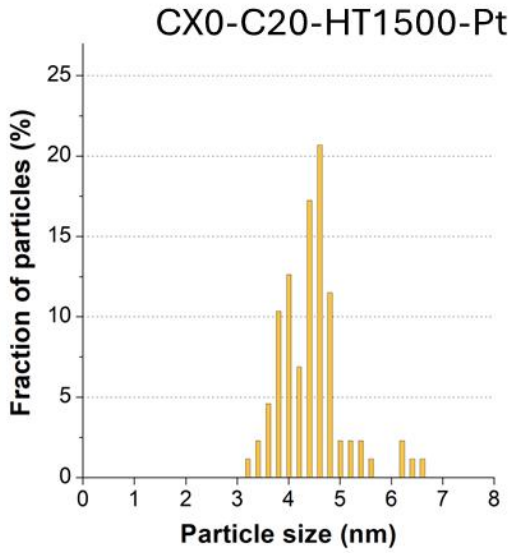
CX0-C20-HT1500-Pt
Fraction of particles (%)
Particle size (nm)

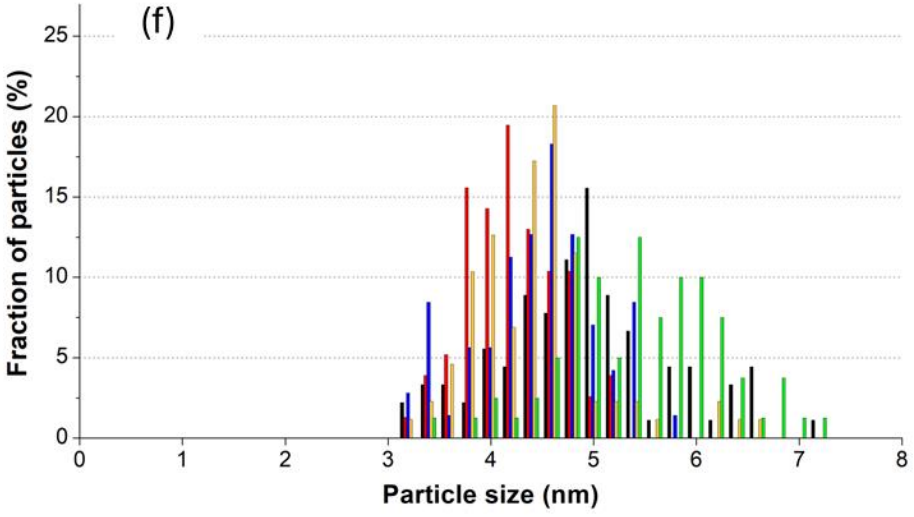
(f)
Fraction of particles (%)
Particle size (nm)

Figure 2.11. TEM micrographs and corresponding particle size distribution of (a) XC-72-Pt, (b) CX0-Pt, (c) CX0-C20-Pt, (d) CX0-C60-Pt, (e) CX0-C20-HT1500-Pt and (f) complete Pt nanoparticle size distribution of XC-72-Pt (■). CX0-Pt (■), CX0-C20-Pt (■), CX0-C60-Pt (■) and CX0-C20-HT1500-Pt (■), after aging with 20,000 cycles between 0.6 and 1.0 V *vs.* RHE at 0.1 $V.s^{-1}$ in RDE configuration, corresponding to the *EoL*.

Meanwhile, the *MA* of carbon xerogel-supported catalysts (**Figure 2.10c**) remains relatively stable while that of the commercial catalyst significant decreases (*MA* loss of 22% and 41.5% after 5,000 and 20,000 cycles respectively). Consequently, the *MA* values become very different between the carbon black-supported catalyst (1.24 $A.g_{Pt}^{-1}$ for XC-72-Pt), and carbon xerogel-supported catalysts (3.79 $A.g_{Pt}^{-1}$ for CX0-Pt, 3.15 $A.g_{Pt}^{-1}$ for CX0-C20-Pt and 3.25 $A.g_{Pt}^{-1}$ for CX0-C20-HT1500-Pt). Again, CX0-C60-Pt exhibits a lower value, with a final *MA* of 1.37 $A.g_{Pt}^{-1}$. This value is close to that of XC-72-Pt, although the initial *MA* of CX0-C60-Pt was lower to begin with. Extended cycling could lead eventually to a further decrease of *MA*, bringing values of all catalysts closer to those of XC-72-Pt for all samples. The measurements of *MA* and *SA* confirm that there is an optimal Pt nanoparticle size at which the available surface area is maximized and where the surface atoms possess a balanced reactivity towards ORR [46]. Nevertheless, the presence of the CVD layer does not appear to significantly reduce nor aggravate Pt nanoparticles agglomeration upon aging.

For all samples, the Tafel plot always remains below 80 $mV.dec^{-1}$, indicating that the ORR still proceeds through a 4-electron mechanism even after 20,000 cycles. An exception is CX0-C60-Pt, whose average Tafel plot remains below 80 $mV.dec^{-1}$ after 5,000 cycles but increases to 86 $mV.dec^{-1}$ after 20,000 cycles. Note that this value should be treated cautiously as the values measured at *EoL* differed significantly between the three AST procedures performed on this sample (error of ± 13 $mV.dec^{-1}$ observed, on the average of three measurements). However, in general, no significant modification of the Tafel slope was observed, indicating that the ORR keeps proceeding through a 4-electron pathway upon aging.

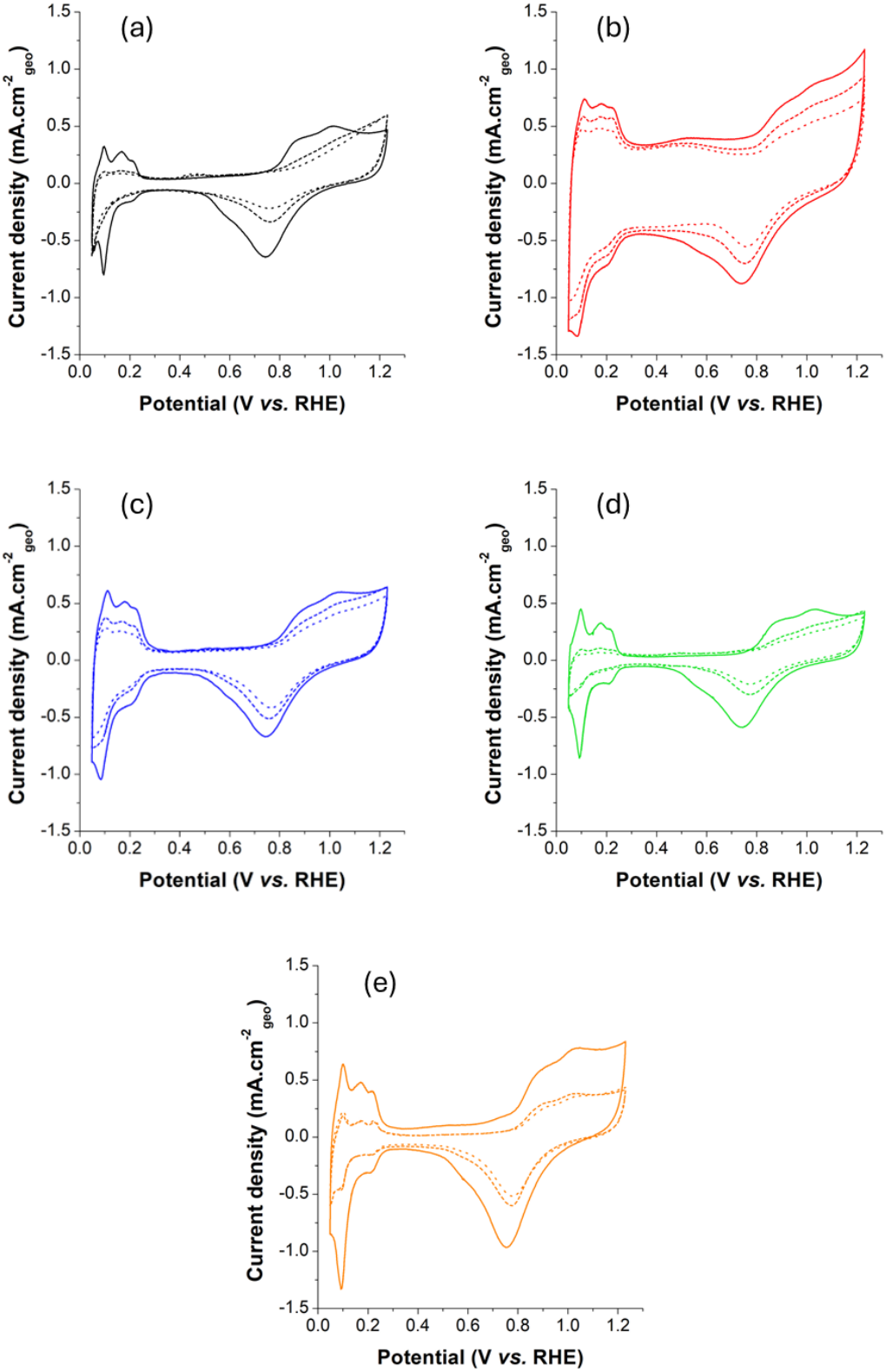

Figure 2.12. Cyclic voltammetry curves in RDE configuration of (a) XC-72-Pt, (b) CX0-Pt, (c) CX0-C20-Pt, (d) CX0-C60-Pt and (e) CX0-C20-HT1500-Pt, recorded at 0.02 V.s^{-1}, at *BoL* (plain line), *MoL* (dashed line) and *EoL* (dotted line).

Finally, the double-layer capacitance, C_{dl}, was calculated at each aging step. A slight decrease is sometimes observed for all materials after 5,000 cycles, but values do not evolve significantly after 20,000 cycles. This trend could mean that carbon corrosion does occur, but it remains mild, with no evidence of structural collapse of the carbon support. Testing these catalysts under higher potential conditions (above 1.0 V *vs.* RHE) could be of interest to simulate start-stop cycles [27]. These potentials would further accelerate platinum degradation [47] but could also lead to an aging of the carbon support so severe that perhaps no differences would be seen between all the carbons.

Overall, the general performance of CVD-treated CXs show little improvements compared to their untreated counterpart. Surface modification *via* a CVD duration of 20 min offered a small benefit without compromising the overall pore texture (and thus the expected mass transport properties in a real fuel cell electrode), but the longer treatment of 60 min led to a more unpredictable behavior with lower activity towards ORR than the catalyst supported on the pristine CX0. It is also clear that this treatment alone does not prevent significant nanoparticle growth. Combining CVD treatment with the introduction of additional anchoring sites on the carbon surface *via* heteroatom doping could help mitigate the phenomena leading to the growth of Pt nanoparticles, although it could come at the expense of the carbon surface crystallinity and resistance to corrosion. Consequently, in the next chapter, both CX0 and CX0-C20 will be further investigated for nitrogen incorporation. Owing to the poor performances observed in RDE configuration, CX0-C60 will not be considered further in this thesis.

2.4. Conclusion

In this chapter, a pristine carbon xerogel (CX0) and its counterparts subjected to three post-treatments were selected for evaluation as durable and efficient electrocatalyst support for PEMFC catalytic layers. The post-treated samples correspond to the CX0 subjected to 20 and 60 min by Chemical Vapor Deposition (CVD), as well as the CX coated 20 min by CVD and subsequently graphitized at 1,500 ºC under inert atmosphere. These samples, developed in Chapter 1, were specifically selected because they possess a secondary carbon layer with increased surface ordering compared to the pristine CX0 while retaining the initial meso/macropore texture of the pristine CX0, which should ensure keeping the mass transport properties of the carbon. To evaluate their quality as catalyst support, Pt nanoparticles were deposited on these carbon materials, with a target metal loading of 20 wt.%, using a well-known

method (reduction in liquid phase). After physico-chemical characterization, the samples were tested in liquid electrolyte, on Rotating Disk Electrode (RDE), to assess their catalytic activities and resilience towards aging. Their electrocatalytic performances as Oxygen Reduction Reaction (ORR) catalyst were also compared to those of a commercial catalyst supported on classical carbon black (Vulcan XC-72).

First, it was observed that nanoparticles were deposited homogenously on all samples. It was also observed that the nanoparticles grow slightly larger on CVD-treated CXs, with a maximum reached for the one coated during 60 min (CX0-C60-Pt) with an average nanoparticle size of 3.7 ± 0.6 nm. Nonetheless, the nanoparticle size of all catalysts remains within the same range with only minor variations in particle size distributions. Regarding initial catalytic performances, the catalyst supported on the pristine CX0 (CX0-Pt) exhibited catalytic activities comparable with that of the commercial catalyst. Catalytic activities were found even higher for the catalysts supported on the same CX sample after 20 min of CVD (CX0-C20-Pt and CX0-C20-HT1500-Pt), likely because the nanoparticles were closer to their optimal size for the ORR, (usually estimated to be close to 3.5 nm). Meanwhile, CX0-C60-Pt yielded mixed results. This behavior may be attributed to the higher hydrophobicity of this material. This hydrophobicity could limit the electrolyte accessibility to some of the catalytic sites, as suggested by the large value obtained for CO equivalent diameter, thereby leading to lower catalytic performances. These observations indicate that longer CVD durations can be detrimental for catalyst use and that the CVD treatment conditions must be properly optimized. Upon accelerated aging, the catalytic behavior observed for catalysts supported on pristine or post-treated CX was relatively similar, with an increase in specific activity, while the mass activity remains relatively constant. This behavior was attributed to the Pt nanoparticles agglomeration upon aging.

This indicates that additional strategies to mitigate degradation phenomena could be explored. In this context, a heteroatom-doping strategy will be explored in Chapter 3, with the aim of strengthening the bonds between the Pt nanoparticles and the carbon support. Further graphitization of the deposited CVD layer through treatment at temperatures above 1,500 ºC could also be envisaged, but would increase the overall material cost. This treatment will not be performed in this thesis, but could be the subject of future works.

2.5. References

[1] P. Sharma, O.P. Pandey, Proton Exchange Membrane Fuel Fells: Fundamentals, Advanced Technologies, and Practical Applications, in: PEM Fuel Cells, Elsevier, 2022: pp. 1–24.

[2] S.M. Haile, Fuel Cell Materials and Components, *Acta Materialia*, 51 (2003) 5981–6000.

[3] N. Job, J. Marie, S. Lambert, S. Berthon-Fabry, P. Achard, Carbon Xerogels as Catalyst Supports for PEM Fuel Cell Cathode, *Energy Conversion and Management*, 49 (2008) 2461–2470.

[4] C. Moreno-Castilla, F.J. Maldonado-Hódar, Carbon Aerogels for Catalysis Applications: An Overview, *Carbon*, 43 (2005) 455–465.

[5] R.W. Pekala, Organic Aerogels from the Polycondensation of Resorcinol with Formaldehyde, *Journal of Materials Science*, 24 (1989) 3221–3227.

[6] C. Alegre, D. Sebastián, M.J. Lázaro, Carbon Xerogels Electrochemical Oxidation and Correlation with their Physico-Chemical Properties, *Carbon*, 144 (2019) 382–394.

[7] K.H. Kangasniemi, D.A. Condit, T.D. Jarvi, Characterization of Vulcan Electrochemically Oxidized under Simulated PEM Fuel Cell Conditions, *Journal of The Electrochemical Society*, 151 (2004) E125.

[8] N. Macauley, D.D. Papadias, J. Fairweather, D. Spernjak, D. Langlois, R. Ahluwalia, K.L. More, R. Mukundan, R.L. Borup, Carbon Corrosion in PEM Fuel Cells and the Development of Accelerated Stress Tests, *Journal of The Electrochemical Society*, 165 (2018) F3148–F3160.

[9] M.L.C. Piedboeuf, A.F. Léonard, G. Reichenauer, C. Balzer, N. Job, How Do the Micropores of Carbon Xerogels Influence their Electrochemical Behavior as Anodes for Lithium-Ion Batteries?, *Microporous and Mesoporous Materials*, 275 (2019) 278–287.

[10] B. Karaman, H. Tonnoir, D. Huo, B. Carré, A.F. Léonard, J.C. Gutiérrez, M.L. Piedboeuf, A. Celzard, V. Fierro, C. Davoisne, R. Janot, N. Job, CVD-Coated Carbon Xerogels for Negative Electrodes of Na-Ion Batteries, *Carbon*, 225 (2024) 119077.

[11] A. Zubiaur, N. Job, Streamlining of the Synthesis Process of Pt/Carbon Xerogel Electrocatalysts with High Pt Loading for the Oxygen Reduction Reaction in Proton Exchange Membrane Fuel Cells Applications, *Applied Catalysis B: Environmental*, 225 (2018) 364–378.

[12] C. Alegre, M.E. Gálvez, R. Moliner, V. Baglio, A.S. Aricò, M.J. Lázaro, Towards an Optimal Synthesis Route for the Preparation of Highly Mesoporous Carbon Xerogel-Supported Pt Catalysts for the Oxygen Reduction Reaction, *Applied Catalysis B: Environmental*, 147 (2014) 947–957.

[13] J. Rouquerol, P. Llewellyn, F. Rouquerol, Is the BET Equation Applicable to Microporous Adsorbents?, in: Studies in Surface Science and Catalysis, 2007: pp. 49–56.

[14] I.N. Leontyev, A.B. Kuriganova, N.G. Leontyev, L. Hennet, A. Rakhmatullin, N. V. Smirnova, V. Dmitriev, Size Dependence of the Lattice Parameters of Carbon Supported

Platinum Nanoparticles: X-Ray Diffraction Analysis and Theoretical Considerations, *RSC Advances*, 4 (2014) 35959–35965.

[15] G. Bergeret, P. Gallezot, Particle Size and Dispersion Measurements, in: Handbook of Heterogeneous Catalysis, Wiley, 2008: pp. 738–765.

[16] F. Maillard, S. Pronkin, E.R. Savinova, Influence of Size on the Electrocatalytic Activities of Supported Metal Nanoparticles in Fuel Cells Related Reactions, in: Handbook of Fuel Cells, 2010.

[17] K.J.J. Mayrhofer, S.J. Ashton, J. Kreuzer, M. Arenz, An Electrochemical Cell Configuration Incorporating an Ion Conducting Membrane Separator between Reference and Working Electrode, *International Journal of Electrochemical Science*, 4 (2009) 1–8.

[18] A. Zubiaur, Development of New Catalysts for Proton Exchange Membrane Fuel Cells (PEMFCs), PhD thesis, Université de Liège, 2017.

[19] K. Ke, K. Hiroshima, Y. Kamitaka, T. Hatanaka, Y. Morimoto, An Accurate Evaluation for the Activity of Nano-Sized Electrocatalysts by a Thin-Film Rotating Disk Electrode: Oxygen Reduction on Pt/C, *Electrochimica Acta*, 72 (2012) 120–128.

[20] M.L.C. Piedboeuf, A.F. Léonard, K. Traina, N. Job, Influence of the Textural Parameters of Resorcinol-Formaldehyde Dry Polymers and Carbon Xerogels on Particle Sizes upon Mechanical Milling, *Colloids and Surfaces A: Physicochemical and Engineering Aspects*, 471 (2015) 124–132.

[21] U.A. Paulus, T.J. Schmidt, H.A. Gasteiger, R.J. Behm, Oxygen Reduction on a High-Surface Area Pt/Vulcan Carbon Catalyst: A Thin-Film Rotating Ring-Disk Electrode Study, *Journal of Electroanalytical Chemistry*, 495 (2001) 134–145.

[22] F.L. Deschamps, J.G. Mahy, A.F. Léonard, N. Job, Rotating Disk Electrode Measurements on Low and High Loading Catalyst Layers: Diffusion Limitations and Application to Pt Catalysts Supported on Porous Micrometric Carbon Xerogel Particles Designed for Proton Exchange Membrane Fuel Cells, *Journal of Electroanalytical Chemistry*, 933 (2023) 117279.

[23] F. Maillard, E.R. Savinova, U. Stimming, CO Monolayer Oxidation on Pt Nanoparticles: Further Insights into the Particle Size Effects, *Journal of Electroanalytical Chemistry*, 599 (2007) 221–232.

[24] S. Trasatti, O.A. Petrii, Real Surface Area Measurements in Electrochemistry, *Journal of Electroanalytical Chemistry*, 327 (1992) 353–376.

[25] I.E.L. Stephens, A.S. Bondarenko, U. Grønbjerg, J. Rossmeisl, I. Chorkendorff, Understanding the Electrocatalysis of Oxygen Reduction on Platinum and its Alloys, *Energy & Environmental Science*, 5 (2012) 6744.

[26] O. Antoine, R. Durand, RRDE Study of Oxygen Reduction on Pt Nanoparticles inside Nafion: H2O2 Production in PEMFC Cathode Conditions, *Journal of Applied Electrochemistry*, 30 (2000) 839–844.

[27] N. Garland, T. Benjamin, J. Kopasz, DOE Fuel Cell Program: Durability Technical Targets and Testing Protocols, *ECS Transactions*, 11 (2007) 923–931.

[28] Y. Garsany, O.A. Baturina, K.E. Swider-Lyons, S.S. Kocha, Experimental Methods for Quantifying the Activity of Platinum Electrocatalysts for the Oxygen Reduction Reaction, *Analytical Chemistry*, 82 (2010) 6321–6328.

[29] F. Stoeckli, D. Huguenin, A. Laederach, On the Characterization of Microporous Carbon Blacks by Various Techniques, *Chimia*, 47 (1993) 211.

[30] S. Lambert, N. Job, L. D'Souza, M. Pereira, R. Pirard, B. Heinrichs, J. Figueiredo, J. Pirard, J. Regalbuto, Synthesis of Very Highly Dispersed Platinum Catalysts Supported on Carbon Xerogels by the Strong Electrostatic Adsorption Method, *Journal of Catalysis*, 261 (2009) 23–33.

[31] R. Sellin, J.-M. Clacens, C. Coutanceau, A Thermogravimetric Analysis/Mass Spectroscopy Study of the Thermal and Chemical Stability of Carbon in the Pt/C Catalytic System, *Carbon*, 48 (2010) 2244–2254.

[32] M.A. van Spronsen, J.W.M. Frenken, I.M.N. Groot, Observing the Oxidation of Platinum, *Nature Communications*, 8 (2017) 429.

[33] F. Yi, S.Q. Arlington, J. Gorham, W. Osborn, E.J. Crumlin, S. Nemsak, D.A. LaVan, Growth and Decomposition of Pt Surface Oxides, *The Journal of Physical Chemistry Letters*, 13 (2022) 6171–6176.

[34] Md.M. Rahman, K. Inaba, G. Batnyagt, M. Saikawa, Y. Kato, R. Awata, B. Delgertsetsega, Y. Kaneta, K. Higashi, T. Uruga, Y. Iwasawa, K. Ui, T. Takeguchi, Synthesis of Catalysts with Fine Platinum Particles Supported by High-Surface-Area Activated Carbons and Optimization of their Catalytic Activities for Polymer Electrolyte Fuel Cells, *RSC Advances*, 11 (2021) 20601–20611.

[35] F. Maillard, S. Schreier, M. Hanzlik, E.R. Savinova, S. Weinkauf, U. Stimming, Influence of Particle Agglomeration on the Catalytic Activity of Carbon-Supported Pt Nanoparticles in CO Monolayer Oxidation, *Physical Chemistry Chemical Physics*, (2005) 385–393.

[36] C. Alegre, M. Gálvez, R. Moliner, M. Lázaro, Influence of the Synthesis Method for Pt Catalysts Supported on Highly Mesoporous Carbon Xerogel and Vulcan Carbon Black on the Electro-Oxidation of Methanol, *Catalysts*, 5 (2015) 392–405.

[37] N. Job, S. Lambert, A. Zubiaur, C. Cao, J.-P. Pirard, Design of Pt/Carbon Xerogel Catalysts for PEM Fuel Cells, *Catalysts*, 5 (2015) 40–57.

[38] R. Yu, L. Chen, Q. Liu, J. Lin, K.-L. Tan, S.C. Ng, H.S.O. Chan, G.-Q. Xu, T.S.A. Hor, Platinum Deposition on Carbon Nanotubes via Chemical Modification, *Chemistry of Materials*, 10 (1998) 718–722.

[39] M. Canal-Rodríguez, A. Arenillas, N. Rey-Raap, G. Ramos-Fernández, I. Martín-Gullón, J.A. Menéndez, Graphene-Doped Carbon Xerogel Combining High Electrical Conductivity and Surface Area for Optimized Aqueous Supercapacitors, *Carbon*, 118 (2017) 291–298.

[40] J. Marie, S. Berthon-Fabry, P. Achard, M. Chatenet, A. Pradourat, E. Chainet, Highly dispersed platinum on carbon aerogels as supported catalysts for PEM fuel cell-electrodes: Comparison of two different synthesis paths, *Journal of Non-Crystalline Solids*, 350 (2004) 88–96.

[41] Y. Liu, C. Ji, W. Gu, J. Jorne, H.A. Gasteiger, Effects of Catalyst Carbon Support on Proton Conduction and Cathode Performance in PEM Fuel Cells, *Journal of The Electrochemical Society*, 158 (2011) B614.

[42] M.S. Wilson, F.H. Garzon, K.E. Sickafus, S. Gottesfeld, Surface Area Loss of Supported Platinum in Polymer Electrolyte Fuel Cells, *Journal of The Electrochemical Society*, 140 (1993) 2872.

[43] M. Watanabe, K. Tsurumi, T. Mizukami, T. Nakamura, P. Stonehart, Activity and Stability of Ordered and Disordered Co-Pt Alloys for Phosphoric Acid Fuel Cells, *Journal of The Electrochemical Society*, 141 (1994) 2659.

[44] M. Shao, A. Peles, K. Shoemaker, Electrocatalysis on Platinum Nanoparticles: Particle Size Effect on Oxygen Reduction Reaction Activity, *Nano Letters*, 11 (2011) 3714–3719.

[45] M. Peuckert, T. Yoneda, R.A.D. Betta, M. Boudart, Oxygen Reduction on Small Supported Platinum Particles, *Journal of The Electrochemical Society*, 133 (1986) 944–947.

[46] K. Kinoshita, Particle Size Effects for Oxygen Reduction on Highly Dispersed Platinum in Acid Electrolytes, *Journal of The Electrochemical Society*, 137 (1990) 845–848.

[47] X. Wang, R. Kumar, D.J. Myers, Effect of Voltage on Platinum Dissolution, *Electrochemical and Solid-State Letters*, 9 (2006) A225.

Annex 2.1. Use of CVD by-product as electrocatalyst support

After performing the Chemical Vapor Deposition (CVD) process, the presence of large chunks of carbon deposits was observed on the inner walls of the oven tube. This carbon originates from the ethylene decomposition outside of the intended substrate (*i.e.* the carbon xerogel powder). Normally, this by-product of CVD is scratched off the tube and discarded between each CVD deposition. Nevertheless, this waste is also of carbon nature. Thus, a quick evaluation of this material was performed to assess its potential as carbon support for electrocatalyst. A CVD treatment was conducted for 20 min in regular conditions and in a clean oven. After the treatment, the carbon xerogel (CX) powder was first retrieved. Then, a small quantity of the carbon by-product deposited on the inner part of the tube was scratched off and collected. This material is referred to as CVD-BP.

N_2 adsorption-desorption isotherms and XRD diffractograms were collected in the first place. The XRD diffractogram of CVD-BP is displayed in **Figure A1**. A large number of reflections can be observed. This diffractogram is characteristic of a carbon material containing large amounts of well-ordered carbon structures, such as graphite, carbon nanotubes or fullerenes [1]. This observation is not unexpected, as CVD of hydrocarbons is known to yield such carbon structures [2–4]. Nonetheless, a few peaks remain unidentified on the diffractogram. These peaks could originate from impurities due to the inherently raw nature of the sample, recovered simply from the tube wall without any subsequent treatment. They may correspond to nickel, or nickel-aluminum compounds. Indeed, the reflections of Ni(111), Ni(200) and Ni(220) are consistent with the unidentified peaks [5]. Since the CVD treatment is conducted in a stainless-steel tube, the inclusion of nickel-containing alloys in the carbon powder retrieved is possible.

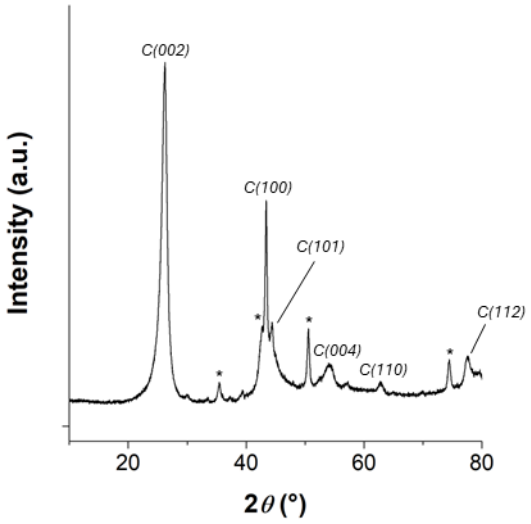

Figure A1.1. X-ray diffractogram of CVD-BP. *: non identified peaks.

Crystallographic parameters were also calculated and compared with those of CX0-C20. Results are compiled in **Table A2.1.1**. The lateral carbon crystallites size, L_a, was calculated at 3.81 and 52.15 nm, while the stacking height L_c of crystallites was calculated at 1.03 and 8.53 nm, for CX0-C20 and CVD-BP, respectively. Carbon crystallites of the CVD by-product are larger than those of CXs, both laterally and vertically. The interlayer distance d_{002} is calculated equal to 0.393 and 0.341 nm for CX0-C20 and CVD-BP, respectively. d_{002} of CVD-BP is close to that of graphite (d_{002} = 0.335 nm). Thus, this powder has a degree of surface ordering significantly larger than the CX material. This CVD by-product appears to consist of a complex mix of graphitic structures and carbon nanotubes. The presence of other unidentified carbon species could also be expected. Overall, this material could be of interest as a carbon support, as large degree of graphitization is associated with lower rates of carbon oxidation in PEMFCs [6].

Table A2.1.1. Crystalline parameters determined by X-ray diffraction.

Sample	L_a[a] (nm) ± 0.03	L_c[b] (nm) ± 0.03	d_{002}[c] (nm) ± 0.004
CX0-C20	3.81	1.03	0.393
CVD-BP	52.15	8.53	0.341

[a] L_a: Lateral crystallite size, calculated from Scherrer's equation on C(002) peak.

[b] L_c: Crystallite stacking length, calculated from Scherrer's equation on the carbon 10 reflection.

[c] d_{002}: Graphene interlayer distance, calculated from Bragg's law.

The porosity of the material was also observed with N_2 adsorption-desorption measurements, displayed in **Figure A2.1.2**. Both CX0-C20 and CVD-BP present a type I + II isotherm, according to the IUPAC classification. The adsorbed quantity rises quickly at low relative pressure, indicating the presence of micropores in both samples.

Textural properties were calculated and also compared with those of CX0-C20 (**Table A2.1.2**). Both samples possess similar micropore features, with A_{BET} equal to 174 and 171 $m^2.g^{-1}$ for CX0-C20 and CVD-BP. The micropore volume V_{DUB}, derived from A_{BET}, was found identical for both samples: 0.07 $cm^3.g^{-1}$. The external surface area S_{ext} was calculated equal to 128 $m^2.g^{-1}$ for CX0-C20 and 147 $m^2.g^{-1}$ for CVD-BP. Both samples appear to share similar pore texture, despite their different nature. Moreover, the pore texture of CVD-BP could also enable homogeneous deposition of the catalytic phase. Thus, based on the XRD diffractogram and N_2 adsorption isotherms collected, this CVD disposal material could be regarded as a potential carbon support, as it combines sufficient porosity with a high degree of surface ordering.

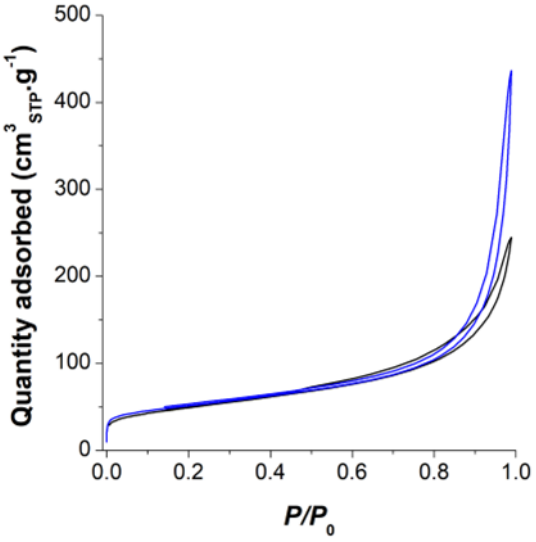

Figure A2.1.2. Nitrogen adsorption-desorption isotherms of CVD-BP (—) and CX0-C20 (—).

Following this preliminary assessment, Pt nanoparticles were deposited on the material *via* the formic acid reduction already described in this chapter. Synthesis parameters were first kept identical, with a target Pt loading of 20 wt.%. This sample is referred to as CVD-BP-Pt20. Nevertheless, it was noticed after the synthesis that the mass increase after Pt deposition was

low. A mass increase of 9.2% was observed, lower than what is observed with CX powders, where a 20 wt.% target loading consistently yields an actual mass increase ranging roughly from 18 to 21% (note that the mass should increase by 25% to reach an actual loading of 20 wt.%). Another synthesis was thus performed with a higher Pt target loading: 30 wt.%. The mass of Pt precursor added during the synthesis was increased accordingly. This sample is referred to as CVD-BP-Pt30. The mass increase after Pt deposition was found to be 18.7%. Once again, the mass increase is lower than expected (a 43% mass increase should be observed, provided a 30 wt.% Pt loading is reached). Nevertheless, this mass increase is comparable to what is obtained with CX powders, suggesting that a similar Pt loading was achieved in this case. Overall, the deposition of Pt nanoparticles on CVD-BP appear more challenging than on CX powders. This behavior may be attributed to the composition of the material. Indeed, the surface of graphene and carbon nanotubes is known to be chemically inert [7,8]. As a result, the bonding energy between the carbon support and the Pt atoms could be low, leading to weak metal-support interactions and difficulties for the Pt nanoparticles to anchor onto the carbon surface.

Table A2.1.2. Textural properties and morphological parameters.

Sample	A_{BET}[a] ($m^2.g^{-1}$)	S_{ext}[b] ($m^2.g^{-1}$) ± 5%	V_{DUB}[c] ($cm^3.g^{-1}$)
CX0-C20	174	128	0.07
CVD-BP	171	147	0.07

[a] A_{BET}: BET surface area, calculated from nitrogen adsorption-desorption isotherms at 77 K.

[b] S_{ext}: external surface area, calculated from nitrogen adsorption-desorption isotherms at 77 K, from t-plot.

[c] V_{DUB}: micropore volume, calculated from calculated from nitrogen adsorption-desorption isotherms at 77 K using Dubinin-Radushkevich equation.

The electrocatalytic performances of both CVD-BP-Pt20 and CVD-BP-Pt30 were evaluated in RDE configuration with the methods already described in this chapter. The results obtained were compared with those of CX0-C20-Pt. The ink composition remained similar, regardless of the Pt loading, namely: 9.9 mg of catalyst was mixed with 1.8 mL of ultrapure Milli-Q® water, 0.7 mL of isopropanol, and 0.25 mL of a Nafion® suspension in water and 1-propanol

(Ion Power, 5 wt.%, 1100 EW). Cyclic voltammetries under argon are displayed in **Figure A2.1.3a**. It was observed that the Pt signal in the hydrogen adsorption and desorption regions (between 0.05 and 0.3 V *vs.* RHE) is significantly lower for CVD-BP-Pt20 and CVD-BP-Pt30 than for CX0-C20-Pt. The capacitive current (at ~0.4 V *vs.* RHE) remain similar for all samples. This indicates that similar carbon surface is seen across samples. This is in agreement with N_2 isotherms which showed that both CVD-BP and CX0-C20 had similar pore texture.

CO stripping measurements are shown in **Figure A2.1.3b**. The presence of two CO oxidation peaks are observed for CVD-BP-Pt20 and CVD-BP-Pt30, contrasting with the single peak observed for CX0-C20-Pt. The first oxidation peak, at higher potential (~0.8 V *vs.* RHE) corresponds to the CO oxidation on isolated Pt nanoparticles. This peak is also observed on CX0-C20-Pt, at a similar potential. The position of this peak is known to depend on the Pt nanoparticle size distribution, particularly when nanoparticles are below 3 nm in diameter [9]. The second peak, at lower potential (~0.65 V *vs.* RHE) corresponds to CO oxidation on Pt agglomerates [10]. Its intensity is comparable with the first peak, both for CVD-BP-Pt20 and CVD-BP-Pt30. This indicates the presence of a large fraction of agglomerated Pt clusters. Values of *ECSA* and d_{CO} were calculated. *ECSA* was found equal to 58, 35 and 101 $m^2.g^{-1}$, while d_{CO} was found equal to 4.8, 7.9 and 2.8 nm for CVD-BP-Pt20, CVD-BP-Pt30 and CX0-C20-Pt, respectively. These results are in agreement with the presence of Pt agglomerates. Moreover, increasing the target Pt loading to 30 wt.% does not significantly increase the Pt signal and only further increases the proportion of these agglomerates, resulting in lower *ECSA* values.

Finally, cyclic voltammetry was performed in O_2-satured electrolyte (**Figure A2.1.3c**). The ORR curves of CVD-BP-Pt20 and CVD-BP-Pt30 are shifted towards lower potentials compared to ORR curve of CX0-C20-Pt, corresponding to a lower catalytic activity towards ORR. The ORR curve of CVD-BP-Pt30 is slightly shifted towards higher potentials compared to that of CVD-BP-Pt20, indicating a higher catalytic activity. Nevertheless, neither catalysts exhibit promising catalytic performances compared to those of CX0-C20-Pt. These performances likely result from the poor deposition of Pt catalyst. Indeed, Pt nanoparticles should be around 3-4 nm in size [11] and should be dispersed homogenously on the carbon support to maximize the catalytic activity. However, Pt nanoparticles deposited on CVD-BP do not meet these assumptions. For this reason, accelerated aging of these catalysts was not performed.

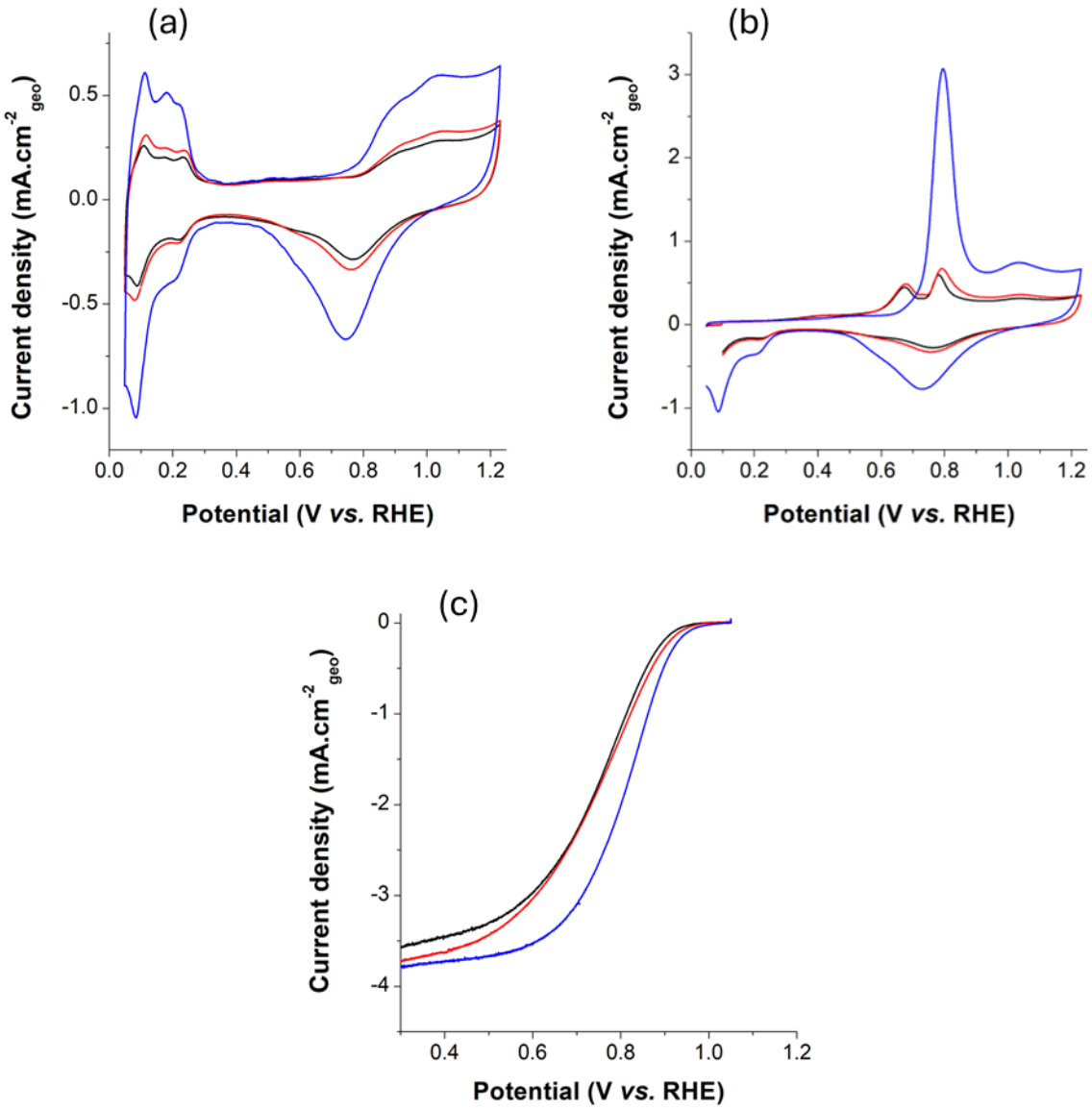

Figure A2.1.3. Electrochemical measurements performed in RDE configuration in 0.5 M H_2SO_4 at 25 ºC. (a) Cyclic voltammetry under argon at a rate of 20 $mV.s^{-1}$, (b) CO electro-oxidation curves at a rate of 20 $mV.s^{-1}$, (c) Cyclic voltammetry under O_2 at a scan rate of 1 $mV.s^{-1}$ and an electrode rotation of 1600 rpm, of CVD-Pt20 (—), CVD-Pt30 (—) and CX0-C20-Pt (—).

In conclusion, the pore texture of this CVD by-product was initially found adequate for deposition of a catalytic phase. However, the highly crystalline nature of the material resulted in a poor deposition of Pt nanoparticles, with the presence of large agglomerates. The presence of agglomerates inevitably decreases the dispersion of the Pt nanoparticles (*i.e.* the fraction of Pt atoms exposed at the surface and active towards ORR). Therefore, the electrochemical

performances were found inferior compared to those of a carbon xerogel-supported catalyst treated in similar conditions. At the current stage, this carbon powder retrieved as a by-product of the CVD treatment cannot be considered a suitable carbon support for PEMFC catalytic layers.

References

[1] T. Belin, F. Epron, Characterization methods of carbon nanotubes: a review, *Materials Science and Engineering: B*, 119 (2005) 105–118.

[2] A. Hussain, Y. Liao, Q. Zhang, E.-X. Ding, P. Laiho, S. Ahmad, N. Wei, Y. Tian, H. Jiang, E.I. Kauppinen, Floating catalyst CVD synthesis of single walled carbon nanotubes from ethylene for high performance transparent electrodes, *Nanoscale*, 10 (2018) 9752–9759.

[3] K.A. Shah, B.A. Tali, Synthesis of carbon nanotubes by catalytic chemical vapour deposition: A review on carbon sources, catalysts and substrates, *Materials Science in Semiconductor Processing*, 41 (2016) 67–82.

[4] Y. Zhang, L. Zhang, C. Zhou, Review of Chemical Vapor Deposition of Graphene and Related Applications, *Accounts of Chemical Research*, 46 (2013) 2329–2339.

[5] C. Jayaseelan, A. Abdul Rahuman, R. Ramkumar, P. Perumal, G. Rajakumar, A. Vishnu Kirthi, T. Santhoshkumar, S. Marimuthu, Effect of sub-acute exposure to nickel nanoparticles on oxidative stress and histopathological changes in Mozambique tilapia, Oreochromis mossambicus, *Ecotoxicology and Environmental Safety*, 107 (2014) 220–228.

[6] Y. Shao, G. Yin, Y. Gao, Understanding and approaches for the durability issues of Pt-based catalysts for PEM fuel cell, *Journal of Power Sources*, 171 (2007) 558–566.

[7] S. Nasiri, C. Greff, K. Wang, M. Yang, Q. Li, P. Moretti, M. Zaiser, Multilayer Structures of Graphene and Pt Nanoparticles: A Multiscale Computational Study, *Advanced Engineering Materials*, 22 (2020).

[8] A. Eftekhari, H. Garcia, The necessity of structural irregularities for the chemical applications of graphene, *Materials Today Chemistry*, 4 (2017) 1–16.

[9] F. Maillard, M. Eikerling, O. V. Cherstiouk, S. Schreier, E. Savinova, U. Stimming, Size effects on reactivity of Pt nanoparticles in CO monolayer oxidation: The role of surface mobility, *Faraday Discussions*, 125 (2004) 357.

[10] F. Maillard, S. Schreier, M. Hanzlik, E.R. Savinova, S. Weinkauf, U. Stimming, Influence of particle agglomeration on the catalytic activity of carbon-supported Pt nanoparticles in CO monolayer oxidation, *Physical Chemistry Chemical Physics*, (2005) 385–393.

[11] M. Peuckert, T. Yoneda, R.A.D. Betta, M. Boudart, Oxygen Reduction on Small Supported Platinum Particles, *Journal of The Electrochemical Society*, 133 (1986) 944–947.

- Chapter 3 -

SYNTHESIS AND STUDY OF THE DURABILITY OF NITROGEN-DOPED CARBON XEROGELS AS CATALYST SUPPORTS FOR PROTON EXCHANGE MEMBRANE FUEL CELL ELECTRODES

Abstract

In Chapter 2, a carbon xerogel (CX) with appropriate pore texture and several Chemical Vapor Deposition (CVD)-treated counterparts were used to prepare Pt/C catalysts for PEM fuel cells. In this chapter, two of these carbon materials, the pristine CX and its analogue treated 20 min by CVD were selected and doped with nitrogen atoms *via* a plasma treatment, using N_2 as a nitrogen precursor. The aim was to introduce anchoring sites for the Pt nanoparticles on the surface of the carbon coating deposited by CVD. The physico-chemical and electrochemical characteristics of the resulting catalysts were assessed. The performances and durability were determined in a three-electrode setup and were also compared to those of their undoped counterparts. Overall, the presence of nitrogen moieties at the surface of the carbon xerogel was confirmed by XPS. It was also demonstrated that the doping treatment has no significant impact on the carbon xerogel pore texture and that the platinum was properly deposited on the carbon support. However, the evolution of the catalytic activity towards Oxygen Reduction Reaction (ORR) remained similar on untreated and N-doped carbon xerogel-supported catalysts and the benefits associated with nitrogen incorporation, particularly improved durability of the active layer upon aging, was not clearly observed.

Contributions

The catalysts synthesis, N_2 adsorption-desorption measurements, XRD analyses and the complete electrochemical characterization of the catalysts were carried out by the PhD candidate. The nitrogen doping *via* plasma treatment was performed by Innovative Coating Solutions, located in Gembloux, while the XPS analysis and data treatment was performed in Université de Namur, with the help of Dr. Cédric Vandenabeele and Driélle Müller da Silva. The elemental analysis was performed by Dr. Jimena Castro-Guttiérez from the team Matériaux Bio-Sourcés in Institut Jean Lamour, located in Epinal, France. TEM micrographs were obtained by the PhD candidate, with the assistance of Dr. Philippe Compère, from Département de Biologie, Ecologie et Evolution in Université de Liège. The SEM photographs were collected by Zoé Deckers, another PhD candidate of the Nanomaterials, Catalysis, Electrochemistry (NCE) group in Université de Liège. Finally, the TGA measurements were performed by Dr. Alexandre F. Léonard from the CARPOR platform in Université de Liège.

3.1. Introduction

A key factor limiting the large-scale deployment of Proton Exchange Membrane Fuel Cells (PEMFCs) is the durability of the catalytic layer. Indeed, during PEMFC long-term operation, the catalytic layer progressively loses its performances, which is associated with degradation phenomena such as Pt nanoparticle coalescence, detachment or Ostwald ripening, as explained thoroughly in the Introduction section [1,2]. These phenomena depend on many variables including the state of the carbon support surface. In particular, the nature of surface functional groups plays a significant role in catalyst-support interactions [3] as nanoparticles poorly anchored to the carbon support migrate faster [4].

In Chapter 1, a carbon layer was deposited by Chemical Vapor Deposition (CVD) onto a pore-texture controlled carbon xerogel (CX) and its subsequent graphitization was performed. The objective was to provide a more ordered carbon surface to limit carbon corrosion during fuel cell operation. This assumption was put to test in Chapter 2. However, it was observed that the CVD treatment alone is insufficient and that additional strategies could be explored to further tailor the CX surface. Indeed, alternative strategies exist to improve the performances and durability of PEMFC active layers. Another common approach consists in modifying the surface chemistry of the carbon support *via* heteroatom doping methods [5].

Among the different heteroatoms, nitrogen stands out as particularly attractive as nitrogen moieties can be beneficial towards metal catalyst deposition on a carbon support. Indeed, the change in charge density induced by nitrogen doping can promote better electrocatalyst deposition, including a higher bonding energy between the Pt and the C atoms [3,6], limiting Pt migration and agglomeration. Nitrogen doping can also lead to a better dispersion of the catalyst onto the surface [7–9]. Moreover, owing to its similar atomic radius with carbon, grafting nitrogen into a carbon matrix enables to induce changes in the electronic environment of the carbon while minimizing the carbon lattice mismatch [10]. A nitrogen doping strategy could thus be applied to a CX to obtain more durable carbon supports [11].

Two main approaches can be considered to introduce nitrogen into a carbon structure [12]. The first approach is *in situ* doping, in which carbon material synthesis and nitrogen incorporation occur at once. In this approach, a nitrogen-rich precursor is directly added to the synthesis mixture. This method is compatible with CX synthesis. In this case, a water-soluble nitrogen precursor, typically melamine, urea, or dicyandiamide, is added to the mix [11,13]. The second approach relies on post-treatments (*i.e. ex situ* doping), where an already-synthesized carbon

material is modified with a N-containing source. In contrast to *in situ* approaches, post-treatments tend to modify only the surface chemistry of the carbon while the bulk remains untouched. A wide variety of post-treatment strategies exist [14]. Nonetheless, N-doping *via* post-treatment is typically achieved by exposing the carbon material to a N-containing source that decomposes at high temperature (> 800 ºC). Common nitrogen sources are ammonia (ammonolysis treatment) [15] or pyridine [16]. Plasma treatments using a NH_3 [17] or N_2 source [18] are also viable options for efficient doping of carbon materials, including CXs [19]. In this thesis, the use of an *ex situ* doping method was preferred. This choice was motivated by two considerations. First, variations in the final pore texture of CXs can be observed across syntheses if distinct formaldehyde aqueous solutions are used over time, even if the pH of the synthesis mixture is kept similar. Thus, to ensure consistency, only one CX with appropriate pore texture was synthesized. Second, in the present case, only nitrogen atoms located at the surface of the CX can play a role in the interactions between the support and the electrocatalyst. Thus, incorporating nitrogen atoms in the bulk of the carbon material is not relevant.

In this Chapter, the pristine carbon xerogel and its analogue treated by CVD for 20 min, synthesized in Chapter 1, were subjected to nitrogen doping *via* plasma treatment in a N_2 atmosphere. This post-treatment method was preferred to the commonly used ammonolysis or plasma treatment with NH_3 source, due to the hazardous nature of ammonia. The plasma process made it possible to achieve controlled levels of nitrogen incorporation. A low N content was obtained for CX, while two distinct moderate N contents were obtained for the CVD-treated xerogel by varying the treatment duration. Pt nanoparticles were then deposited *via* formic acid reduction of a Pt precursor and the catalyst properties, such as the metal loading and Pt nanoparticles size were assessed. Finally, the electrochemical performances and stability upon aging were also evaluated, prior to and after N-doping, in RDE configuration.

3.2. Experimental

3.2.1. Preparation of the N-doped carbon supports

In Chapter 1, a carbon xerogel with an average pore size of 70 nm and BET surface area of 674 $m^2.g^{-1}$, denoted as CX0 hereafter, was synthesized and subjected to a CVD treatment of various durations. This CVD treatment was found to cover the carbon xerogel surface with a partially crystallized layer [20]. Moreover, among the different conditions investigated, the CVD duration of 20 min was found optimal as it did not impair the meso/macropore texture of the

carbon material, essential for diffusion phenomena inside the catalytic layer. The carbon xerogel powder retrieved from this CVD treatment of 20 min is denoted as CX0-C20. The BET surface area of CX0-C20 was found equal to 174 $m^2.g^{-1}$ while the average pore size of the carbon xerogel was 75 nm.

A plasma treatment using a N_2 source was then performed to graft nitrogen atoms on the surface of CX0 and CX0-C20. NH_3-based plasmas are more commonly employed due to their higher reactivity [21]. Nevertheless, a N_2-based plasma was preferred here, as nitrogen gas is significantly safer to handle than ammonia gas. This treatment was performed by Innovative Coating Solutions, a company located in Gembloux (Belgium). The reactors used for plasma treatment have geometries designed to maximize the sample exposure to the plasma, ensuring that as much of the material surface as possible can interact with the plasma during treatment (**Figure 3.1**). The plasma treatment of CX0 (*i.e.* the carbon xerogel not subjected to CVD treatment) was performed in a Rotating Drum Reactor [22]. 0.5 g of CX0 (in powder form) was inserted inside the reactor. A plasma discharge was then obtained *via* the application of a radiofrequency electric field to an Ar/N_2 gas mixture. The applied power was modulated to 200 W for a duration of 30 min. In this type of reactor, contact between the sample and plasma is ensured through rotation of the vessel. This sample is referred to as CX0-N30, in reference with the plasma treatment duration (30 min).

The plasma treatment of CX0-C20 was performed in an Agitating Bed Reactor. 0.5 g of CX0-C20 powder was inserted inside the reactor. In this type of reactor, carbon particles are put in motion inside the reactor vessel to reach the plasma through either a vibrating or stirring system [22,23]. The plasma discharge was obtained with the polarization of N_2 gas *via* a microwave frequency electromagnetic field. The applied power was modulated to 100 W and two different residence durations were chosen: 30 and 120 min. The samples resulting from plasma treatments are labelled according to the treatment duration, CX0-C20-N30 and CX0-C20-N120. It should be noted that carbon xerogel powders were treated in two different reactor configurations: a rotating drum reactor and an agitating bed reactor. This difference is purely circumstantial and arose from the availability of the agitating bed reactor, a more suitable reactor technology for low amounts of powders. Despite this difference, both reactors feature specially designed geometries to expose as much as possible the entire sample surface to the plasma, with a narrow residence time distribution, to achieve homogeneous treatments. Both reactors also possess similar advantages and disadvantages [22]. Namely, they are among the most commonly available types of reactor and possess a high powder load and throughput

suitable for industrial applications. In both these types of reactors, the powder uniformity can be limited, as bulk particles can be less exposed to the plasma than those at the surface ones. Internal reactor designs can help mitigating this issue [23,24]. Considering that mixing is different in both reactor configurations, some variability in the amount of nitrogen inserted at the sample surface is inherently expected. Nonetheless, XPS spectra analyses demonstrate that the nature of the nitrogen species is not markedly impacted by the change of reactor (see **Section 3.3.1**).

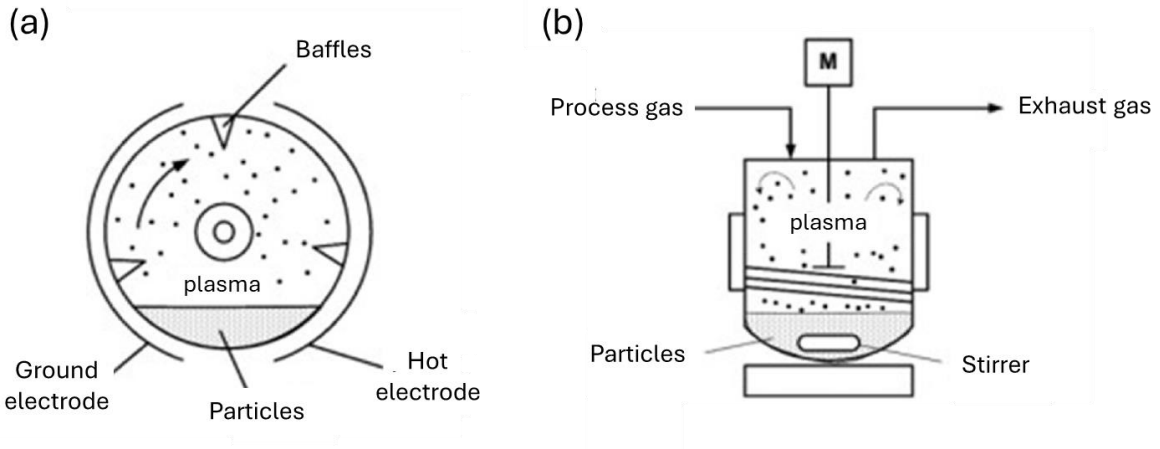

Figure 3.1. Schematic illustration of two reactors configurations: (a) rotating drum reactor and (b) agitating drum reactor, reproduced from [23].

The synthesis of Pt/carbon xerogel catalysts was then performed through the reduction of Pt^{4+}, from $H_2PtCl_6.6H_2O$ platinum precursor, using formic acid as a reductant. The synthesis procedure is identical to the one described the **Section 2.2.1** of Chapter 2. Formic acid reduction is a simple one-step method to deposit homogeneously small Pt nanoparticles on carbon xerogels without producing Pt aggregates [25,26]. The carbon xerogel-supported catalysts retrieved from the Pt deposition step are referred to as CX0-Pt, CX0-C20-Pt, CX0-N30-Pt, CX0-C20-N30-Pt and CX0-C20-N120-Pt. CX0-Pt and CX0-C20-Pt were already evaluated as a support for electrocatalyst in Chapter 2, but are also presented here to allow for a fair comparison between the nitrogen-doped CXs and their undoped counterparts.

3.2.2. Physicochemical characterization

X-ray photoelectron spectroscopy (XPS) analysis was directly performed on the carbon xerogels to assess the quantity of species, and especially nitrogen, present at the carbon surface (<10 nm in depth). XPS measurements were done using a ThermoFisher K-Alpha photoelectron spectrometer. The sample powders were deposited onto double-sided copper tape. A monochromatized Al Kα line (1486.6 eV) served as the photon source. Survey spectra and high-resolution spectra were recorded at pass energies of 150 eV and 20 eV, respectively, with 3 scans for survey spectra and 20 scans for high-resolution spectra, using a 250 μm diameter X-ray spot. An electron flood gun was activated during analysis to prevent charging. Data were analyzed with Thermo Avantage software (Version 6.6.0). X-ray photoelectron spectrometry (XPS) analysis was used to probe the atomic percentages of different species (C, N, O). Samples were also characterized after Pt deposition with Pt spectra to verify whether the Pt deposition synthesis impacts significantly the N atoms.

Elemental analysis of the pristine and N-doped carbon xerogels was performed to investigate their bulk composition, prior to the metal catalyst deposition. Elemental analysis was performed in a Vario EL Cube analyzer (Elementar) to measure the bulk C, H, N and O contents. Prior to measurements, the samples were dried overnight at 105 °C to remove moisture. Then, a small amount of material (~2 mg) was placed in the equipment to be burned in a furnace from which the gas was separated using trapping and chromatographic columns. A thermal conductivity detector quantified the gases, from which carbon, hydrogen and nitrogen contents can be calculated. The oxygen content was measured separately in another column using a similar procedure.

X-Ray Diffraction (XRD), Scanning Electron Microscopy (SEM), Transmission Electron Microscopy (TEM), ThermoGravimetric Analysis (TGA) and N_2 adsorption-desorption measurements were also used in this chapter to obtain properties of the nitrogen-doped carbon xerogels and corresponding catalysts. The equipment and procedures used are identical as those described in details in Chapters 1 and 2, unless otherwise stated. The results were also compared to those previously obtained for CX0, CX0-Pt, CX0-C20, and CX0-C20-Pt in the previous two chapters. N_2 adsorption-desorption was used to determine the specific surface area (A_{BET}) using the Brunauer, Emmett and Teller (BET) equation, selecting in each case the relative pressure range according to the Rouquerol's criterion [27]. The micropore volume, V_{DUB}, was also

calculated using the Dubinin-Radushkevich equation and the external surface area of the carbon nodules, S_{ext}, was obtained through the t-plot method.

XRD diffractograms were used to retrieve the lateral crystallite size (L_a), stacking height (L_c) of graphenic domains of carbon xerogels and the crystal size of Pt nanoparticles (d_{XRD}). L_a, L_c and d_{XRD} were calculated from Scherrer's equation [28] using the carbon 10 and (002) and the platinum Pt(111) diffraction peaks respectively:

$$d = \frac{k\lambda}{\beta\cos(\theta)} \tag{3.1}$$

where k is a shape factor without dimension, equal to 1.84 for L_a and 0.89 for d_{XRD} and L_c [29]. λ is the X-ray wavelength ($\lambda_{K\alpha}$ = 0.15418 nm), β is the Full Width at Half Maximum (FWHM) and θ is the Bragg angle (º). Moreover, the interlayer spacing $d_{(002)}$ corresponding to the distance between two layers of graphene was also calculated from XRD diffractograms using Bragg's law [30]:

$$d_{(002)} = \frac{\lambda}{2\sin(\theta)} \tag{3.2}$$

where θ is the Bragg angle (º) of the C(002) peak.

SEM was employed to observe the morphology of CX0, CX0-C20 and CX0-C20-N120. TGA measurements under air were performed on the catalysts to obtain the actual amount of Pt deposited on the carbon samples, as a comparison to the target Pt loading, by burning the carbon and measuring the remaining mass. Finally, TEM micrographs were obtained for all catalysts to determine the arithmetic average diameter, d_{TEM}, of the Pt nanoparticles calculated on a sufficiently large number of Pt nanoparticles (> 50). The surface-weighed (d_S) and volume-weighed (d_V) diameters of the nanoparticles were calculated as:

$$d_s = \sum \frac{n_i d_i^3}{n_i d_i^2} \tag{3.3}$$

$$d_V = \sum \frac{n_i d_i^4}{n_i d_i^3} \tag{3.4}$$

where n_i is the number of particles of diameter d_i.

3.2.3. Electrochemical characterization

The electrochemical characterization method is identical to the one explained in details in Chapter 2, unless otherwise stated.

Materials

Catalysts underwent characterization using a Rotating Disk Electrode (RDE) using a three-electrode setup with a 5-mm diameter glassy carbon as working electrode, a platinum grid as counter-electrode and a saturated calomel electrode (SCE) as a reference electrode. All voltages are reported *versus* the reversible hydrogen electrode (RHE) hereafter, with values corrected to account for the change of reference.

Catalytic layer preparation

Catalytic inks of all the catalysts were prepared as described in **Section 2.2.3** of Chapter 2, with a Pt loading of 33 $\mu g_{Pt}.cm^{-2}_{geo}$ on the working electrode, and a Nafion®-to-Carbon (*N/C*) mass ratio of 1.4.

For CX0-C20-N30-Pt and CX0-C20-N120-Pt samples, a different ink composition was used. This choice was motivated by poor active layer deposition when using the usual recipe. Indeed, when water and isopropanol mix was used as a solvent, very heterogeneous and irregular deposits were obtained after the sintering step. It was also observed that the active layer was not deposited on the entire glassy carbon surface. Even after extended sonication of the ink (>1 h) was performed to improve mixing, the active layer still did not uniformly cover the glassy carbon surface. The poor deposition of the active layer led to inconsistent catalytic activity measurements. To address this issue, N-methyl-2-pyrrolidone (NMP) was used as a solvent instead of water and isopropanol. On the one hand, the handling of NMP-based inks is far more hazardous than water-based inks. On the other hand, however, it produced more homogeneous active layers and thus yielded more reproducible electrochemical measurements. Trials and observations that motivated the use of NMP are presented in Annex 3.1. Thus, for CX0-C20-N30-Pt and CX0-C20-N120-Pt samples, catalytic inks were prepared by mixing 9.9 mg of catalyst with 1 mL of NMP and 0.25 mL of Nafion®. Note that the *N/C* ratio was maintained identical across all samples.

Prior to electrochemical characterization, a few drops of the electrolyte (H_2SO_4, 0.5 M) were deposited onto the active layer and put under vacuum to remove the air trapped in the active layer. This step is performed to ensure complete wetting of the active layer by the electrolyte.

A comprehensive assessment of the catalyst performances and durability before and after surface modification of the support was subsequently performed on RDE, using 0.5 M H_2SO_4 as electrolyte. Moreover, Accelerated Stress Tests (AST) were performed and CO stripping and Oxygen Reduction Reaction (ORR) measurements under O_2 atmosphere were obtained for each aging step.

CO stripping

CO stripping measurements were used to determine the ElectroChemically active Surface Area (*ECSA*) of platinum [31]. The *ECSA* was determined using the Faraday charge of the CO electro-oxidation peak between 0.65 and 1.23 V *vs.* RHE, assuming that a complete monolayer of CO adsorbed on Pt requires 4.2 $C.m^{-2}_{Pt}$ for being oxidized [32].

The *ECSA* and the CO equivalent nanoparticle diameter, d_{CO}, were determined as:

$$ECSA = \frac{Q_H}{4.2\ L\ A} \tag{3.5}$$

$$d_{CO} = \frac{6}{\rho_{Pt}\ ECSA} \tag{3.6}$$

where Q_H is the integral of the charge of the CO electro-oxidation peak (C), 4.2 $C.m^{-2}_{Pt}$ is the theoretical adsorption charge density required to oxidize one complete monolayer of CO adsorbed onto the Pt surface, L is the loading of Pt of the working electrode ($g_{Pt}.m^{-2}_{geo}$), A is the surface area of the electrode (m^2_{geo}), equal to 1.9635×10^{-5} m^2 and ρ_{Pt} is the density of platinum (21.45×10^6 $g.m^{-3}$).

The double layer capacity per mass of carbon C_{dl} (in $F.g^{-1}_C$) was also be calculated:

$$C_{dl} = \frac{i_{capa}}{m_C v} \tag{3.7}$$

where i_{capa} is the capacitive current (A), taken in the area 0.4-0.5 V *vs.* RHE, v is the scan rate ($V.s^{-1}$), and m_C (g) is the mass of carbon present in the active layer.

Measurement of the activity for the oxygen reduction reaction

The catalytic activity towards ORR of the different catalysts was measured in O_2-saturated electrolyte. To this end, the potential was increased to 1.05 V *vs.* RHE and decreased back to 0.3 V *vs.* RHE at a scan rate of 1 $mV.s^{-1}$. To get rid of the capacitive current originating from the large specific surface area of the carbon supports, the background curves performed under

the same conditions under Ar-saturated electrolyte. The catalytic activity was expressed as the specific activity (*SA*) and mass activity (*MA*). ORR measurements were also recorded at different working electrode rotation speeds, beginning at 400 rpm then 900, 1600 and 2500 rpm; all the experimental curves are provided in Annex 3.2.

SA ($A.m_{Pt}^{-2}$) and *MA* ($A.g_{Pt}^{-1}$) were obtained from ORR curves plotted at 1600 rpm, using the following equations:

$$SA = \frac{i}{ECSA\ L} \tag{3.8}$$

$$MA = \frac{i}{L} \tag{3.9}$$

As noted in Chapter 2, due to the large thicknesses and developed porosity of carbon xerogels, currents were compared at higher potentials (0.95 V *vs.* RHE) than those commonly reported in the literature (0.9 V *vs.* RHE), in accordance to a previous study [33].

Accelerated Stress Tests

After assessing the *Beginning of Life* (*BoL*) performances, Accelerated Stress Tests (AST) were performed, identically with the AST performed in Chapter 2. First, the catalytic layer was subjected to 5,000 voltammetry cycles. Cycles were performed between 0.6 V and a fixed upper potential of 1.0 V *vs.* RHE at 100 $mV.s^{-1}$, while the cell was kept at 80 ºC under constant Ar bubbling. After the 5,000 cycles, the electrolyte solution was renewed and the cell was allowed to cool down. The catalytic layer was then characterized again using the same CO stripping and ORR measurements, corresponding to the *Middle of Life* (*MoL*) status. Finally, the catalytic layer underwent 15,000 more voltammetry cycles, in the same conditions as the first 5,000 cycles. Eventually the electrolyte solution was replaced again and the cell cooled down. The catalytic layer was electrochemically characterized a third time at ambient temperature, corresponding to the *End of Life* (*EoL*) of the material. To ensure reproducibility of the measurements, aging and corresponding characterization was completed on a minimum of two active layers.

3.3. Results and discussion

3.3.1. Physicochemical properties of carbon materials

CX0-C20 and CX0-C20-N120 were first observed and compared with a Scanning Electron Microscope (SEM) to distinguish any impact of the plasma treatment (**Figure 3.2**). CX0 was also included for reference. The network of covalently bonded carbon xerogel nodules is observed in all cases. One can see that the plasma treatment does not lead to significant changes in the carbon structure, in agreement with previous studies conducted on similar carbon xerogel materials [20,34].

The atomic composition of carbon xerogels subjected to nitrogen doping was investigated with XPS and elemental analysis. The results are summarized in **Table 3.1**. Regarding elemental analysis, the total (bulk) nitrogen quantity was found equal to 0.4 wt.% for CX0-N30, 0.9 wt.% for CX0-C20-N30 and 1.9 wt.% for CX0-C20-N120. A small decrease in carbon content is observed following N-doping, which can be attributed to the partial substitution by nitrogen atoms during the plasma treatment.

Table 3.1. Elemental composition from XPS and elemental analysis.

Sample	*XPS* **Atomic percentage** (at.%) ± 0.5			*Elemental analysis* **Atomic percentage** (at.%) ± 0.5		
	Carbon	**Oxygen**	**Nitrogen**	**Carbon**	**Oxygen**	**Nitrogen**
CX0	96.8	3.2	Not detected	97.5	2.5	<0.1
CX0-N30	94.1	4.4	1.5	94.9	4.8	0.3
CX0-C20	98.3	1.7	Not detected	98.8	1.2	<0.1
CX0-C20-N30	93.1	3.7	3.2	95.6	3.5	0.9
CX0-C20-N120	88.5	4.3	7.2	94.4	3.8	1.8

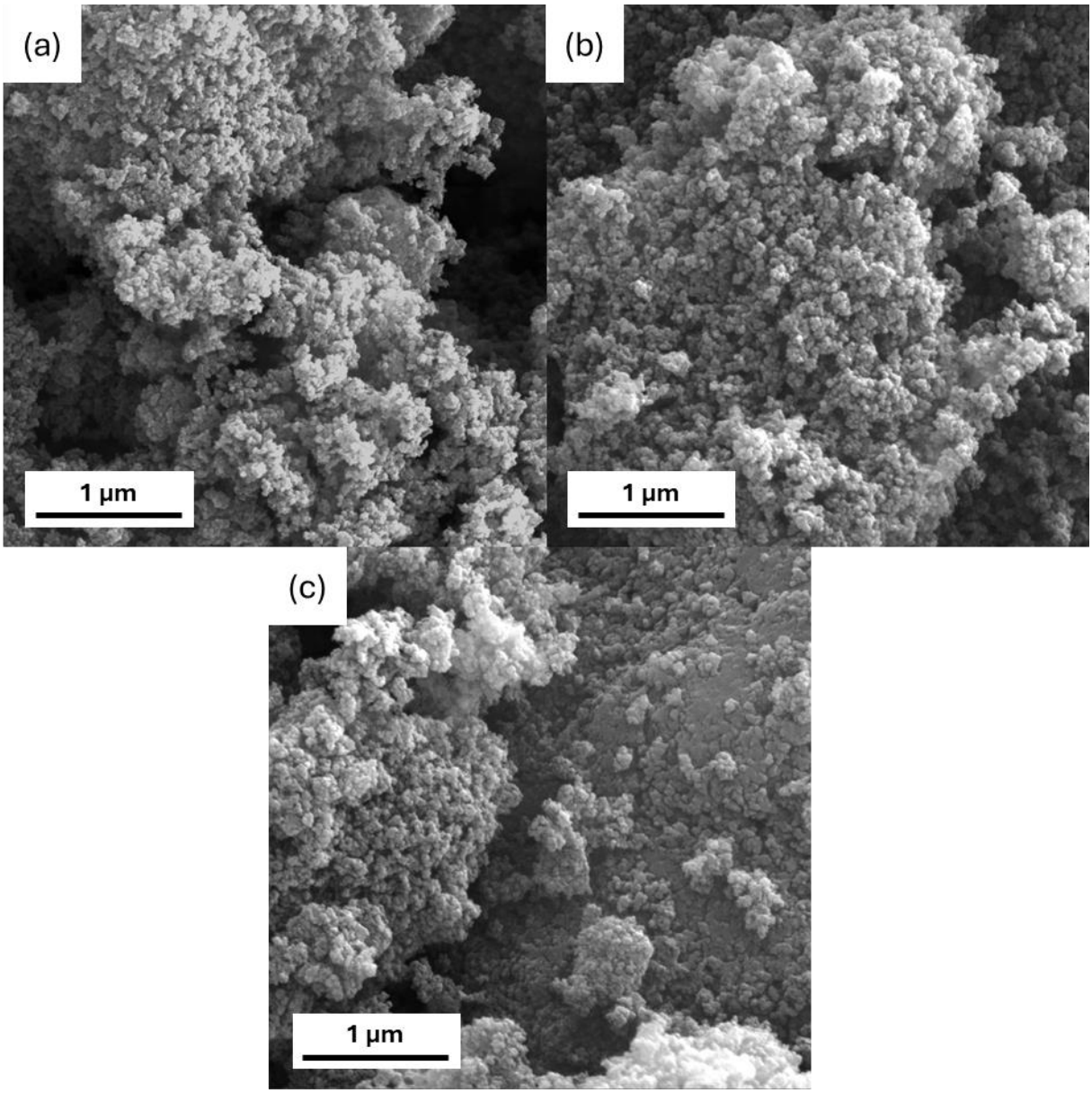

Figure 3.2. SEM images of (a) CX0, (b) CX0-C20 and (c) CX0-C20-N120 carbon supports.

A visual representation of the most common configurations that nitrogen can take in a carbon lattice is provided in **Figure 3.3**. No significant presence of N was observed for the samples CX0 and CX0-C20, *i.e.* before doping by plasma treatment. For the pristine CX0, processed in a rotating drum reactor with a plasma power of 200 W for 30 min, 1.5 at.% of N was detected *via* XPS. CX0-C20 was also processed using an agitating bed reactor with a plasma power of 100 W with two residence durations in the reactor of 30 and 120 min. The shorter treatment, CX0-C20-N30, yielded 3.2 at.% while the longer one, CX0-C20-N120, yielded 7.2 at.% of nitrogen on the carbon surface. These values follow the trend already observed in elemental

analysis: the N content is lowest for CX0-N30 and highest for CX0-C20-N120. Moreover, these results show that the amount of nitrogen can be partially controlled by adjusting the treatment duration in the reactor. The nitrogen contents obtained are consistent with values commonly reported in the literature. While various nitrogen-doping methods exist, nitrogen contents between 1 and 10 at.% are typically observed [35–37]. A nitrogen content higher than 8-10 at.% could even prove detrimental due to the increased electrical resistance, rendering the material less suitable for electrochemical applications [38]. In contrast, a nitrogen content below 1 at.% is generally considered insufficient to induce discernable changes between the carbon support and the catalyst [39].

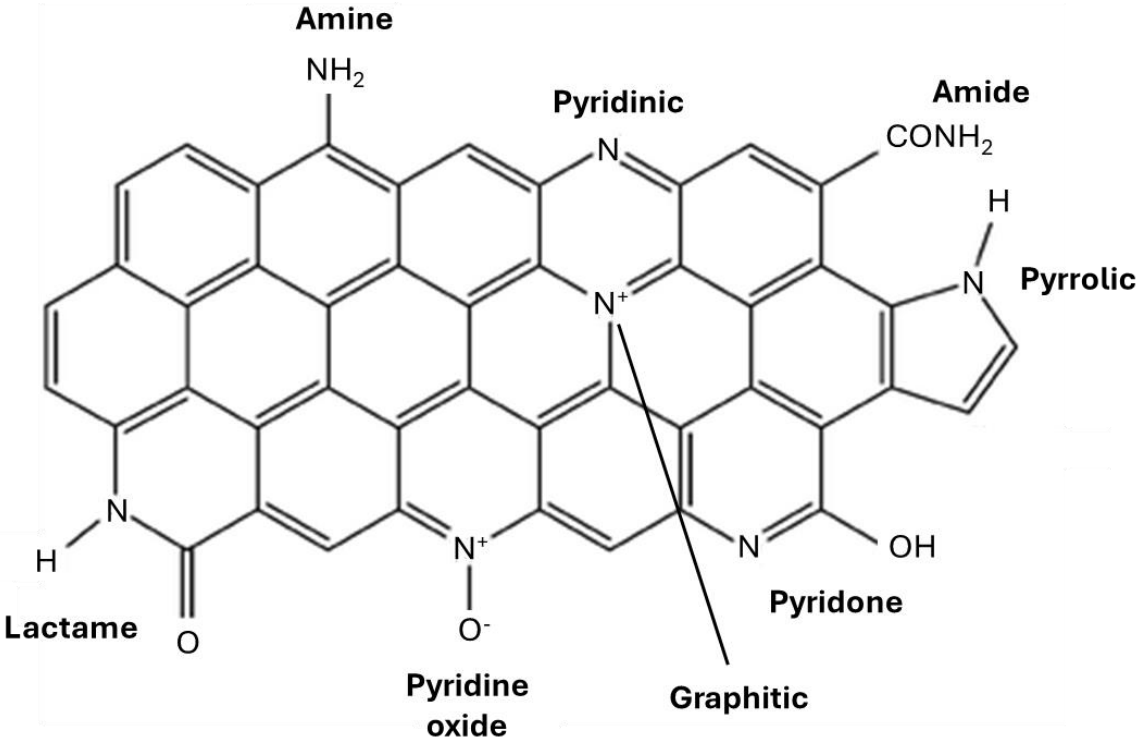

Figure 3.3. Schematic representation of the most common configurations of nitrogen in a sp^2 carbon lattice.

These results indicate that a suitable amount of nitrogen can be incorporated *via* N_2 plasma treatment. Plus, the use of an agitating bed reactor appears to yield higher nitrogen contents. However, given the difference in substrate nature between the surface of CX0 (hard carbon) and CX0-C20 (graphitizable and more ordered, see Chapter 1), and the difference in plasma power (200 W for CX0, 100 W for CX0-C20), it is not possible to determine whether this

observation arises from the reactor configuration itself or from the nature of the carbon substrate. Due to time constraints, CX0 could not be processed again in the same reactor and experimental conditions as CX0-C20.

The N1s XPS spectra confirm that nitrogen was successfully incorporated into the carbon xerogel surface structure. The broad N1s peak, displayed in **Figure 3.4**, hints at the presence of multiple nitrogen moieties. Thus, the spectra were also deconvoluted to identify which nitrogen functional groups are present [40]. These deconvolutions were performed as accurately as possible. Nevertheless, considering the low intensity of the N signal on certain samples (*e.g.* for CX0-N30), slight deviations in the results obtained from the peaks deconvolution cannot be excluded. Notwithstanding, deconvolution of the spectra showed the presence of graphitic, pyridinic, and pyrrolic nitrogen species, along with a minor contribution from pyridinic nitrogen oxides (**Table 3.2**). For CX0-N30, the most common type is pyrrolic nitrogen, representing 51% of the nitrogen fraction detected, closely followed by pyridinic nitrogen (41%). The quantity of graphitic nitrogen is lower (8%). For CX0-C20-N30 and CX0-C20-N120, the same trend is observed: a large quantity of pyrrolic and pyridinic nitrogen is observed, namely 42 and 41% of pyrrolic nitrogen, and 46 and 50% of pyridinic nitrogen for CX0-C20-N30 and CX0-C20-N120, respectively. The quantity of graphitic nitrogen is also lower, with 12 and 9% for CX0-C20-N30 and CX0-C20-N120, respectively. No significant presence (*i.e.* > 0.5 at.%) of nitrogen oxide species (*i.e.* pyridinic N-oxide) that could form after exposure of the carbon to air [41], was observed. The proportion of each nitrogen species remains fairly consistent across all samples. Thus, the overall nitrogen amount did not drastically alter the nature of the incorporated nitrogen groups.

Table 3.2. Deconvolution of XPS N1s spectra.

Sample	**Fraction of N functional groups** (%) ± 4		
	Pyridinic	Pyrrolic	Graphitic
CX0-N30	41	51	8
CX0-C20-N30	46	42	12
CX0-C20-N120	50	41	9

Pyridinic-N corresponds to sp^2 hybridized nitrogen atoms located at the edge of a graphene plane, where nitrogen forms two bonds with adjacent carbon atoms. This functional group donates one electron to the conjugated π bond system. It also provides Lewis basicity due to its lone electron pair [42]. When this pyridinic species is oxidized, it is referred to as pyridinic nitrogen oxide. Pyrrolic-N refers to sp^3 hybridized N atoms incorporated into a heterocyclic ring of five carbons. These specific atoms donate two electrons to the delocalized π system [43]. Finally, graphitic N refers to nitrogen atoms that substitute carbon atoms within the graphene lattice. They also donate two electrons to the delocalized π-system [44]. The positive effect of pyridinic, pyrrolic and graphitic nitrogen towards ORR is well established [45]. It is however difficult to disentangle the exact contribution of each nitrogen-containing functional group. As a result, it is challenging to identify which ones should be prioritized to achieve a targeted effect.

N_2 adsorption-desorption isotherms were collected and are shown in **Figure 3.5**. Textural properties calculated from these isotherms are gathered in **Table 3.3**. All materials present a type I + II isotherm, according to the IUPAC classification. The adsorbed quantity rises quickly at low relative pressure, indicating the presence of micropores. This type of isotherms shows the dual porosity of carbon xerogels, which are both microporous but also meso/macroporous materials. The shape of all isotherms remains similar at large relative pressure ($P/P_0 > 0.9$), suggesting that neither CVD nor plasma treatment affects the structural integrity and accessibility of the meso/macropores.

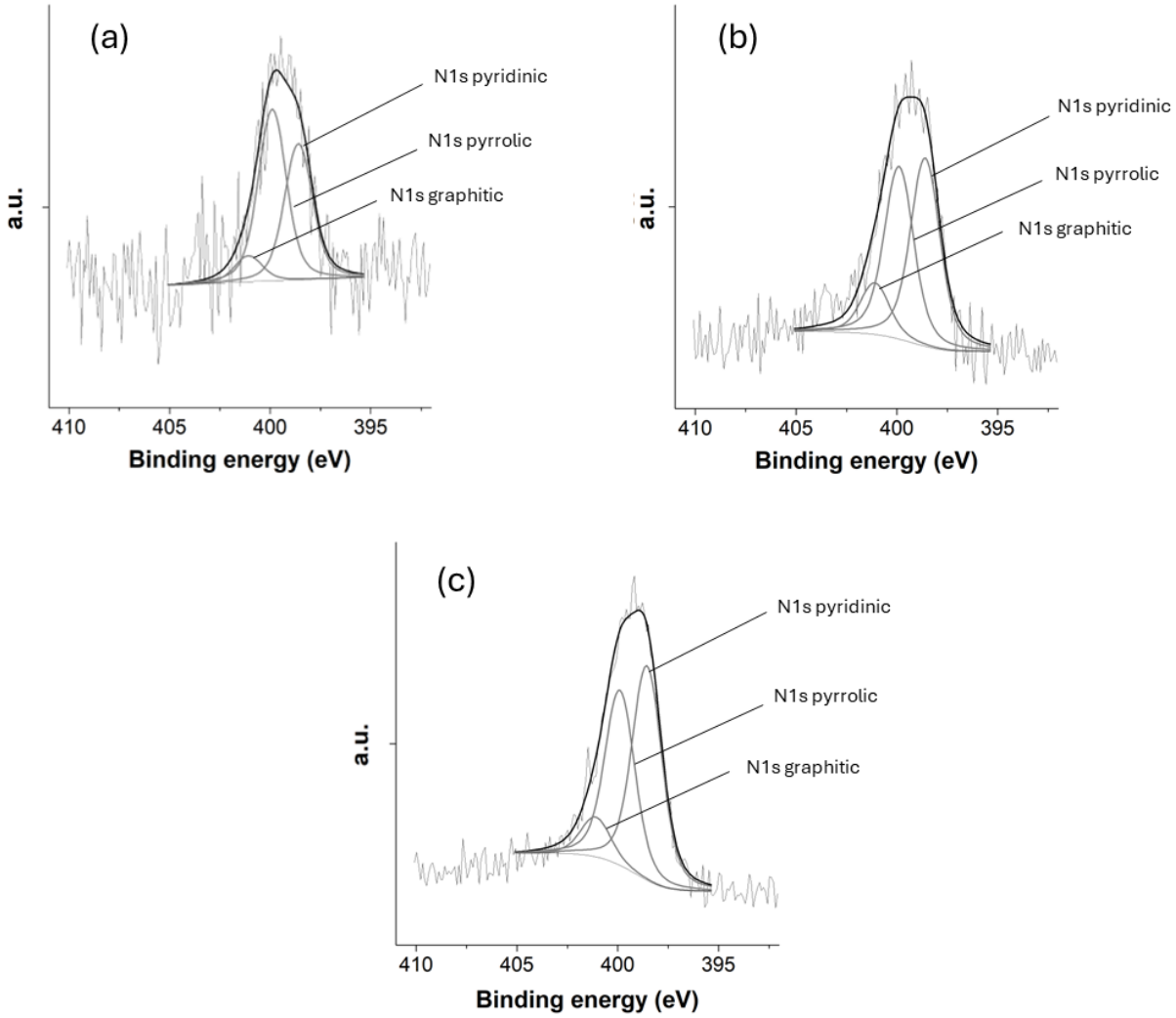

Figure 3.4. Deconvolution of N1s XPS spectra of (a) CX0-N30, (b) CX0-C20-N30, and (c) CX0-C20-N120.

The BET surface area decreases from 674 (CX0) to 174 $m^2.g^{-1}$ (CX0-C20) upon CVD treatment. This observation was discussed in details in Chapter 1 and was attributed to the covering of the micropores by the CVD carbon layer. The BET surface area remains practically unchanged upon N-doping treatment: A_{BET} values of 674 and 656 $m^2.g^{-1}$ are observed for CX0 and CX0-N30, respectively. A slight increase is observed for CX0-C20 after plasma treatment, from 174 to 200 $m^2 \cdot g^{-1}$ for CX0-C20 and CX0-C20-N30, respectively, although this variation is too small to suggest any significant pore blockage or restructuring. Finally, the BET surface area remains also nearly constant between CX0-C20-N30 and CX0-C20-N120, despite different plasma treatment durations (30 and 120 min), with 200 and 203 $m^2.g^{-1}$, respectively.

Similar observations can be drawn from the external surface area values, S_{ext}, (*i.e.* the surface excluding micropores within the nodules) estimated with the t-plot method. Comparing CX0 and CX0-C20, S_{ext} decreases from 201 to 128 $m^2.g^{-1}$. This observation was also already discussed in Chapter 1 and was attributed to a partial clogging of the meso/macropores by the CVD-deposited layer [34]. Upon N-doping, S_{ext} equals 201 to 204 $m^2.g^{-1}$ for CX0 and CX0-N30, respectively, and goes from 128 to 142 and 147 $m^2.g^{-1}$, for CX0-C20, CX0-C20-N30 and CX0-C20-N120. These changes are also minor and, as previously observed from BET surface areas, N-doping does not seem to alter significantly the pore texture of the carbon xerogel materials.

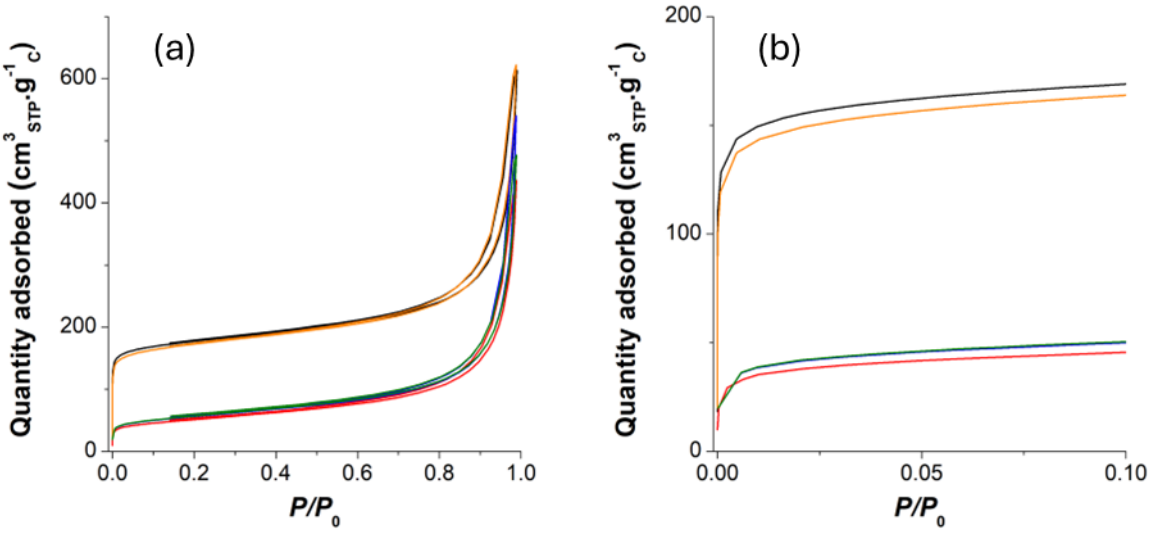

Figure 3.5. Pore texture characterization of the carbon supports. (a) N_2 adsorption-desorption isotherms of CX0 (—), CX0-N30 (—), CX0-C20 (—), CX0-C20-N30 (—) and CX0-C20-N120 (—). (b) Focus on the low relative pressure region.

Table 3.3. Textural properties and morphological parameters of the carbon supports.

Sample	A_{BET}[a] ($m^2.g_C^{-1}$) ± 5%	V_{DUB}[b] ($cm^3.g_C^{-1}$) ± 0.01	S_{ext}[c] ($m^2.g_C^{-1}$) ± 5%
CX0	674	0.26	201
CX0-N30	656	0.25	204
CX0-C20	174	0.07	128
CX0-C20-N30	200	0.08	142
CX0-C20-N120	203	0.08	147

[a] A_{BET}: BET specific surface area, calculated from nitrogen adsorption-desorption isotherms at 77 K.

[b] V_{DUB}: micropore volume, calculated from nitrogen adsorption-desorption isotherms at 77 K using the Dubinin-Radushkevich equation.

[c] S_{ext}: external surface area, calculated from nitrogen adsorption-desorption isotherms at 77 K using the t-plot method.

The evolution of the carbon support crystallinity was also observed by XRD, before and after nitrogen doping treatment (see **Figure 3.6**). Common peaks of highly disordered carbons can be observed. A broad and intense peak is observed around 23° and corresponds to the C(002) reflection. The Bragg angle and broadness of this peak is typical of materials with a large degree of amorphousness, containing only short-range graphitic domains. A second peak of less intensity around 44° corresponds to the carbon 10 reflection (sometimes noted (10l), as in reference [46]). Crystalline parameters are gathered in **Table 3.4**. As was observed in Chapter 1, the CVD layer deposited exhibits a slightly higher degree of organization compared to the pristine carbon xerogel. Moreover, it was also evidenced in Chapter 1, after a post-treatment treatment at 1,500 ºC, that this carbon coating is graphitizable, contrasting with the inherent nature of carbon xerogels, considered as hard carbons [47].

Upon nitrogen doping, L_a increases slightly from 3.45 to 3.53 nm while L_c goes from 0.99 to 1.02 nm for CX0 and CX0-N30, respectively. $d_{(002)}$ decreases from 0.405 to 0.398 nm. For CVD-treated xerogels, L_a goes from 3.81 to 3.61 nm and L_c goes from 1.03 to 1.01 nm for CX0-C20 and CX0-C20-N120, respectively. These variations are minor and fall within the experimental margin of error. Overall, the N-doping plasma treatment does not significantly alter the structural ordering of the carbon matrix. XRD measurement was not performed on

CX0-C20-N30 due to insufficient material quantity. Nevertheless, as just observed with CX0-C20-N120, nitrogen doping does not induce changes to the carbon structure.

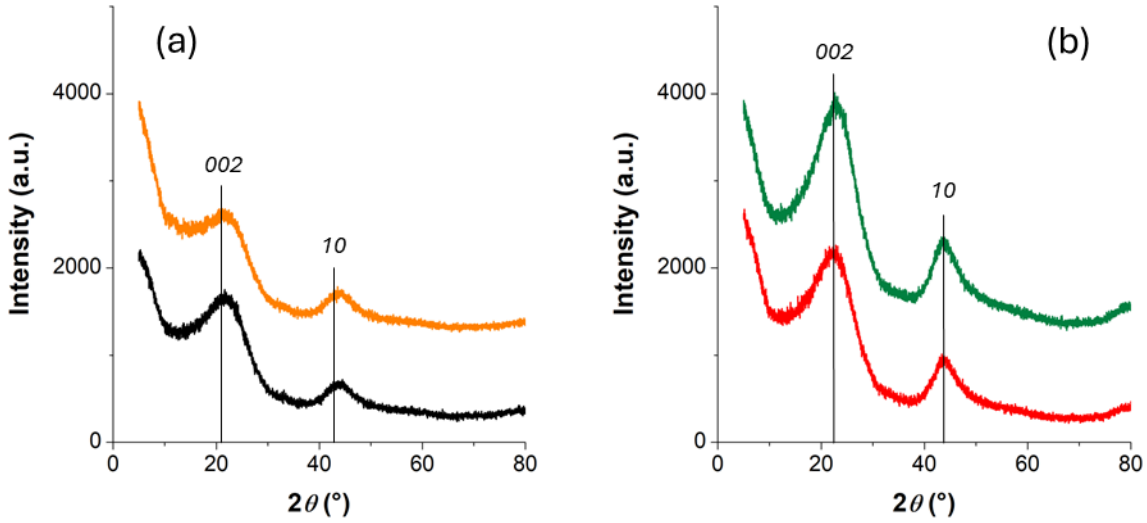

Figure 3.6. X-ray diffractograms of the carbon supports: (a) CX0 (—) and CX0-N30 (—), and (b) of CX0-C20 (—) and CX0-C20-N120 (—). The diffractograms are shifted vertically for readability. XRD measurement was not performed on CX0-C20-N30 due to insufficient material quantity.

Table 3.4. Crystalline parameters determined by X-ray diffraction.

Sample	L_a[a] (nm) ± 0.1	L_c[b] (nm) ± 0.1	$d_{(002)}$[c] (nm) ± 0.004
CX0	3.45	0.99	0.405
CX0-N30	3.53	1.02	0.398
CX0-C20	3.81	1.03	0.393
CX0-C20-N120	3.61	1.01	0.391

[a] L_a: Lateral crystallite size, calculated from Scherrer's equation.

[b] L_c: Crystallite stacking length, calculated from Scherrer's equation.

[c] $d_{(002)}$: Graphene interlayer distance, calculated from Bragg's law.

Note: Crystalline parameters were not obtained on CX0-C20-N30 due to insufficient material quantity to perform XRD measurement.

3.3.2. Physicochemical properties of catalysts

Pt nanoparticles were deposited on the different carbon supports (pristine, CVD-treated, N-doped, and CVD-treated + N-doped) v*ia* a formic acid reduction at 80 ºC, using $PtCl_6^{2-}$ anion as a Pt source. TGA under air was then performed to evaluate the actual Pt content in the catalyst. TGA curves are provided in **Figure 3.7**. The remaining mass observed above 600 ºC accounts for the quantity of Pt. Note that the measured Pt content could be overestimated due to the formation of Pt oxides, already observed at ambient temperature with XPS measurements. It should however be mentioned that the decomposition of these oxides is generally observed above 300 ºC [48]. Still, assuming the most extreme case where all Pt is converted into PtO_2 above 600 °C, the resulting overestimation of Pt content would not exceed 14%. After analysis, the Pt content was found to vary between 15.8 wt.% (for CX0-N30-Pt) and 19.0 wt.% (for CX0-C20-Pt), with an average value commonly hovering around 17.2 wt.% (**Table 3.5**). This value is in accordance to other Pt deposition syntheses performed through formic acid reduction [25,26].

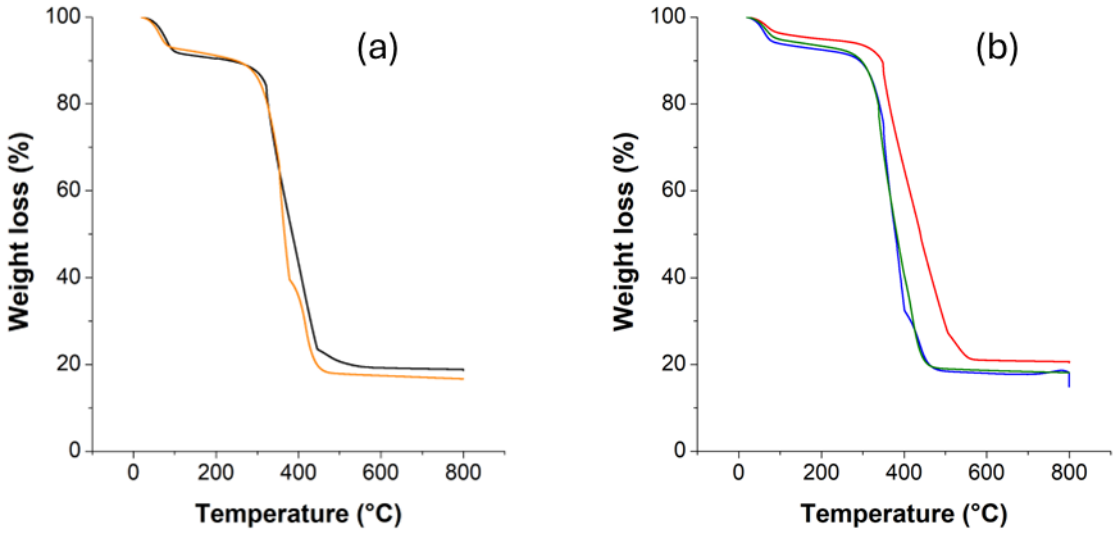

Figure 3.7. TGA curves of (a) CX0-Pt (—) and CX0-N30-Pt (—), (b) CX0-C20-Pt (—), CX0-C20-N30-Pt (—) and CX0-C20-N120-Pt (—).

Table 3.5. Catalysts properties determined by different analyses.

Catalyst	Pt_{TGA}[a] (wt.%)	d_{TEM}[b] (nm)	σ[c] (nm)	d_S[d] (nm)	d_V[d] (nm)	d_{XRD}[e] (nm) ± 0.3
CX0-Pt	17.4 ± 1.3	3.4	0.4	3.5	3.5	2.6
CX0-C20-Pt	19.0 ± 1.4	3.6	0.6	3.7	3.9	3.0
CX0-N30-Pt	15.8 ± 1.2	2.8	0.5	3.0	3.1	3.0
CX0-C20-N30-Pt	16.7 ± 1.3	3.5	0.6	3.8	3.9	2.7
CX0-C20-N120-Pt	16.9 ± 1.3	3.2	0.4	3.2	3.3	2.6

[a] Pt_{TGA}: mass fraction remaining at the end of TGA experiment.

[b] d_{TEM}: average arithmetic diameter of nanoparticles estimated from TEM micrographs.

[c] σ: standard deviation associated with d_{TEM}.

[d] d_S and d_V: surface- and volume-weighted average diameter of nanoparticles calculated from **Equations (3.3)** and **(3.4),** obtained from TEM micrographs.

[e] d_{XRD}: average size of crystallites calculated from X-ray diffraction peaks from **Equation (3.1)**.

After successful deposition of Pt confirmed by TGA, the obtained nanoparticles were observed by TEM. As shown on TEM micrographs in **Figure 3.8** and **Figure 3.9**, Pt nanoparticles are well distributed onto the carbon xerogels. For all the samples, the mean Pt diameter, d_{TEM}, was calculated over a number of nanoparticles > 50. For the catalyst supported on the pristine xerogel, CX0-Pt, the average diameter is 3.4 nm, whereas for CX0-N30-Pt it decreases to 2.8 nm. For CVD-treated xerogels, d_{TEM} was calculated equal to 3.6 nm for CX0-C20-Pt and slightly decreases to 3.5 nm and 3.2 nm for CX0-C20-N30-Pt and CX0-C20-N120-Pt, respectively. Similarly, a decrease in d_{TEM} is observed after nitrogen doping but no significant change in size distribution is observed.

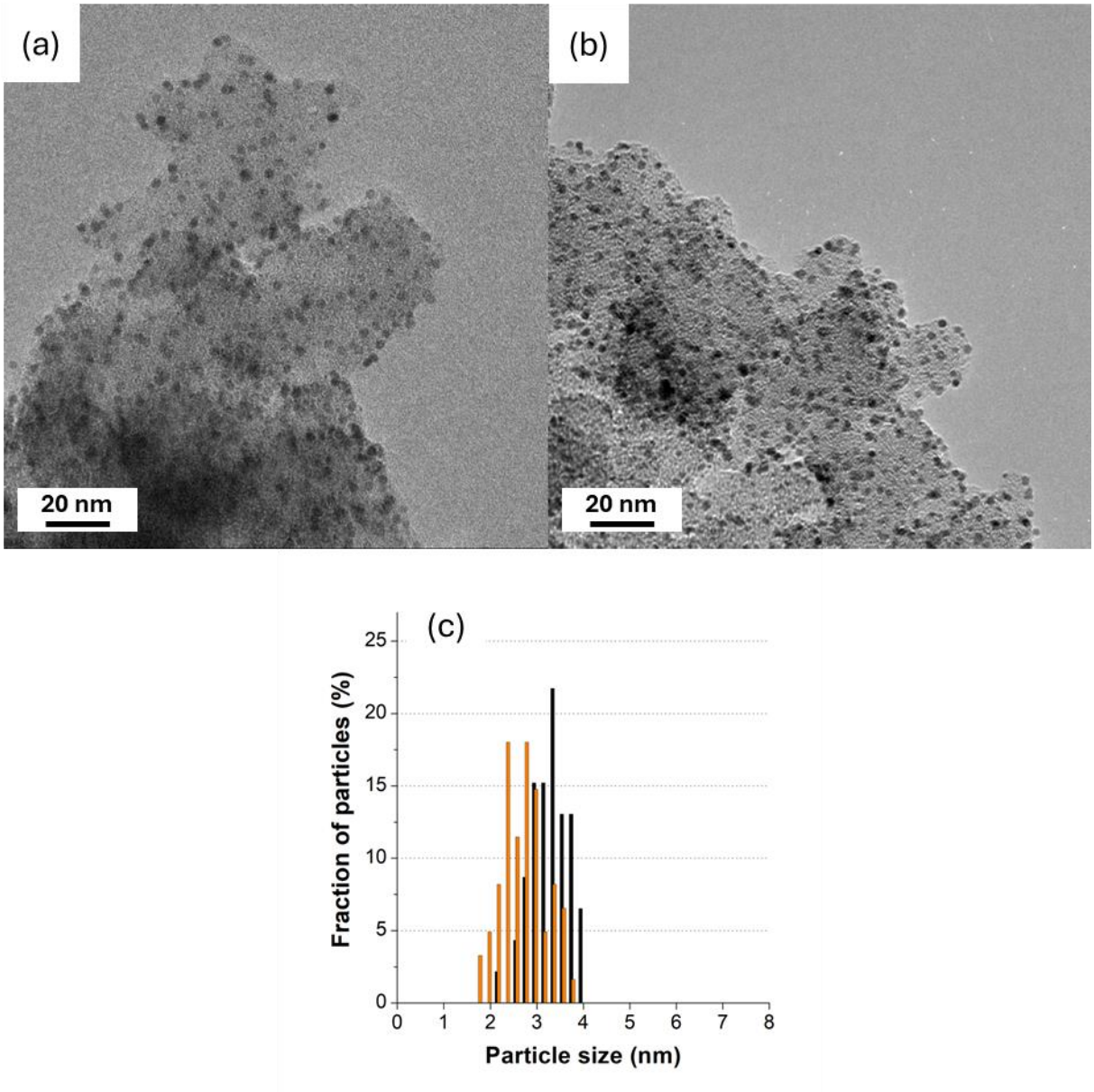

Figure 3.8. TEM micrographs before aging of catalysts with pristine and nitrogen-doped pristine xerogel as support: (a) CX0-Pt, (b) CX0-N30-Pt, and (c) initial Pt nanoparticle size distribution of CX0-Pt (■) and CX0-N30-Pt (■).

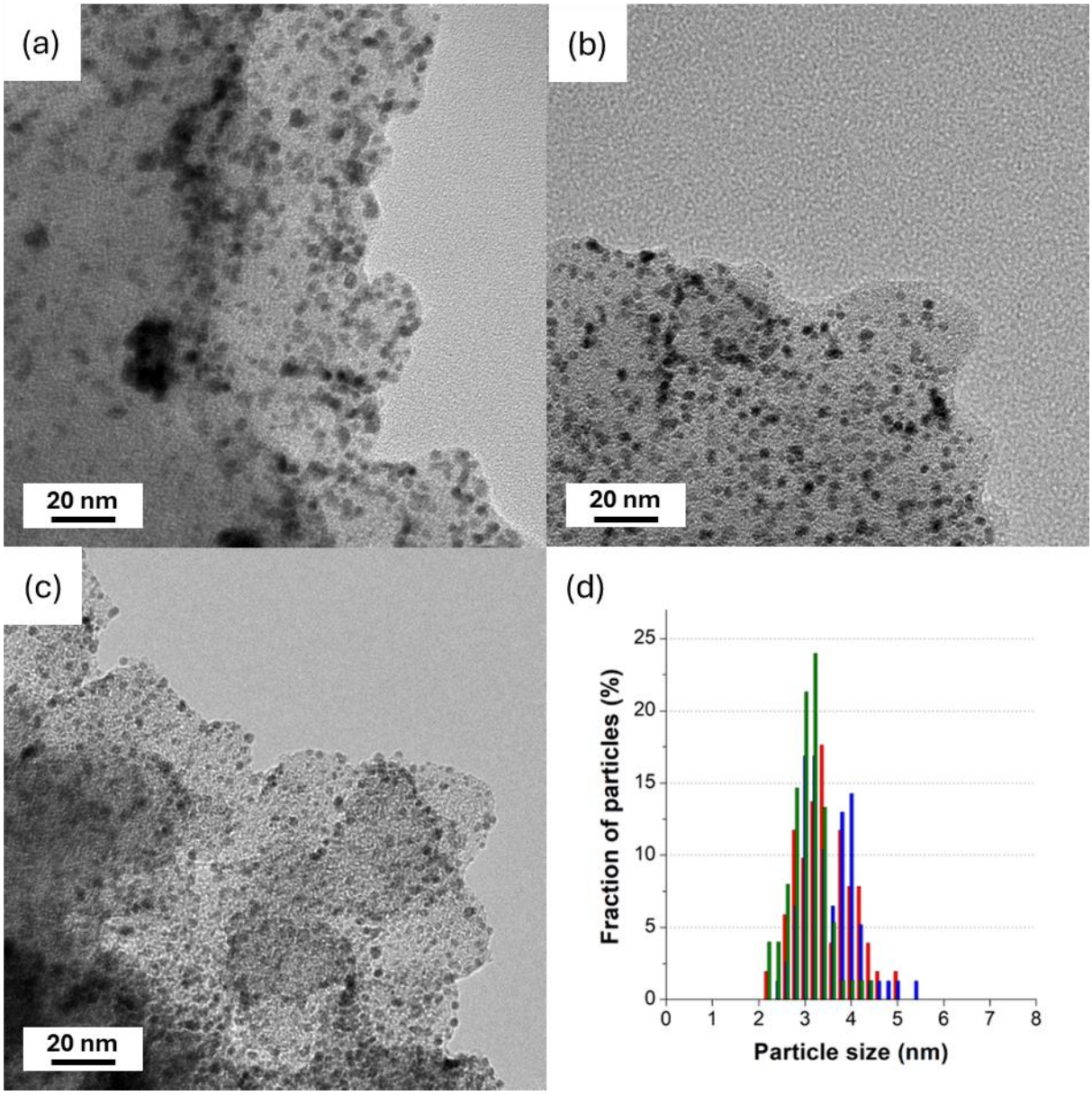

Figure 3.9. TEM micrographs before aging of catalysts with CVD-coated supports: (a) CX0-C20-Pt, (b) CX0-C20-N30-Pt, (c) CX0-C20-N120-Pt and (d) initial Pt nanoparticle size distribution of CX0-C20-Pt (■), CX0-C20-N30-Pt (■), and CX0-C20-N120-Pt (■).

XRD diffractograms of the catalysts were also recorded (**Figure 3.10**). The average Pt crystallite size, d_{XRD}, was estimated using the Scherrer's equation applied to the Pt(111) diffraction peak at 39.8°, as summarized in **Table 3.5**. For CX0-Pt and CX0-N30-Pt, d_{XRD} was measured equal to 2.6 and 3.0 nm, respectively. Meanwhile, for CVD-treated samples, d_{XRD} was calculated equal to 3.0 nm for CX0-C20-Pt and drops to 2.8 and 2.6 nm, for CX0-C20-N30-Pt and CX0-C20-N120-Pt, respectively. Overall, the calculated crystallite sizes remain relatively consistent across all samples, ranging from 2.6 to 3.0 nm. The crystallite sizes

measured by XRD align relatively well with the particle sizes observed by TEM. However, the variation in crystallite or nanoparticle size upon N-doping treatment is of very small magnitude (< 1 nm).

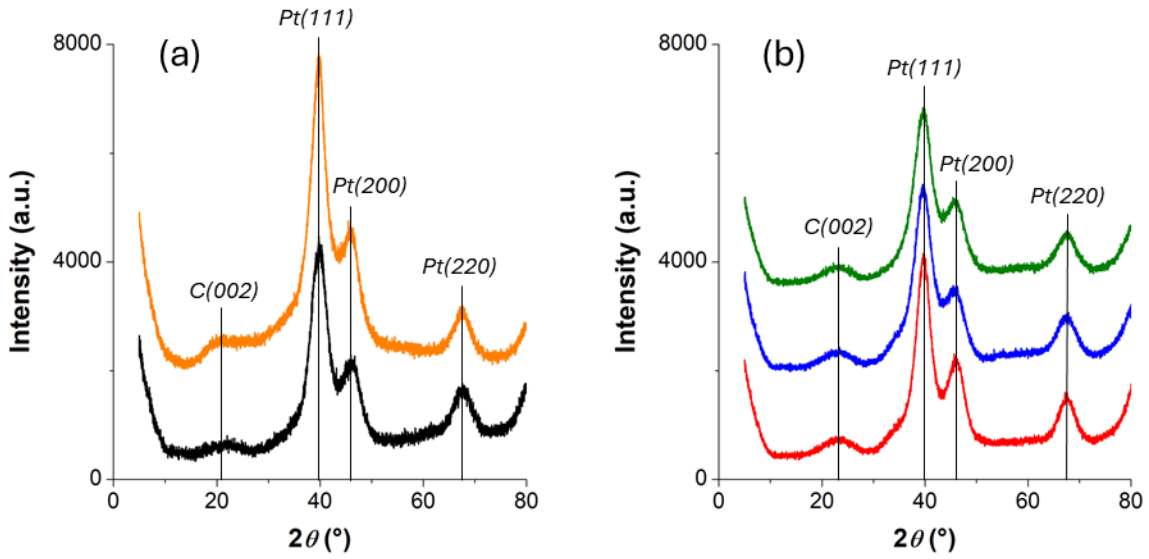

Figure 3.10. X-ray diffractograms of catalysts. (a) CX0-Pt (—) and CX0-N30-Pt (—). (b) CX0-C20-Pt (—), CX0-C20-N30-Pt (—) CX0-C20-N120-Pt (—). The diffractograms are shifted vertically for legibility.

XPS analyses were carried out to examine both the oxidation state of Pt and the stability of the nitrogen moieties after the Pt deposition was performed. As shown in **Table 3.6**, nitrogen remains clearly detectable in all samples following formic acid reduction. After Pt deposition, the surface N content decreases from 1.5 to 1.1 at.% for CX0-N30, from 3.2 to 2.8 at.% for CX0-C20-N30 and from 7.2 to 6.7 at.% for CX0-C20-N120. A slight decrease in nitrogen content is thus observed for all samples. These small variations are not concerning as they fall relatively within the usual frame of XPS error (± 0.5 at.%), which is critical to preserve the desired effect of nitrogen providing a stronger bond between the catalytic metal particles and the carbon support. Nevertheless, the leaching of nitrogen species during the Pt deposition step is an observable phenomenon [49] that cannot be completely ruled out in the present case.

The Pt 4f spectra of all samples were also plotted (**Figure 3.11**). Asymmetrical double peaks are observed, which correspond to the $4f_{7/2}$ and $4f_{5/2}$ spin–orbital splitting of Pt species [50]. After deconvolution of the spectra, three doublets can be observed. The $4f_{7/2}$ peaks appear at

71.7, 72.4 and 75.0 eV, while the corresponding $4f_{5/2}$ peaks appear at 75.0, 76.0 and 78.4 eV. Their presence can be attributed to Pt^0, Pt^{2+}, and Pt^{4+}, respectively, corresponding to metallic Pt, PtO, and PtO_2 [51]. The presence of Pt oxides is usually reported between ambient temperature and 250 ºC, as oxygen chemisorption from air can easily occur at step and kink sites present on the surface of the Pt nanoparticles [52]. The fraction of oxidized Pt (Pt^{2+} and Pt^{4+}) increases between CX0-Pt and CX0-C20-Pt, with 35.3 and 41.9%, respectively (**Table 3.7**). Upon N-doping, the fraction of Pt oxides on the surface of the Pt nanoparticles remains similar, with 35.3 and 37.3% of the Pt detected, for CX0-Pt and CX0-N30-Pt. For the CVD-treated xerogels, the fraction of Pt oxides, also measured from the Pt 4f XPS spectra, is equal to 41.9, 39.7 and 33.8% for CX0-C20-Pt, CX0-C20-N30-Pt and CX0-C20-N120-Pt, respectively. A small decrease is thus observed as the plasma treatment duration increases.

Table 3.6. Elemental surface composition of Pt samples, determined by XPS.

Catalyst	**Atomic percentage** (at.%) ± 0.5			
	Carbon	**Oxygen**	**Nitrogen**	**Platinum**
CX0-Pt	84.1	7.0	Not detected	8.9
CX0-N30-Pt	84.4	4.1	1.1	10.5
CX0-C20-Pt	85.1	6.3	Not detected	8.6
CX0-C20-N30-Pt	82.7	5.6	2.8	8.9
CX0-C20-N120-Pt	81.8	7.2	6.7	4.7

The binding energies of Pt $4f_{7/2}$ and $4f_{5/2}$ were also examined. For all samples, binding energies vary by less than 0.2 eV (**Table 3.7**). It has been reported that a shift of the Pt $4f_{7/2}$ and $4f_{5/2}$ peaks toward higher binding energies occurs as the nanoparticle size decreases. This phenomenon is ultimately linked to the reaction intermediates adsorption strength onto the Pt nanoparticles, a behavior that is largely governed by the quantity of low-coordinated sites of the nanoparticles [53,54]. Nevertheless, no major shift in binding energy is observed. This is also an indicator that no significant difference in particle size, *i.e.* > ~1 nm, is expected to be

observed across the samples. In other words, Pt nanoparticles are expected to possess comparable initial sizes, as actually confirmed with TEM micrographs.

This small variation observed both by TEM and XPS, is somewhat different to what is usually observed in the literature, where it is commonly reported that the incorporation of N dopants in a graphene structure leads to smaller Pt clusters and to narrower nanoparticle size distribution [11,55,56]. It is well-established that the nucleation and growth of metal nanoparticles is dependent on the electronic interaction between the metal atoms and the carbon support surface. In the case of nitrogen-doped carbons, the introduction of heteroatoms disrupts the π-conjugation network of the sp^2 carbon lattice [57]. This change in conjugation has a significant influence on the growth and stability of the metal on the carbon. DFT studies indicate that carbon atoms in the vicinity of nitrogen substitutional carry a slightly positive delta charge. This positive charge could promote the bonding with Pt species such as, in the present case, the anionic Pt precursor, $PtCl_6^{2-}$. Meanwhile, nitrogen atoms tend to repel the Pt atoms [58]. Therefore, Pt does not anchor directly on nitrogen but rather at a next-nearest carbon site. It is thus these next-nearest carbon sites that drive the force for Pt nucleation and usually lead to more energetically favorable Pt nucleation and growth [3,59]. Nevertheless, it is important to emphasize that this assumption represent a trend. The electronic effects induced on the carbon surface by nitrogen atoms are difficult to generalize, and may vary between theoretical predictions and experimental observations [11,60]. Moreover, in the synthesis protocol used here, the Pt precursor is added after the reductant. Therefore, the reduction reaction starts immediately, which could limit the contact time between the $PtCl_6^{2-}$ anion and the carbon, and thus limit the impact of N on Pt nucleation and growth. Finally, given the initial nanoparticle size is already in the optimal range of ~3 nm [61], a further reduction in size would not necessarily be beneficial.

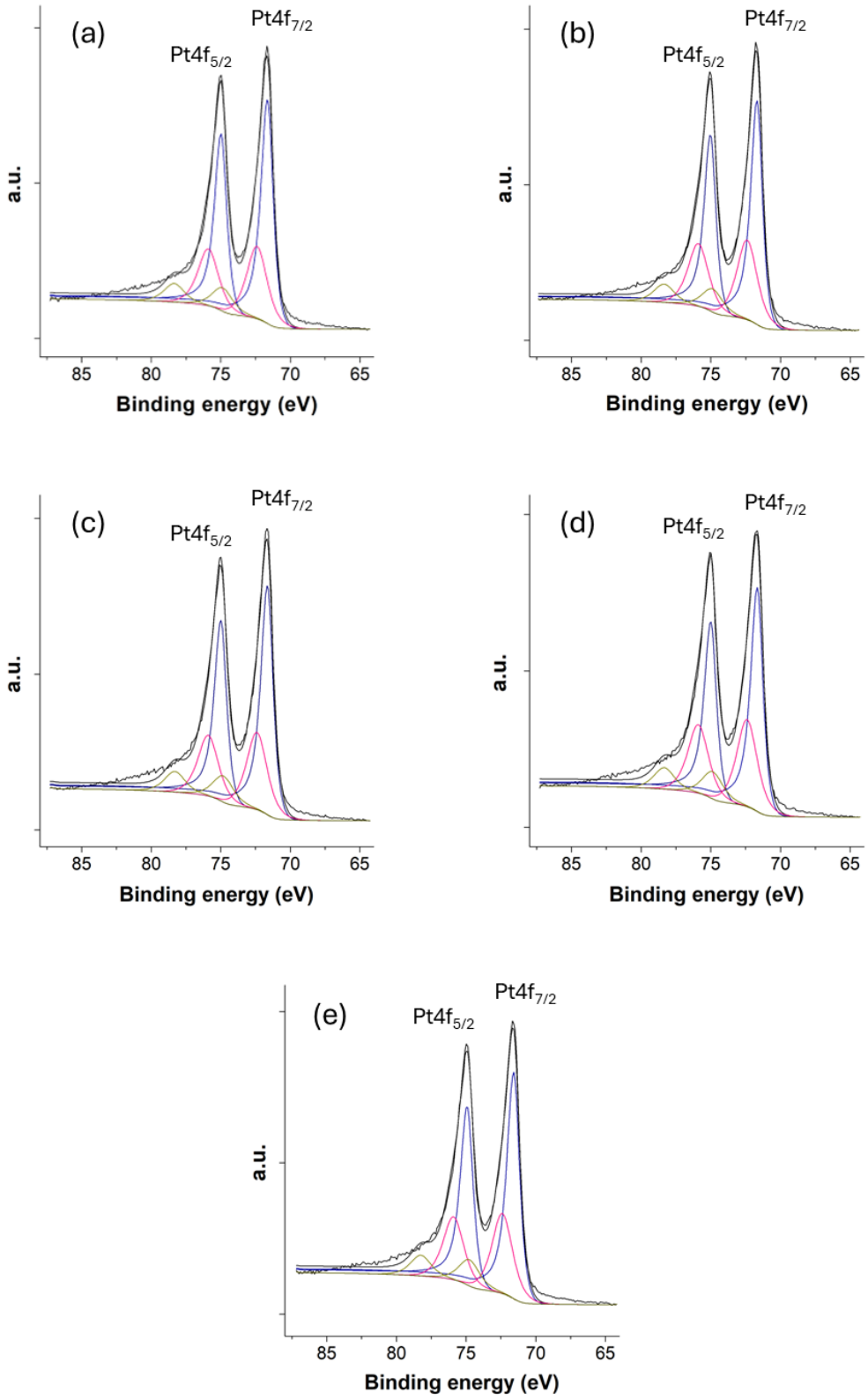

Figure 3.11. Deconvolution of Pt4f XPS spectra of catalysts: (a) CX0-Pt, (b) CX0-C20-Pt, (c) CX0-N30-Pt, (d) CX0-C20-N30-Pt and (e) CX0-C20-N120-Pt, with the $4f_{5/2}$ and $4f_{7/2}$ peaks assignment of Pt^0 (—), Pt^{2+} (—) and Pt^{4+} (—).

Table 3.7. Deconvolution of Pt4f peaks, from XPS analysis.

Catalyst	Fraction of Pt species (%) ± 4%			Peaks binding energy (eV) ± 0.1	
	Pt(0)	Pt(II)	Pt(IV)	$Pt_{5/2}$	$Pt_{7/2}$
CX0-Pt	64.7	26.6	8.8	74.98	71.68
CX0-N30-Pt	62.7	28.0	9.4	75.08	71.68
CX0-C20-Pt	58.1	32.5	9.4	75.08	71.78
CX0-C20-N30-Pt	60.3	30.5	9.2	75.08	71.78
CX0-C20-N120-Pt	66.2	25.0	8.8	74.98	71.68

3.3.3. Electrochemical characterization of the catalysts

A complete evaluation of the catalysts electrochemical performances was performed in RDE configuration. To this end, cyclic voltammetry under argon, CO stripping and ORR activity measurements were conducted in 0.5 M H_2SO_4 electrolyte at 25 ºC. Catalytic properties were measured on the fresh catalytic layer (*BoL*), but also after 5,000 cycles between 0.6 and 1.0 V *vs.* RHE at 80 ºC (corresponding to the *MoL*), and after 15,000 additional cycles under the same conditions (corresponding to the *EoL*). Different parameters were retrieved from these measurements, including the electrochemically active surface area of Pt (*ECSA*) and the CO equivalent Pt nanoparticle diameter (d_{CO}). The mass activity (*MA*) and surface activity (*SA*) determined at 0.95 V *vs.* RHE as well as the Tafel slope (*b*), were also observed and are displayed in **Table 3.8**. As a reminder, this potential was selected to remove any contributions from internal mass transport limitations linked to the active layer thickness, as already discussed in **Section 2.2.3** of Chapter 2.

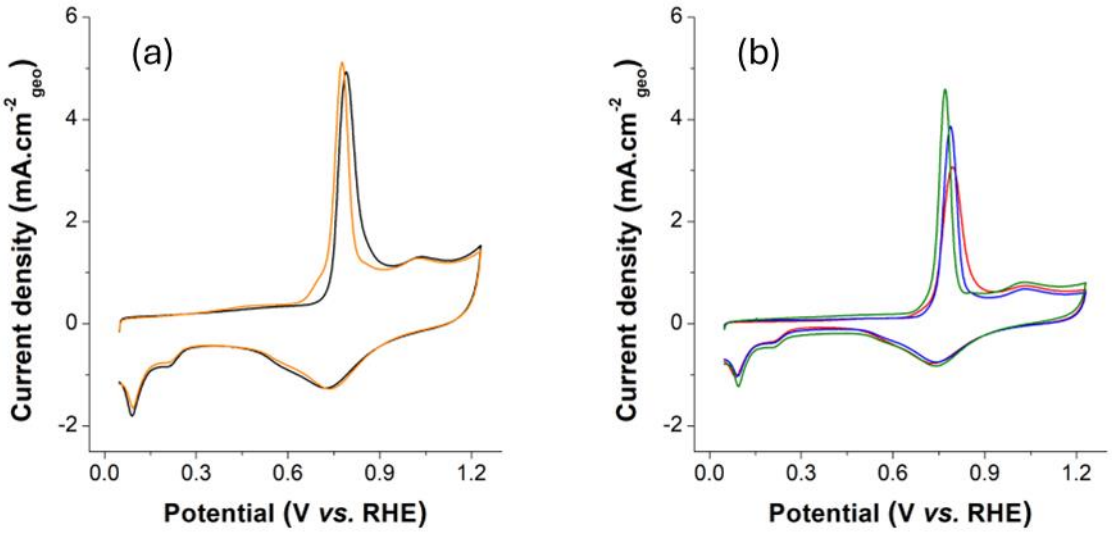

Figure 3.12. CO electro-oxidation curves of fresh catalysts performed in 0.5 M H_2SO_4 at 25ºC at a rate of 20 mV.s^{-1}, of (a) CX0-Pt (—) and CX0-N30-Pt (—), and (b) CX0-C20-Pt (—), CX0-C20-N30-Pt (—) and CX0-C20-N120-Pt (—).

Comparisons between CX0-Pt and CX0-C20-Pt were already discussed in Chapter 2. In summary, the *ECSA* was found to slightly decrease in the case of the CVD-treated carbon support, from 117 to 101 m².g$^{-1}_{Pt}$ for CX0-Pt and CX0-C20-Pt, respectively. This was attributed to nanoparticles growing slightly larger on the CVD-treated sample, as evidenced by TEM micrographs in Chapter 2 (**Figure 2.11**). Both CX0-Pt and CX0-C20-Pt exhibit the same catalytic activity behavior, characterized by an increase in *SA* upon aging, while the *MA* remains relatively stable. This increase of *SA* can be explained as follows. First, aging leads to a slight growth of Pt nanoparticles, due to phenomena such as Ostwald ripening, nanoparticle dissolution and/or migration. Second, the ratio between facet sites and edge/corner sites changes with particle size. Larger nanoparticles contain fewer low-coordination sites, which can result in a more favorable binding energy for ORR intermediates. This can ultimately increase the ORR kinetics and thus increase the *SA* [62] without changing much the *MA* given the simultaneous loss of *ECSA*.

The catalytic behavior of the N-doped samples was evaluated as well and compared with their non-doped counterparts (*i.e.* CX0-Pt *versus* CX0-N30-Pt and CX0-C20-Pt *versus* CX0-C20-N30-Pt and CX0-C20-N120-Pt). This comparison is essential to determine how the incorporation of nitrogen atoms into the carbon matrix influences the electrochemical performances. First, CO stripping measurements were used to determine the *ECSA* from the

CO electrooxidation peak (**Table 3.8**). The initial *ECSA* of CX0-Pt and CX0-N30-Pt measured from the peak surface (shown in **Figure 3.12a**) are nearly identical, 117 and 116 $m^2.g^{-1}_{Pt}$, respectively. For the CVD-treated samples, CX0-C20-Pt and CX0-C20-N30-Pt also display equivalent initial values, namely 101 and 107 $m^2.g^{-1}_{Pt}$. d_{CO}, derived from the *ECSA*, was found equal to 2.8 and 2.6 nm. As seen on **Figure 3.12b**, the position of the CO oxidation peak remains similar for CX0-C20-Pt and CX0-C20-N30-Pt. In contrast, for a higher nitrogen content (CX0-C20-N120-Pt), the *ECSA* and d_{CO} are measured at 84 $m^2.g^{-1}_{Pt}$ and 3.4 nm, respectively. These observations suggest that low levels of nitrogen incorporation (1.5 and 3.2 at.%) do not significantly affect Pt size, while a higher nitrogen incorporation (7.2 at.%) can lead to the formation of slightly larger nanoparticles. Note that the size difference observed in CO stripping was not observed in TEM. As a reminder, d_{TEM} was found equal to 3.5 ± 0.5 nm for CX0-C20-N30-Pt and 3.2 ± 0.5 nm for CX0-C20-N120-Pt. Nevertheless, beneficial effects are sometimes reported upon aging thanks to the better particles anchoring, even when Pt particle growth and dispersion remain largely unchanged [11]. Finally, another notable difference in the CO stripping curves is the evolution of the double layer capacity of the carbon support, C_{dl}. CX0-Pt and CX0-N30-Pt display a relatively high C_{dl}, calculated equal to 128 and 101 $F.g^{-1}$ respectively from **Equation (3.7)**, while it significantly decreases for CX0-C20-Pt, CX0-C20-N30-Pt and CX0-C20-N120-Pt (33, 30 and 48 $F.g^{-1}$, respectively). The high value observed for CX0-Pt and CX0-N30-Pt can be attributed to the extensive micropore network accessible to the electrolyte. Since the CVD treatment blocks most of the carbon xerogel micropores, the surface onto which ions can accumulate is proportionally reduced in the case of the CVD-coated samples.

The evolution of *ECSA* and d_{CO} was also observed upon aging. The normalized *ECSA* of all materials is presented in **Figure 3.13a.** The *ECSA* retention after *MoL* is on average 67, 65, 61, 65 and 65% for CX0-Pt, CX0-C20-Pt, CX0-N30-Pt, CX0-C20-N30-Pt and CX0-C20-N120-Pt, respectively. At *EoL*, this *ECSA* retention drops further to 59, 53, 54, 53 and 53%. The *ECSA* losses across all materials are similar, both at *MoL* and *EoL*. The lowest *ECSA* drop is actually observed with CX0-Pt. At *EoL*, the d_{CO} also increases to 4.0, 5.2, 4.6, 5.0 and 6.4 nm for CX0-Pt, CX0-C20-Pt, CX0-N30-Pt, CX0-C20-N30-Pt and CX0-C20-N120-Pt, respectively (*versus* 2.4, 2.8, 2.4, 2.6 and 3.4 nm at *BoL*). Thus, neither the CVD treatment nor the nitrogen doping treatment seem to significantly mitigate the nanoparticles growth.

ORR curves were then used to determine *SA*, *MA* and Tafel slope (**Figure 3.14**). For CX0-Pt and CX0-N30-Pt, the initial *SA* goes from 0.022 $A.m^{-2}_{Pt}$ to 0.037 $A.m^{-2}_{Pt}$ while *MA* goes from

2.69 $A.g^{-1}_{Pt}$ to for CX0-Pt to and 4.27 $A.g^{-1}_{Pt}$. This corresponds to a *SA* increase of 68% and a *MA* increase of 59%. Upon aging, at *EoL*, both samples converge to similar values, with *SA* of 0.060 and 0.055 $A.m^{-2}_{Pt}$, and *MA* of 3.78 and 3.39 $A.g^{-1}_{Pt}$ for CX0-Pt and CX0-N30-Pt, respectively (**Figure 3.13b-c**). These results suggest that initial catalytic activities might be slightly improved upon nitrogen doping but that this small benefit is largely lost after long-term cycling.

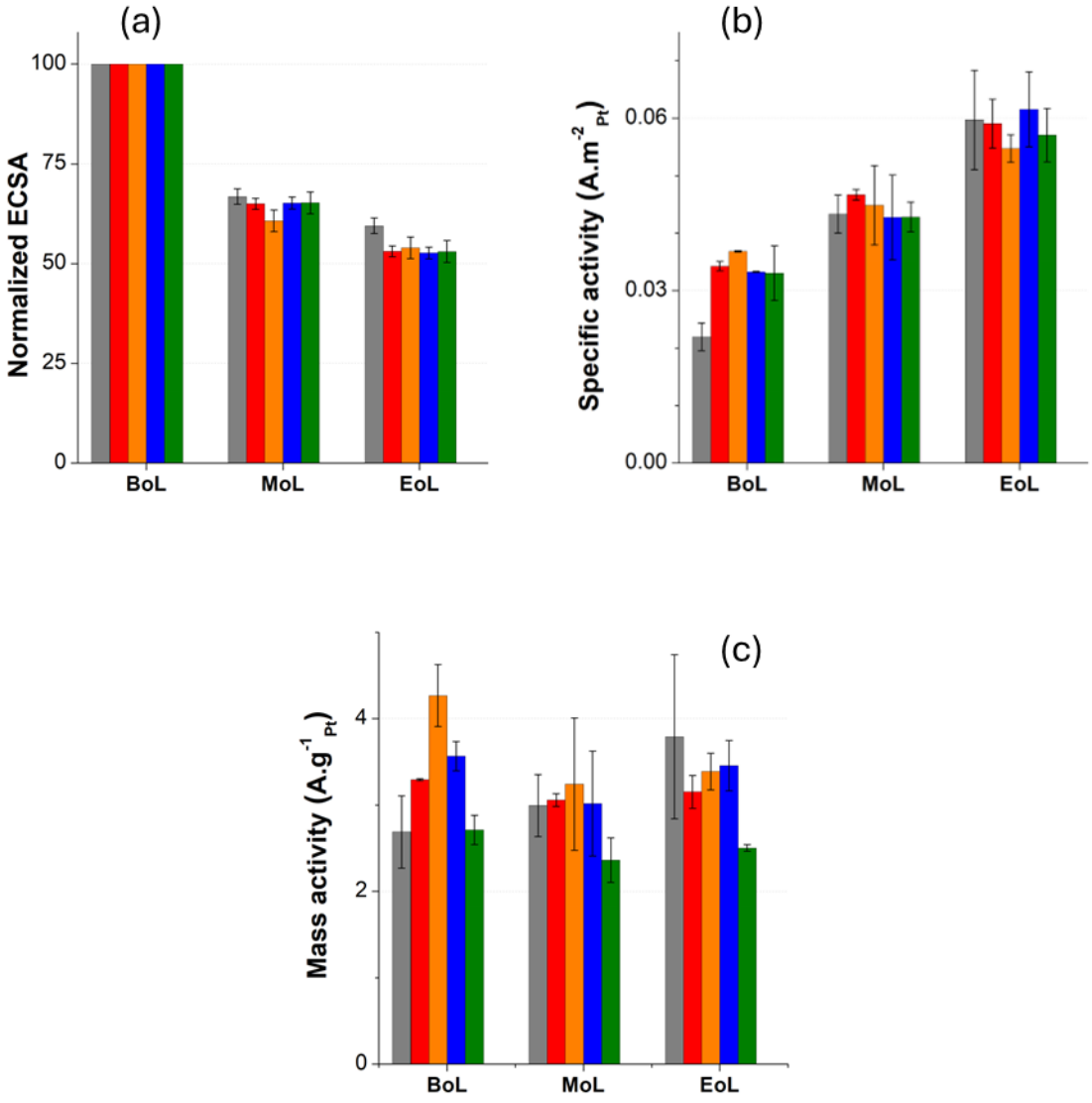

Figure 3.13. Evolution of the electrochemical properties of the catalysts during Accelerated Stress Tests at 80 ºC, measurements performed in RDE configuration in 0.5 M H_2SO_4 at 25 ºC. (a) Normalized ElectroChemically active Surface Area of Pt, (b) specific activity at 0.95 V *vs.* RHE, and (c) mass activity at 0.95 V *vs.* RHE. CX0-Pt (■), CX0-N30-Pt (■) CX0-C20-Pt (■), CX0-C20-N30-Pt (■), and CX0-C20-N120-Pt (■).

For CVD-treated samples, similar initial *SA* values of 0.034, 0.033 and 0.033 $A.m^{-2}_{Pt}$ were calculated, and *MA* values of 3.29, 3.57 and 2.71 $A.g^{-1}_{Pt}$ were found for CX0-C20-Pt, CX0-C20-N30-Pt and CX0-C20-N120-Pt, respectively. Upon aging, no major differences are observed, with *SA* increasing to 0.059, 0.055 and 0.057 $A.m^{-2}_{Pt}$; and *MA* remaining stable at 3.15, 3.46 and 2.50 $A.g^{-1}_{Pt}$ for CX0-C20-Pt, CX0-C20-N30-Pt and CX0-C20-N120-Pt, respectively (**Figure 3.13b-c**). Sample CX0-C20-N30-Pt actually display slightly higher catalytic activity than CX0-C20-N120-Pt. As was already observed with the *ECSA* measurements, a nitrogen content of 7.2 at.% might prove excessive. Overall, all N-doped samples display the same behavior as CX0-Pt and CX0-C20-Pt, namely an increase in *SA*, and a *MA* that remains somewhat constant. The explanation of this behavior was previously given in Chapter 2. In short, the nanoparticles growth upon aging leads to a more favorable adsorption of ORR reaction intermediates and thus a higher specific catalytic activity towards ORR, compensating for the loss of *ECSA*.

Finally, the Tafel slopes were also calculated and are displayed in **Table 3.8**. The initial Tafel slopes of fresh catalysts are comprised between 60 and 72 $mV.dec^{-1}$ for all samples (**Figure 3.14b**). This indicates that the ORR proceeds mostly through a $(2+2)e^-$ mechanism, even after N-doping [63]. After aging, no variation of the Tafel slope greater than 10 $mV.dec^{-1}$ is observed. This confirms that the $(2+2)e^-$ mechanism remains unchanged across all catalysts throughout durability tests, regardless if the carbon xerogel support was treated by CVD and/or by nitrogen doping treatment.

After the AST, the active layer could be recovered from the working electrode, and samples were prepared for TEM observation. It must be noted that the amount of active layer retrieved is very small (< 1 mg) and is thus insufficient for complementary analyses, even for XPS. As done with TEM micrographs taken at *BoL*, a minimum of 50 nanoparticles were used to determine the nanoparticle size distribution. TEM micrographs and particle size distribution for CX0-Pt and CX0-N30-Pt are shown in **Figure 3.15**. A mean nanoparticle diameter centered around 4.3 nm for CX0-Pt and 3.8 nm for CX0-N30-Pt was observed. Pt nanoparticles appear slightly less agglomerated after N-doping although both d_{TEM} values fall within the margin of error.

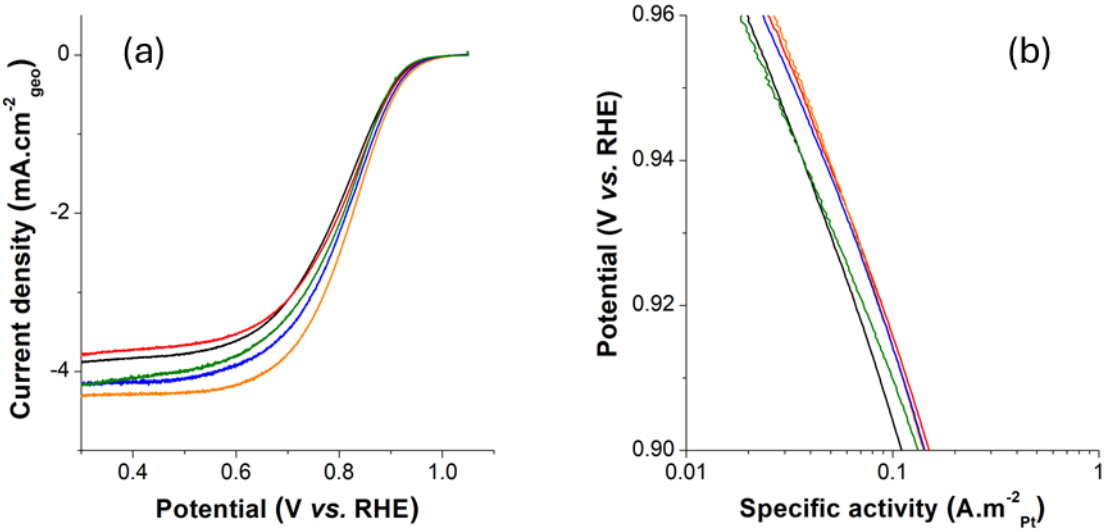

Figure 3.14. ORR measurements on fresh catalysts performed in 0.5 M H_2SO_4 at 25ºC. (a) Cyclic voltammetry under O_2 at a scan rate of 1 $mV.s^{-1}$ and an electrode rotation speed of 1600 rpm, (b) Corresponding Tafel plots, of CX0-Pt (—), CX0-N30-Pt (—), CX0-C20-Pt (—), CX0-C20-N30-Pt (—) and CX0-C20-N120-Pt (—).

TEM micrographs and particle size distributions of CVD-treated samples are shown in **Figure 3.16**. The mean Pt nanoparticle diameters are centered around 4.6 nm for CX0-C20-Pt and 4.5 nm for CX0-C20-N30-Pt. Moderate N incorporation does not appear to significantly alter Pt aging. However, a clear difference is observed for CX0-C20-N120-Pt, where the nanoparticles are noticeably larger, with an average diameter of approximately 5.7 nm. This observation aligns with the electrochemical data, as CX0-C20-N120-Pt exhibits the lowest *ECSA* and highest d_{CO} values at *EoL* among the series.

From all these observations, it appears that the highest N content (7.2 at.%) is mostly detrimental to the catalyst performances, as it leads to larger nanoparticle size after aging. Thus, excessive nitrogen incorporation seems to disrupt rather than enhance catalytic layer stability. In contrast, the lower nitrogen incorporations (1.5 and 3.2 at.%) do not result in significant changes but are not detrimental either. These samples behave very similarly to their undoped counterpart. To obtain even more insights, it could have been interesting to also manufacture and test CX0-C20 with a lower nitrogen content (*i.e.* 1-2 at.% N).

Table 3.8. Evolution of the catalyst properties determined by RDE electrochemical analyses.

Catalyst		CO stripping		ORR		
		***ECSA*[a]**	***d*$_{CO}$[b]**	***SA*[c]**	***MA*[c]**	***b*[d]**
		($m^2.g^{-1}_{Pt}$)	(nm)	($A.m^{-2}_{Pt}$)	($A.g^{-1}_{Pt}$)	($mV.dec^{-1}$)
CX0-Pt	BoL	117 ± 7	2.4 ± 0.1	0.022 ± 0.002	2.69 ± 0.42	67 ± 4
	MoL	78 ± 2	3.6 ± 0.1	0.043 ± 0.003	2.99 ± 0.36	64 ± 2
	EoL	70 ± 3	4.0 ± 0.2	0.060 ± 0.009[e]	3.79 ± 0.95[e]	62 ± 2
CX0-C20-Pt	BoL	101 ± 4	2.8 ± 0.1	0.034 ± 0.001	3.29 ± 0.01	71 ± 2
	MoL	65 ± 1	4.3 ± 0.1	0.047 ± 0.001	3.06 ± 0.07	62 ± 1
	EoL	53 ± 1	5.2 ± 0.1	0.059 ± 0.004	3.15 ± 0.19	61 ± 1
CX0-N30-Pt	BoL	116 ± 10	2.4 ± 0.2	0.037 ± 0.001	4.27 ± 0.36	72 ± 1
	MoL	70 ± 6	4.0 ± 0.4	0.045 ± 0.007	3.24 ± 0.77	71 ± 1
	EoL	62 ± 7	4.6 ± 0.5	0.055 ± 0.002	3.39 ± 0.21	71 ± 3
CX0-C20-N30-Pt	BoL	107 ± 5	2.6 ± 0.1	0.033 ± 0.001	3.57 ± 0.17	60 ± 3
	MoL	70 ± 2	4.0 ± 0.1	0.043 ± 0.007	3.02 ± 0.61	67 ± 4
	EoL	56 ± 1	5.0 ± 0.1	0.062 ± 0.007	3.46 ± 0.29	68 ± 1
CX0-C20-N120-Pt	BoL	84 ± 7	3.4 ± 0.3	0.033 ± 0.005	2.71 ± 0.17	68 ± 2
	MoL	55 ± 3	5.1 ± 0.3	0.043 ± 0.003	2.36 ± 0.26	69 ± 8
	EoL	45 ± 4	6.4 ± 0.3	0.057 ± 0.005	2.50 ± 0.04	69 ± 8

[a] *ECSA*: Electrochemically activity surface area of Pt normalized to the mass of Pt on the electrode, calculated from CO stripping measurement (**(3.5**).
[b] d_{CO}: CO equivalent particle diameter of the Pt particles calculated from **Equation (3.6)**.
[c] *SA* and *MA*: Specific Activity and Mass Activity measured at 0.95 V *vs.* RHE (**Equations (3.8)** and **(3.9)**).
[d]: Tafel plot obtained calculated from ORR measurements.
[e]: Error > 20% observed between measurements. Note: The values presented in this table correspond to the average of at least two measurements.

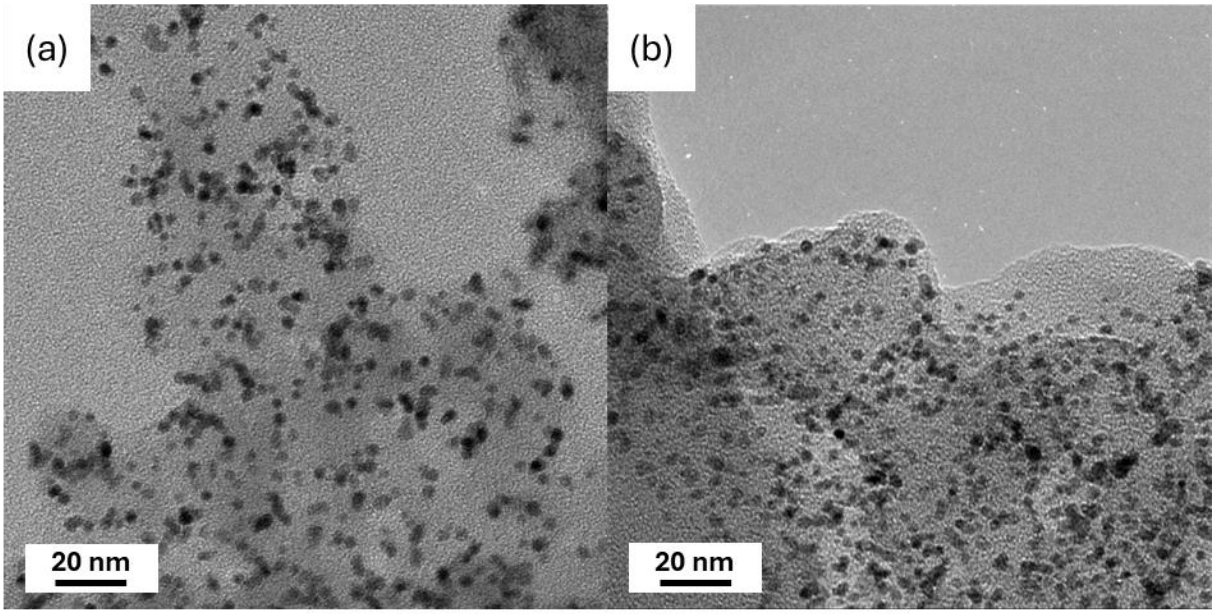

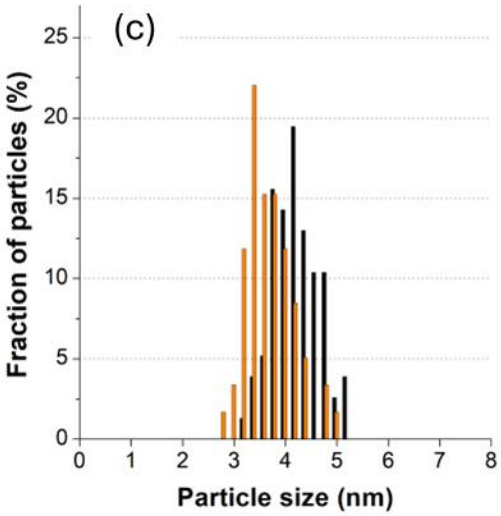

Figure 3.15. TEM micrographs of (a) CX0-Pt, (b) CX0-N30-Pt, and (c) Pt nanoparticle size distribution of CX0-Pt (■) and CX0-N30-Pt (■), after aging with 20,000 potential cycles between 0.6 and 1.0 V *vs.* RHE at 0.1 $V.s^{-1}$ in RDE configuration, corresponding to the *EoL*.

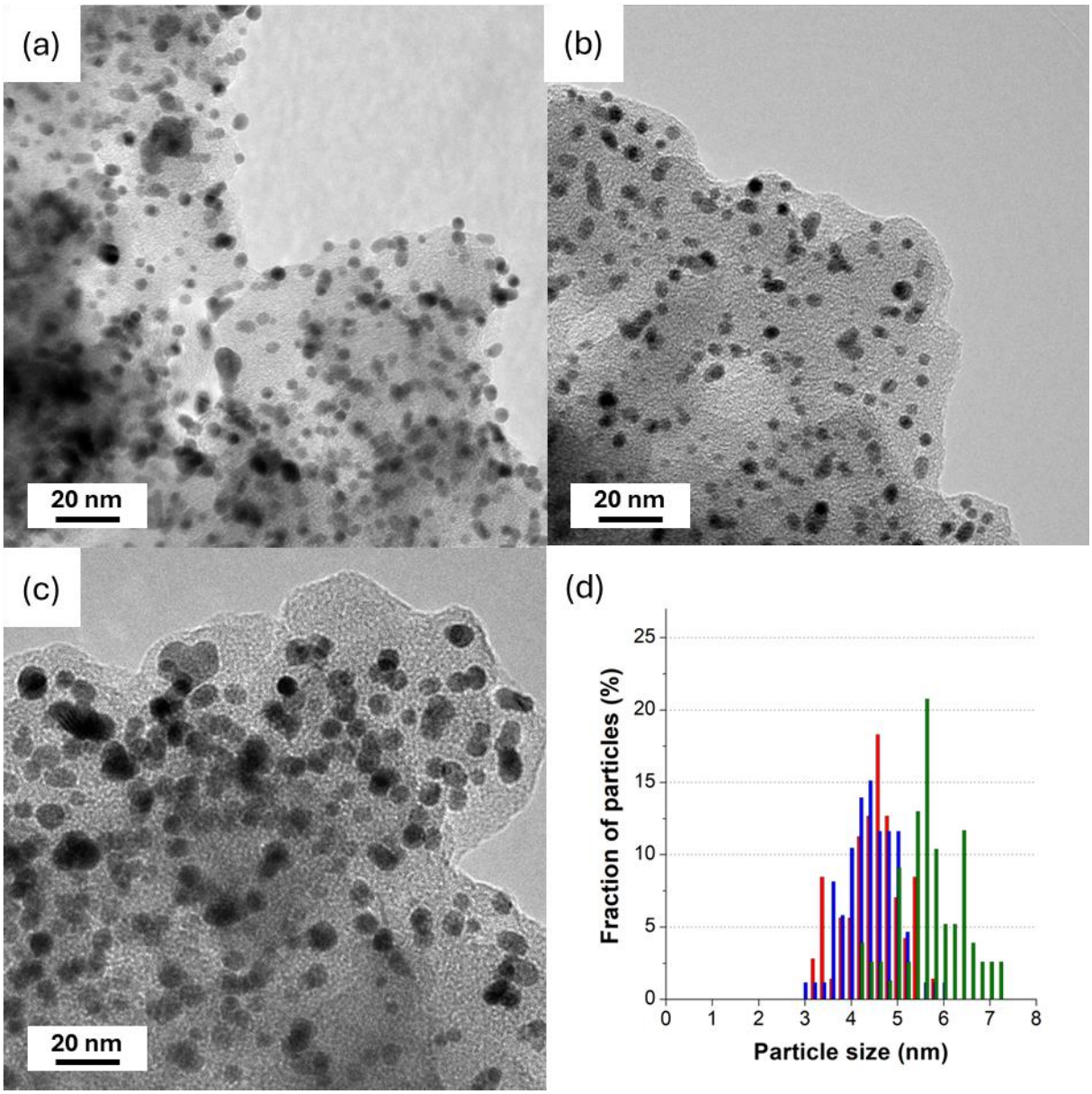

Figure 3.16. TEM micrographs of (a) CX0-C20-Pt, (b) CX0-C20-N30-Pt, (c) CX0-C20-N120-Pt and (d) final Pt nanoparticle size distribution of CX0-C20-Pt (■), CX0-C20-N30-Pt (■), and CX0-C20-N120-Pt (■), after aging with 20,000 potential cycles between 0.6 and 1.0 V *vs.* RHE at 0.1 $V.s^{-1}$ in RDE configuration, corresponding to the *EoL*.

In this chapter, the better anchoring of Pt nanoparticles onto the carbon support usually associated with N-doping [60] was not observed, despite the carbon support surface electronic environment being notably different due to the N incorporation. Indeed, the presence of nitrogen on the carbon surface was observed with XPS and the carbon surface comprises nitrogen functional groups that have been reported in the literature to be positive towards ORR (pyridinic, pyrrolic and graphitic) were detected. Moreover, the total percentage of these groups

(1.5 and 7.2 at.%) falls within typical reported ranges [19]. These nitrogen groups remain even after Pt deposition *via* reduction in formic acid, and are thus present in the catalytic layer. Similarly, Pt deposition is not hindered by nitrogen. This is evidenced by TGA measurements that show comparable metal content across all samples. Plus, TEM micrographs of fresh catalysts show that moderate nitrogen content (1.5 at.%) seem to even slightly improve Pt nanoparticle dispersion. Higher nitrogen contents (7.2 at.%) are initially not detrimental either. The pore texture of the carbon xerogel also remains essentially intact. BET surface area and micropore volume was nearly unchanged after plasma treatment. Finally, after observation of CX0-C20-N120 by SEM, no evidence of structural collapse of the carbon structure was observed, indicating that N-doped carbon xerogels can be used as catalyst support, as already reported by Alegre *et al.* [11].

Thus, the results obtained here may appear unexpected. Indeed, numerous studies report that Pt nanoparticles supported on N-doped carbon supports can exhibit initial performances with an increase in *SA* and *MA* [64] or higher initial *ECSA* [6], but also improved stability upon aging [65]. However, this increase in durability must be considered with caution. The application of a nitrogen doping treatment can induce many modifications to the carbon support, such as changes in the atomic surface composition, the surface area or even the degree of graphitization. These modifications can influence the growth of Pt nanoparticles deposited on the carbon support, thereby affecting their initial size [8]. It is well-known that the size of the nanoparticles plays in an important role in governing both the catalytic activity and long-term stability of a catalyst [66]. Consequently, the comparison of a N-doped carbon support and its undoped counterpart can be highly biased if differences in nanoparticles growth on these supports are not accounted for. A compensatory effect could be observed as nanoparticles grow closer or further away from their optimal value (~3.5 nm for Pt nanoparticles [67]) when deposited on N-doped supports. In this context, studies in which Pt nanoparticles of identical sizes were obtained on both N-doped and undoped carbon support are of particular interest.

For instance, Hornberger *et al.* [68] doped a Vulcan XC-72 carbon black with nitrogen and obtained a carbon with a bulk nitrogen content of 2.7at.%. Using XPS, they also observed the presence of pyrrolic, pyridinic and graphitic moieties. The Pt nanoparticles deposited on this N-doped carbon black exhibited the same average diameter as the ones deposited on the undoped carbon black, *i.e.* 2 nm. Upon subjecting their catalysts to AST (30,000 cycles of potential between 0.6-0.95 V *vs.* RHE, in RDE configuration and 0.1 M $HClO_4$ electrolyte, as well as 30,000 potential steps between 0.6-1.1 V, in MEA configuration), no major differences

were observed across catalysts regarding the evolution of the catalytic activities (*SA* and *MA*) and *ECSA*. The authors concluded that the environment of the N species may need further refinement to observe the beneficial effects of nitrogen. Similarly, Cosenza *et al.* [60], performed N doping on a Vulcan XC-72 carbon black using different treatments and parameters. They achieved a nitrogen surface composition ranging from 1.2 to 4.4 at.%, like in the present study, with the presence of pyridinic, pyrrolic, graphitic and amine N moieties. After TEM analysis, the N-doped carbon support did not exhibit a significant change in the average nanoparticle diameter, as they obtained nanoparticles of 2.7 nm for the undoped material and 2.7-2.8 nm on their different N-doped materials. Upon electrochemical characterization in RDE configuration in 0.1 M $HClO_4$ electrolyte, they observed that the initial catalytic activity of the different catalysts was similar, whether the carbon support was doped or not. An increase in the *ECSA* at higher nitrogen content was observed, which they attributed to a more uniform coverage of Pt due to the nitrogen functional groups. Nonetheless, upon aging (1000 cycles between 0.6-1.0 V *vs.* RHE, in RDE configuration), similar losses in *MA* and *ECSA* were observed for all samples, regardless of the nitrogen content. The catalysts were also observed with TEM after aging and all catalysts exhibited comparable nanoparticle growth upon aging. The authors suggested that the electronic effects induced by nitrogen may not always be beneficial. Finally, Parnière *et al.* [64] also doped a Vulcan XC-72 carbon black, and obtained a N-doped material with a surface containing 3.4 wt.% of nitrogen, as well as the nitrogen moieties usually reported (amine, graphitic, pyrrolic and pyridinic nitrogen). As determined by TEM, the average Pt nanoparticle diameter was 2.6 and 2.7 nm on undoped and N-doped support, respectively. Fresh catalysts exhibited slightly higher *ECSA* and catalytic activities (*SA* and *MA*) with the N-doped carbon support. Upon accelerated aging in severe conditions (60,000 cycles between 1.0-1.5 V *vs.* RHE, in RDE configuration, in 0.1 M $HClO_4$ electrolyte), the *MA* and *ECSA* of both catalysts decreased similarly. Meanwhile, the *SA* increased on the N-doped catalyst while it decreased for the undoped counterpart. This increase in *SA* was attributed to the stronger anchoring of the nanoparticles due to nitrogen, although no particle size analysis was provided after aging. Although not mentioned by the authors, the presence of very small nanoparticles (< 2 nm) growing preferentially on the N-doped support and not detected on TEM micrographs, could also play a role in the observed catalytic behavior.

Overall, the literature generally suggests that the incorporation of nitrogen is beneficial to provide stronger interactions between Pt nanoparticles and the carbon support. However, the interplay of all the modifications possibly induced by the nitrogen doping treatment can make

it difficult to properly compare materials, and may lead to biased conclusions. Although theoretical studies often predict a better anchoring of Pt nanoparticles on N-doped carbon supports, such benefits are not always observed in experimental studies, as illustrated in this chapter and in the three studies discussed above.

Nonetheless, despite the modest impact of nitrogen doping on the catalyst durability observed here, it is still important to emphasize the interesting advantage carbon xerogel possess over carbon black-support catalysts, in terms of pore texture and mass transport control [69]. To continue the assessment of catalysts performances and durability, samples were selected to undergo further evaluation in a Membrane Electrode Assembly (MEA) configuration. Both CX0-N30-Pt and CX0-C20-N30-Pt were selected, as they have the most reasonable nitrogen incorporation level. They were selected along with CX0-Pt, CX0-C20-Pt and CX0-C20-HT1500-Pt, characterized together in Chapter 2. CX0-C20-N120-Pt was excluded from this aging in MEA configuration. This choice is motivated by the clear performance decay and higher nanoparticle size upon aging.

3.4. Conclusion

In this chapter, a carbon xerogel (CX) previously coated with a secondary carbon layer using Chemical Vapor Deposition (CVD) was subjected to a plasma treatment using a N_2 source. This treatment was performed to incorporate N-containing functional groups into the carbon surface. Upon XPS analysis, it was observed that the plasma treatment successfully introduced different amounts of nitrogen. After spectra deconvolution, the N moieties incorporated were identified as pyridinic, pyrrolic and graphitic N. These moieties are commonly associated with improved Pt nanoparticles anchoring and stability in PEM fuel cell electrocatalysts. The N-doped carbon xerogels were also characterized by various methods after their exposure to plasma to verify that the carbon structure was not altered. No major changes in the carbon morphology, pore structure or crystallinity were detected.

Pt nanoparticles were then successfully deposited on all carbon materials *via* formic acid reduction of $PtCl_6^{2-}$. XPS analysis confirmed that the nitrogen-containing functional groups remain stable and are not modified during the Pt nanoparticle deposition. Thus, doped and undoped carbon xerogel-supported catalysts were characterized in acidic liquid electrolyte in Rotating Disk Electrode configuration. Their initial catalytic activities and durability towards aging after 5,000 and 20,000 potential cycles were assessed. Despite the successful

incorporation of nitrogen, catalysts supported on N-doped carbon xerogels did not exhibit a marked increase of stability upon aging. Small and moderate nitrogen contents (1.5 and 3.2 at.%) did not play a significant beneficial or detrimental role as the catalytic activities after complete aging procedure remained similar to their undoped counterparts. However, for higher nitrogen surface content (7.2 at.%), the exposed surface of Pt (*ECSA*) was found lower than for all the other samples, and TEM observations indicated the formation of larger nanoparticles upon aging. This suggests that high nitrogen content can be detrimental to the catalyst stability. Based on the information presented in this chapter and in Chapter 2, the carbon xerogels with low nitrogen contents (1.5 and 3.2 at.%) were selected, along with the pristine CX, the CVD-treated CX and high-temperature and CVD-treated CX (assessed in Chapter 2), for further evaluation under more realistic operating conditions *i.e.* as Membrane-Electrodes Assemblies in a PEMFC test bench.

3.5. References

[1] L. Castanheira, W.O. Silva, F.H.B. Lima, A. Crisci, L. Dubau, F. Maillard, Carbon Corrosion in Proton-Exchange Membrane Fuel Cells: Effect of the Carbon Structure, the Degradation Protocol, and the Gas Atmosphere, *ACS Catalysis*, 5 (2015) 2184–2194.

[2] E. Guilminot, A. Corcella, F. Charlot, F. Maillard, M. Chatenet, Detection of Pt[sup z+] Ions and Pt Nanoparticles Inside the Membrane of a Used PEMFC, *Journal of The Electrochemical Society*, 154 (2006) B96.

[3] C.K. Acharya, D.I. Sullivan, C.H. Turner, Characterizing the Interaction of Pt and PtRu Clusters with Boron-Doped, Nitrogen-Doped, and Activated Carbon: Density Functional Theory Calculations and Parameterization, *The Journal of Physical Chemistry C*, 112 (2008) 13607–13622.

[4] J. Wu, X.Z. Yuan, J.J. Martin, H. Wang, J. Zhang, J. Shen, S. Wu, W. Merida, A Review of PEM Fuel Cell Durability: Degradation Mechanisms and Mitigation Strategies, *Journal of Power Sources*, 184 (2008) 104–119.

[5] Z. Zhao, H. Chen, W. Zhang, S. Yi, H. Chen, Z. Su, B. Niu, Y. Zhang, D. Long, Defect Engineering in Carbon Materials for Electrochemical Energy Storage and Catalytic Conversion, *Materials Advances*, 4 (2023) 835–867.

[6] L. Perini, C. Durante, M. Favaro, V. Perazzolo, S. Agnoli, O. Schneider, G. Granozzi, A. Gennaro, Metal–Support Interaction in Platinum and Palladium Nanoparticles Loaded on Nitrogen-Doped Mesoporous Carbon for Oxygen Reduction Reaction, *ACS Applied Materials & Interfaces*, 7 (2015) 1170–1179.

[7] S.-M. Hwang, Y. Choi, M.G. Kim, Y.-J. Sohn, J.Y. Cheon, S.H. Joo, S.-D. Yim, K.A. Kuttiyiel, K. Sasaki, R.R. Adzic, G.-G. Park, Enhancement of Oxygen Reduction Reaction Activities by Pt Nanoclusters Decorated on Ordered Mesoporous Porphyrinic Carbons, *Journal of Materials Chemistry A*, 4 (2016) 5869–5876.

[8] Y. Zhou, R. Pasquarelli, T. Holme, J. Berry, D. Ginley, R. O'Hayre, Improving PEM Fuel Cell Catalyst Activity and Durability Using Nitrogen-Doped Carbon Supports: Observations from Model Pt/HOPG Systems, *Journal of Materials Chemistry*, 19 (2009) 7830.

[9] L.F. Mabena, S. Sinha Ray, S.D. Mhlanga, N.J. Coville, Nitrogen-Doped Carbon Nanotubes as a Metal Catalyst Support, *Applied Nanoscience*, 1 (2011) 67–77.

[10] L. Dai, Y. Xue, L. Qu, H.-J. Choi, J.-B. Baek, Metal-Free Catalysts for Oxygen Reduction Reaction, *Chemical Reviews*, 115 (2015) 4823–4892.

[11] C. Alegre, D. Sebastián, M. Gálvez, E. Baquedano, R. Moliner, A. Aricò, V. Baglio, M. Lázaro, N-Doped Carbon Xerogels as Pt Support for the Electro-Reduction of Oxygen, *Materials*, 10 (2017) 1092.

[12] X. Feng, Y. Bai, M. Liu, Y. Li, H. Yang, X. Wang, C. Wu, Untangling the Respective Effects of Heteroatom-Doped Carbon Materials in Batteries, Supercapacitors and the ORR to Design High Performance Materials, *Energy & Environmental Science*, 14 (2021) 2036–2089.

[13] D. Tang, X. Sun, D. Zhao, J. Zhu, W. Zhang, X. Xu, Z. Zhao, Nitrogen-Doped Carbon Xerogels Supporting Palladium Nanoparticles for Selective Hydrogenation Reactions: The Role of Pyridine Nitrogen Species, *ChemCatChem*, 10 (2018) 1291–1299.

[14] W. Al-Hajri, Y. De Luna, N. Bensalah, Review on Recent Applications of Nitrogen-Doped Carbon Materials in CO_2 Capture and Energy Conversion and Storage, *Energy Technology*, 10 (2022).

[15] X.-F. Li, K.-Y. Lian, L. Liu, Y. Wu, Q. Qiu, J. Jiang, M. Deng, Y. Luo, Unraveling the Formation Mechanism of Graphitic Nitrogen-Doping in Thermally Treated Graphene with Ammonia, *Scientific Reports*, 6 (2016) 23495.

[16] Z. Su-Bing, S. Si-Xiu, Wei-Wei, X. Jun-Jian, L. Yan, The Preparation of Nitrogen-doped Carbon Nanotubes from Pyridine, *Acta Physico-Chimica Sinica*, 20 (2004) 1320–1323.

[17] Y.-C. Lin, C.-Y. Lin, P.-W. Chiu, Controllable Graphene N-doping with Ammonia Plasma, *Applied Physics Letters*, 96 (2010).

[18] Y. Wang, Y. Shao, D.W. Matson, J. Li, Y. Lin, Nitrogen-Doped Graphene and Its Application in Electrochemical Biosensing, *ACS Nano*, 4 (2010) 1790–1798.

[19] P. Sharma, A. Bilican, W. Schmidt, C. Ochoa-Hernández, M. Etter, C. Weidenthaler, Nitrogen Doping in Carbon Xerogels via Ammonia Pyrolysis: A Case Study, *Materials Today Chemistry*, 40 (2024) 102238.

[20] M.L.C. Piedboeuf, A.F. Léonard, G. Reichenauer, C. Balzer, N. Job, How Do the Micropores of Carbon Xerogels Influence their Electrochemical Behavior as Anodes for Lithium-Ion Batteries?, *Microporous and Mesoporous Materials*, 275 (2019) 278–287.

[21] M. Tatoulian, F. Arefi-Khonsari, N. Shahidzadeh-Ahmadi, J. Amouroux, Comparison of the Efficiency of N2 and NH3 plasma Treatments to Improve the Adhesion of PP Films to in situ Deposited Al Coatings Study of Ageing Phenomena in Terms of Acid-base Properties, *International Journal of Adhesion and Adhesives*, 15 (1995) 177–184.

[22] C.R. Vandenabeele, S. Lucas, Technological Challenges and Progress in Nanomaterials Plasma Surface Modification – A Review, *Materials Science and Engineering: R: Reports*, 139 (2020) 100521.

[23] C. Arpagaus, A. Sonnenfeld, Ph.R. von Rohr, A Downer Reactor for Short-time Plasma Surface Modification of Polymer Powders, *Chemical Engineering & Technology*, 28 (2005) 87–94.

[24] C. Vahlas, B. Caussat, P. Serp, G.N. Angelopoulos, Principles and Applications of CVD Powder Technology, *Materials Science and Engineering: R: Reports*, 53 (2006) 1–72.

[25] A. Zubiaur, N. Job, Streamlining of the Synthesis Process of Pt/Carbon Xerogel Electrocatalysts with High Pt Loading for the Oxygen Reduction Reaction in Proton Exchange Membrane Fuel Cells Applications, *Applied Catalysis B: Environmental*, 225 (2018) 364–378.

[26] C. Alegre, M.E. Gálvez, R. Moliner, V. Baglio, A.S. Aricò, M.J. Lázaro, Towards an Optimal Synthesis Route for the Preparation of Highly Mesoporous Carbon Xerogel-Supported Pt Catalysts for the Oxygen Reduction Reaction, *Applied Catalysis B: Environmental*, 147 (2014) 947–957.

[27] J. Rouquerol, P. Llewellyn, F. Rouquerol, Is the BET Equation Applicable to Microporous Adsorbents?, in: Studies in Surface Science and Catalysis, 2007: pp. 49–56.

[28] G. Bergeret, P. Gallezot, Particle Size and Dispersion Measurements, in: Handbook of Heterogeneous Catalysis, 2008: pp. 738–765.

[29] I.N. Leontyev, A.B. Kuriganova, N.G. Leontyev, L. Hennet, A. Rakhmatullin, N. V. Smirnova, V. Dmitriev, Size Dependence of the Lattice Parameters of Carbon Supported Platinum Nanoparticles: X-Ray Diffraction Analysis and Theoretical Considerations, *RSC Advances*, 4 (2014) 35959–35965.

[30] J. Biscoe, B.E. Warren, An X-Ray Study of Carbon Black, *Journal of Applied Physics*, 13 (1942) 364–371.

[31] F. Maillard, E.R. Savinova, U. Stimming, CO Monolayer Oxidation on Pt Nanoparticles: Further Insights into the Particle Size Effects, *Journal of Electroanalytical Chemistry*, 599 (2007) 221–232.

[32] S. Trasatti, O.A. Petrii, Real Surface Area Measurements in Electrochemistry, *Journal of Electroanalytical Chemistry*, 327 (1992) 353–376.

[33] F.L. Deschamps, J.G. Mahy, A.F. Léonard, N. Job, Rotating Disk Electrode Measurements on Low and High Loading Catalyst Layers: Diffusion Limitations and Application to Pt Catalysts Supported on Porous Micrometric Carbon Xerogel Particles Designed for Proton Exchange Membrane Fuel Cells, *Journal of Electroanalytical Chemistry*, 933 (2023) 117279.

[34] B. Karaman, H. Tonnoir, D. Huo, B. Carré, A.F. Léonard, J.C. Gutiérrez, M.L. Piedboeuf, A. Celzard, V. Fierro, C. Davoisne, R. Janot, N. Job, CVD-Coated Carbon Xerogels for Negative Electrodes of Na-Ion Batteries, *Carbon*, 225 (2024) 119077.

[35] S. Pylypenko, A. Borisevich, K.L. More, A.R. Corpuz, T. Holme, A.A. Dameron, T.S. Olson, H.N. Dinh, T. Gennett, R. O'Hayre, Nitrogen: Unraveling the Secret to Stable

Carbon-Supported Pt-Alloy Electrocatalysts, *Energy & Environmental Science*, 6 (2013) 2957–2964.

[36] C. Alegre, D. Sebastián, M.J. Lázaro, Carbon Xerogels Electrochemical Oxidation and Correlation with their Physico-Chemical Properties, *Carbon*, 144 (2019) 382–394.

[37] J.Y. Yook, J. Jun, S. Kwak, Amino Functionalization of Carbon Nanotube Surfaces with NH3 Plasma Treatment, *Applied Surface Science*, 256 (2010) 6941–6944.

[38] A. Kozhushner, Q. Li, L. Elbaz, Heteroatom-Doped Carbon Supports with Enhanced Corrosion Resistance in Polymer Electrolyte Membrane Fuel Cells, *Energies*, 16 (2023) 3659.

[39] R. Brandiele, C. Durante, M. Zerbetto, N. Vicentini, T. Kosmala, D. Badocco, P. Pastore, G.A. Rizzi, A.A. Isse, A. Gennaro, Probing the Correlation between Pt-Support Interaction and Oxygen Reduction Reaction Activity in Mesoporous Carbon Materials Modified with Pt-N Active Sites, *Electrochimica Acta*, 277 (2018) 287–300.

[40] R.J.J. Jansen, H. van Bekkum, XPS of Nitrogen-Containing Functional Groups on Activated Carbon, *Carbon*, 33 (1995) 1021–1027.

[41] J.R. Pels, F. Kapteijn, J.A. Moulijn, Q. Zhu, K.M. Thomas, Evolution of Nitrogen Functionalities in Carbonaceous Materials during Pyrolysis, *Carbon*, 33 (1995) 1641–1653.

[42] S. Maldonado, K.J. Stevenson, Influence of Nitrogen Doping on Oxygen Reduction Electrocatalysis at Carbon Nanofiber Electrodes, *The Journal of Physical Chemistry B*, 109 (2005) 4707–4716.

[43] N.P. Subramanian, X. Li, V. Nallathambi, S.P. Kumaraguru, H. Colon-Mercado, G. Wu, J.-W. Lee, B.N. Popov, Nitrogen-Modified Carbon-Based Catalysts for Oxygen Reduction Reaction in Polymer Electrolyte Membrane Fuel Cells, *Journal of Power Sources*, 188 (2009) 38–44.

[44] K. Kakaei, M.D. Esrafili, A. Ehsani, Oxygen Reduction Reaction, in: Graphene Surfaces: Particles and Catalysts, 2019: pp. 203–252.

[45] H. Wang, T. Maiyalagan, X. Wang, Review on Recent Progress in Nitrogen-Doped Graphene: Synthesis, Characterization, and Its Potential Applications, *ACS Catalysis*, 2 (2012) 781–794.

[46] M. Kakunuri, S. Kali, C.S. Sharma, Catalytic Graphitization of Resorcinol-Formaldehyde Xerogel and its Effect on Lithium Ion Intercalation, *Journal of Analytical and Applied Pyrolysis*, 117 (2016) 317–324.

[47] B. Karaman, H. Tonnoir, D. Huo, J. Castro Gutiérrez, B. Carré, A.F. Léonard, M. Bermont, Z. Deckers, A. Celzard, V. Fierro, C. Davoisne, R. Janot, N. Job, Post-Treatments on Carbon Xerogels to Improve their Performance as Negative Electrodes of Na-Ion Batteries, *Carbon*, 246 (2026) 120841.

[48] F. Yi, S.Q. Arlington, J. Gorham, W. Osborn, E.J. Crumlin, S. Nemsak, D.A. LaVan, Growth and Decomposition of Pt Surface Oxides, *The Journal of Physical Chemistry Letters*, 13 (2022) 6171–6176.

[49] A. Parnière, Électrodes pour Piles à Combustible à base de Carbones Modifiés, Université de Montpellier, 2023.

[50] E.I. Vovk, A. V. Kalinkin, M.Yu. Smirnov, I.O. Klembovskii, V.I. Bukhtiyarov, XPS Study of Stability and Reactivity of Oxidized Pt Nanoparticles Supported on TiO_2, *The Journal of Physical Chemistry C*, 121 (2017) 17297–17304.

[51] A.S. Aricò, A.K. Shukla, H. Kim, S. Park, M. Min, V. Antonucci, An XPS Study on Oxidation States of Pt and its Alloys with Co and Cr and its Relevance to Electroreduction of Oxygen, *Applied Surface Science*, 172 (2001) 33–40.

[52] M.A. van Spronsen, J.W.M. Frenken, I.M.N. Groot, Observing the Oxidation of Platinum, *Nature Communications*, 8 (2017) 429.

[53] M.-H. Yeh, S.-H. Chang, L.-Y. Lin, H.-L. Chou, R. Vittal, B.-J. Hwang, K.-C. Ho, Size Effects of Platinum Nanoparticles on the Electrocatalytic Ability of the Counter Electrode in Dye-Sensitized Solar Cells, *Nano Energy*, 17 (2015) 241–253.

[54] C. Dong, C. Lian, S. Hu, Z. Deng, J. Gong, M. Li, H. Liu, M. Xing, J. Zhang, Size-Dependent Activity and Selectivity of Carbon Dioxide Photocatalytic Reduction over Platinum Nanoparticles, *Nature Communications*, 9 (2018) 1252.

[55] L.-S. Zhang, X.-Q. Liang, W.-G. Song, Z.-Y. Wu, Identification of the Nitrogen Species on N-Doped Graphene Layers and Pt/NG Composite Catalyst for Direct Methanol Fuel Cell, *Physical Chemistry Chemical Physics*, 12 (2010) 12055.

[56] C.L. Muhich, J.Y. Westcott, T.C. Morris, A.W. Weimer, C.B. Musgrave, The Effect of N and B Doping on Graphene and the Adsorption and Migration Behavior of Pt Atoms, *The Journal of Physical Chemistry C*, 117 (2013) 10523–10535.

[57] M.N. Groves, C. Malardier-Jugroot, M. Jugroot, Improving Platinum Catalyst Durability with a Doped Graphene Support, *The Journal of Physical Chemistry C*, 116 (2012) 10548–10556.

[58] T. Holme, Y. Zhou, R. Pasquarelli, R. O'Hayre, First Principles Study of Doped Carbon Supports for Enhanced Platinum Catalysts, *Physical Chemistry Chemical Physics*, 12 (2010) 9461–9468.

[59] Y. Zhou, T. Holme, J. Berry, T.R. Ohno, D. Ginley, R. O'Hayre, Dopant-Induced Electronic Structure Modification of HOPG Surfaces: Implications for High Activity Fuel Cell Catalysts, *The Journal of Physical Chemistry C*, 114 (2010) 506–515.

[60] A. Cosenza, C. Roiron, G. Ferro, P. Atanassov, Nitrogen-Doped Carbon Supports for Pt-Based Fuel Cell Electrocatalysts, *Chemical Engineering Journal*, 512 (2025) 162816.

[61] M. Peuckert, T. Yoneda, R.A.D. Betta, M. Boudart, Oxygen Reduction on Small Supported Platinum Particles, *Journal of The Electrochemical Society*, 133 (1986) 944–947.

[62] M. Shao, A. Peles, K. Shoemaker, Electrocatalysis on Platinum Nanoparticles: Particle Size Effect on Oxygen Reduction Reaction Activity, *Nano Letters*, 11 (2011) 3714–3719.

[63] J. Marie, S. Berthon-Fabry, P. Achard, M. Chatenet, A. Pradourat, E. Chainet, Highly Dispersed Platinum on Carbon Aerogels as Supported Catalysts for PEM Fuel Cell-Electrodes: Comparison of Two Different Synthesis Paths, *Journal of Non-Crystalline Solids*, 350 (2004) 88–96.

[64] A. Parnière, P.-Y. Blanchard, S. Cavaliere, N. Donzel, B. Prelot, J. Rozière, D.J. Jones, Nitrogen Plasma Modified Carbons for PEMFC with Increased Interaction with Catalyst and Ionomer, *Journal of The Electrochemical Society*, 169 (2022) 044502.

[65] S. Zhu, Y. Huang, T. Yu, Y. Lei, X. Zhu, T. Yang, J. Gu, C. Wang, Enhance the Durability of the Oxygen Reduction Reaction Catalyst through the Synergy of Improved Graphitization and Nitrogen Doping of Carbon Carrier, *International Journal of Hydrogen Energy*, 51 (2024) 956–965.

[66] W. Sheng, S. Chen, E. Vescovo, Y. Shao-Horn, Size Influence on the Oxygen Reduction Reaction Activity and Instability of Supported Pt Nanoparticles, *Journal of The Electrochemical Society*, 159 (2011) B96–B103.

[67] K. Kinoshita, Particle Size Effects for Oxygen Reduction on Highly Dispersed Platinum in Acid Electrolytes, *Journal of The Electrochemical Society*, 137 (1990) 845–848.

[68] E. Hornberger, T. Merzdorf, H. Schmies, J. Hübner, M. Klingenhof, U. Gernert, M. Kroschel, B. Anke, M. Lerch, J. Schmidt, A. Thomas, R. Chattot, I. Martens, J. Drnec, P. Strasser, Impact of Carbon N-Doping and Pyridinic-N Content on the Fuel Cell Performance and Durability of Carbon-Supported Pt Nanoparticle Catalysts, *ACS Applied Materials & Interfaces*, 14 (2022) 18420–18430.

[69] I. Esparbé, E. Brillas, F. Centellas, J.A. Garrido, R.M. Rodríguez, C. Arias, P.-L. Cabot, Structure and Electrocatalytic Performance of Carbon-Supported Platinum Nanoparticles, *Journal of Power Sources*, 190 (2009) 201–209.

Annex 3.1. Choice of ink formulation for catalysts supported on N-doped CVD-treated carbon xerogels

The catalysts inks examined in Chapter 2 were prepared by mixing the catalyst with a certain amount of Nafion® and of water and isopropanol (IPA), with water and IPA acting as a solvent. Provided the catalytic inks were sonicated long enough, consistent and reproducible catalytic properties were obtained, especially for fresh catalysts. Nevertheless, when water/IPA-based catalytic inks of CX0-C20-N30-Pt or CX0-C20-N30-Pt were prepared, and were deposited on the working electrode glassy carbon and sintered, very heterogeneous deposits were obtained, even after extended sonication of the ink (>1 h). This was attributed to the more hydrophobic character of those two samples, due to the higher amount of nitrogen at the surface.

To address this issue, two alternative solvents, ethanol and N-methyl-2-pyrrolidone (NMP), were considered to prepare layers on RDE with CX0-C20-N30-Pt. Ethanol was first preferred because of its low toxicity. For the ethanol-based ink, the catalytic layer deposition was noticeably more homogeneous. However, ethanol-based inks showed a tendency to spread excessively outside of the glassy carbon during deposition. An NMP-based ink was also tested. Although NMP is much less environmentally friendly than ethanol and water, it is also commonly used as a dispersion solvent for catalytic inks [1]. The spreading of NMP-based inks was less pronounced than for ethanol-based ones. Moreover, a relatively homogenous deposit was also observed.

Catalytic performances obtained with the different ink solvents were compared and are gathered in **Table A3.1.1**. A single measurement was carried out for the water/IPA-based ink, while two and three measurements were performed and averaged for the ethanol and NMP-based inks, respectively. The first notable observation concerns the *ECSA*, determined from area under CO electrooxidation peak (**Figure A3.1.1a**). For water/IPA-based and ethanol-based inks, the *ECSA* is equal to 70 and 67 $m^2.g^{-1}_{Pt}$, respectively. This value is rather low and more typical of carbon-black supported catalysts [2], such as the XC-72-Pt characterized in Chapter 2. In contrast, the NMP-based ink exhibits an *ECSA* of 107 $m^2.g^{-1}_{Pt}$. This value resembles much more that of other carbon xerogels (the *ECSA* of CX0-C20-was measured equal to 101 $m^2.g^{-1}_{Pt}$). It is thus possible that the Pt is not fully accessible after processing the catalytic layers using water/IPA mix or ethanol. Moreover, similar capacitive currents can be observed in the region 0.4-0.5 V *vs.* RHE in **Figure A3.1.1a-b**. This indicates that the low *ECSA* observed for water/IPA and ethanol-

based inks is not attributable to poor preparation nor to a loss of the active layer during measurements.

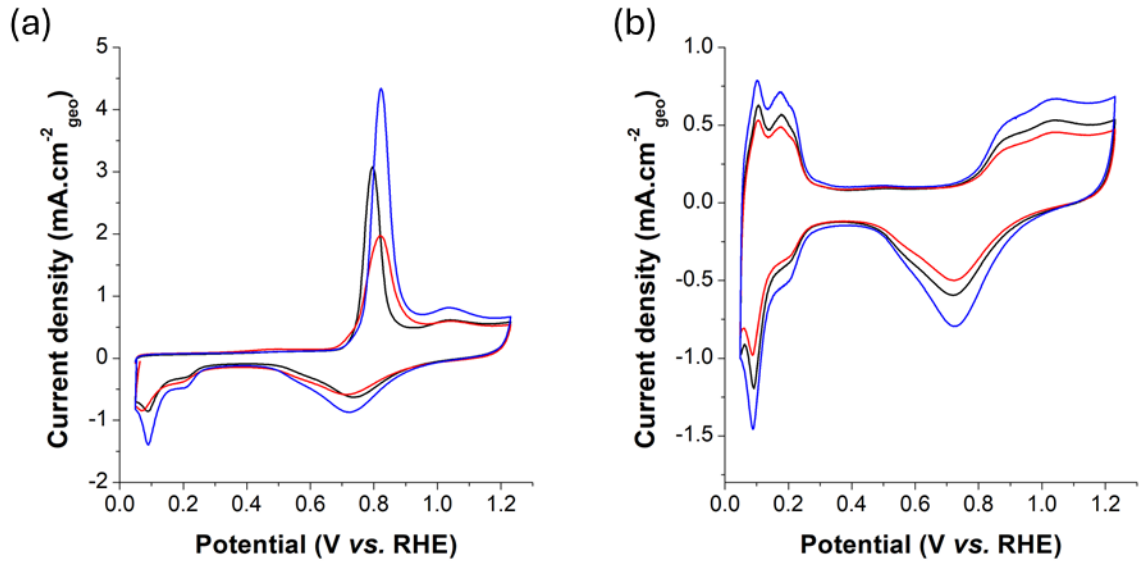

Figure A3.1.1. Electrochemical measurements of fresh catalysts performed in RDE configuration in 0.5 M H_2SO_4 at 25 ºC. (a) CO electro-oxidation curves and (b) cyclic voltammetry curves under Ar, of a water/IPA-based ink (■), ethanol-based ink (■) and NMP-based ink (■).

SA and *MA* were determined from ORR curves (**Figure A3.1.2a-c**). The *SA* are similar for all three solvents: 0.032, 0.041 and 0.033 $A.m^{-2}_{Pt}$ for water/IPA-based, ethanol-based and NMP-based ink, respectively. Since *SA* is normalized by the exposed surface of Pt, these small variations indicate that the intrinsic catalytic behavior of Pt nanoparticles remains essentially unchanged, regardless of the solvent used in the ink formulation. In contrast, the initial *MA* differ more noticeably: 2.21, 2.79 and 3.57 $A.g^{-1}_{Pt}$ for water/IPA-based, ethanol-based and NMP-based ink, respectively. The NMP-based ink shows a performance close to that of previously characterized carbon xerogels (CX0-C20-Pt has an initial M*A* of 3.29 $A.g^{-1}_{Pt}$). Regarding Tafel slopes, no significant variations are observed, regardless of the solvent. The slope consistently fall within the 60 – 70 $mV.dec^{-1}$ range, typical of the $(2+2)e^-$ mechanism.

Table A3.1.1. Catalyst properties of CX0-C20-N3.2-Pt determined by electrochemical analyses.

Ink solvent		CO stripping		ORR		
		ECSA[a] ($m^2.g^{-1}_{Pt}$)	d_{CO}[b] (nm)	***SA***[c] ($A.m^{-2}_{Pt}$)	***MA***[c] ($A.g^{-1}_{Pt}$)	***b***[d] ($mV.dec^{-1}$)
Water + IPA	**BoL**	70	4.0	0.032	2.21	71
	MoL	50	5.6	0.039	1.97	71
Ethanol	**BoL**	67 ± 4	4.2 ± 0.3	0.041 ± 0.005	2.79 ± 0.51	70 ± 1
	MoL	43 ± 3	6.6 ± 0.4	0.051 ± 0.005	2.22 ± 0.32	69 ± 1
NMP	**BoL**	107 ± 5	2.6 ± 0.1	0.033 ± 0.001	3.57 ± 0.17	60 ± 4
	MoL	70 ± 2	4.0 ± 0.1	0.043 ± 0.007	3.02 ± 0.61	67 ± 3

[a] *ECSA*: Electrochemically activity surface area of Pt normalized to the mass of Pt on the electrode, calculated from CO stripping measurement (Equation 3.5).

[b] d_{CO}: CO equivalent particle diameter of the Pt particles calculated from Equation 3.6.

[c] *SA* and *MA*: specific activity and mass activity measured at 0.95 V *vs.* RHE (Equations 3.8 and 3.9).

[d] *b*: Tafel plot obtained calculated from ORR measurements.

Fresh active layers that were deposited on the glassy carbon and dried were recovered for TEM observation for ethanol-based and NMP-based inks, as displayed in **Figure A3.1.3a-b**. The nanoparticle diameter d_{TEM} was observed, and found equal to 3.1 ± 0.5 nm for the ethanol-based ink and 3.5 ± 0.5 nm for NMP-based ink. No significant differences are observed, both for nanoparticles size and dispersion **(Figure A3.1.3c).**

Inks were then subjected to 5,000 potential cycles between 0.6 and 1.0 V *vs.* RHE, to simulate aging. The catalytic properties were then evaluated again. As expected, *ECSA* decreases for all samples. Interestingly, the relative *ECSA* loss is comparable across ink formulations, namely 29, 37 and 35% for water/IPA-based, ethanol-based and NMP-based ink, respectively. The relative evolution of *SA* and *MA* is also interesting to observe. *SA* increases for all inks, with increases of 22, 24, and 30% for water/IPA-based, ethanol-based and NMP-based inks. Meanwhile, *MA* decreases by 11, 20 and 15% for water/IPA-based, ethanol-based and NMP-based inks.

The underlying reasons for these trends are discussed in the main text. Most importantly, all inks exhibit a comparable aging pattern, despite having different absolute values. It shows that electrochemical measurements are consistent. However, the very heterogeneous deposition of the active layer with water/IPA-based and ethanol-based inks may be the reason why regular

values of *ECSA* and catalytic activity were not obtained with these inks. Therefore, the NMP-based ink was selected for the complete electrochemical assessment, as it provides absolute values of *ECSA* and *MA* that enables meaningful comparisons with undoped carbon xerogels.

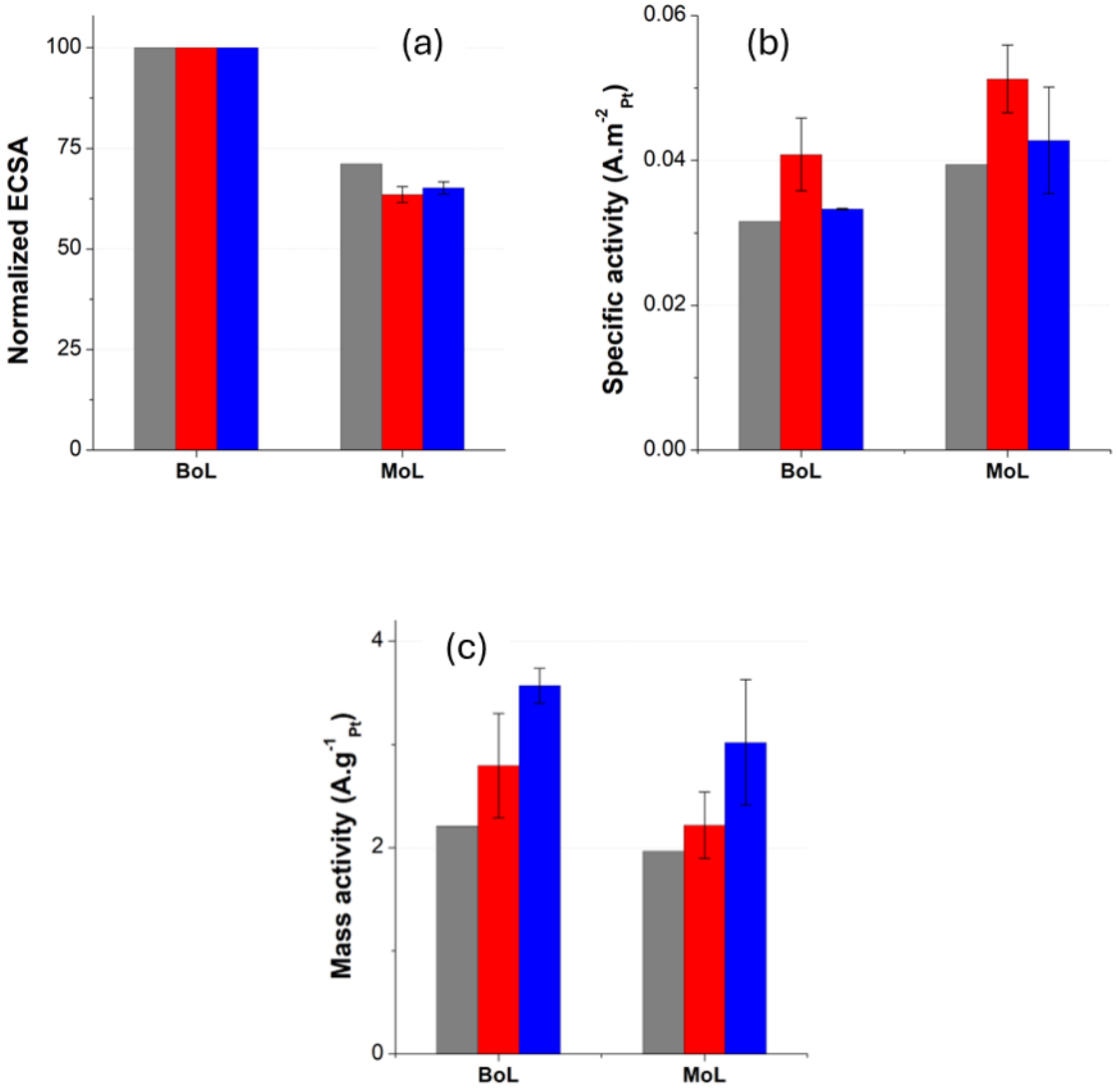

Figure A3.1.2. Evolution during Accelerated Stress Tests in RDE configuration of CX0-C20-N3.2-Pt with (a) the normalized ElectroChemically active Surface Area of Pt, (b) the specific activity at 0.95 V *vs.* RHE and (c) the mass activity at 0.95 V *vs.* RHE for a water/IPA-based ink (■), ethanol-based ink (■) and NMP-based ink (■).

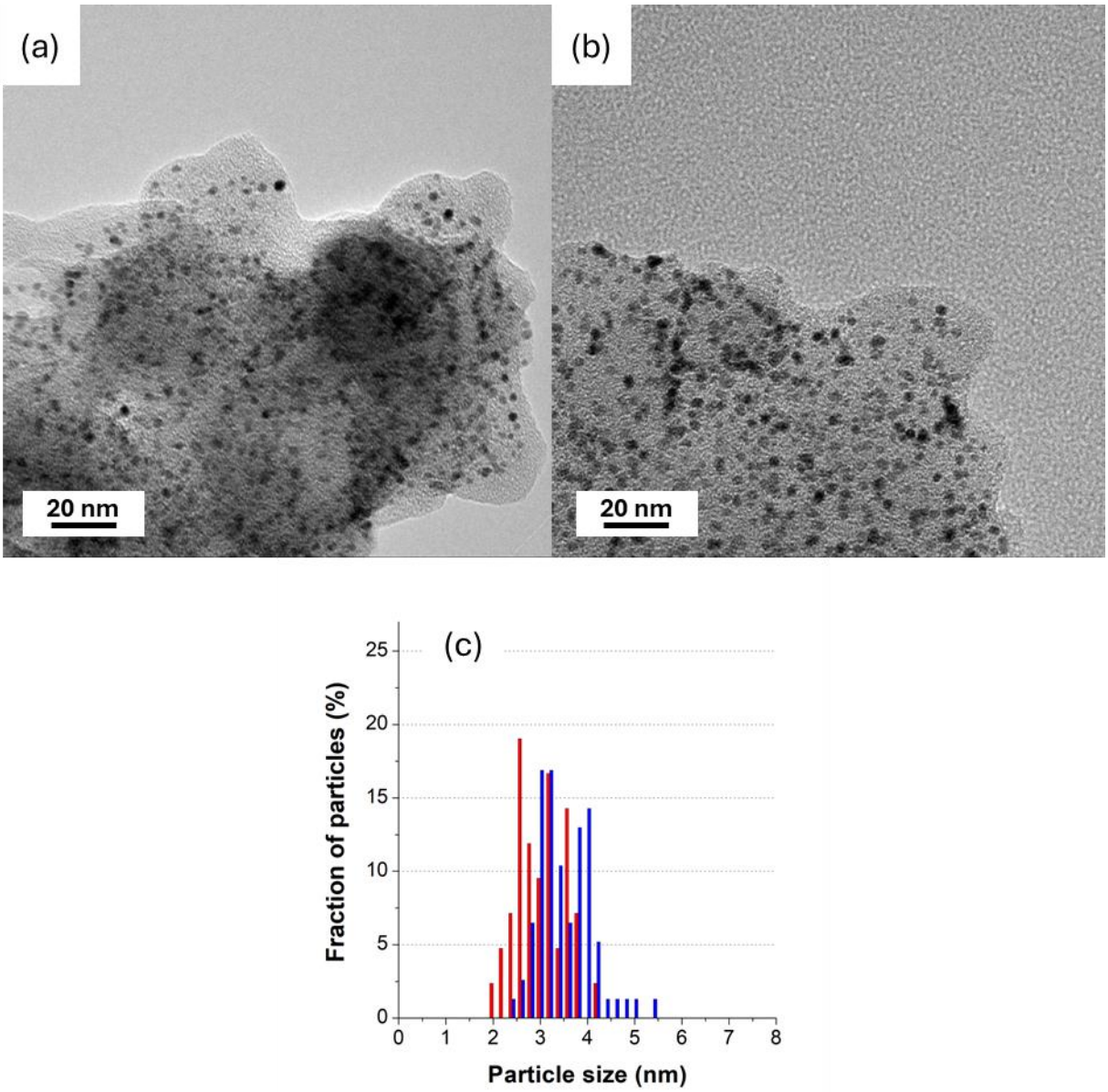

Figure A3.1.3. TEM micrographs of a CX0-C20-N3.2-Pt active layer made with (a) an ethanol-based ink and (b) an NMP-based ink. (c) Pt nanoparticles size distribution of the ethanol-based ink (■) and the NMP-based ink (■).

References

[1] T.-H. Kim, J.-Y. Yi, C.-Y. Jung, E. Jeong, S.-C. Yi, Solvent effect on the Nafion agglomerate morphology in the catalyst layer of the proton exchange membrane fuel cells, *International Journal of Hydrogen Energy*, 42 (2017) 478–485.

[2] F. Maillard, S. Schreier, M. Hanzlik, E.R. Savinova, S. Weinkauf, U. Stimming, Influence of particle agglomeration on the catalytic activity of carbon-supported Pt

nanoparticles in CO monolayer oxidation, *Physical Chemistry Chemical Physics*, (2005) 385–393.

Annex 3.2. Cyclic voltammetry under O_2 at different working electrode rotation speeds

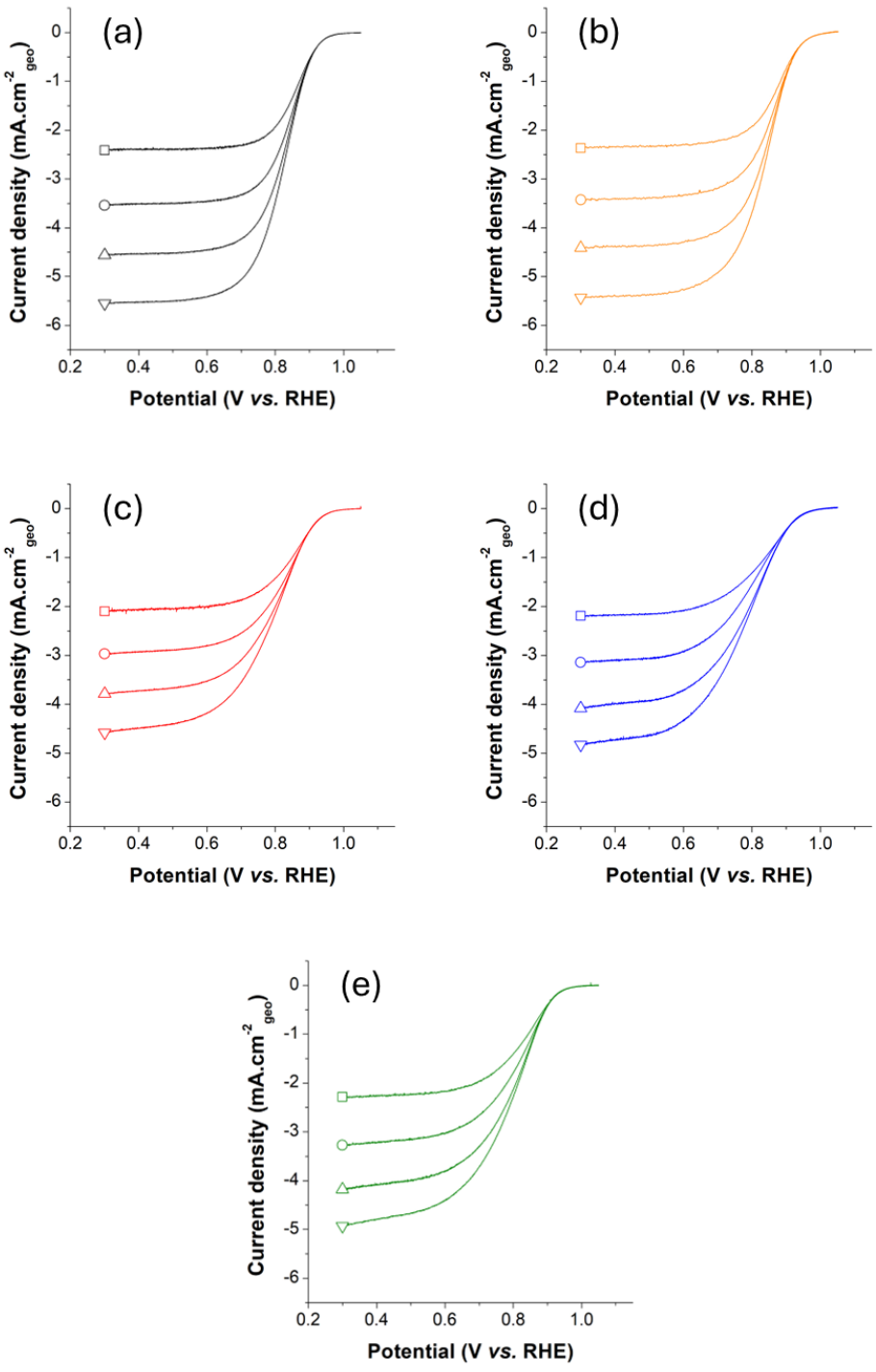

Figure A3.2.1. Cyclic voltammetry at *BoL* under O_2 and 25 ºC, performed with a scan rate of 1 mV.s^{-1} and an electrode rotation of 400 (—□—), 900 (—○—), 1600 (—△—) and 2500 (—▽—) rpm, of (a) CX0-Pt (—), (b) CX0-N30-Pt (—), (c) CX0-C20-Pt (—), (d) CX0-C20-N30-Pt (—) and (e) CX0-C20-N120-Pt (—).

- Chapter 4 -

DURABILITY OF CARBON XEROGEL-SUPPORTED CATALYSTS IN MEMBRANE-ELECTRODES ASSEMBLY CONFIGURATION

Abstract

In the final chapter of this thesis, the catalysts identified as the most promising in Chapters 2 and 3 were selected for evaluation in Membrane-Electrodes Assembly (MEA) configuration on a Proton Exchange Membrane Fuel Cell test bench. These materials were first integrated as the cathodic layer catalyst into MEAs. Following the same approach as in previous chapters, the catalytic layers obtained were subjected to accelerated aging *via* cell voltage cycling, and their performances were evaluated before and after aging. Their durability was also benchmarked against a commercial carbon-black supported catalyst with a similar Pt loading. Overall, carbon xerogel-supported catalysts displayed better performances than the commercial carbon-black supported catalyst. Moreover, the catalyst supported on the carbon xerogel post-treated with chemical vapor deposition and subsequent high-temperature treatment at 1,500 ºC exhibited the best durability in MEA configuration.

Contributions

The preparation and electrochemical characterization of the MEAs were performed by the PhD candidate. Tom Servais, another PhD candidate of the Nanomaterials, Catalysis, Electrochemistry (NCE) group in Université de Liège, provided valuable training regarding the use of the spray-coater and operation of the fuel cell test bench. In the same way as in Chapters 2 and 3, the TEM micrographs were obtained with the assistance of Dr. Philippe Compère, from Département de Biologie, Ecologie et Evolution in Université de Liège.

4.1. Introduction

Extensive research is currently carried out on Proton Exchange Membrane Fuel Cells (PEMFCs) to improve their performances following various criteria. Nevertheless, the degradation of the PEMFC electrodes upon operation still limits their long-term durability and large-scale deployment. In this thesis, a carbon xerogel was selected as a catalyst support. This choice is primarily motivated by their tunable porosity that enables good dispersion of the Pt metal over the support and efficient mass transport [1]. Nonetheless, these carbon materials remain prone to corrosion that lead to catalyst degradation during operation [2,3]. To this end, various post-treatment strategies were applied to a carbon xerogel, with the aim of modifying its surface and therefore enhancing the durability of the electrodes made from this new catalyst support. In Chapter 2, the carbon xerogel was submitted to a Chemical Vapor Deposition (CVD) treatment and subsequently to a high-temperature treatment at 1,500 ºC. Then, in Chapter 3, the carbon xerogel and the carbon-coated carbon xerogel were submitted to a plasma-assisted nitrogen doping. Pt nanoparticles were subsequently deposited on all these carbon supports to obtain a series of catalysts. In both Chapters 2 and 3, accelerated stress tests (ASTs) were carried out on these different catalysts in liquid electrolyte (H_2SO_4 aqueous solution), on a Rotating Disk Electrode (RDE).

This three-electrode setup offers some practical advantages. Indeed, it is a simple setup to implement and it enables the evaluation of catalysts performances without the direct use of H_2 [4]. Small amounts of catalysts (~100 mg) are enough to perform the analysis. Moreover, in an RDE configuration, the liquid electrolyte provides abundant protonic pathways, resulting in measurements of catalytic activity with minimal proton transport limitations. As such, the three-electrode setup allows for a quick and reliable comparison of catalytic activities of different catalysts [5]. Nevertheless, while RDE experiments are excellent at providing an initial screening of catalyst materials, they are not completely representative of actual fuel cell conditions. Indeed, the choice of electrolyte directly affects the catalytic activity measured [6] as well as the durability of the catalytic layer upon aging [7]. Thus, assessing the true potential of a catalyst material is achieved by integrating the catalyst material into a Membrane-Electrodes Assembly (MEA) configuration [8]. In this configuration, analogous to that in PEMFC stacks, the cathodic catalytic layer is positioned between a proton exchange membrane and a gas diffusion layer, and assembled with a second (anodic) catalytic layer to form a complete cell that is further sandwiched between bipolar plates. Different variables can be controlled, such as the temperature, the cell backpressure, the gas flowrate and humidity inside

both electrodes, *etc.* The control of these variables allows for an accurate evaluation of the catalytic performances in real conditions; those performances are usually measured under the form of voltage-current curves, reflecting both the activity and the efficiency of the cell [9].
The aging of the catalytic layer can also be performed in MEA configuration, with accelerated stress test (AST) procedures. In principle, each AST procedure should be designed to target a single degradation mechanism within the MEA. Thus, several accelerated stress test protocols exist, each applying one specific stressor to the cell while keeping the other operating parameters constant. In general, three main cell parameters can be repeatedly varied to induce accelerated aging to a MEA: the cell voltage (*i.e.* the potential difference between the anode and the cathode) [10], the relative humidity [11] and the temperature [12]. Here, in this chapter, following the methodology adopted in Chapter 2 and 3, accelerated aging of the catalytic layer was obtained by inducing repeated variations in the cell voltage. It can be noted that, considering the anode exhibit negligible overpotential in PEMFCs, the anode can be used as a reference, with a potential equal to 0 V (*vs.* RHE) [13].

Such changes in the cell accelerate the degradation of both the Pt nanoparticles and the carbon support, particularly at the cathode side [14]. AST procedures targeting specifically Pt degradation involve repeated cycling of the cell voltage between 0.6 to around 0.95 V [15]. This window simulates regular PEMFC operation as the cells typically run at 0.6 V, while voltages around 0.95 V correspond to the open circuit voltage observed during idle stop operation [16]. In this voltage window, carbon corrosion is thermodynamically possible but usually remains kinetically limited [17]. In contrast, AST procedures targeting carbon support degradation typically use more extreme conditions, either by holding the cell voltage around 1.2 V [15] or by cycling it between 1.0 and around 1.5 V [18]. This window is used to simulate the startup/shutdown of the cell, where the cathode potential can approach 1.5 V *vs.* RHE, leading to severe carbon support degradation. However, such procedures are not necessarily well-suited for an initial screening, as they can cause extensive degradation of the entire catalytic layer.

This chapter is dedicated to the integration of the previously characterized catalysts into an MEA configuration, as cathodic catalytic layer. Indeed, it is at the cathode that the most severe degradation phenomena (carbon oxidation, Ostwald ripening, nanoparticle migration, *etc.*) predominantly occur in the cell [14]. After the MEAs were manufactured, the evaluation of their performances and durability under accelerated stress tests conditions was performed. To this end, voltage cycling was carried out within a voltage window (0.6-1.0V) that promotes Pt

degradation while limiting severe degradation of the carbon support. The *post mortem* analysis of the catalysts enabled detecting modifications in the Pt nanoparticles configuration. The different carbon xerogel-supported catalysts were also compared to a benchmark carbon black-supported catalyst, also characterized in Chapter 2.

4.2. Experimental

4.2.1. Materials selection

A resorcinol-formaldehyde carbon xerogel with an appropriate pore size, denoted as CX0 thereafter, was synthesized and fully characterized in Chapter 1 [14]. The material exhibited a BET surface area of 674 $m^2.g^{-1}$ and an average pore size of 71 nm, suitable for PEMFC applications [1]. This carbon xerogel was then subjected to a Chemical Vapor Deposition (CVD) treatment. The most promising material as a carbon support for catalyst was obtained for a CVD duration of 20 min. The carbon xerogel retrieved from this CVD treatment is denoted as CX0-C20. In addition to the CVD treatment, a high-temperature post-treatment at 1,500 °C was applied to CX0-C20. This sample is referred to as CX0-C20-HT1500. Details of these procedures can be found in Chapter 1. A plasma treatment using a N_2 source was also applied to CX0 and CX0-C20, to graft nitrogen atoms onto their surfaces. The plasma treatment procedure is described in Chapter 3. These samples are referred to as CX0-N30 and CX0-C20-N30.

The synthesis of Pt/CX catalysts was then performed on the above-mentioned carbon materials by direct reduction of a precursor (H_2PtCl_6) in liquid phase, using formic acid as a precursor. The synthesis procedure is described in the **section 2.2.1** of Chapter 2. The carbon xerogel-supported catalysts retrieved from the Pt deposition step are referred to as CX0-Pt, CX0-C20-Pt, CX0-C20-HT1500-Pt, CX0-N30-Pt and CX0-C20-N30-Pt. A commercial Pt/carbon black catalyst (De Nora, Vulcan XC-72, 20 wt. % Pt), denoted as Vulcan XC-72-Pt, was also chosen as benchmark. The main characteristics of all the materials, measured in previous chapters, are compiled in **Table 4.1**.

4.2.2. Membrane-Electrodes assembly preparation

The Membrane-Electrodes Assemblies (MEAs) were prepared by spray-coating. Catalytic layers were all deposited onto a 7 cm × 7 cm Nafion® N117 proton exchange membrane (PEM). The ink used had a constant formulation, with a carbon content of 0.5 wt.% and a Nafion-to-Carbon (*N/C*) mass ratio of 0.8 [19]. For the solvent, a water-to-isopropanol (*W/I*) mass ratio of 1.28 was selected. These proportions allow for a homogenous deposition while preventing clogging of the spray nozzle during operation. For the anode, a commercial carbon black-supported catalyst, already assessed in Chapter 2 (De Nora, Vulcan XC-72, 20 wt.% Pt, named XC-72-Pt) was used. Since the cathode is typically the element limiting the cell performances due to the slow ORR kinetics, it is essential to use an anode that that does not introduce additional limitations in the system. Thus, spray-coating was performed with a Pt loading target of 0.12 $mg_{Pt}.cm^{-2}_{geo}$ for both the anode and cathode. Using the same Pt loading in each electrode ensures that the anode is not the limiting side during fuel cell operation. For the cathode, the ink was prepared with the catalyst of interest. Inks were prepared and stirred 24 h prior to the spraying procedure. This cathode loading is close to the 2020 DoE benchmark total electrode loading of Pt of 0.125 $mg_{Pt}.cm^{-2}_{geo}$. The present total Pt loading is equal to 0.24 $mg_{Pt}.cm^{-2}_{geo}$ as identical loadings were used both at the anode and cathode. However, the anode loading can easily be decreased to values as low as 0.05 $mg_{Pt}.cm^{-2}_{geo}$ in actual PEMFC stacks [20], resulting in a total Pt loading of 0.17 $mg_{Pt}.cm^{-2}_{geo}$ (0.05 $mg_{Pt}.cm^{-2}_{geo}$ at the anode and 0.12 $mg_{Pt}.cm^{-2}_{geo}$ at the cathode).

The spray-coating was performed following these steps:

(i) The Nafion® membrane was first put onto a porous fabric fiberglass sheet deposited on a vacuum plate heated at 90 ºC. A 5 cm × 5 cm mask was centered on the membrane to define an electrode surface area of 25 cm²;

(ii) The cathode ink was sprayed on a 7 cm × 7 cm (49 cm²) area at a rate of 0.3 $mL.min^{-1}$ using 40 cycles for a total duration of 20 min. A schematic representation of the trajectory followed by the spray during one cycle is provided in **Figure 4.1a**. After removing the mask, a 5 cm × 5 cm electrode was obtained;

(iii) After the cathode deposition onto the PEM, the PEM was flipped and step (1) and (2) were repeated identically to deposit the anode, using the commercial catalyst-based ink.

The thickness of the deposited active layer was checked by profilometry [21]. To do so, inks were first deposited on a glass slide, using the exact same spraying program, prior to any

deposition on the Nafion® membrane. The spraying conditions were kept identical, with the only difference being the use of a 2.5 cm × 2.5 cm mask. Parallel strips of the active layer deposited on the glass slide were gently removed with a toothpick, so as to obtain at least 5 base strips. These channels serve as baseline markers to deduce the thickness of the deposit Profilometry measurements were then performed using a Bruker DektakXT® stylus contact profilometer. A stylus was moved across the 2.5 cm × 2.5 cm active layer deposit, perpendicularly to the channels (see **Figure 4.1b**). The stylus force was set at 1 µN and was moved at a speed of 833 $\mu m.s^{-1}$. The vertical position of the stylus was recorded every 2.78 µm. To obtain cells suitable for the test bench, the spray-coated membrane was then sandwiched between 250 µm-thick 5 cm × 5 cm Gas Diffusion layers (Quintech, Freudenberg H23C6) and 200 µm thick silicone gaskets (Quintech, GS-LB-SIL-PET-200) to ensure impermeability to gases. The assembly was pressed at 30,000 N for 210 s with a hydraulic press heated at 130 ºC to obtain the complete MEA. The MEA was then placed between two graphite bipolar plates with regular serpentine gas channels. The MEA and bipolar plates were kept assembled by two flanges tightened up together at 5 N.m using a click torque wrench. The overall assembly was then connected to the fuel cell test bench (potentiostat, gas tubes, heating rods).

4.2.3. Measurement procedure

A home-made fuel cell test bench coupled with a Biologic HCP-803 potentiostat was used to perform MEA characterization and accelerated stress tests. Four different gases were used to perform the measurements: Nitrogen (AirLiquide, ALPHAGAZ™ 1, ≥ 99.995%), Air (AirLiquide, ALPHAGAZ™ 1), Oxygen (AirLiquide, ALPHAGAZ™ 1, ≥ 99.995%) and Hydrogen (AirLiquide, ALPHAGAZ™ 1, ≥ 99.999%). All gases were humidified prior to entering the cell with Bronkhorst controlled evaporation mixing devices fed with ultrapure Milli-Q® water (18.2 MΩ.cm). The relative humidity was set at 100% for all gases at all time. The cell was also constantly heated at 70 ºC with the help of two heating resistors inserted into the stainless-steel flanges of the cell, and connected to a thermocouple inserted into one of the two bipolar plates. A back pressure of 5×10^4 Pa was also applied. The hydrogen-fed anode was assumed to exhibit negligible (anodic) overpotential, thereby not contributing to the voltage measured. Each MEA was submitted to accelerated stress tests performed over a period of four days on the fuel cell test bench. The reproducibility of measurements performed on this fuel cell test bench installation has been previously validated [22] and the accelerated aging protocol was adapted from reference [3]. At least two MEAs were characterized for each sample to

ensure proper reproducibility of the measurements with deviations not exceeding 20%. Indeed, at the lab scale, obtaining reproducible results can be challenging, especially if one considers the full chain of events, from electrode manufacturing to ASTs. As examples, the reproducibility of two MEAs of the same material is assessed in **Annex 4.1** for CX0-C20-Pt and CX0-C20-HT1500-Pt.

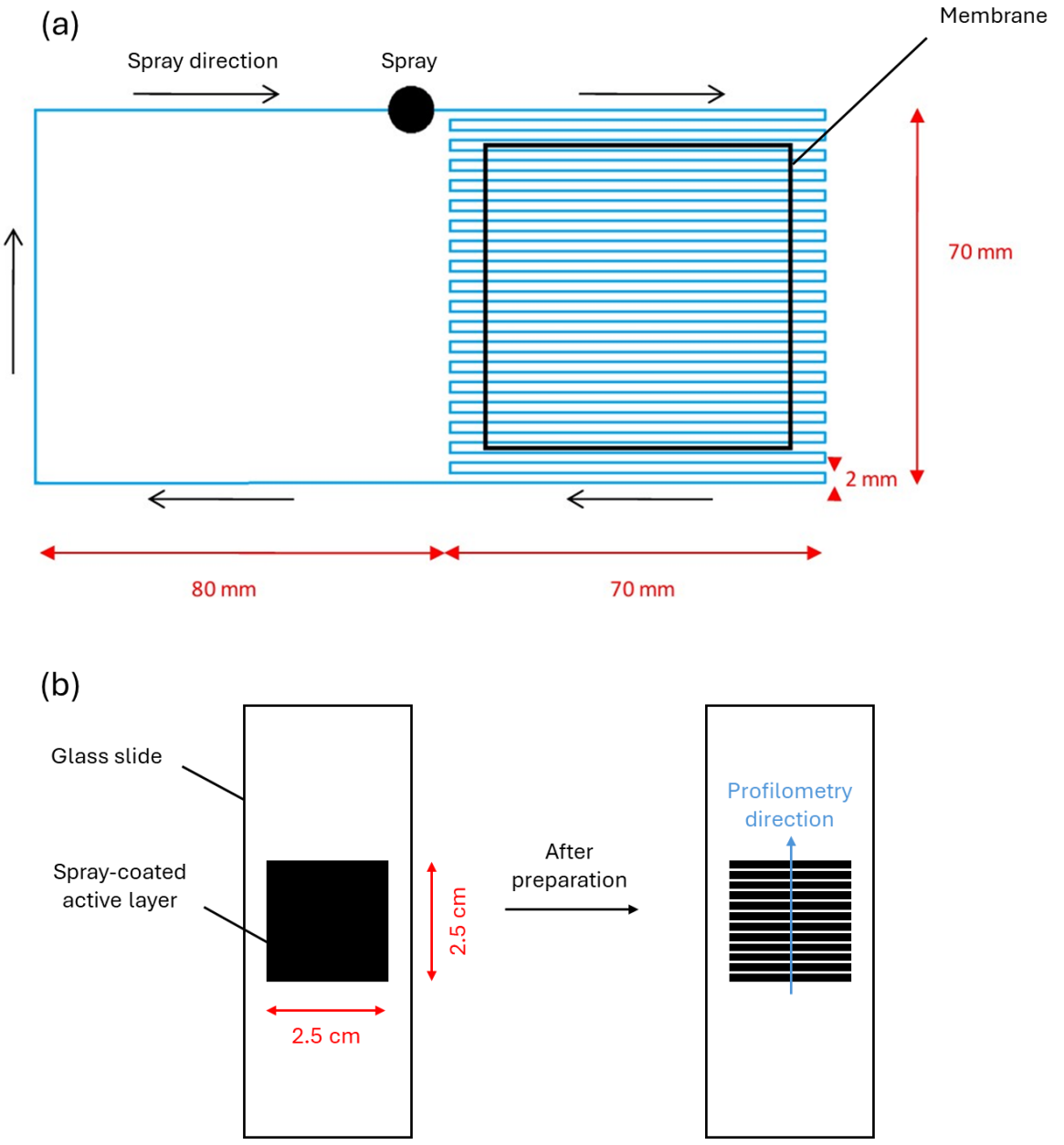

Figure 4.1. (a) Schematic representation of the spray trajectory during spray-coating on Nafion® membrane, reproduced from [22], and (b) illustration of the method used to determine the active layers thickness profiles *via* profilometry.

During Day 1, the conditioning of the cell was performed. The system was held at 0.6 V for several hours. This voltage value was chosen for conditioning because it provides sufficient current to stabilize the cell. To check for stabilization, dynamic voltage-current (E-i) polarization curves were recorded every 60 min until two consecutive identical curves were obtained. During the conditioning, the anode was supplied with H_2 (500 mL.min^{-1}) and the cathode supplied with air (2,000 mL.min^{-1}).

During Day 2, Beginning of Life (*BoL*) performances were assessed. Polarization curves under air were recorded every 60 min for a minimum of 3 h until two consecutive curves were obtained. The same procedure was subsequently performed to obtain polarization curves under O_2. During the acquisition of polarization curves, the anode was supplied with H_2 (500 mL.min^{-1}) and the cathode supplied with either air or O_2 (2,000 mL.min^{-1}).

During Day 3, the MEA was then subjected to an AST protocol consisting of alternating the cell voltage between 1.0 V (held for 3 s) and 0.6 V (held for 3 s), repeated for a total of 10,000 cycles. During the aging, the anode was supplied with H_2 (300 mL.min^{-1}) and the cathode with air (300 mL.min^{-1}). Middle of Life *(MoL)* performances were assessed with the same protocol as that described for Day 2. As a reminder, this voltage cycling window 0.6-1.0 V was selected to degrade preferentially the Pt nanoparticles while preventing severe carbon corrosion. Indeed, significant carbon oxidation encountered at cathode potentials above 1.0 V *vs.* RHE could lead to excessive degradation of the catalytic layer.

During Day 4, the MEA was subjected to 20,000 AST cycles performed in the same conditions as mentioned previously. During the aging, the anode was supplied with H_2 (300 mL.min^{-1}) and the cathode supplied with air (300 mL.min^{-1}). End of Life *(EoL)* performances were assessed with the same protocol as Day 2 again. *EoL* thus corresponds to a total of 30,000 cycles.

Cyclic voltammetry curves under nitrogen at both electrodes (300 mL.min^{-1}) were also recorded at the beginning of each day to obtain a corrected CV and to evaluate the electrochemically active surface area (*ECSA*) of Pt throughout the aging process. During these measurements, hydrogen was supplied to the anode (300 mL.min^{-1}), and nitrogen was supplied to the cathode (300 mL.min^{-1}). Cyclic voltammetries were recorded between 0.05 and 1.20 V with a scan rate of 20 mV.s^{-1}. Three complete voltammetry cycles were performed to ensure a stable signal of Pt, although only the last cycle was used for calculations.

Cycling voltammetry allowed to retrieve the *ECSA via* the integration of the area under the Hydrogen Underpotential Deposition (H_{UPD}) peak, occurring between 0.15 and 0.35 V, and corresponding to the charge needed to oxidize the hydrogen adsorbed at the Pt surface. Thus:

$$ECSA = \frac{Q_{\mathrm{H}}}{2.1\ L\ A} \tag{4.1}$$

where Q_H is the integral of the charge of the H_{UPD} peak (C), 2.1 $C.m^{-2}_{Pt}$ is the theoretical charge required to oxidize one complete monolayer of H adsorbed onto Pt, L is the loading of Pt of the working electrode ($g_{Pt}.m^{-2}_{geo}$), A is the geometric surface area of the electrode (m^2_{geo}). The double layer capacitance per surface area, C_{dl} (in $mF.cm^{-2}_{geo}$), was also calculated from cyclic voltammetry curves, with:

$$C_{\mathrm{dl}} = \frac{i_{\mathrm{capa}}}{S\ v} \tag{4.2}$$

where i_{capa} is the capacitive current (mA), taken in the area 0.4-0.5 V where no faradaic reactions related to Pt are observed, v is the scan rate ($V.s^{-1}$), and S the surface area of the electrode, equal to 25 cm² in each MEA.

Finally, the fresh and aged catalysts were observed with Transmission Electron Microscopy (TEM). A JEOL JEM-ARM 200F Cold FEG equipped with a spherical aberration probe corrector and operated with an acceleration voltage of 200 kV to was used to determine the Pt nanoparticle size distribution, before and after aging. For aged catalysts, after *EoL*, the MEA was disassembled and the carbon material that had been spray-coated was scratched from the Nafion® membrane and collected. Prior to observations, the powder samples were then dispersed into ethanol and mixed homogeneously with help of an ultrasonic bath. A drop of the suspension was then spread onto a copper grid (PELCO® TEM grid, 200 mesh Cu), and was left to dry under ambient air. From transmission electron microscopy (TEM) micrographs, the arithmetic average diameter, d_{TEM}, of the Pt nanoparticles was calculated on a sufficiently large number of Pt nanoparticles (> 50).

4.3. Results and discussion

4.3.1. Physico-chemical characterization of the catalysts

The electrochemical assessment of the catalysts was previously performed in a Rotating Disk Electrode (RDE) configuration in Chapters 2 and 3. In the present chapter, the catalyst

characterization was conducted in a MEA configuration, truly representative of a real PEM fuel cell system. For the sake of clarity, the main features of the fresh catalysts, as observed in Chapters 2 and 3, are summarized in the next paragraphs.

Table 4.1. Main characteristics of the catalysts determined by different analyses in Chapters 2 and 3.

Sample	A_{BET}[a]	S_{ext}[b]	N_{XPS}[c]	Pt_{TGA}[d]	$ECSA_{RDE}$[e]
	$m^2.g^{-1}_C$ ± 5%	$m^2.g^{-1}_C$ ± 5%	at.% ± 0.5	wt.% ± 1.3	$m^2.g_{Pt}^{-1}$
XC-72-Pt	197	140	n.d.[f]	16.1	74 ± 4
CX0-Pt	674	201	n.d.[f]	17.4	117 ± 7
CX0-C20-Pt	174	128	n.d.[f]	19.0	101 ± 4
CX0-N30-Pt	656	204	1.5	15.8	116 ± 10
CX0-C20-N30-Pt	200	142	3.2	16.7	107 ± 5
CX0-C20-HT1500-Pt	187	141	n.d.[f]	16.7	99 ± 23

[a] A_{BET}: BET specific surface area, calculated from nitrogen adsorption-desorption isotherms at 77 K.

[b] S_{ext}: external surface area, calculated from nitrogen adsorption-desorption isotherms at 77 K using the t-plot method.

[c] N_{XPS}: atomic percentage of nitrogen at the carbon surface, determined by XPS.

[d] Pt_{TGA}: mass fraction remaining at the end of TGA experiment and considered as being Pt.

[e] $ECSA_{RDE}$: Electrochemically activity surface area of Pt normalized by the mass of Pt on the electrode, determined in RDE configuration.

[f] Not determined: sample not subjected to N doping and thus not expected to contain significant amounts of N.

The results or thermogravimetric analysis under air, performed in previous chapters to evaluate the actual Pt content in the catalyst, are gathered in **Table 4.1**. It varies between 15.8 wt.% (for CX0-N30-Pt) and 19.0 wt.% (for CX0-C20-Pt), with an average value of 17.2 wt.%. These values are slightly lower than the target loading of 20 wt.%, suggesting that not all the Pt atoms in solution were deposited on the carbon support. Nevertheless, these loading are in good agreement with other Pt deposition syntheses performed through formic acid reduction [23,24]. TEM was also performed in Chapters 2 and 3 to determine the initial particle size distribution of the Pt nanoparticles on the different carbon supports; the results are recapitulated in **Figure 4.2** and **Figure 4.3**, and in **Table 4.2**. d_{TEM} was calculated to be 3.4, 3.4, 3.6, 2.8, 3.5 and 3.7 nm, for XC-72-Pt, CX0-Pt, CX0-C20-Pt, CX0-N30-Pt, CX0-C20-N30-Pt and CX0-C20-HT1500-Pt, respectively.

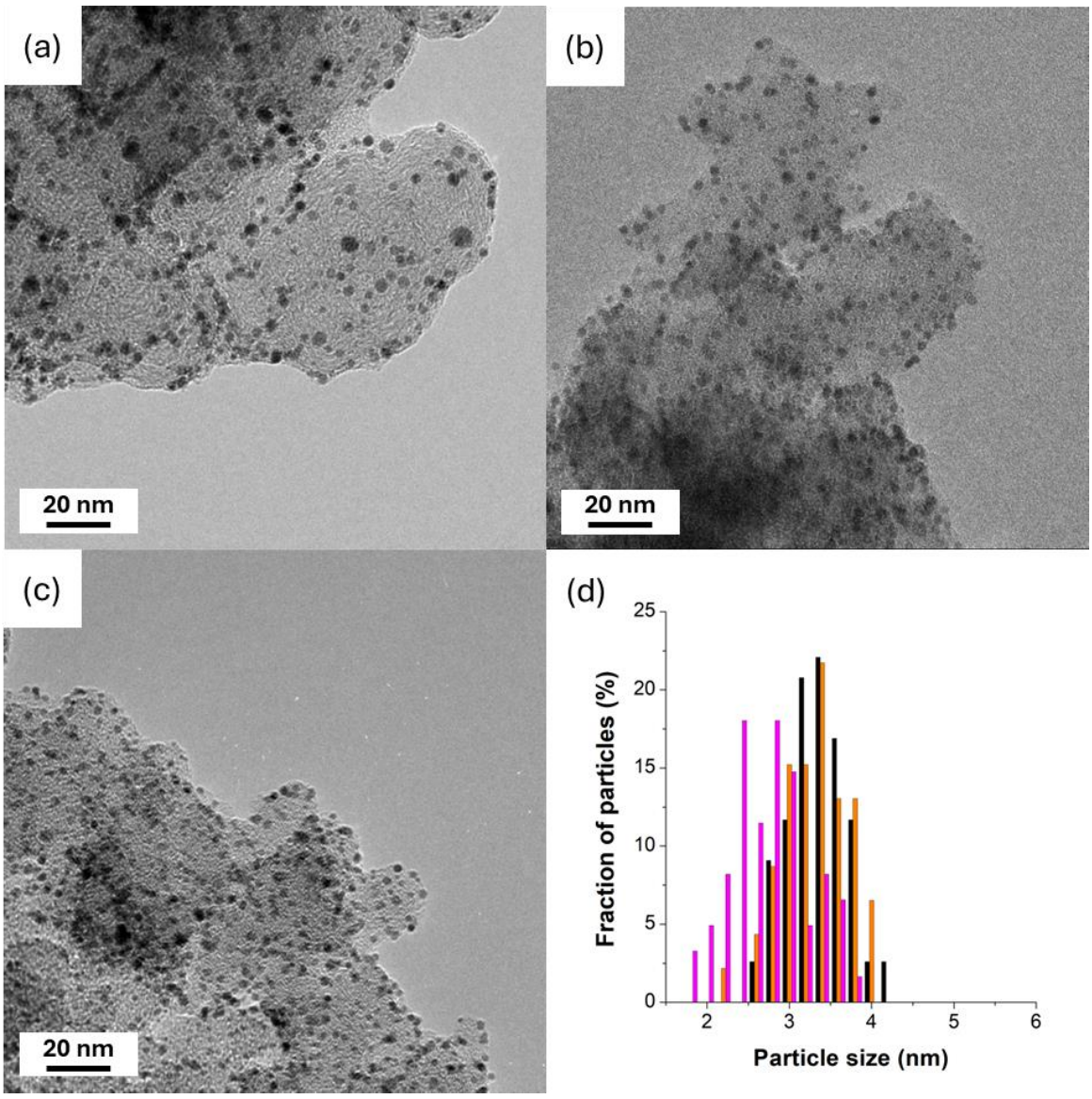

Figure 4.2. TEM micrographs of fresh (a) XC-72-Pt, (b) CX0-Pt, (c) CX0-N30-Pt, and (d) initial Pt nanoparticle size distribution of XC-72-Pt (■), CX0-Pt (■) and CX0-C20-Pt (■).

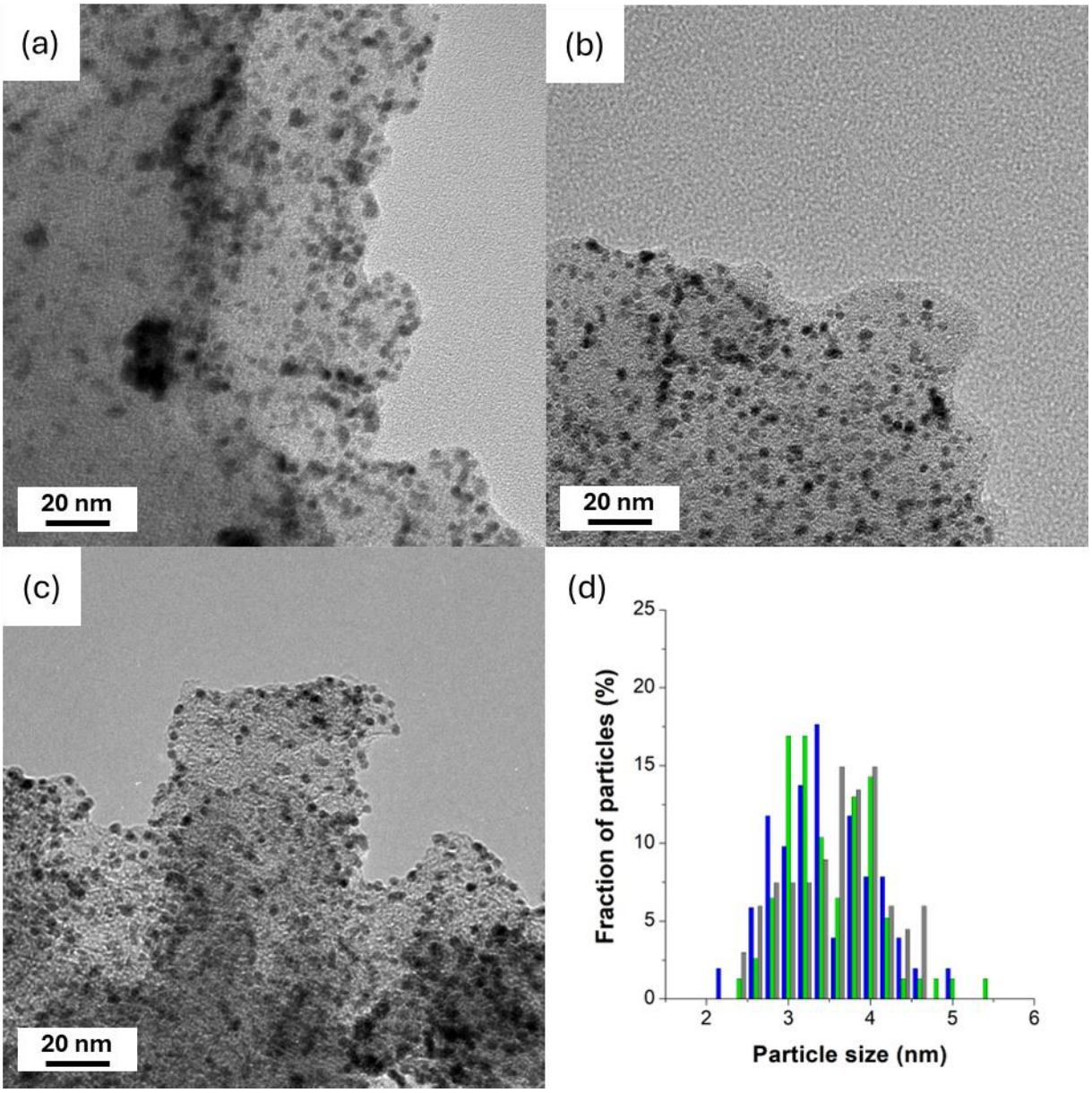

Figure 4.3. TEM micrographs of fresh (a) CX0-C20-Pt, (b) CX0-C20-N30-Pt, (c) CX0-C20-HT1500-Pt, and (d) initial Pt nanoparticle size distribution of CX0-C20-Pt (■), CX0-C20-N30-Pt (■) and CX0-C20-HT1500-Pt (■).

The average nanoparticle diameter remains relatively similar across samples. The only notable difference stems from CX0-N30-Pt where d_{TEM} is smaller (2.8 nm). As discussed in Chapter 3, this reduction in nanoparticle size can be attributed to nitrogen doping, which promotes better Pt nanoparticles deposition due to changes in charge density of the carbon network induced by nitrogen atoms [25]. Overall, the Pt dispersion is suitable for PEMFC applications. These samples were then selected for spray-coating and subsequent evaluation in MEA configuration.

Table 4.2. Pt nanoparticle size observed by TEM.

Catalyst	d_{TEM}[a] (nm)	
	Initial	**After AST**
	± 20%	
XC-72-Pt	3.4	9.2
CX0-Pt	3.4	7.7
CX0-C20-Pt	3.6	8.7
CX0-N30-Pt	2.8	7.0
CX0-C20-N30-Pt	3.5	9.5
CX0-C20-HT1500-Pt	3.7	7.3

[a] d_{TEM}: average arithmetic diameter of nanoparticles estimated from TEM micrographs for fresh catalysts and aged catalysts. Calculations were done on a number of nanoparticles > 50.

4.3.2. Characterization of the catalytic layers

The thickness profiles of the active layers deposited by spray-coating on a glass slide were obtained by profilometry and are provided in **Annex 4.2**. The catalytic layer prepared using the commercial carbon-black supported catalyst, XC-72-Pt, exhibits an average thickness of approximately 4–5 µm. In contrast, carbon-xerogel supported catalytic layers are thicker, reaching approximately 9–10 µm. This average thickness remains essentially unchanged regardless of the post-treatment the carbon xerogel was submitted to. The layer thicknesses observed here are in good accordance with other values reported for carbon black and carbon xerogel-supported catalytic layers deposited by spray-coating [21]. Moreover, the difference of thickness between carbon black and carbon xerogel-based inks was expected. Carbon xerogels are notably challenging to grind below *ca.* 5 µm [26]. In contrast, carbon blacks consist of smaller, spherical nodules. Moreover, carbon xerogels exhibit low density due to the large meso/macropore network. Consequently, active layers supported on carbon xerogels are thicker than those prepared with common carbon black supports for the same carbon mass [1].

4.3.3. Fuel cell characterization of the fresh catalysts

Cyclic voltammograms of fresh catalysts are displayed in **Figure 4.4**. The recorded current variations can be ascribed to faradaic contributions due to electron charge transfers occurring at the working electrode surface. During the cathodic scan (positive current) at low voltages (between 0.05-0.3 V), the increase of current can be attributed to the desorption and oxidation of hydrogen species, previously adsorbed on the Pt surface. This area corresponds to the Hydrogen Underpotential Deposition (H_{UPD}) region. It is established that the oxidation of a complete monolayer of H adsorbed on Pt is equal to approximately 2.1 $C.m^{-2}_{Pt}$ [27]. Thus, the *ECSA* can be determined using this cyclic voltammogram by integrating the charge associated with the H desorption peak (H_{UPD}, see **Equation (4.1)**). Moreover, the hydrogen desorption region exhibits two distinct zones for all catalysts with a first peak observed around 0.14 V, and a second peak observed around 0.21 V, These peaks are usually associated to the hydrogen desorption from Pt(110) and Pt(100) step sites, respectively [28]. Then, during the cathodic scan at high voltages (between 0.6-1.1 V), the current peak corresponds to the formation of Pt oxides, such as PtOH, PtO and PtO_2. Upon reversing the scan direction, the subsequent reduction of Pt oxides is observed, at high voltages and anodic scan (negative current). Finally, at low voltages and anodic scan, the protons H^+ are reduced and adsorb at the Pt surface.

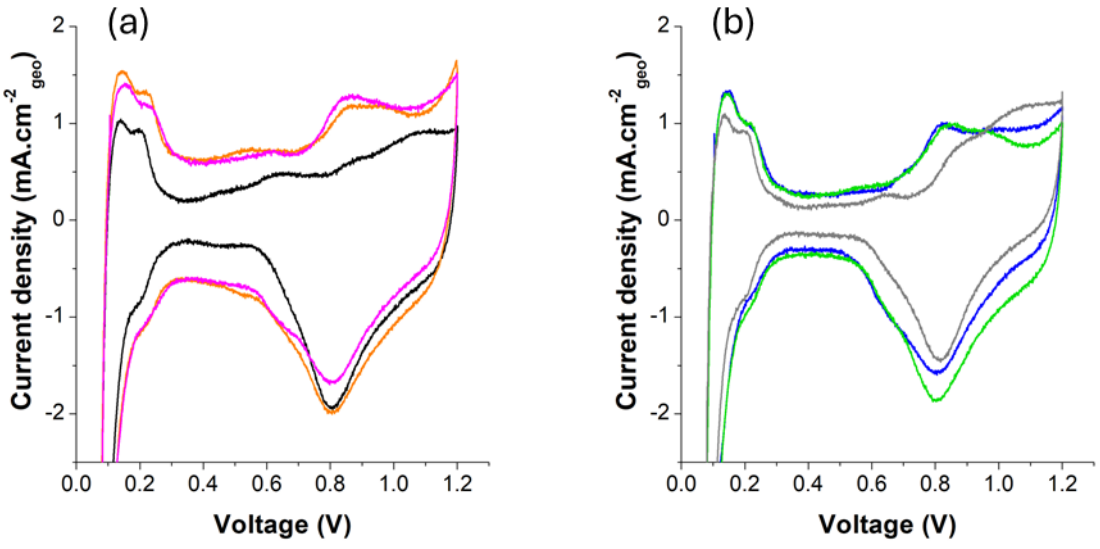

Figure 4.4. Cyclic voltammetry curves of fresh catalysts, recorded at 0.02 $V.s^{-1}$ with the anode under H_2 and the cathode under N_2 flow. (a) XC-72-Pt (—), CX0-Pt (—) and CX0-N30-Pt (—). (b) CX0-C20-Pt (—), CX0-C20-N30-Pt (—) and CX0-C20-HT1500-Pt (—). H_2

is injected at the anode with a flow of 300 mL.min^{-1} and N_2 is injected at the cathode with a flow of 300 mL.min^{-1}. Both gases are injected with a relative humidity of 100% and the cell is fixed at 70 ºC with a backpressure of 0.5 bar.

Table 4.3. Evolution of the catalyst properties in MEA configuration.

Catalyst		*ECSA*[a] ($m^2.g^{-1}_{Pt}$)	$J_{0.5}$[b] ($A.cm^{-2}_{geo}$)		C_{dl}[c] ($mF.cm^{-2}_{geo}$)
			Under air	Under O_2	
			± 20 %	± 20 %	
XC-72-Pt	BoL	24 ± 1	0.63	1.03	12 ± 1
	MoL	6 ± 1	0.39	0.75	5 ± 1
	EoL	3 ± 1	0.18	0.39	5 ± 1
CX0-Pt	BoL	34 ± 3	0.67	1.18	30 ± 1
	MoL	7 ± 1	0.48	0.86	28 ± 1
	EoL	4 ± 1	0.25	0.52	27 ± 2
CX0-C20-Pt	BoL	31 ± 4	0.72	1.36	14 ± 1
	MoL	9 ± 2	0.48	1.05	13 ± 1
	EoL	4 ± 1	0.31	0.68	13 ± 1
CX0-N30-Pt	BoL	31 ± 1	0.61	1.08	31 ± 1
	MoL	8 ± 1	0.35	0.78	27 ± 2
	EoL	3 ± 1	0.22	0.45	28 ± 2
CX0-C20-N30-Pt	BoL	33 ± 1	0.65	1.26	14 ± 1
	MoL	12 ± 2	0.49	0.96	12 ± 2
	EoL	6 ± 2	0.29	0.60	14 ± 2
CX0-C20-HT1500-Pt	BoL	27 ± 1	0.69	1.22	8 ± 1
	MoL	9 ± 2	0.55[d]	0.99[d]	6 ± 1
	EoL	4 ± 1	0.38[d]	0.77[d]	6 ± 2

[a] *ECSA*: Electrochemically active surface area of Pt, measured from H_{UPD} from **Equation (4.1)**.

[b] $J_{0.5}$: Current density measured at 0.5 V.

[c] C_{dl}: Double layer capacity, determined from **Equation (4.2)**.

[d] Values taken from MEA n°1 (see **Annex 4.1**), as a deviation > 20% is observed across MEAs.

As shown in **Figure 4.4**, the previously identified peaks exhibit similar shapes and positions for all samples, indicating comparable electrochemical behaviors. The *ECSA* values, obtained *via* the charge integration of the H_{UPD} region, are reported in **Table 4.3**.

Initial *ECSA* values were calculated equal to 24, 34, 31, 31, 33 and 27 $m^2.g^{-1}_{Pt}$ for XC-72-Pt, CX0-Pt, CX0-C20-Pt, CX0-N30-Pt, CX0-C20-N30-Pt and CX0-C20-HT1500-Pt, respectively. The exposed surface area of Pt remains similar across samples, although the lowest *ECSA* is observed for the carbon-black supported catalyst, XC-72-Pt. The *ECSA* measured in MEA configuration are different than those measured in RDE configuration (24, 34, 31, 31, 33 and 27 $m^2.g^{-1}_{Pt}$ *vs.* 74, 117, 101, 116, 107 and 99 $m^2.g^{-1}_{Pt}$, (see **Table 4.1**). This discrepancy between *ECSA* measurements in RDE or MEA configuration is commonly observed. It arises from the fact that, in MEA configuration, not all Pt nanoparticles are properly connected to the Nafion® ionomer network, and are therefore electrochemically inactive. In contrast, in RDE configuration, the proton-conducting medium is a liquid (0.5 M H_2SO_4 was used in Chapter 3), that is normally able to access all Pt sites. Thus, if the electrode is well designed, all Pt nanoparticles are electrochemically active, resulting in higher *ECSA* values. Despite this difference in absolute values, the trends observed in RDE are also observed in MEA configuration: the sample with the highest *ECSA* is CX0-Pt, and the one with the lowest *ECSA* is the carbon black-supported catalyst, XC-72-Pt. However, it is necessary to emphasize that, in MEA configuration, the ink formulation and the catalytic layer deposition parameters can strongly impact the overall performances of the MEA [29]. These parameters should therefore be optimized for each catalyst type. In this thesis, the ink formulation is better optimized for carbon xerogel-supported catalysts. Therefore, the *ECSA* reported here for XC-72-Pt may somewhat be sub-optimal compared to the *ECSA* obtained for all the carbon xerogel-supported catalysts.

At intermediate voltages, between 0.3 and 0.6 V, no charge transfer reactions occur. Nevertheless, a small current is observed. This originates from the capacitive charging of the electrode, due to the accumulation or removal of the species at the electrode/electrolyte interface when a potential difference is applied [30]. The capacitive current, free of any faradaic contribution, is proportional to the electrode area *i.e.* to the carbon surface accessible to the electrolyte. The double layer capacitance C_{dl} per surface area was calculated from **Equation (4.2)**. To do so, the capacitive current was taken as the average current measured between 0.4 and 0.5 V. The scan rate of the cyclic voltammetry was kept equal to 0.02 $V.s^{-1}$ and the surface area of the membrane was 25 cm^2. The resulting C_{dl} was found equal to 12, 30, 14, 31, 14 and

8 mF.cm$^{-2}_{geo}$ for XC-72-Pt, CX0-Pt, CX0-C20-Pt, CX0-N30-Pt, CX0-C20-N30-Pt and CX0-C20-HT1500-Pt, respectively. C_{dl} values are the highest for CX0-Pt and CX0-N30-Pt with 30 and 31 mF.cm$^{-2}_{geo}$., In Chapter 3, the micropore volume of CX0-Pt and CX0-N30-Pt were calculated equal to 0.26 and 0.25 cm^3.g$_c^{-1}$ and the external surface area at 201 and 204 m^2.g$_c^{-1}$, respectively. The high capacitance values are thus consistent with the developed microporosity of these carbon xerogels. Moreover, values are similar as they share similar pore texture, since N-doping treatment does not heavily impact the porosity of the carbon xerogel material (see Chapter 3). Meanwhile, for the carbon black material in the same conditions, the capacitive current is lower, 12 mF.cm$^{-2}_{geo}$. As observed in Chapter 2, carbon black materials have a less developed microporosity than carbon xerogel materials, with a micropore volume of 0.08 cm^3.g$_c^{-1}$. It is therefore not surprising that the capacitive current of XC-72-Pt is also smaller than that of CX0-Pt. CVD-treated samples also display lower C_{dl} than CX0-Pt, namely 14 mF.cm$^{-2}_{geo}$ for both CX0-C20-Pt and CX0-C20-N30-Pt. This behavior, also observed in RDE configuration in Chapter 2, is attributed to the extensive micropores closing during CVD treatment that reduces the accessible carbon surface as the micropore volume drops to 0.07 and 0.08 cm^3.g$_c^{-1}$ for CX0-C20-Pt and CX0-C20-N30-Pt. Finally, C_{dl} of CX0-C20-HT1500-Pt is smaller, 8 mF.cm$^{-2}_{geo}$. This difference may be attributed to an increase in hydrophobicity of CX0-C20-HT1500-Pt induced by the 1,500 ºC heat treatment, thereby potentially hindering the Nafion® ionomer to be distributed within the active layer.

The dynamic polarization curves of fresh catalysts were recorded both under air and under O_2 atmosphere at the cathode. The corresponding curves can be found in **Figure 4.5**. As expected, the current density produced decrease as the voltage increases. The current evolution is governed by different overpotentials, as explained in details in the Introduction section of this thesis. Briefly, at low currents and high voltages, the current produced is limited by ORR kinetics, *i.e.* by the energy barrier to overcome for the ORR to occur. At intermediate currents and voltages, additional losses arise from the ionic and electronic resistances generated by the different cell elements. At high currents and low voltages, the mass transport overpotential related to too slow diffusion of O_2 molecules inside the catalytic layer, also becomes significant and ultimately limits the current produced to a given value (limiting current density). The current densities at a voltage of 0.5 V are compared in **Table 4.3**. This voltage was selected as it is close to the maximum power output that is delivered by the cell, as displayed on **Figure 4.6**. This maximum power density represents a trade-off between the current generation and

voltage losses. The power output of a PEMFC typically reaches a maximum at an operating voltage of around 0.5 to 0.7 V [22].

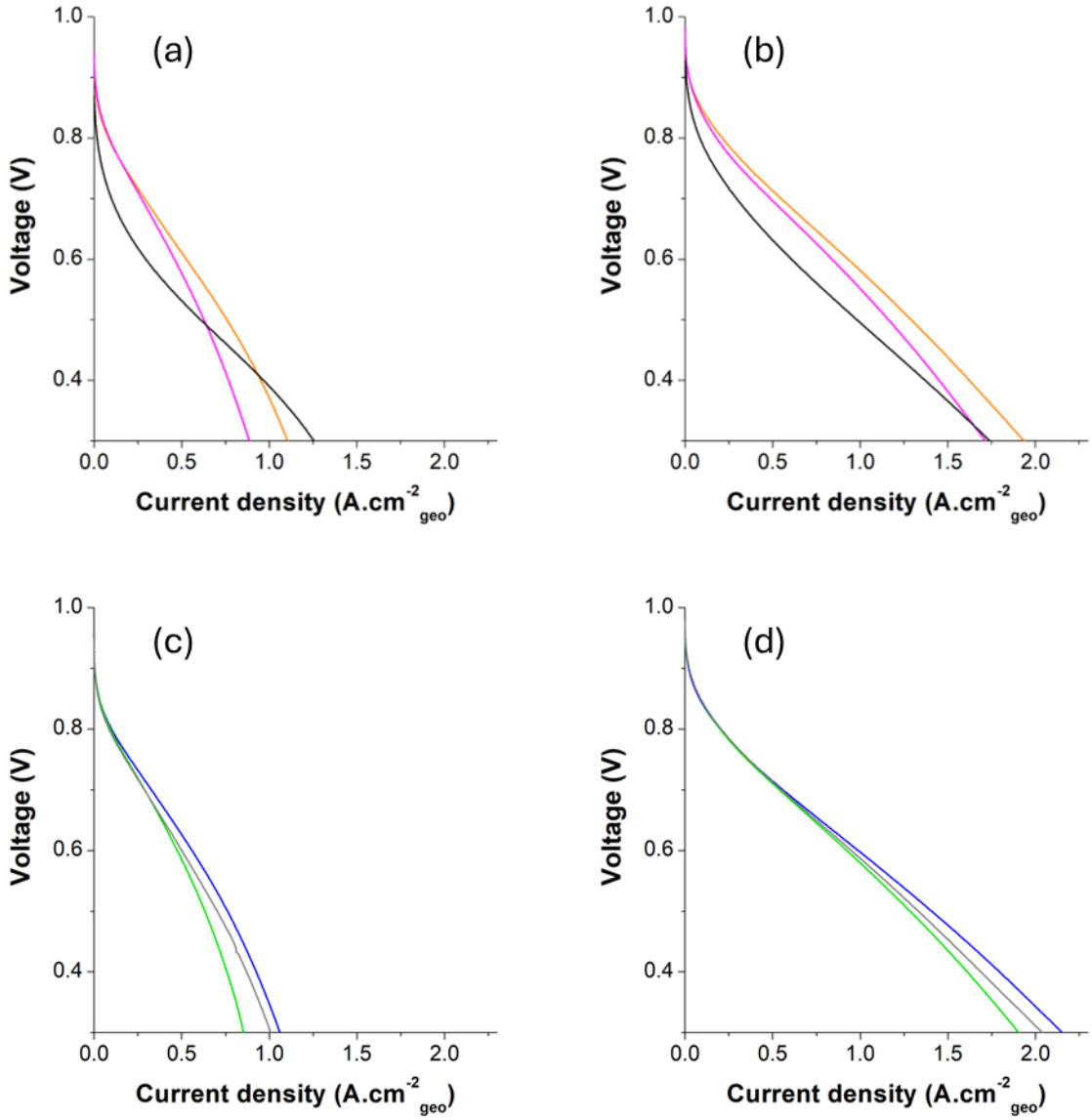

Figure 4.5. Dynamic polarization curves recorded at 0.05 $V.s^{-1}$ in MEA configuration of XC-72-Pt (—), CX0-Pt (—), CX0-C20-Pt (—), CX0-N30-Pt (—), CX0-C20-N30-Pt (—) and CX0-C20-HT1500-Pt (—) at *BoL*, (a,c) under air and (b,d) under O_2. H_2 is injected at the anode with a flow of 500 $mL.min^{-1}$ and air or O_2 is injected at the cathode with a flow of 2,000 $mL.min^{-1}$. Both gases are injected with a relative humidity of 100% and the cell is fixed at 70 ºC with a backpressure of 0.5 bar.

At 0.5 V, the carbon black-supported catalyst delivers current densities of 0.63 and 1.03 $A.cm^{-2}_{geo}$ while the pristine CX0-Pt leads to higher values of current densities, with 0.67 and 1.18

A.cm$^{-2}_{geo}$ under air and O_2, respectively. It can be observed that the current generated in the kinetic part drops faster for the carbon-black supported catalyst than for carbon-xerogel supported catalysts. Upon CVD and high-temperature treatment, current densities of 0.72 and 0.69 A.cm$^{-2}_{geo}$, under air; and 1.36 and 1.22 A.cm$^{-2}_{geo}$ under O_2 are generated for CX0-C20-Pt and CX0-C20-HT1500-Pt, respectively. Thus, the initial current densities slightly increase compared to CX0-Pt. This increase is minor but is consistent with the RDE measurements performed in Chapter 2. The current densities can also be compared after N doping. For CX0-Pt and CX0-N30-Pt, current densities at 0.5 V are 0.67 and 0.61 A.cm$^{-2}_{geo}$, and 1.18 and 1.08 A.cm$^{-2}_{geo}$, under air and O_2, respectively. For CX0-C20-Pt and CX0-C20-N30-Pt, the obtained values are 0.72 and 0.65, and 1.36 and 1.26 A.cm$^{-2}_{geo}$, under air and O_2, respectively. Initially, the N-doped catalysts do not display higher current densities than their undoped counterparts.

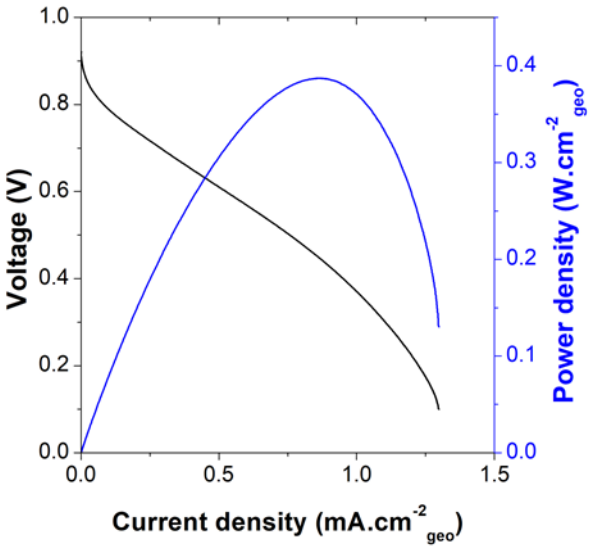

Figure 4.6. Dynamic polarization curve under air (—) and corresponding power density curve (—) of CX0-Pt, prior to AST. H_2 is injected at the anode with a flow of 500 mL.min^{-1} and air or O_2 is injected at the cathode with a flow of 2,000 mL.min^{-1}. Both gases are injected with a relative humidity of 100% and the cell is fixed at 70 ºC with a backpressure of 0.5 bar.

It can also be observed that diffusion issues are less pronounced for the carbon black-supported catalyst, XC-72-Pt than for the carbon xerogel-supported catalysts, which seems contradictory with the assumed advantage of carbon nanostructuration. Nevertheless, as observed in

profilometry, the average thickness of carbon-black supported catalytic layers is around 4–5 µm while those of CX-supported is around 9–10 µm (see **Annex 4.2**), while Pt loading and carbon mass are the same by choice. At constant carbon mass, the large grain size of carbon xerogels leads to thicker catalytic layers and additional mass transport resistance, which is however partially compensated by the mesopore structure of the carbon. Electrodes of equal thicknesses for both carbon black and carbon xerogel could be assembled for fairer comparison, but would require different catalyst Pt loadings to start with. Given the well-developed porosity of carbon xerogels, it is expected that, at equivalent electrode thickness, mass transport limitations would be reduced.

4.3.4. Fuel cell characterization after Accelerated Stress Tests

Catalysts were subjected to accelerated aging, first through 10,000 voltage steps (corresponding to the *MoL*) and in a second step, to 20,000 additional voltage steps (corresponding to *EoL*). Cyclic voltammetries and polarization curves were recorded at each aging step (see **Figure 4.7** and **Figure 4.8**), and key electrochemical parameters (*ECSA*, C_{dl} and the current density at 0.5 V) were extracted and compiled in **Table 4.3**. After 30,000 cycles, at *EoL*, the *ECSA* of Pt drops down drastically to 3, 4, 4, 3, 6 and 4 $m^2.g^{-1}_{Pt}$ for XC-72-Pt, CX0-Pt, CX0-C20-Pt, CX0-N30-Pt, CX0-C20-N30-Pt and CX0-C20-HT1500-Pt, respectively. The *ECSA* loss is very substantial, *ca.* 85% for all samples. The highest *ECSA* value after aging is observed for CX0-C20-N30-Pt. This *ECSA* loss can be attributed to several phenomena occurring during AST. Pt nanoparticles typically undergo migration and agglomeration during aging [31]. Additionally, nanoparticles detachment and Ostwald ripening can also occur. These phenomena lead to the decrease observed in the intensity of the Pt signal.

To mitigate these effects, the application of post-treatments, particularly N-doping, was performed on the carbon xerogel so as to enhance the interaction between the Pt and the carbon support [32]. This stronger anchoring could in turn limit the nanoparticles agglomeration and the *ECSA* loss. However, in the present case, the effect of N-doping is very moderate. Although the highest *ECSA* retained is for the CVD-treated and N-doped carbon xerogel-supported catalyst, the overall *ECSA* retention remain similar across the entire series of catalysts.

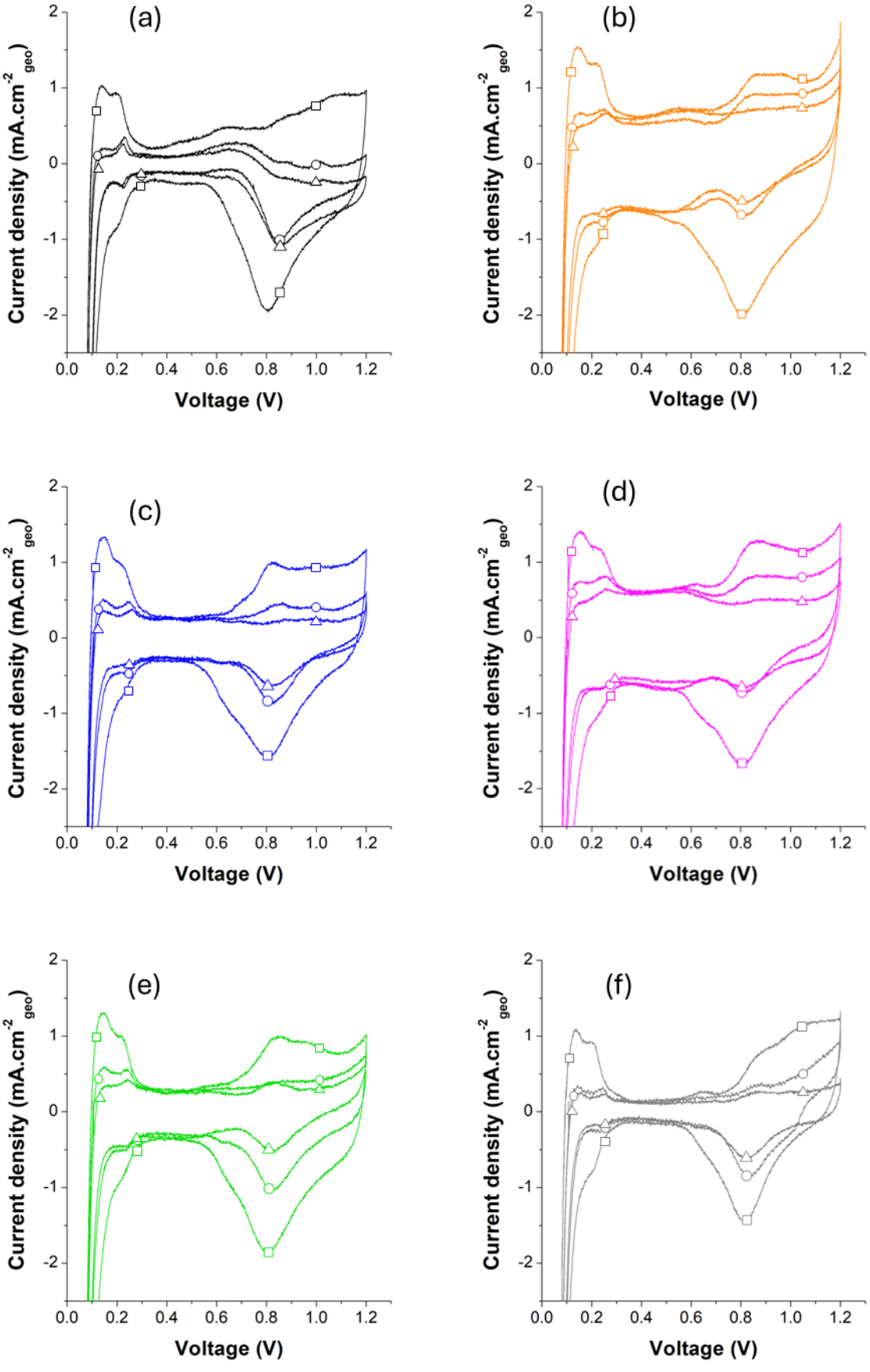
(a)
(b)
(c)
(d)
(e)
(f)
Current density (mA.cm$^{-2}_{geo}$)
Voltage (V)
2
1
0
-1
-2
0.0
0.2
0.4
0.6
0.8
1.0
1.2

Figure 4.7. Cyclic voltammetry curves of catalysts, recorded at 0.02 $V.s^{-1}$ with the anode under H_2 and the cathode under N_2 flow at *BoL* (—□—), *MoL* (—○—) and *EoL* (—△—) of (a) XC-72-Pt (—), (b) CX0-Pt (—) , (c) CX0-C20-Pt (—), CX0-N30-Pt (—), CX0-C20-N30-Pt (—) and CX0-C20-HT1500-Pt (—). H_2 is injected at the anode with a flow of 300 $mL.min^{-1}$ and N_2 is injected at the cathode with a flow of 300 $mL.min^{-1}$. Both gases are injected with a relative humidity of 100% and the cell is fixed at 70 ºC with a backpressure of 0.5 bar.

The evolution of the double layer capacitance, C_{dl}, was also observed during aging. As shown in **Table 4.3**, a decrease in C_{dl} is observed after 10,000 cycles for all the samples, although the decrease becomes much more moderate between 10,000 and 30,000 cycles. This is consistent with the observations also made in RDE configuration in Chapter 3. C_{dl} decreases significantly for XC-72-Pt, from 12 $mF.cm^{-2}_{geo}$ at *BoL* to 5 $mF.cm^{-2}_{geo}$ at *EoL*. This could indicate that a significant quantity of carbon has oxidized into CO_2. Some detachment of Nafion® upon aging could also contribute to this behavior [33], as the catalyst ink of XC-72-Pt may not be fully optimized for this carbon black material. The evolution of C_{dl} is much less pronounced for carbon xerogels: The double layer capacitance of CX0-Pt decreases from 30 to 27 $mF.cm^{-2}_{geo}$ while CX0-C20-Pt decreases only from 14 to 13 $mF.cm^{-2}_{geo}$. For N-doped samples, C_{dl} slightly decrease from 31 to 28 $mF.cm^{-2}_{geo}$ for CX0-N30-Pt and stay constant throughout aging at 14 $mF.cm^{-2}_{geo}$ for CX0-C20-N30-Pt. Finally, C_{dl} also slightly decreases from 8 to 6 $mF.cm^{-2}_{geo}$ for CX0-C20-HT1500-Pt. These results could indicate that carbon xerogels exhibit better resistance to electrochemical corrosion compared to conventional carbon black supports. Nevertheless, the purpose of this accelerated aging procedure was to degrade preferentially Pt nanoparticles while limiting carbon support degradation. As mentioned in the introduction of this chapter, more aggressive procedures targeting carbon corrosion exist and could be applied at a later stage of the material testing.

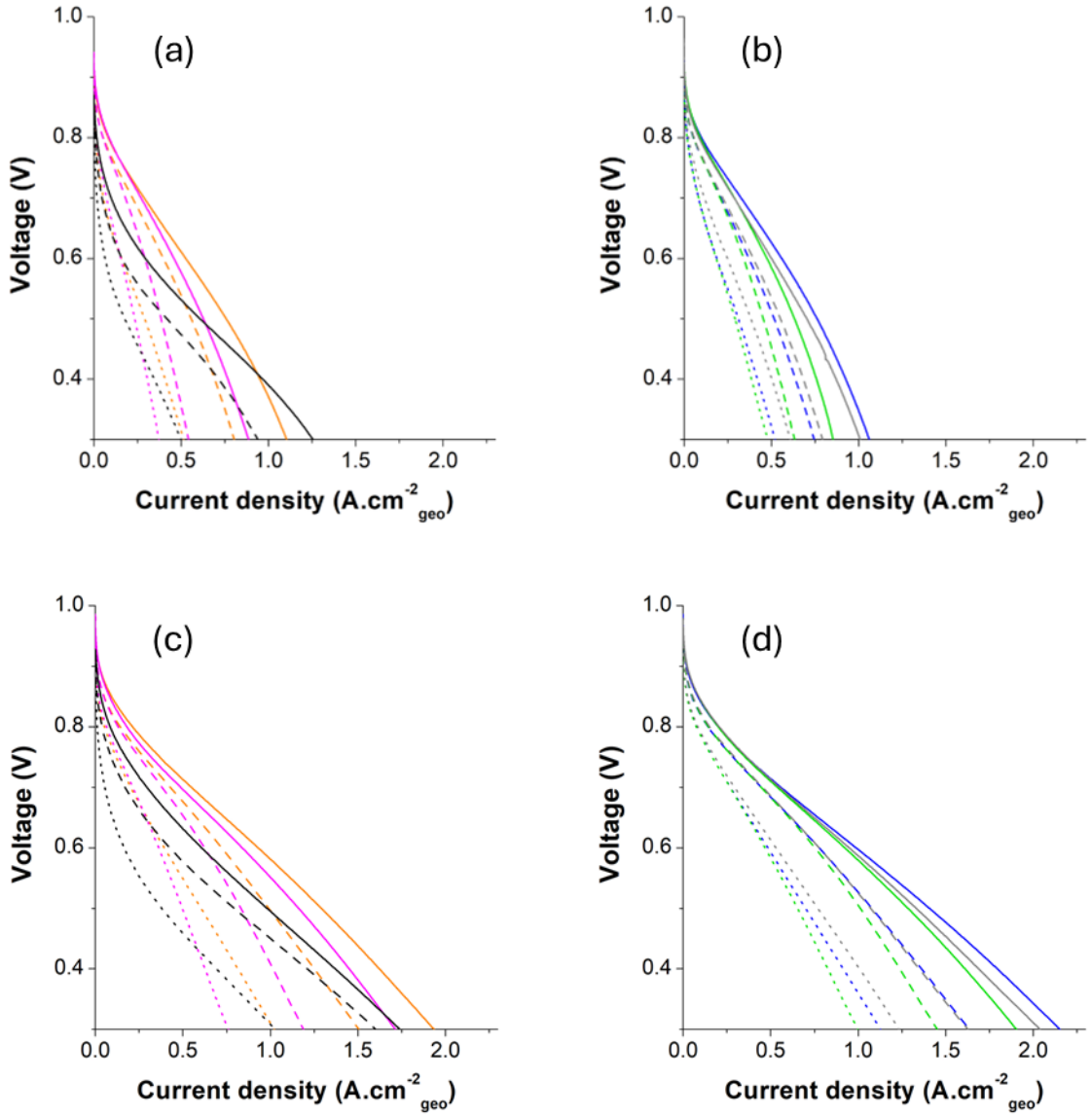

Figure 4.8. Dynamic polarization curves in MEA configuration of XC-72-Pt (—), CX0-Pt (—), CX0-C20-Pt (—), CX0-N30-Pt (—), CX0-C20-N30-Pt (—) and CX0-C20-HT1500-Pt (—) recorded at 0.05 $V.s^{-1}$, at *BoL* (plain line), *MoL* (dashed line) and *EoL* (dotted line), (a,c) under air and (b,d) under O_2. H_2 is injected at the anode with a flow of 500 $mL.min^{-1}$ and air or O_2 is injected at the cathode with a flow of 2,000 $mL.min^{-1}$. Both gases are injected with a relative humidity of 100% and the cell is fixed at 70 ºC with a backpressure of 0.5 bar.

Current densities were reported at 0.5 V at *BoL*, *MoL* and *EoL* in **Table 4.3**. Values for XC-72-Pt go from 0.63 and 1.03 $A.cm^{-2}_{geo}$ at *BoL* to 0.18 and 0.39 $A.cm^{-2}_{geo}$ at *EoL*, under air and O_2,

respectively. This represents a total loss of 71% under air and 62% under O_2 at *EoL*. CX0-Pt and CX0-C20-Pt exhibit slightly lower loss of 63 and 57% under air, and 56 and 50% under O_2, respectively. CX0-C20-HT1500-Pt displays an even smaller loss of 45% under air and 37% under O_2. This sample exhibits the highest current retention upon aging. Nevertheless, it must be noted that the results obtained with this sample were also less reproducible than for other catalysts. The different polarization curves obtained for CX0-C20-Pt and CX0-C20-HT1500-Pt, and used to calculate average values reported in **Table 4.3**, are presented in **Annex 4.1.** This lack of reproducibility could possibly be explained by the higher hydrophobic character of CX0-C20-HT1500-Pt, which leads to catalytic inks that are more difficult to stabilize and spray-coat in the same way from electrode to electrode. Nonetheless, these results are encouraging and seem to show that a more ordered surface brings some stability to the Pt nanoparticles. Thus, post-treatment of carbon-coated carbon xerogels at additional temperatures above 1,500 ºC would be of interest to perform. Regarding N-doped samples, the loss of current density losses amounts to 64 and 55% under air, and 58 and 52% under O_2, for CX0-N30-Pt and CX0-C20-N30-Pt, respectively. These values are close to those reported for their undoped counterparts.

Finally, the catalysts were recovered from the aged MEAs after 30,000 voltage steps and observed under TEM. The corresponding micrographs can be found in **Figure 4.9**. For all samples, a large number of agglomerated Pt clusters can be observed. Some isolated nanoparticles are also observed although in much lower numbers compared to the fresh catalysts. The diameter of these remaining isolated nanoparticles was calculated and compared to those of fresh catalysts (**Table 4.2**). For XC-72-Pt, d_{TEM} is equal to 9.2 nm (initially: 3.4 nm). For undoped CXs, d_{TEM} is equal to 7.7 and 7.0 nm (initially: 3.4 and 2.8 nm) for CX0-Pt and CX0-N30-Pt, respectively. The final nanoparticle size is smaller for the N-doped sample, but it should be reminded that the initial nanoparticles diameter was also smaller to begin with. For CVD-treated samples, d_{TEM} is equal to 8.7, 9.5 and 7.3 nm (initially: 3.6, 3.5 and 3.7 nm) for CX0-C20-Pt, CX0-C20-N30-Pt and CX0-C20-HT1500-Pt, respectively.

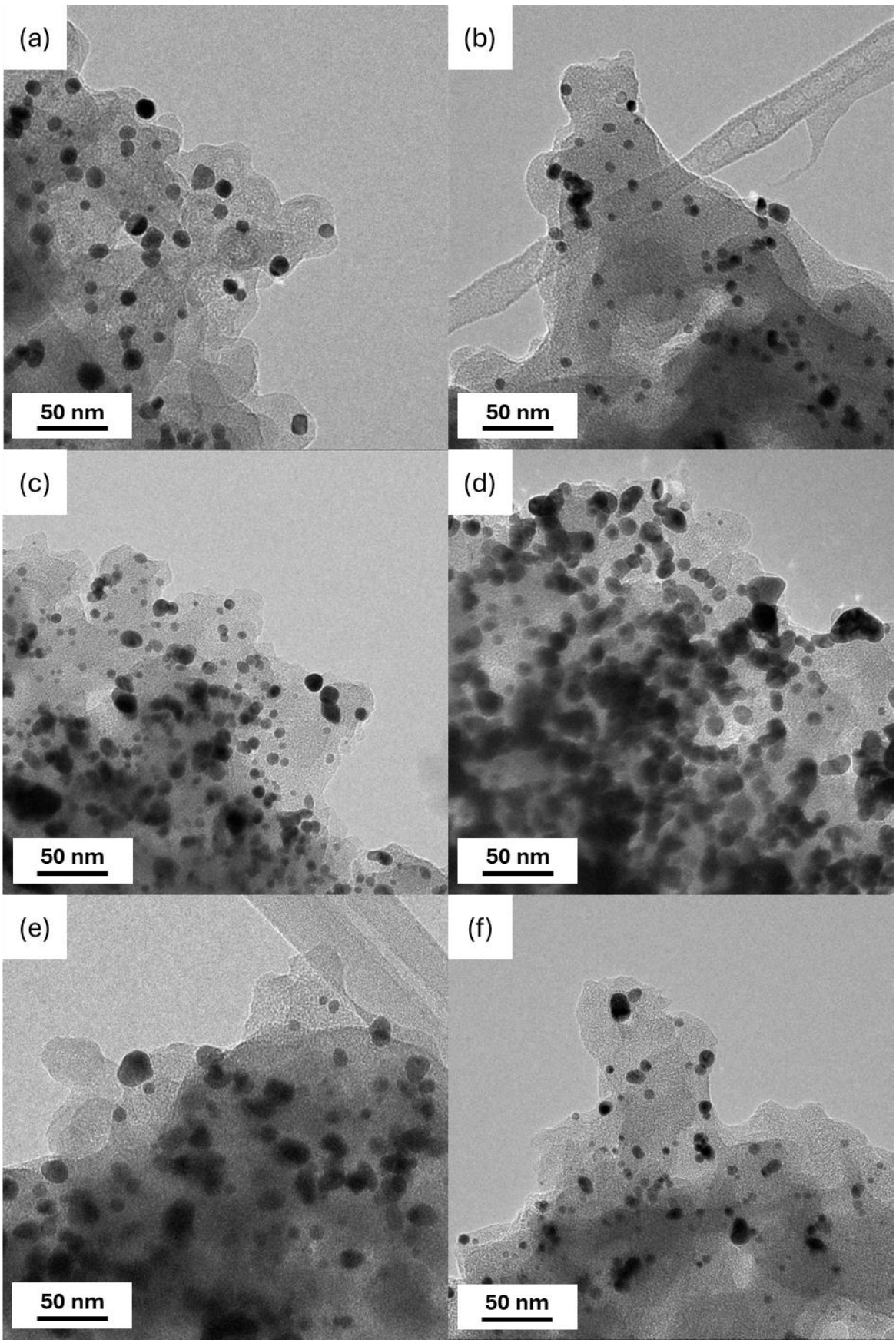

Figure 4.9. TEM micrographs after ASTs of (a) XC-72-Pt, (b) CX0-Pt, (c) CX0-N30-Pt, (d) CX0-C20-Pt, (e) CX0-C20-N30-Pt and (f) CX0-C20-HT1500-Pt.

The high-temperature treatment may have partially prevented Pt agglomeration. Nevertheless, besides agglomeration, it should also be noted that, on all the catalysts, a large number of carbon grains observed were devoid of Pt, most likely as a result of extensive Pt nanoparticles detachment or Pt dissolution. Thus, the significant loss of ECSA observed is certainly the consequence of Pt agglomeration, detachment and dissolution, although the respective proportion of each is difficult to determine.

Based on these results obtained in MEA configuration on the fuel cell test bench, it is evident that carbon xerogel demonstrate good quality as carbon supports. The pristine CX0-Pt catalyst showed superior performances to the commercial reference. Nevertheless, as previously noted, in MEA configuration, the overall catalytic performances rely heavily on the electrode processing, which should be refined for all catalysts. In this thesis, the carbon black-supported catalyst was treated in the same conditions as the carbon xerogel-supported material, despite clear intrinsic differences between the materials. Thus, measurements of XC-72-Pt do not necessarily reflect the maximal achievable performances of the material. Nevertheless, the key objective is to compare the evolution of the values upon aging, rather than their absolute values. Regarding post-treatments, carbon coating by CVD, and its subsequent high-temperature treatment, appear promising. First, satisfactory deposition of the Pt nanoparticles was observed on all the post-treated carbon xerogel supports. Second, the combination of CVD and HT treatment slightly improved the MEA stability without adversely affecting mass transport inside the catalytic layer. Nevertheless, the improvements observed here remain modest and a post-treatment of carbon-coated carbon xerogels at temperatures above 1,500 ºC would be interesting to perform.

The results obtained in this chapter do not bring clear evidence that nitrogen-doping post-treatment of the carbon support improve the catalyst performance or durability. On the one hand, this observation is consistent with the results reported in Chapter 3, with ASTs performed in RDE configuration. On the other hand, these results appear less encouraging than reported elsewhere, where the incorporation of N in the carbon matrix seem to mitigate the aging of catalytic layers [34]. Nonetheless, as discussed in Chapter 3, the reported improvement in catalytic layer durability is often not decorrelated with the possible modifications induced by the nitrogen doping treatment, such as changes in carbon pore texture or crystallinity, or increase in the number of nucleation sites, which ultimately influences the growth of Pt nanoparticles [35]. Indeed, the Pt nanoparticles may grow closer or further away from their optimal size (~3.5 nm [6]) upon deposition on a N-doped carbon support. This optimum

corresponds the size at which the *MA* of the Pt nanoparticles towards ORR is maximized. However, this variation in Pt growth may lead to a compensatory effect that can be misinterpreted as stabilization. For instance, if Pt nanoparticles initially grow smaller on a N-doped carbon support, with sizes below the optimum, their growth upon aging will lead to a decrease in *ECSA* that will be compensated by an increase in catalytic activity, which can be interpreted as a stabilization of the catalytic performances. Thus, conclusions regarding improved durability of the catalytic layer should be interpreted with caution due to this possible bias.

Regarding the nitrogen doping, additional strategies could be explored in future works. For instance, the incorporation of nitrogen could be combined with the other two post-treatments, CVD and high-temperature treatment. Nitrogen-doping could be performed on the carbon xerogel previously subjected to CVD and high-temperature treatment. The integration of these steps into a single process, using adequate equipment as well as a carbon and nitrogen-rich precursor, could also be performed. This could help expand and corroborate the findings reported in this thesis.

4.4. Conclusion

The durability of various carbon xerogel-supported catalysts was evaluated in a MEA configuration using a PEMFC test bench, and was compared to that of a commercial Pt catalyst supported on carbon black. The carbon xerogel investigated corresponds to the material synthesized in Chapter 1, that was subjected to various post-treatments, namely carbon coating by CVD treatment, high-temperature treatment, and nitrogen doping. The successful deposition of a secondary carbon layer onto the xerogel surface, as well as the incorporation of the nitrogen-containing functional groups were observed and all samples were characterized in previous chapters. The most appropriate Pt catalysts supported on carbon xerogels were assessed and selected in the previous chapters based on their physico-chemical and electrochemical properties.

Overall, in MEA configuration, Pt nanoparticles deposited on carbon xerogels display better initial catalytic activities than those supported on carbon black. Nevertheless, this statement must be nuanced as the formulation of the carbon-black supported catalyst ink may not be optimal. Regarding post-treated carbon xerogel samples, small increases in current produced at

0.5 V were observed after CVD treatment and high-temperature treatment. Meanwhile, the current produced at 0.5 V remains similar for N-doped samples, compared to their undoped counterparts. No significant differences were observed regarding the initial electrochemical surface area of Pt, which remained consistently in the range of 24 to 33 $m^2.g^{-1}_{Pt}$ across the entire catalyst series.

The electrochemical performance was also assessed after aging, *i.e.* after 30,000 voltage steps between 0.6 and 1.0 V. This voltage range was chosen to focus on Pt nanoparticles degradation while minimizing strong carbon degradation. Indeed, overly aggressive degradation of the carbon is not well-suited for initial screening of the catalytic layer durability, if the Pt itself is insufficiently stable. The *ECSA* of all materials decreased, in the range of *ca.* 85%. This phenomenon is largely due to Pt nanoparticles detachment and agglomeration occurring during aging, as was observed on the TEM micrographs of the aged catalysts. All catalytic layers show an *ECSA* that decreased to roughly 3-4 $m^2.g^{-1}_{Pt}$. The performances also decrease upon aging as a result of the Pt particles evolution. The current produced at 0.5 V after 30,000 voltage steps decreases by 71% under air flow for the commercial catalyst. This loss is higher to that observed in the case of the pristine CX catalyst, which exhibit an 63% loss. Compared to the commercial catalyst, this loss is also slightly alleviated after N-doping treatment, with a 64% decrease for the N-doped carbon xerogel and 58% for the N-doped carbon-coated carbon xerogel. Nevertheless, catalysts supported on N-doped carbon xerogels do not exhibit clear evidence of improved stability compared to their undoped counterparts. These observations are relatively opposed to what is commonly reported in the literature, despite the nitrogen functional groups identified and their proportions being similar to those mentioned in other reports.

The highest current retention is observed for the catalyst supported on carbon-coated carbon xerogel subsequently treated at 1,500 ºC. For this sample, the lowest current decrease after aging is observed, namely 45%. This result indicates that surface modification *via* CVD followed by high-temperature treatment can offer better MEA stability, without compromising the mass transport properties of the carbon support given that the mesopore structure remains intact. Nevertheless, it is clear that this treatment alone does not effectively suppress nanoparticle migration. Plus, reproducibility issues were encountered with this sample, indicating that this treatment requires further investigation. Finally, it is important to note that this increase in durability was not reported with measurements performed in RDE configuration in Chapter 2. RDE measurements provide a useful initial indication of the material

electrocatalytic performances. However, assembling the material in MEA configuration provides a much more realistic assessment of these performances.

4.5. References

[1] N. Job, J. Marie, S. Lambert, S. Berthon-Fabry, P. Achard, Carbon Xerogels as Catalyst Supports for PEM Fuel Cell Cathode, *Energy Conversion and Management*, 49 (2008) 2461–2470.

[2] N. Job, S. Lambert, A. Zubiaur, C. Cao, J.-P. Pirard, Design of Pt/Carbon Xerogel Catalysts for PEM Fuel Cells, *Catalysts*, 5 (2015) 40–57.

[3] A. Zubiaur, Development of New Catalysts for Proton Exchange Membrane Fuel Cells (PEMFCs), PhD thesis, Université de Liège, 2017.

[4] K. Shinozaki, J.W. Zack, R.M. Richards, B.S. Pivovar, S.S. Kocha, Oxygen Reduction Reaction Measurements on Platinum Electrocatalysts Utilizing Rotating Disk Electrode Technique, *Journal of The Electrochemical Society*, 162 (2015) F1144–F1158.

[5] U.A. Paulus, T.J. Schmidt, H.A. Gasteiger, R.J. Behm, Oxygen Reduction on a High-Surface Area Pt/Vulcan Carbon Catalyst: A Thin-Film Rotating Ring-Disk Electrode Study, *Journal of Electroanalytical Chemistry*, 495 (2001) 134–145.

[6] K. Kinoshita, Particle Size Effects for Oxygen Reduction on Highly Dispersed Platinum in Acid Electrolytes, *Journal of The Electrochemical Society*, 137 (1990) 845–848.

[7] I. Takahashi, S.S. Kocha, Examination of the Activity and Durability of PEMFC Catalysts in Liquid Electrolytes, *Journal of Power Sources*, 195 (2010) 6312–6322.

[8] M. Fathi Tovini, A. Hartig-Weiß, H.A. Gasteiger, H.A. El-Sayed, The Discrepancy in Oxygen Evolution Reaction Catalyst Lifetime Explained: RDE vs MEA - Dynamicity within the Catalyst Layer Matters, *Journal of The Electrochemical Society*, 168 (2021) 014512.

[9] Wolf. Vielstich, Arnold. Lamm, H.A.. Gasteiger, Harumi. Yokokawa, Handbook of Fuel Cells : Fundamentals, Technology, and Applications, Wiley, 2003.

[10] Y. Sugawara, A.P. Yadav, A. Nishikata, T. Tsuru, Dissolution and Surface Area Loss of Platinum Nanoparticles under Potential Cycling, *Journal of Electroanalytical Chemistry*, 662 (2011) 379–383.

[11] J. Liu, Y. Yin, J. Zhang, T. Zhang, X. Zhang, H. Chen, Mechanical degradation of catalyst layer under accelerated relative humidity cycling in a polymer electrolyte membrane fuel cell, *Journal of Power Sources*, 512 (2021) 230487.

[12] Q. Guo, Z. Qi, Effect of Freeze-Thaw Cycles on the Properties and Performance of Membrane-Electrode Assemblies, *Journal of Power Sources*, 160 (2006) 1269–1274.

[13] P. Mandal, B.K. Hong, J.-G. Oh, S. Litster, Understanding the Voltage Reversal Behavior of Automotive Fuel Cells, *Journal of Power Sources*, 397 (2018) 397–404.

[14] P. Zihrul, I. Hartung, S. Kirsch, G. Huebner, F. Hasché, H.A. Gasteiger, Voltage Cycling Induced Losses in Electrochemically Active Surface Area and in H_2 /Air-Performance of PEM Fuel Cells, *Journal of The Electrochemical Society*, 163 (2016) F492–F498.

[15] N. Garland, T. Benjamin, J. Kopasz, DOE Fuel Cell Program: Durability Technical Targets and Testing Protocols, *ECS Transactions*, 11 (2007) 923–931.

[16] A. Ohma, K. Shinohara, A. Iiyama, T. Yoshida, A. Daimaru, Membrane and Catalyst Performance Targets for Automotive Fuel Cells by FCCJ Membrane, Catalyst, MEA WG, *ECS Transactions*, 41 (2011) 775–784.

[17] N. Macauley, D.D. Papadias, J. Fairweather, D. Spernjak, D. Langlois, R. Ahluwalia, K.L. More, R. Mukundan, R.L. Borup, Carbon Corrosion in PEM Fuel Cells and the Development of Accelerated Stress Tests, *Journal of The Electrochemical Society*, 165 (2018) F3148–F3160.

[18] E. Pahon, D. Hissel, N. Yousfi-Steiner, A Review of Accelerated Stress Tests Dedicated to Proton Exchange Membrane Fuel Cells – Part I: Fuel Cell Component Level, *Journal of Power Sources*, 546 (2022) 231895.

[19] Y. Liu, M.W. Murphy, D.R. Baker, W. Gu, C. Ji, J. Jorne, H.A. Gasteiger, Proton Conduction and Oxygen Reduction Kinetics in PEM Fuel Cell Cathodes: Effects of Ionomer-to-Carbon Ratio and Relative Humidity, *Journal of The Electrochemical Society*, 156 (2009) B970.

[20] M. Shao, Q. Chang, J.P. Dodelet, R. Chenitz, Recent Advances in Electrocatalysts for Oxygen Reduction Reaction, *Chemical Reviews*, 116 (2016).

[21] F.L. Deschamps, J.G. Mahy, A.F. Léonard, S.D. Lambert, A. Dewandre, B. Scheid, N. Job, A Practical Method to Characterize Proton Exchange Membrane Fuel Cell Catalyst Layer Topography: Application to Two Coating Techniques and Two Carbon Supports, *Thin Solid Films*, 695 (2020) 137751.

[22] F. Deschamps, Mise au Point de Méthodes d'Etude de Catalyseurs Supportés sur Carbones Nanostructurés pour Piles à Combustible à Membrane Echangeuse de Protons, PhD thesis, Université de Liège, 2022.

[23] A. Zubiaur, N. Job, Streamlining of the Synthesis Process of Pt/Carbon Xerogel Electrocatalysts with High Pt Loading for the Oxygen Reduction Reaction in Proton Exchange Membrane Fuel Cells Applications, *Applied Catalysis B: Environmental*, 225 (2018) 364–378.

[24] C. Alegre, M.E. Gálvez, R. Moliner, V. Baglio, A.S. Aricò, M.J. Lázaro, Towards an Optimal Synthesis Route for the Preparation of Highly Mesoporous Carbon Xerogel-Supported Pt Catalysts for the Oxygen Reduction Reaction, *Applied Catalysis B: Environmental*, 147 (2014) 947–957.

[25] L.F. Mabena, S. Sinha Ray, S.D. Mhlanga, N.J. Coville, Nitrogen-Doped Carbon Nanotubes as a Metal Catalyst Support, *Applied Nanoscience*, 1 (2011) 67–77.

[26] M.L.C. Piedboeuf, A.F. Léonard, K. Traina, N. Job, Influence of the Textural Parameters of Resorcinol-Formaldehyde Dry Polymers and Carbon Xerogels on Particle Sizes upon Mechanical Milling, *Colloids and Surfaces A: Physicochemical and Engineering Aspects*, 471 (2015) 124–132.

[27] S. Trasatti, O.A. Petrii, Real Surface Area Measurements in Electrochemistry, *Journal of Electroanalytical Chemistry*, 327 (1992) 353–376.

[28] O. Diaz-Morales, T.J.P. Hersbach, C. Badan, A.C. Garcia, M.T.M. Koper, Hydrogen Adsorption on Nano-Structured Platinum Electrodes, *Faraday Discussions*, 210 (2018) 301–315.

[29] C. Lafforgue, P. Toudret, F. Micoud, M. Heitzmann, J.-F. Blachot, M. Chatenet, Manufacturing of Carbon-Supported Platinum Cathodes for Proton Exchange Membrane Fuel Cell using the Doctor Blade Process: Microstructure and Performance, *Journal of Power Sources*, 627 (2025) 235851.

[30] M. Eikerling, A.A. Kornyshev, Electrochemical Impedance of the Cathode Catalyst Layer in Polymer Electrolyte Fuel Cells, *Journal of Electroanalytical Chemistry*, 475 (1999) 107–123.

[31] L. Dubau, L. Castanheira, G. Berthomé, F. Maillard, An Identical-Location Transmission Electron Microscopy Study on the Degradation of Pt/C Nanoparticles under Oxidizing, Reducing and Neutral Atmosphere, *Electrochimica Acta*, 110 (2013) 273–281.

[32] Y. Zhou, T. Holme, J. Berry, T.R. Ohno, D. Ginley, R. O'Hayre, Dopant-Induced Electronic Structure Modification of HOPG Surfaces: Implications for High Activity Fuel Cell Catalysts, *The Journal of Physical Chemistry C*, 114 (2010) 506–515.

[33] P.C. Okonkwo, Proton Exchange Membrane Fuel Cell Catalyst Layer Degradation Mechanisms: A Succinct Review, *Catalysts*, 15 (2025) 97.

[34] H.-Y. Lee, T.H. Yu, C.-H. Shin, A. Fortunelli, S.G. Ji, Y. Kim, T.-H. Kang, B.-J. Lee, B. V. Merinov, W.A. Goddard, C.H. Choi, J.-S. Yu, Low Temperature Synthesis of New Highly Graphitized N-doped Carbon for Pt Fuel Cell Supports, Satisfying DOE 2025 Durability Standards for both Catalyst and Support, *Applied Catalysis B: Environmental*, 323 (2023) 122179.

[35] T. Holme, Y. Zhou, R. Pasquarelli, R. O'Hayre, First Principles Study of Doped Carbon Supports for Enhanced Platinum Catalysts, *Physical Chemistry Chemical Physics*, 12 (2010) 9461–9468.

Annex 4.1. Reproducibility of the Membrane-Electrodes Assemblies

In this chapter, each catalyst material was spray-coated onto a minimum of three membranes to manufacture three identical MEAs. Moreover, for each catalyst, at least two MEAs were characterized and subjected to aging. This step is necessary to ensure the reliability of the obtained data. Polarization curves of two MEAs are provided in **Figure A4.1.1** for CX0-C20-Pt and **Figure A4.1.2** for CX0-C20-HT1500-Pt. In addition, the current density produced at 0.5 V is reported in **Table A4.1.1**. For both materials, similar initial performances (at *BoL*) with deviations ≤20% across membranes (see **Table A4.1.2** and **Table A4.1.3**) are observed across a large range of voltage (from 0.4 to 0.85 V). The only exception is a variation of 22% at 0.85 V for CX0-C20-HT1500-Pt with the cathode under air. Nevertheless, the kinetic region, corresponding to low current densities, superimposes relatively well across MEAs for both CX0-C20-Pt and CX0-C20-HT1500-Pt. At higher currents, small variations between MEAs start to appear. Since carbon xerogel-supported catalysts lead to relatively thick active layers, achieving strictly identical electrode architecture is challenging. Nevertheless, despite these small variations, these MEAs are suitable for accelerated stress testing.

After 10,000 cycles, at *MoL*, no significant variation in current densities are observed between the two MEAs of CX0-C20-Pt, whether measurements are performed under air or O_2. Meanwhile, variations begin to appear for CX0-C20-HT1500-Pt MEAs, especially under air with a maximum deviation of 71% at 0.85 V. The deviation is less pronounced under O_2 and reaches a maximum of 34% at 0.85 V. Finally, after 30,000 cycles, at *EoL*, differences in current become quite visible between the two CX0-C20-Pt MEAs at low current densities (0.7 and 0.85 V), with variations >20%. However, at higher current densities (0.4 and 0.55 V), both membranes display similar current densities with a variation <20%. Meanwhile, clear variations across the entire polarization curves are observed for the two MEAs of CX0-C20-HT1500-Pt, both under air and O_2 with very strong deviations, reaching a maximum of 146 and 137% under air and O_2, respectively, at 0.85 V.

The AST applied to the MEAs are prolonged and harsh. Thus, some degree of variability in catalyst degradation is expected. Nevertheless, the polarization curves of CX0-C20-Pt remain relatively similar throughout aging and fall within a 20% margin error. This indicates that the MEAs are manufactured consistently and that ASTs are conducted accurately and reliably.

Meanwhile, the lower reliability of CX0-C20-HT1500-Pt is difficult to explain but could possibly be due to the high hydrophobicity of the carbon support, which could result in catalytic inks that are more difficult to stabilize and spray-coat in a reproducible manner. Adjusting the ink composition, for example by modifying the water-to-isopropanol ratio, could potentially improve the ink stability.

Table A4.1.1. Evolution of the current density of two sets of identically manufactured MEAs upon aging.

Catalyst		$J_{0.5}$ [a] ($A.cm^{-2}_{geo}$)	
		Under air	Under O_2
CX0-C20-Pt MEA n°1	BoL	0.76	1.41
	MoL	0.51	1.08
	EoL	0.31	0.70
CX0-C20-Pt MEA n°2	BoL	0.69	1.33
	MoL	0.45	1.01
	EoL	0.30	0.65
CX0-C20-HT1500-Pt MEA n°1	BoL	0.70	1.33
	MoL	0.55	1.07
	EoL	0.38	0.77
CX0-C20-HT1500-Pt MEA n°2	BoL	0.67	1.18
	MoL	0.52	0.92
	EoL	0.19	0.43

[a] $J_{0.5}$: Current density measured at 0.5 V.

Table A4.1.2. Variation in the current density measured across membranes, with the cathode under air.

	Variation in current density (%)					
	CX0-C20-Pt			CX0-C20-HT1500-Pt		
Voltage (V)	**BoL**	**MoL**	**EoL**	**BoL**	**MoL**	**EoL**
0.4	12	15	5	2	7	40
0.55	9	13	8	8	19	90
0.7	7	6	34	16	64	135
0.85	5	1	68	22	71	146

Table A4.1.3. Variation in the current density measured across membranes, with the cathode under O_2.

	Variation in current density (%)					
	CX0-C20-Pt			CX0-C20-HT1500-Pt		
Voltage (V)	**BoL**	**MoL**	**EoL**	**BoL**	**MoL**	**EoL**
0.4	5	7	5	11	13	33
0.55	6	5	16	13	17	73
0.7	6	3	53	14	23	124
0.85	<1	<1	75	20	34	137

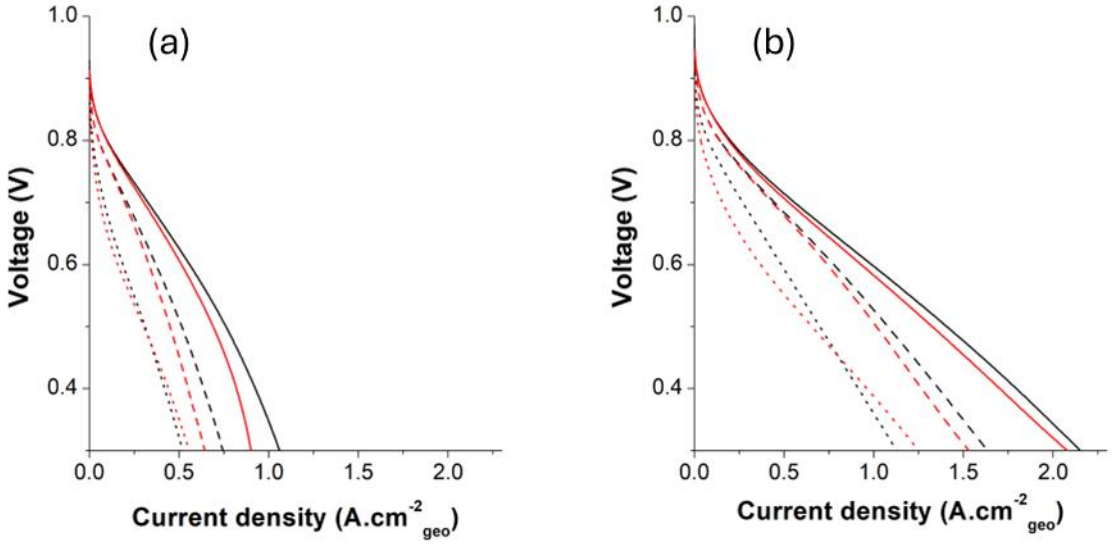

Figure A4.1.1. Dynamic polarization curves of CX0-C20-Pt recorded at 0.05 $V.s^{-1}$, (a) under air and (b) under O_2, at *BoL* (plain line), (b) *MoL* (dashed line) and (c) *EoL* (dotted line). MEA n°1 (—) and n°2 (—). H_2 is injected at the anode with a flow of 500 $mL.min^{-1}$ and air or O_2 is injected at the cathode with a flow of 2,000 $mL.min^{-1}$. Both gases are injected with a relative humidity of 100% and the cell is fixed at 70 ºC with a backpressure of 0.5 bar.

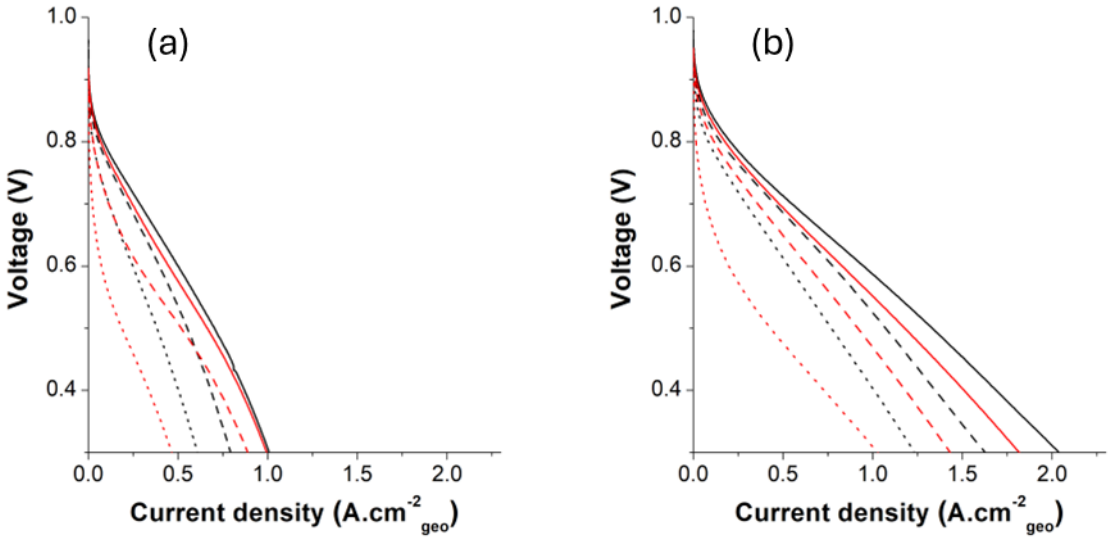

Figure A4.1.2. Dynamic polarization curves of CX0-C20-HT1500-Pt recorded at 0.05 $V.s^{-1}$, (a) under air and (b) under O_2, at *BoL* (plain line), (b) *MoL* (dashed line) and (c) *EoL* (dotted line). MEA n°1 (—) and n°2 (—). H_2 is injected at the anode with a flow of 500 $mL.min^{-1}$ and air or O_2 is injected at the cathode with a flow of 2,000 $mL.min^{-1}$. Both gases are

injected with a relative humidity of 100% and the cell is fixed at 70 ºC with a backpressure of 0.5 bar.

Annex 4.2. Additional figures

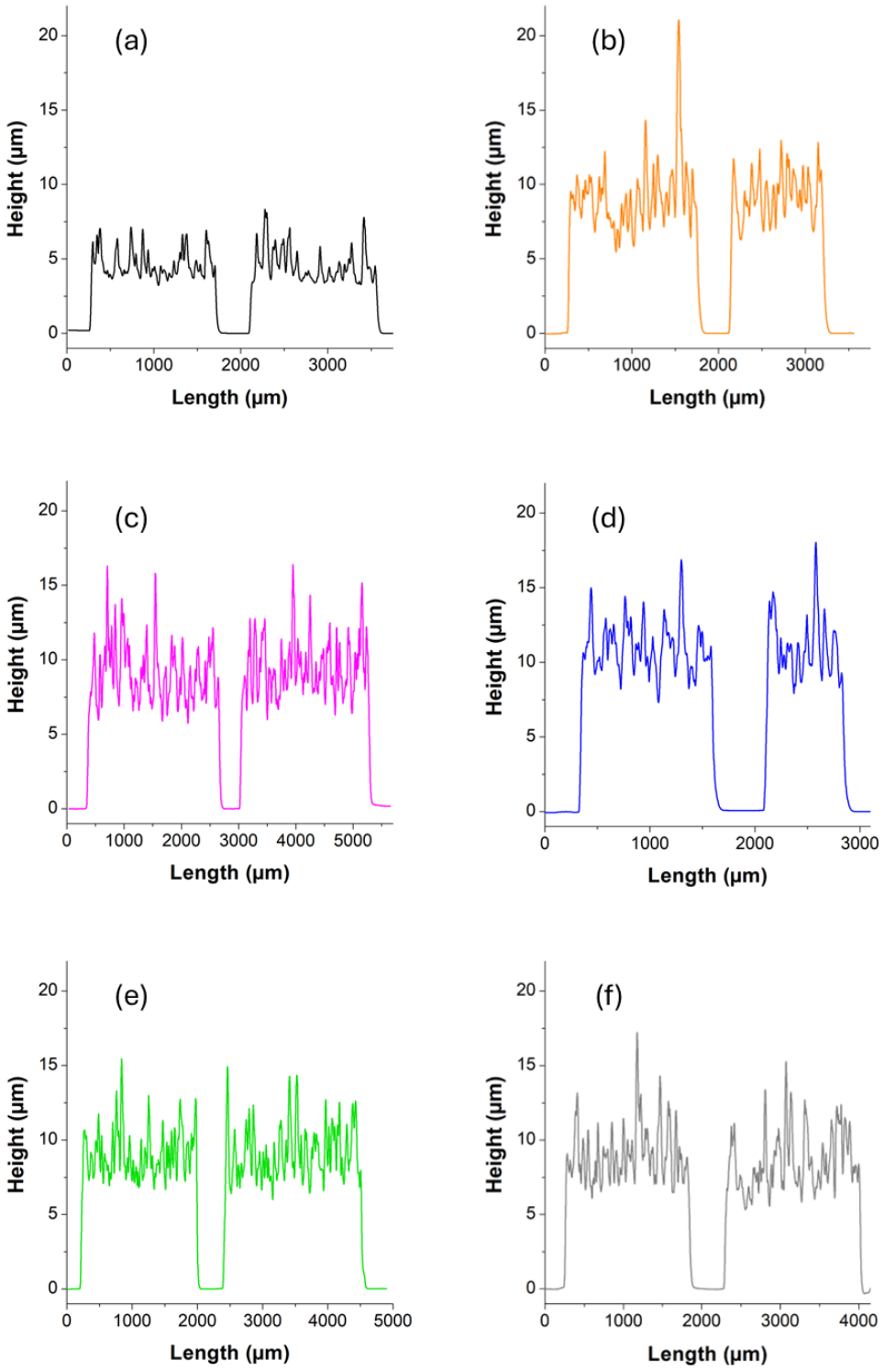

Figure A4.2.3. Thickness profiles of the active layer of XC-72-Pt (—), CX0-Pt (—), CX0-C20-Pt (—), CX0-N30-Pt (—), CX0-C20-N30-Pt (—) and CX0-C20-HT1500-Pt (—) deposited on a glass slide *via* spray-coating.

Conclusion and outlook

The objective of this thesis was to develop durable carbon materials suitable for use as electrocatalyst support in Proton Exchange Membrane Fuel Cell (PEMFC) catalytic layers. This layer consists of platinum nanoparticles supported on a carbon structure and mixed with a proton-conducting ionomer. Nevertheless, various limitations related to this catalytic layer can be encountered. For instance, severe gas diffusion limitations can occur if the catalytic layer architecture is not properly optimized to provide sufficient diffusion pathways for the gaseous reactants and evacuate the water produced. In addition, both the platinum nanoparticles and carbon support undergo degradation upon long-term operation of the fuel cell. This degradation includes nanoparticle agglomeration, migration and detachment, but also support oxidation (*i.e.* carbon corrosion). Addressing these issues requires the fabrication of catalytic layers from materials able to mitigate these phenomena. Particularly, it is essential to design a carbon material with a surface and pore texture optimized for metal electrocatalyst deposition and gas diffusion, that also remains stable upon prolonged fuel cell operation.

Carbon blacks are widely used as carbon supports in commercial PEMFC catalytic layers. However, they have some limitations. First, tuning the architecture of the catalytic layer is challenging. Indeed, the pore texture of carbon black-based catalytic layers is not easily controllable and the arrangement of agglomerates can be altered during the electrode processing. Second, carbon blacks exhibit limited resistance to the carbon corrosion that can occur at the cathode side of PEMFCs. The different conditions encountered in this electrode, such as the operating voltage (> 0.6 V *vs.* RHE), the presence of water and Pt, as well as temperatures around 70 ºC, constitute an oxidative environment that accelerates the carbon corrosion kinetics. Thus, in this thesis, carbon xerogels (CX) were used as an alternative to carbon blacks. Carbon xerogels are hard carbon material made of interconnected microporous nodules, the size of which can be tuned by selecting the appropriate values of reaction variables, enabling a good adjustment of their meso/macropore texture. This tunability makes carbon xerogels good materials for mass transport control compared to carbon blacks. Nevertheless, carbon xerogels are materials exhibiting a highly disordered surface structure, and as such, are exposed to fast corrosion kinetics. Therefore, controlling the surface ordering of the carbon

xerogel surface is also essential to ultimately obtain a carbon support with both a tuned pore texture and a high degree of graphitization at its surface.

Accordingly, the first objective of this thesis was to synthesize a carbon xerogel with a pore texture appropriate for a PEMFC catalytic layer application, *i.e.* a carbon material with sufficient pore volume and adequate pore size to minimize mass transport limitations, enable good water management, and that provides enough surface area for the homogeneous deposition of a catalytically active phase (*i.e.* Pt nanoparticles). This carbon xerogel was then subjected to different post-treatments aimed at modifying its surface so as to (i) decrease the rate of carbon corrosion to avoid severe carbon losses and prevent nanoparticle detachment and (ii) strengthen the interaction between the support and the electrocatalyst and thus limit the nanoparticles migration and aggregation. The Pt nanoparticles were then deposited on the pristine and post-treated carbon xerogels. The impact of these post-treatments on the physico-chemical properties of the carbon xerogel was assessed. More importantly, the electrochemical performance of these catalysts, *i.e.* their catalytic activity towards the Oxygen Reduction Reaction (ORR), was measured in two electrochemical configurations, first in a Rotating Disk Electrode (RDE) configuration, and second in a Membrane-Electrodes Assembly (MEA) configuration. Finally, their durability upon accelerated aging was also evaluated in these two configurations.

Carbon-coating of carbon xerogels

In the first chapter, a carbon xerogel with a pore size centered around 70 nm, a BET surface area of 674 $m^2.g^{-1}$ and an external surface area (*i.e.* excluding the internal micropores) of 201 $m^2.g^{-1}$. was synthesized and used as a base material throughout this thesis. It was previously shown through experiments that this pore size is suitable for PEMFC catalytic layer applications while the corresponding external surface area is sufficient for efficient Pt deposition [1]. This xerogel was then subjected to two different post-treatments. The first one consisted in a Chemical Vapor Deposition (CVD) treatment based on the thermal cracking of ethylene. This aimed at depositing a uniform carbon layer onto the surface of the carbon xerogel. Various CVD durations, ranging from 5 to 60 min, were investigated to quantify the impact of the layer thickness on the physico-chemical properties of the carbon xerogel and to determine the most suitable conditions. A second post-treatment consisted in exposing the CVD-treated carbon xerogel to a high temperature of 1,500 ºC under inert atmosphere, which aimed at further

increasing the surface ordering of the deposited carbon layer. This heat treatment was performed on the most appropriate CVD-coated carbon xerogel but not on the pristine carbon xerogel: indeed, given that carbon xerogels are classified as hard carbons (*i.e.* non-graphitizable), it is well-known that they cannot be crystallized by this method.

The carbon layer deposited by CVD was found inherently more ordered than the original carbon xerogel surface. Indeed, an increase of surface crystallinity was clearly observed *via* HR-TEM and XRD analyses after CVD and high-temperature treatments. Thus, in contrast to the original carbon xerogel surface, the carbon layer was found to exhibit a graphitizable nature. The CVD coating was also found to significantly cover the micropore texture. However, none of the chosen treatments detrimentally impacted the external surface area of the carbon nodules (*i.e.* the carbon surface excluding the internal micropores) and the meso/macropore texture of the carbon xerogel, essential for gas transport, water management, and deposition of metal nanoparticles. Among the different CVD durations performed, the carbon xerogel treated for 20 min by CVD was selected as the optimal carbon support, as it enabled the clear deposition of secondary layer, evidence by a marked decrease in the micropore volume, without extensive treatment duration. This CVD-coated carbon xerogel after high-temperature treatment at 1,500 ºC was also selected for Pt deposition. Finally, the CX treated in the most intense conditions, namely 60 min of CVD, was also selected for electrocatalyst manufacturing in the following chapter.

Catalytic phase deposition and electrochemical characterization

The central objective of this thesis was the evaluation of the electrochemical performances of Pt catalysts supported on post-treated carbon xerogels. The aim was to evaluate how their performances compare with regards to equivalent catalysts supported on pristine CX and on commercial carbon blacks. In Chapter 2, the three post-treated carbon xerogels identified in Chapter 1, along with the pristine CX, were loaded with Pt nanoparticles *via* a standard Pt deposition procedure. Transmission electron microscopy (TEM) was used to visually characterize the catalysts. It was observed that nanoparticles were deposited homogenously on all samples with only minor variations in particle size distributions. Moreover, the observed nanoparticle sizes (3.4 to 3.7 nm) remained compatible with PEMFC applications. The catalytic activities and Pt ElectroChemically active Surface Area (*ECSA*) were assessed in a three-electrode configuration, in 0.5 M H_2SO_4 aqueous electrolyte, using a Rotating Disk Electrode

(RDE). The electrochemical performances of these catalysts were also evaluated after accelerated aging. The aging procedure consisted in 5,000 and 20,000 cycles of potential between 0.6 and 1.0 V *vs.* RHE at 80 ºC. A commercial carbon black-supported catalyst was also tested and characterized in the same conditions as the carbon xerogel-supported catalysts.

The results obtained in RDE configuration confirmed that the initial electrochemical performances of a catalyst supported on a carbon xerogel with appropriate pore texture were on par with those of a carbon black-supported catalyst. The initial catalytic performances also showed that the catalyst supported on the carbon xerogel treated 20 min by CVD exhibits slightly better performances that the untreated counterpart. Nonetheless, the performances were more nuanced with the carbon xerogel coated for 60 min. These changes in catalytic activity were attributed to the above-mentioned variations in Pt nanoparticles size on the different carbon surfaces upon CVD treatment. In terms of resilience upon aging, Pt nanoparticles tend to agglomerate less upon aging after CVD and high-temperature treatment. However, as previously stated, the nanoparticles were initially slightly larger. Moreover, all carbon xerogel-supported catalysts displayed a tendency for increasing catalytic activity upon aging. This was attributed to the nanoparticles average size that initially may have been too small.

Study of nitrogen doping

The third chapter focused on surface nitrogen-doping of carbon xerogels, performed *via* a N_2-based plasma treatment. This post-treatment was performed on the pristine CX and on the CX coated 20 min by CVD, as designed in Chapter 1. By varying the plasma working parameters, different nitrogen contents at the surface of these two carbon xerogels were obtained. Surface analyses performed with XPS allowed to determine the total nitrogen percentage at the surface of the carbon xerogels, which ranged between 1.5 and 7.2 at.%. Moreover, the presence of pyridinic, pyrrolic and graphitic nitrogen species was reported. This range of nitrogen content, as well as the nitrogen-containing functional groups observed on these samples are commonly reported in the literature to bring a positive effect on the catalyst-support interaction [2]. Pt nanoparticles were deposited on these N-doped carbon xerogels following the same procedure as in Chapter 2, and their electrochemical evaluation was again performed in RDE configuration, in 0.5 M H_2SO_4 electrolyte. The same accelerated aging procedure as in Chapter 2 was also used again.

TEM analysis showed that the size of the Pt nanoparticles decreased slightly in the case of N-doped CX while it remained relatively stable with the CX that was CVD-coated prior to N-doping. However, despite the successful incorporation of nitrogen, catalysts supported on N-doped carbon xerogels did not exhibit a marked increase of stability upon aging, compared to their undoped counterparts. Indeed, the catalytic activity towards ORR measured after complete aging procedure remained similar. Moreover, at higher nitrogen surface content (7.2 at.%), the *ECSA* was lower than that measured for the other carbon xerogel-supported catalysts, suggesting that high nitrogen content can even play a detrimental role. The results obtained here differ from the trends usually reported in the literature, where the incorporation of N in a carbon matrix is often associated with enhanced catalytic layer durability. It is worth noting that the carbon xerogel employed in this thesis differs from more commonly studied carbon supports (carbon black, carbon nanotubes, *etc.*). Nonetheless, the use of carbon xerogel as N-doped carbon support for PEMFC catalytic layer should not represent an issue, as shown from the work of Alegre *et al.* [3]. Nonetheless, the exact effects of nitrogen doping are complex and not always fully understood. Undoubtedly, the incorporation of heteroatoms in a carbon support induce changes in the charge and spin density of the carbon network, which could ultimately improve the durability of PEMFC catalytic layers. However, as was highlighted in Chapter 3, the heteroatom doping treatment can also induce changes in the crystallinity, pore texture or number of nucleation sites of the carbon support, which can affect the Pt nanoparticle growth. Thus, nanoparticles of different sizes can be obtained, either closer or further away from their optimum size, ~ 3.5 nm. Since the catalytic activity towards ORR and catalytic layer stability is directly related to the Pt nanoparticles size, the reported improvement of Pt nanoparticles stability on N-doped supports could be biased. Finally, considering that heteroatom doping introduce additional steps and a raised processing cost, the study performed in this thesis questions the viability of nitrogen doping treatment towards improved durability of PEMFC catalytic layers.

Durability study

The final chapter consisted in a durability study in Membrane-Electrodes Assembly (MEA) configuration, on a fuel cell test bench. Five carbon xerogel-supported Pt catalysts with the best durability under accelerated aging observed in RDE configuration in previous chapters were selected and were processed into MEA. These five catalysts included the pristine CX as well as four post-treated carbon xerogels. This includes the CX treated 20 min by CVD, and the CX treated 20 min by CVD, subsequently subjected to high temperature-treated. It also includes the

N-doped CX as well as the CX treated 20 min by CVD and subsequently N-doped. All these catalysts encompass the three different post-treatments investigated in this thesis. Similar to Chapter 2, the commercial carbon black-supported catalyst was also evaluated in this configuration. The durability in operating PEMFC of all these samples was again evaluated after accelerated aging, which consisted first in 10,000 cycles of steady potential steps at 0.6 and 1.0 V *vs.* RHE, then followed by 20,000 additional cycles. The commercial catalyst exhibited relatively poor initial electrochemical performances compared to the active layers supported on carbon xerogel. This observation contrasts to what was observed in Chapter 2, and to what is usually reported in the literature. This difference was ascribed to the catalyst ink formulation used in ths thesis that was better optimized for carbon xerogel-supported catalysts than for the carbon black-supported catalyst, leading to a larger fraction of Pt not being utilized. Nonetheless, the retention upon aging of the *ECSA* and current density could still be assessed and compared to that of the carbon xerogel-supported catalysts. Regarding the active layers supported on carbon xerogel, a small increase in durability is observed on the CVD-treated CX, compared to the pristine CX. However, the durability of the two active layers supported on N-doped carbon xerogel remained very similar compared to their undoped counterparts. This result is consistent with the observations reported in Chapter 3. However, it leads to the conclusion that the nitrogen doping strategy explored here did not lead to a clear improvement in terms of catalytic layer durability. Finally, the catalyst supported on the CX treated both by CVD and then by high temperature post-treatments exhibited the most promising durability upon aging, which could be ascribed to the higher degree of surface ordering. However, the reproducibility of the measurements was particularly challenging for this sample, and further studies are required to confirm the findings observed.

Outlook

This thesis aimed at developing more durable carbon supports. To this end, the surface of the carbon xerogel was modified to improve its resistance to oxidation and to strengthen the interaction between the carbon support and the catalyst so as to limit migration and aggregation of Pt nanoparticles. Encouraging results were obtained on the carbon xerogel coated with a carbon layer and subsequently graphitized at high temperature under inert atmosphere. Indeed, a significant increasing in surface ordering was observed while the electrochemical performances of the corresponding catalyst were well-retained upon accelerated aging in test bench configuration. Nevertheless, in this thesis, only one sample subjected to this high-temperature treatment was evaluated. Varying the treatment conditions, such as the temperature

or the duration, would allow to determine optimized conditions that produce the most durable carbon support.

Regarding nitrogen doping, different N atomic percentages at the surface of the carbon xerogel were obtained without modification of its pore texture. However, the durability of catalysts supported on these N-doped carbon xerogels was not significantly better compared to the non-doped counterpart. This raised questions about the actual effectiveness of nitrogen doping to obtain more stable Pt nanoparticles. Nevertheless, other strategies could be applied in the future to further complement the findings reported in this thesis. For instance, it could still be interesting to combine all three post-treatments explored in this thesis, *i.e.* to first perform CVD then high-temperature treatment in optimized conditions, and to eventually perform N-doping *via* plasma treatment in a N_2 atmosphere.

Moreover, instead of carrying out the CVD and N-doping as two separate steps, the use of a nitrogen-rich carbon precursor during the CVD treatment, in place of the ethylene used in this thesis, could provide both carbon and nitrogen sources. This could potentially enable the direct deposition of a N-doped carbon coating at the surface of the carbon xerogel. The deposition of a nitrogen-doped carbon film could also be achieved using a plasma-enhanced chemical vapor deposition treatment [4]. Such treatment would require the use of a different reactor than used with CVD but would also enable a one-step approach. These processes would also need to be adjusted to optimize the carbon coating properties and refine the amount of N-containing functional groups and their relative proportions. More generally, regarding heteroatom doping, the insertion of other p-block doping elements could also be performed in future research. For instance, some carbon materials doped with sulfur-containing or phosphorus-containing functional groups were reported to exhibit higher catalytic activity towards ORR. These heteroatoms, in a similar manner with nitrogen, are known to induce changes in the charge and spin densities of the carbon atoms adjacent to them, which could play a role in Pt nanoparticles stabilization upon aging.

Finally, the most durable catalysts could be exposed to more stringent accelerated aging to further complete the durability study. Indeed, the AST procedures used in this thesis primarily aim at inducing Pt degradation with minimal carbon oxidation. Nevertheless, provided the Pt remains sufficiently stable after these ASTs in mild conditions, the application of higher potential holds, typically between 1.0 and 1.5 V *vs.* RHE, could be employed to simulate startup/shutdown conditions encountered in commercial PEMFC stacks. This would further

complement the durability study and provide deeper insights into the long-term durability of carbon xerogel-supported catalysts.

References

[1] N. Job, J. Marie, S. Lambert, S. Berthon-Fabry, P. Achard, Carbon xerogels as catalyst supports for PEM fuel cell cathode, *Energy Conversion and Management*, 49 (2008) 2461–2470.

[2] H. Wang, T. Maiyalagan, X. Wang, Review on Recent Progress in Nitrogen-Doped Graphene: Synthesis, Characterization, and Its Potential Applications, *ACS Catalysis*, 2 (2012) 781–794.

[3] C. Alegre, D. Sebastián, M. Gálvez, E. Baquedano, R. Moliner, A. Aricò, V. Baglio, M. Lázaro, N-Doped Carbon Xerogels as Pt Support for the Electro-Reduction of Oxygen, *Materials*, 10 (2017) 1092.

[4] J. Hartmann, M. Schreck, T. Baur, H. Huber, W. Assmann, H. Schuler, B. Stritzker, B. Rauschenbach, Incorporation of nitrogen into carbon films produced by PECVD under bias voltage, *Diamond and Related Materials*, 7 (1998) 899–902.